# Designing a beam combiner for faint limiting magnitudes in optical interferometry

Daniel James Mortimer

St Edmund's College

**UNIVERSITY OF CAMBRIDGE**

September 2021

This thesis is submitted for the degree of Doctor of Philosophy

# Declaration

This thesis is the result of my own work and includes nothing which is the outcome of work done in collaboration except as declared in the Preface and specified in the text. I further state that no substantial part of my thesis has already been submitted, or, is being concurrently submitted for any such degree, diploma or other qualification at the University of Cambridge or any other University or similar institution except as declared in the Preface and specified in the text. It does not exceed the prescribed word limit for the Physics and Chemistry Degree Committee.

- Chapter 1 is an introduction to the topics contained in this thesis and is mostly referenced from the literature.
- Chapter 2 discusses the design of the interferometer I am building an instrument for and is mostly referenced from Buscher et al. (2013).
- Chapter 3 is a summary of design requirements for the instrument developed between the project scientist of the interferometer and myself.
- Chapter 4 is my own work.
- In chapter 5 the model for calculating the throughput and visibility loss of the MROI beam train is based on a model produced by group member David Buscher in the H and K bands. This model was updated to include the J band. The throughput and visibility losses of the FOURIER beam combiner is my own work, as is the implementation of the SNR calculation.
- Chapter 6 Provides an overview of the optomechanics for the instrument developed primarily by group member Xiaowei Sun, based on alignment requirements I provided. The cryostat, designed and built by Universal Cryogenics, based on design requirements I provided, is also shown.

- Chapter 7 is my own work with the exception of the Fourier transform spectroscopy code which was provided by group member James Luis. Parameter tuning and subsequent analysis of the recovered spectra are my own work. The laboratory light source used in this chapter is based on an implementation by James Luis which was modified as described in section 7.2.2.

- Chapter 8 is my own work and has been published as Mortimer & Buscher (2022) by the Oxford University Press. All figures in chapter 8 (with the exception of figure 8.1) also appear in the aforementioned publication.

# Summary

Title: Designing a beam combiner for faint limiting magnitudes in optical interferometry

Author: Daniel James Mortimer

In this thesis I present and discuss the work carried out during my PhD in the astrophysics group of the Cavendish Laboratory. The majority of this work has been to develop the Free-space Optical multi-apertUre combineR for IntERferometry (FOURIER), a novel, high sensitivity, near-infrared beam combiner intended to be the first generation science beam combiner for the Magdalena Ridge Observatory Interferometer (MROI). FOURIER is a three telescope, J, H and K band image plane beam combiner.

I first highlight the scientific motivation for a faint limiting magnitude beam combiner and the design requirements this placed on FOURIER. This is followed by a discussion of how the optical design was derived from these requirements. The simulated performance of the instrument is then discussed including the alignment and manufacturing error budget, limiting magnitude estimation, spectral resolution and modelling of thermal effects on cooling the instrument to its liquid nitrogen operating temperature. The cryogenic optomechanics are described as well as a series of laboratory tests of the fringe contrast, spectral resolution and throughput to verify the instruments performance.

In addition to the development of FOURIER I discuss a numerical simulation of an optical interferometer subject to atmospheric seeing, used to quantify previously unaccounted for image plane crosstalk effects arising due to various combinations of atmospheric seeing, long propagation distances and finite sized optics present in long baseline optical interferometers.

# CONTENTS

# LIST OF FIGURES

# LIST OF TABLES

# Acknowledgements

Above all, I would like to thank my supervisor, David Buscher, for all the guidance and support over the last four years. I will always be grateful for your patience and lack of judgement while discussing the same concepts again and again.

I am deeply indebted to the rest of the Cambridge optical interferometry group, in particular David (Xaiowei) Sun for making the time to develop the optomechanics for FOURIER as well as providing 100+ practical tips for building an instrument which you won't find in a textbook. Bodie Seneta for worrying about all the cabling and electronics of FOURIER and also providing many practical tips. Chris Haniff for your frank review of many of my documents, my writing wouldn't be half of what it is today without your guidance. Finally, James Luis, even though you didn't want me to sit next to you in the office it has been an honour to navigate this bizarre world of PhD life with you.

It's unlikely I would be doing a PhD without my longest-term supporters, Mum and Dad. Thank you for all those years of going with me to dark sky sites and countless astronomy lectures, for supporting me in going to the International Astronomical Youth Camp (IAYC) which has given me so much and for not wavering for a second when I decided I was going to teach myself A level maths because that's what I had to do to follow my passion. Your support has been invaluable. I also must mention arguable the proudest grandparents in the world!

And finally, my partner Evi, thank you for being my IT support, LaTeX guide, proofreader, talk reviewer, motivational coach and above all, best friend. Thank you for putting up with me these last few months, I look forward to returning the favour when you write your thesis.

# INTRODUCTION

## 1.1 Introduction

Long Baseline Optical Interferometry (LBOI) is a powerful observational technique by which observations with spatial resolutions 40 times that of 8 m class telescopes are routinely carried out. This chapter includes a discussion of why this technique is needed, followed by a brief historical overview of the development of the field. The interferometric observables are also discussed, as well as the pros and cons of some popular beam combination schemes used to extract these observables. Finally, the scientific motivation of both the Magdalena Ridge Observatory Interferometer (MROI) and the Free-space Optical multi-apertUre combineR for IntERferometry (FOURIER) beam combiner are presented.

## 1.2 Why LBOI

Major advances in the field of observational astronomy are often the result of new hardware or observational techniques becoming available, making new areas of parameter space accessible; whether that is spectrographs precise enough to detect the spectroscopic "wobble" due to an orbiting exoplanet (Mayor & Queloz 1995), or the development of observational techniques that can operate a radio interferometer with Earth sized baselines to image the event horizon of

a black hole (Event Horizon Telescope Collaboration et al. 2019). These are but two examples of what can be achieved when a new parameter space is opened up.

LBOI opens up the parameter space of high angular resolution in the optical. An ideal telescope, that is one not affected by atmospheric turbulence or optical aberrations, is fundamentally limited by the size of the collecting aperture (typically a mirror in modern large telescopes). The diffraction limit is given by $\Theta = 1.22\lambda/D$, where $\Theta$ is the angular resolution, $\lambda$ the wavelength of observation and $D$ the diameter of the collecting aperture. As an example, a 8 m class telescope operating in the near-infrared at a wavelength of $\lambda = 1.65\,\mu$m is "diffraction limited" to 50 milli-arcseconds (mas). The next generation of 30 m class telescopes will have a diffraction limited resolution of 13 mas at the same wavelength. While this is a significant improvement, such resolution is insufficient for some science cases e.g. at this resolution only features on the nearest and most evolved stars such as Betelgeuse, at approximately 42 mas in diameter (Ohnaka et al. 2011), could be resolved. Given that such observatories will also be one of a kind, observing time for regular long term monitoring campaigns using such telescopes will be extremely costly.

In contrast, current generation LBOI has routinely operated on baselines as long as 330 m for the past two decades (Ridgway et al. 2003) with an equivalent diffraction limit of 1.2 mas (again at a wavelength of $\lambda = 1.65\,\mu$m). With kilometre long baselines expected to become available on the same timescale we expect first light for the ELT (Gies et al. 2019), it is clear that optical interferometry has, and will continue to, open up new parameter space in observational astronomy by providing angular resolutions well beyond what is possible with single dish optical telescopes.

## 1.3   Historical perspective

The history of LBOI has arguably been a story of stops and starts as astronomers had to wait for new technology to be developed to keep up with the technical demands of LBOI. The use of the interferometric properties of light for astrophysics dates back to Fizeau (1868), who suggested that by studying the properties of interference fringes generated by observing a star through two widely spaced slits, it would be possible to determine the angular diameter of the star. The challenge was taken up some years later by Stéphan (1873), who initially believed he had observed the disappearance of interference fringes (the condition for resolving the diameter of

the star) for the star Sirius with a slit separation of 50 cm, implying an angular diameter of 271 mas (for observations at λ = 540 nm). Given that modern day interferometric measurements of the angular diameter of Sirius A place it at 6 mas (Davis et al. 2011), we can see that the disappearance of fringes was not due to the star being resolved but instead likely due to atmospheric turbulence. Given the size of telescopes at the time, the technique of directly mounting slits over the aperture would not provide angular resolutions high enough to resolve any stars in the night sky and so attempts stalled.

The field would have to wait for the arrival of Albert Michelson for progress to be made. In Michelson (1890) he laid out the mathematical framework for measuring the visibility: plotting a visibility curve showing the contrast of the interference fringes decreasing as the slit separation came closer to resolving the target before passing through a null when the target was fully resolved. He would soon after demonstrate this by measuring the angular diameter of Jupiter's moons in Michelson (1891) by placing a mask with two adjustable slits over the Lick observatories 12 inch refractor, finding the results to be in good agreement with other attempts to measure the angular diameter of Jupiter's moons by micrometry at the time.

Karl Schwarzchild briefly also contributed to the field of optical interferometry, producing interferometric measurements of binary star systems using the 10 inch refractor of Munich University's observatory (Schwarzschild 1896). While other interferometric measurements of Jupiter's moons were carried out (Hamy 1899), the field of optical interferometry would stall again.

The next breakthrough in optical interferometry would come some 20 years later and achieve the goal set out by Fizeau of measuring the angular diameter of a star. Realising that the method of placing slits directly over the aperture of the telescopes at the time would not produce baselines long enough to resolve a stellar disk, an instrument consisting of a pair of fold mirrors mounted along a beam at the top of the 100 inch telescope on Mt Wilson was employed to redirect starlight from baselines up to 20 feet (6 meters) to within the 100 inch aperture of the primary mirror. From here the beams would then be combined by the telescope optics. Observations carried out by Francis Pease and John Anderson on the night of the 13th December 1920 successfully recorded the disappearance of fringes on Betelgeuse (Michelson & Pease 1921). Other stellar diameters were subsequently measured with the 20 foot interferometer (Pease 1931), as well as some binary stars (Anderson 1920; Merrill 1922).

Attention soon turned to building a 50 foot interferometer. Unfortunately, the 50 foot did not produce many scientific results due to both engineering problems and the limited usefulness of the human eye coupled with atmospheric seeing (Pease 1923) to measure the exact location the visibility passed through a null. Arguably the limit of what visual optical interferometry could do had been reached. It was not until the development of methods for recording interference fringes that the field would develop further.

What is believed to be the first attempt to record fringes to enable quantitative measurements of fringe contrast would come from Willet Beavers (Beavers 1963). This work arguably marks the start of modern LBOI, where fringe contrast could be measured much more accurately and at many baselines, not just where the visibility passes through a null, and so move beyond the measurement of the angular diameter of stars to the diverse field optical interferometry is today.

The first fringes produced by combining light from two independent telescopes was carried out by Labeyrie (1975), demonstrating fringes on the star Vega. The interferometer had baselines up to 12 m. The next milestone that would be crucial for modern long baseline amplitude interferometry was achieved by the Mark I interferometer, which demonstrated fringe tracking (the removal of atmospherically induced piston errors) in March 1979 (Shao & Staelin 1980). The first interferometer to demonstrate image reconstruction in the optical was the Cambridge Optical Aperture Synthesis Telescope (COAST) in September 1995 (Baldwin et al. 1996), imaging the star Capella.

From this point on there was a rapid expansion in the number of interferometers, with most of the interferometers developed in the late 1990's and early 2000's still in operation today. These include the Navy Precision Optical Interferometer (NPOI), formerly The Navy Prototype Optical Interferometer (Armstrong et al. 1998). the Center for High Angular Resolution (CHARA) array (ten Brummelaar et al. 2005), the recently decommissioned Sydney University Stellar Interferometer (SUSI) (Davis et al. 1999), the now decommissioned Palomar Testbed Interferometer (PTI) (Colavita et al. 1999), a forerunner to the now decommissioned Keck interferometer (Colavita et al. 2013), which was the first to demonstrate LBOI on the 8-10 m large telescopes, obtaining first fringes with the 10 m Keck telescopes on the 12th March 2001. This was very closely followed by the Very Large Telescope Interferometer (VLTI), which obtained first fringes on the 8 m Unit telescopes (UTs) on 30th October 2001, just over half a year after the VLTI demonstrated first fringes with a pair of test siderostats (Glindemann et al.

2001).

There is still a lot to be done with this current generation of interferometers. However, the next generation is already under development. A major upgrade to the CHARA interferometer is planned, which would see it change from six 1 m telescopes on baselines up to 330 m upgraded to 12, 2 m telescopes operating on baselines up to 1.2 km. The array will be re-branded the CHARA Michelson Array (CMA) and will use optical fibers to transport the starlight instead of the current evacuated "lightpipes", where telescope light is propagated through free space (Gies et al. 2019). Another interferometer under development is the MROI. The MROI has been designed with the goal of producing model independent images of faint targets. When completed it will comprise of ten 1.4 m telescopes on baselines 7.8-347 m. The goal of the MROI is to perform fringe tracking on targets as faint as 14th magnitude in the H band, this would be 6-7 magnitudes fainter than equivalent systems at current generation LBOI facilities (see table 1.1) and would open up large scale studies on classes of objects previously too faint for LBOI such as Active Galactic Nuclei (AGN) (Buscher et al. 2013).

What I have presented here is only a brief historical background of optical interferometery, focusing solely on milestones in instrumentation development and even then limited to developments that directly led to long baseline amplitude optical interferometry. This does not cover the development of other techniques such as intensity interferometry, heterodyne combination schemes or aperture masking. For a more detailed history of the development of LBOI (with a focus on Mount Wilson's role in the field) I recommend McAlister (2020).

## 1.4 Interferometric observables

A LBOI is a device designed to measure the degree of coherence of two beams of starlight collected by two telescopes separated some distance (baseline) apart. Consider a beam of starlight represented by the complex notation of an electromagnetic plane wave

$$\mathbf{\Psi_0} = |\Psi_0|e^{i\phi_0}, \tag{1.1}$$

where $\Psi_0$ is the amplitude and $\phi_0$ the phase of the plane wave. With its associated electric field being

$$E_0 = \sqrt{\frac{2}{\epsilon_0}} \text{Re}\{\mathbf{\Psi_0}\}, \tag{1.2}$$

where $\epsilon_0$ is the electric permittivity of free space. Due to the very rapid oscillatory period of electromagnetic radiation in the optical (of order a few femtoseconds) what is recorded by a detector is not the oscillatory wave itself, but the mean intensity given by

$$I_0 = |\mathbf{\Psi_0}|^2 = \epsilon_0 E_0{}^2. \tag{1.3}$$

If two beams of starlight, $\mathbf{\Psi_1}$, $\mathbf{\Psi_2}$ are simultaneously shone on a detector the resulting intensity $I$ is the sum of the two electric fields, i.e.

$$I = \epsilon_0 (E_1 + E_2)^2, \tag{1.4}$$

which, from combining equations (1.2) and (1.3) can be written as

$$I = \text{Re}\{|\Psi_1|e^{i\phi_1} + |\Psi_2|e^{i\phi_2}\}^2. \tag{1.5}$$

This gives, following the form of section 1.4.1 of Buscher (2015), after expansion and dropping terms which average to zero over the integration time of a detector, the intensity pattern to be

$$I = |\Psi_1|^2 + |\Psi_2|^2 + 2\text{Re}\{\Psi_1\Psi_2{}^* \cos(\theta)\}. \tag{1.6}$$

Where $\Psi_2{}^*$ denotes the complex conjugate of $\Psi_2$. This is the sum of the intensities of the two individual beams plus a cross term which varies in intensity as a function of $\theta$, the phase (or path difference) between the two beams $(\phi_1 - \phi_2)$. How $\theta$ is varied depends on the design of the optical interferometer and beam combiner (detector instrument), however, it is sufficient to say here that this term typically varies sinusoidally and is responsible for producing interference fringes. The interference fringes provide a measure of the coherence of the two beams being combined as the coherence is given by $C = < \Psi_1\Psi_2{}^* >$ where $<>$ denotes averaging the complex amplitude over time.

The importance of this measure of coherence becomes clear by considering the van Cittert-Zernike theorem (van Cittert 1934; Zernike 1938). This theorem relates the source brightness distribution on-sky (the image) to the complex coherence function by

$$I(x, y) = \int_{-\infty}^{\infty} \int_{-\infty}^{\infty} C(u, v) e^{2\pi i (xu + yv)} \, du \, dv, \tag{1.7}$$

where $x$ and $y$ are perpendicular axes of the 2D on-sky image and $u$ and $v$ corresponding spatial frequencies. This result shows that the on-sky source brightness distribution is the 2D Fourier transform of the complex coherence function. Measuring the interference fringes produced by one baseline samples one point, in what is typically called the "uv plane". Baselines of different length or position angles measure different points in the uv plane.

In theory, by measuring every baseline between a telescope separation of $0\,\text{m}$ to infinity at all position angles one can reproduce a perfect image of the source brightness distribution. Measuring an infinite number of baselines is of course not practical, however, measuring even a single baseline can provide useful information of the target under observation, for example the diameter of a stellar disk on-sky.

From the interference fringes an interferometer produces the complex coherence function could be reconstructed by extracting both its amplitude and phase. The amplitude of the complex coherence function can be extracted by

$$V = \frac{I_{max} - I_{min}}{I_{max} + I_{min}} = |C(u, v)|, \tag{1.8}$$

where $V$ is the ratio of the intensity of the modulation of the interference fringes to the average intensity of the light on the detector. This is referred to in the literature as both the fringe contrast and visibility amplitude and the two phrases are used interchangeably throughout this thesis. The phase of the complex coherence function is given by the position of the central fringe with respect to the zero optical path difference ($\theta = 0$ in equation (1.6)). The complex coherence function is given by $C = V e^{i\Phi}$, where $\Phi$ is the phase of the complex amplitude. In this form, $C = V e^{i\Phi}$ is known as the complex visibility.

In practise, atmospheric seeing makes it impossible to measure the complex visibility directly as the atmosphere introduces random phase perturbation to both beams so $\theta$ is unknown. Two interferometric observables can still be extracted. The first is the power spectrum, $S^{ij}$, between a pair of telescopes $i$ and $j$ given by

$$S^{ij} = C^{ij} C^{ij*} = |C^{ij}|^2. \tag{1.9}$$

This provides information about the amplitude of the complex visibility. The second is the bispectrum formed for a closed triangle of telescopes $i$, $j$ and $k$, given by

$$B^{ijk} = C^{ij} C^{jk} C^{ki}. \tag{1.10}$$

From the bispectrum the closure phase is defined as

$$\Phi^{ijk} = \tan^{-1} \left( \frac{\text{Im}(B^{ijk})}{\text{Re}(B^{ijk})} \right), \tag{1.11}$$

which recovers some of the phase information in the presence of atmospheric turbulence. To demonstrate how closure phase works, consider a measured phase of $\Phi^{ij} = \phi^{ij} + \epsilon_i - \epsilon_j$, where $\phi^{ij}$ is the true phase and $\epsilon_i$, $\epsilon_j$ the atmospheric perturbations associated with telescopes $i$ and $j$, respectively. Repeating this for the three baselines in equation (1.10) the closure phase is given by

$$\Phi^{ijk} = \phi^{ij} + \epsilon_i - \epsilon_j + \phi^{jk} + \epsilon_j - \epsilon_k + \phi^{ki} + \epsilon_k - \epsilon_i = \phi^{ij} + \phi^{jk} + \phi^{ki}. \tag{1.12}$$

Hence all the atmospheric phase perturbations cancel out and the closure phase is a robust measurement.

By combining beams of starlight from separate telescopes and extracting the above observables from the resulting interference fringes, information and even "images" of the on-sky source brightness distribution can be recovered. The power of LBOI lies in the fact that the longer the baseline, the higher the spatial frequency sampled in the uv plane. Telescopes separated by hundreds of meters thus resolve features on-sky that would require a single dish telescope of the same size to resolve. This is a very short overview of how an optical interferometer is used to recover spatial information about objects on-sky. I recommend Monnier (2003); Haniff (2007) for a more detailed discussion of this topic.

## 1.5   Beam Combination Schemes

A beam combiner is typically a stand alone instrument installed at the end of a beam train of an optical interferometer. Its role is to take the path equalised beams of starlight from two or more telescopes and combine them in some form to produce interference, from which the interferometric observables mentioned in the previous section can be extracted. Here I briefly
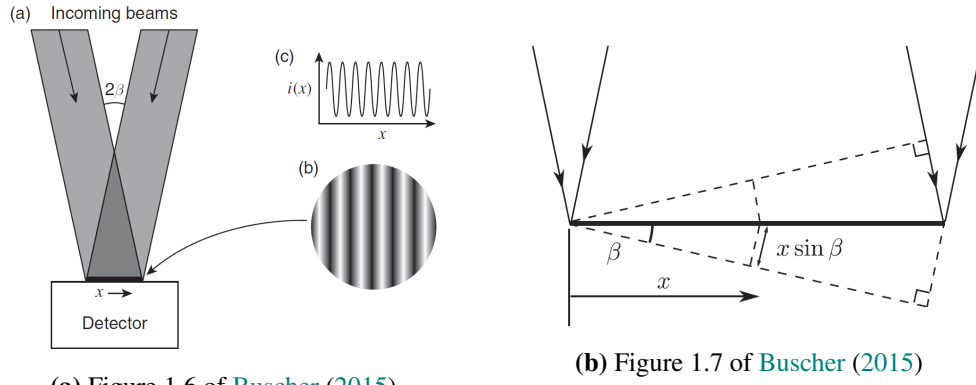
**(a)** Figure 1.6 of Buscher (2015)



**(b)** Figure 1.7 of Buscher (2015)

**Figure 1.1:** Pupil plane combination. Left: the two incoming beams of starlight at an angle $\beta$ with respect to the detector, (a), as well as a 2D image of the spatially modulated interference fringes, (b), and a 1D slice of the intensity, (c). Right: the phase difference introduced between the two beams as a function of position along the detector. Here $\theta$ from equation (1.6) is given by $\theta = 2x \sin(\beta)/\lambda$. © David F Buscher, Practical Optical Interferometry: Imaging at Visible and Infrared Wavelengths, 1st ed 2015, reproduced with permission of the licensor through PLSclear.

discuss the architecture of a few beam combination schemes to highlight their differences, pros and cons. I will mainly discuss a two telescope beam combination system, however, these designs can be scaled up to combine light from more than two telescopes at a time.

### 1.5.1 Pupil plane combination

In this scheme the path equalised, collimated beams of starlight are shone at an angle onto the detector, producing interference fringes over the resulting overlapping pupils. Figure 1.1 shows an example of this beam combination scheme and figure 1.1a displays the two beams of starlight landing on the detector at an angle $\beta$ producing interference fringes. The fringes vary in intensity across the detector, known as spatially modulated interference fringes. The phase difference $\theta$ from equation (1.6) is given by $\theta = 2x \sin(\beta)/\lambda$, where $x$ is the position along the detector and $\lambda$ is the wavelength of observation.

This is arguably the simplest beam combiner design, with the two beams of starlight landing directly onto the detector, maximising system throughput and minimising the number of components which can become misaligned, both of which improve the limiting magnitude of the system (see section 5.7). As Buscher (2015) points out, however, such a scheme is often impractical. The peak-to-peak spacing of the resulting interference fringes is given by $\lambda/2 \sin(\beta)$, so for a wavelength of $\lambda = 0.5\,\mu m$ with $5\,cm$ diameter starlight beams the distance between the combining mirrors and detector would have to be $100\,m$ to achieve a fringe spacing

of 1 mm. This would require a very large beam combining area, as well as the placement of tight angular alignment tolerances on the mirrors which bring the light to the detector.

### 1.5.2   Co-axial pupil plane combination

This scheme also operates with the beams of starlight in the pupil plane. It is referred to as co-axial pupil plane combination as the beams of starlight are parallel to each other at combination. This co-axial scheme is more common than the previously mentioned pupil plane beam combination and is often referred to simply as pupil plane combination.

Co-axial pupil plane combination has no phase variation as a function of position along the detector, as discussed in figure 1.1, and so does not produce spatially modulated interference fringes. Instead, the intensity is uniform at the detector across the combined pupils. Interference fringes are instead generated by the use of a scanning mirror to modulate the Optical Path Difference (OPD) between the two beams and in doing so introducing the phase variation ($\theta$ in equation (1.6)) by $\theta = d(t)/\lambda$, where $d(t)$ is the position of the mirror as a function of time. The result of this is shown in figure 1.2 and produces two output channels, where the intensity of light varies sinusoidally as a function of time, as the light from the two beams move in and out of phase with each other during the mirror scan.

The relative phase of the two beams is shifted $180°$ between the two outputs such that when maximum constructive interference is observed at one output, maximum destructive interference is seen at the other. In theory this means monitoring both channels is unnecessary as they provide the same information, however, doing so is beneficial as it can help calibrate the data for effects such as variation in the total intensity of light from the two beams. Subtracting the recorded intensities of the two outputs will remove any offset in the total amount of light, this can improve the accuracy of the measured visibilities (Buscher 2015).

A single scan of the fringes must be carried out rapidly enough to measure the fringe modulation before atmospheric seeing significantly alters the phase between the two beams. This timescale is characterised by the atmospheric coherence time, $t_0$ which is approximately 20 ms in the near-infrared (see section 5.7.1). Assuming a sampling of four measurements per fringe cycle this means the detector integration time is limited to less than 5 ms.

It is possible to combine multiple measures of the visibility to improve the Signal to Noise Ratio (SNR) of an observation and as a single measure is of order 20 ms it is possible to
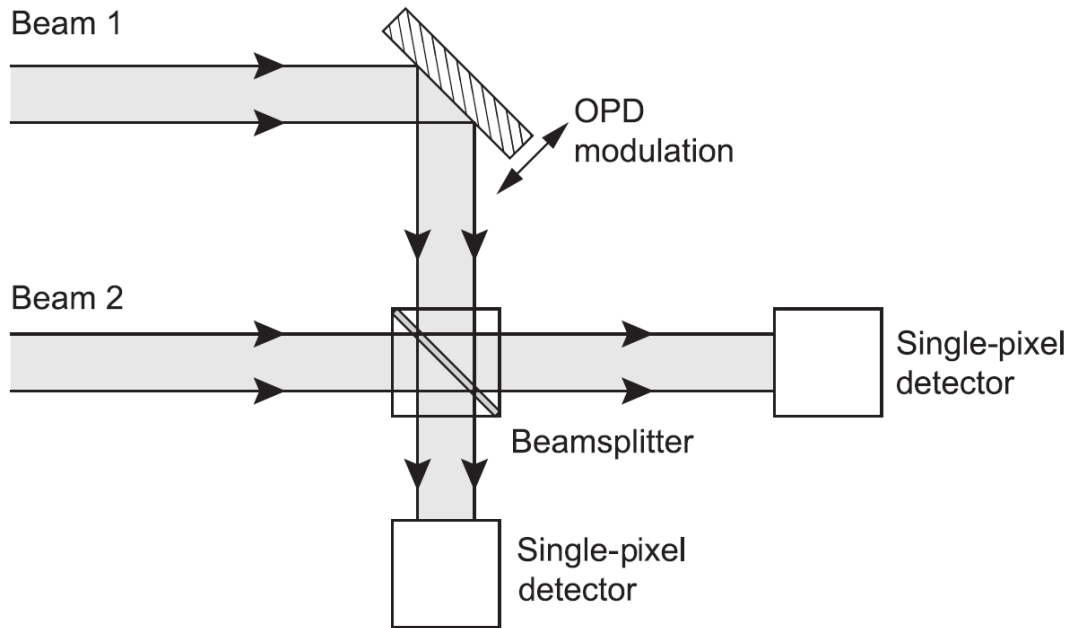
**Figure 1.2:** A diagram of a two beam co-axial pupil plane combiner. The two beams of starlight are combined by the beamsplitter and produce a uniform intensity across the pupil at each detector. This intensity varies as the scanning mirror introduces a phase difference between the two beams. This is figure 4.11 of Buscher (2015). © David F Buscher, Practical Optical Interferometry: Imaging at Visible and Infrared Wavelengths, 1st ed 2015, reproduced with permission of the licensor through PLSclear.

make thousands of scans within a few minutes of observation. However, as detector read noise contributes every time the detector is read out this scheme of making thousands of measures means observations very sensitive to read noise. For this reason a very sensitive, low read noise detector is necessary. One of the key advantages of co-axial pupil plane beam combination is that only a single pixel detector is required and so highly sensitive photomultiplier tubes can be used. This scheme was particularly favoured in the 1980's and 1990's when large format detectors had considerable levels of read noise. It was implemented at the Mark I, II and III interferometers (Shao & Staelin 1980; Shao et al. 1986, 1988), COAST (Baldwin et al. 1994), PTI (Colavita 1999) and SUSI (Davis et al. 1999) to name just a few.

This method of beam combination is still in use today, for example with the CLASSIC/CLIMB combiner at CHARA (Ten Brummelaar et al. 2013) but with the advent of low read noise large format detectors in both the optical and near-infrared it is less commonly used.

The Co-axial pupil plane combination described above can be modified to include spectral dispersion, but requires extra optics after the beams have been combined to spectrally dis-

perse the light and at least one pixel per spectral channel to record the temporally modulated interference fringes as proposed by Baron et al. (2006).

### 1.5.3  Image plane combination

The earliest beam combiners in optical interferometry were the human eye, which were image plane combiners. As mentioned in section 1.3 the earliest works in observational optical interferometry (Stéphan 1873; Michelson 1891; Michelson & Pease 1921) relied on light being combined by two sub-apertures such that the light seen through the telescope in the image plane was modulated by interference fringes. As the name suggests image plane combination takes the collimated beams of starlight and brings them to a common image/focal plane. The simplest way of implementing this is a monolithic lens or mirror with the beams landing on different subsections of the optic and the detector being placed at the focal plane of the optic. This results in overlapped Point Spread Functions (PSFs) modulated by spatial interference fringes.

A disadvantage of image plane combination is the number of pixels which must be read out. Considering the condition that at least four pixels per cycle of the interference fringes must be sampled, and, in the case where multiple baselines are measured simultaneously, ensuring they are well separated and can be measured independently typically means hundreds of pixels must be read out per spectral channel. An example of this is worked out in detail in section 4.7. As discussed in section 1.5.2 reading out so many pixels reduces the SNR of observations, however, with the advent of low and even sub-electron readnoise detectors such as the SAPHIRA detector (Finger et al. 2016) the impact of this has been significantly reduced.

Image plane combiners are becoming more popular. I argue part of the reason for this is that they scale better as more baselines are combined. Figure 1.3 shows the layout for a four-way co-axial pupil plane combiner used at the COAST interferometer. Such a scheme requires four beamsplitters, mirrors and detectors and would require four dispersing optics to be placed in the path of the collimated beams immediately before the focusing lens if spectral dispersion was required. In comparison, the equivalent image plane combiner would require only one focusing optics and detector and spectral dispersion can be implemented with only one dispersive element.

Note that as discussed in section 1.5.2 only one detector is required for a co-axial pupil plane combiner as light from each of the four telescopes is sent to each detector. Though this
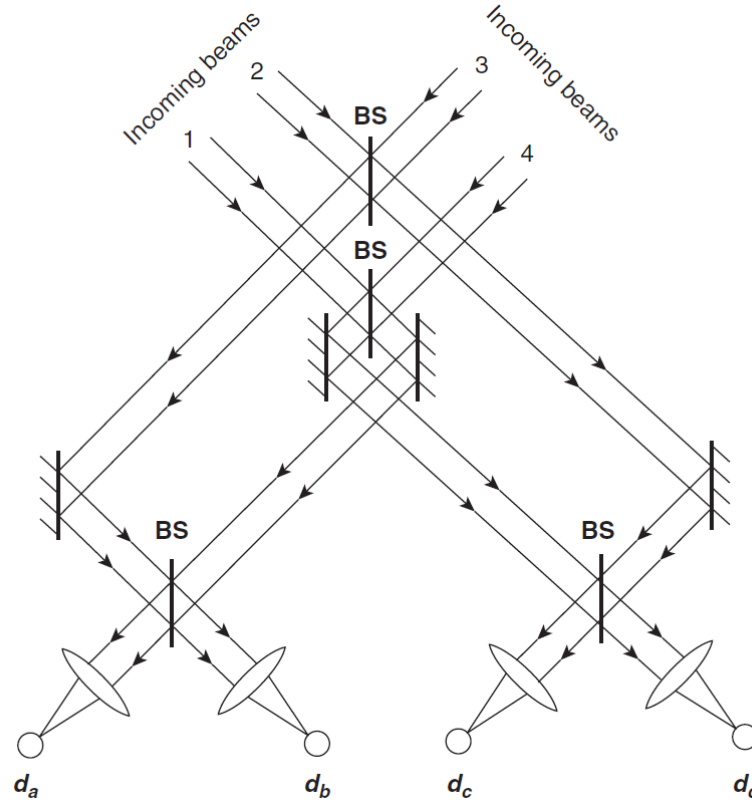
**Figure 1.3:** The schematic for the four way co-axial pupil plane beam combiner which was used at COAST. This shows the requirement of four beam splitters and mirrors, as well as the use of four independent detectors. This is figure 4.14 of Buscher (2015). © David F Buscher, Practical Optical Interferometry: Imaging at Visible and Infrared Wavelengths, 1st ed 2015, reproduced with permission of the licensor through PLSclear.

is another disadvantage of co-axial pupil plane combination, as the more telescopes that are combined the more ways the light from each telescope has to be split to sample all telescope pairs, reducing the SNR for a given detector read. This splitting is not necessary in image plane beam combination.

Some notable image plane beam combiners include AMBER (decommissioned) (Petrov et al. 2007), MATISSE (Lopez et al. 2014) at the VLTI, VEGA (Mourard et al. 2009) and MIRC-X (Anugu et al. 2020) at CHARA and VISION (Armstrong et al. 2018) at NPOI.

### 1.5.4 Wave-guide beam combination

The most recent addition to beam combiner technology discussed here are wave-guided or beam combiner "on a chip" systems. These use integrated optics circuits which take in the starlight
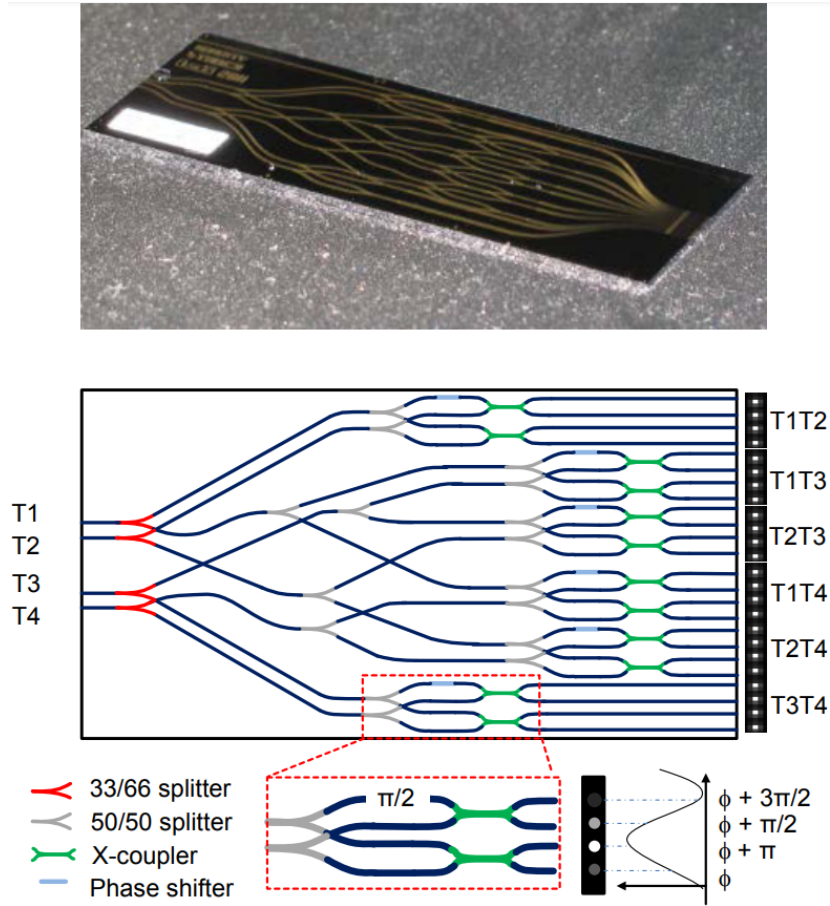
**Figure 1.4:** The wave-guide beam combination chip used in the GRAVITY beam combiner at the VLTI. The top panel shows an image of the chip itself while the middle panel shows the layout, highlighting the four input beams of starlight on the left and the various points they are split off and combined with the light from other telescopes. This is figure 5 of Gravity Collaboration et al. (2017). Credit: GRAVITY collaboration, A&A, 602, A94, 2017, reproduced with permission © ESO.

from each telescope, split it, interfere it with the other beams of starlight and then (typically) produce four outputs per telescope pair with a 90° phase shift between each output. Measuring the light at each of the four outputs then is the equivalent of sampling spatially modulated interference fringes at four discrete locations from which the interferometric observables can be recovered. An example of such a wave-guide circuit is the one used by the GRAVITY beam combiner at the VLTI, shown in figure 1.4.

Here I discuss two advantages this technology offers. The first is that it is easy to scale up for combining many telescopes. Printing a more complex circuit to handle more telescope combination pairs will increase the size of the chip but not at the same rate as the other beam combination schemes discussed here. Even 3D integrated circuits have been produced and

used on-sky (Martinod et al. 2021), opening the possibility of even more compact designs. The second advantage is that as the beam combiner is one solid circuit it is much less prone to misalignments which could affect the quality of the instrument. This makes it much more robust and, in addition to its compact size, ideal for space based interferometry where reliability is crucial.

A current limitation is the optical throughput of these devices. There are significant losses associated with coupling starlight into the chips. Due to the small width of the channels they act like single mode fibres, rejecting all light which does not match this mode and, for atmospherically perturbed starlight this can result in a significant throughput loss (see figure 3.17 of Buscher (2015)). However, many beam combiners use single mode fibres for the high level of spatial filtering they provide (which can boost the SNR, see section 4.6) so this is not an additional loss. The chip itself can be lossy as well, Gravity Collaboration et al. (2017) state that the GRAVITY integrated chip has a mean throughput of $\sim 54\%$ across the K band, though such losses will likely be reduced as the technology is developed further in the future.

## 1.6 Scientific motivation of the MROI/FOURIER project

Optical interferometry is a powerful technique which enables observations at spatial resolutions unobtainable via any other method in the optical. Based on the success and lessons learned in the development of current generation optical interferometers, the MROI is designed to advance the field further in a couple key aspects as discussed below.

### 1.6.1 Limiting magnitude

The sensitivity of an optical interferometer and its beam combiner, characterised by the faintest magnitude a target they can observe, the limiting magnitude, has always been a limitation for optical interferometers. Factors that reduce the limiting magnitude of an optical interferometer are discussed in depth in section 5.7. Briefly here, I discuss three main contributing factors which have restricted the limiting magnitude of optical interferometers to date. The first is the poor throughput due to the necessarily complex beam train required to collect the light at separate telescopes hundreds of meters apart and bring it physically to the same location to be interfered, all while equalising the optical path length along each arm. For example, a beam at

the VLTI undergoes 31 reflections before arriving at the beam combiner (Mathar 2010), 19 at the CHARA (Che et al. 2013) array and 17 at NPOI (Zhang et al. 2006). Both the reflective losses at each imperfect surface and diffraction losses along such long propagation distances reduce the throughput and hence the limiting magnitude.

The second is that the aforementioned complex beam trains can introduce significant levels of wavefront error to the beams of starlight, due to, for example, misalignments, surface errors and geometric aberrations. These wavefront errors reduce the fringe contrast which in turn also worsens the systems limiting magnitude. This is discussed in much more detail in section 5.6.

The third factor is that in order to record high contrast fringes exposure times must be kept to approximately twice the atmospheric coherence time, $t_0$ to "freeze" the Earth's atmosphere. In the near-infrared this is typically of order tens of milliseconds. Such short integration times mean there are fewer stellar photons per integration, reducing the SNR. A notable exception is the GRAVITY beam combiner at the VLTI (Gravity Collaboration et al. 2017) which enables coherent integrations of up to a minute with its cophasing fringe tracker.

This problem cannot be solved by simply building larger telescopes to collect more photons, partially due to the fact that an interferometer requires multiple telescopes, typically 4-10, and the increase in cost of building larger telescopes is multiplied by the number of telescopes needed. This is compounded by the fact that beyond a certain telescope size the SNR of the interference fringes will, counterintuitively, decrease for a larger telescope for a fixed value of the Fried parameter (quality of atmospheric seeing) and level of adaptive optics correction. This is because the gain in flux is offset by an increase in the atmospheric induced Root Mean Square (RMS) wavefront perturbations across the aperture. Correcting for atmospheric perturbations of order higher than tip-tilt is expensive, requiring deformable mirrors and wavefront sensors. For this reason most interferometers only have tip-tilt correction which, according to Buscher (1988), peak in SNR for a telescope at around three times larger than the Fried parameter. The Fried parameter is estimated to be ∼ 0.5 m in the H band at the MROI site meaning the array is limited to telescopes smaller than ∼ 1.5 m with the tip-tilt only adaptive optics. For this reason the MROI Unit Telescopes (UTs) are 1.4 m in diameter (Pirnay et al. 2008).

The limiting magnitudes of some current generation near-infrared beam combiners are given in table 1.1. They are limited to magnitudes between 7th and 9th or brighter.

A notable exception is the GRAVITY beam combiner, the limiting magnitude presented

**Table 1.1:** The limiting magnitude of current generation near-infrared beam combiners. Ref 1 (Anugu et al. 2020), 2 (Ten Brummelaar et al. 2013), 3 (Le Bouquin et al. 2011), 4 (Gravity Collaboration et al. 2017) for 1" seeing in single field mode on the 1.8 m Auxiliary telescopes (AT) and 8 m Unit Telescopes (UTs).

| Beam combiner | array | Limiting magnitude | ref |
|---|---|---|---|
| MIRC-X | CHARA | H = 7.1 | 1 |
| CLASSIC | CHARA | H/K = 8.5 | 2 |
| PIONIER AT | VLTI | H = 7 | 3 |
| GRAVITY AT | VLTI | K = 8 | 4 |
| GRAVITY UT | VLTI | K = 9 | 4 |

in table 1.1 is for "single field mode" observations where both the fringe tracker and science combiner observe light from the same star as is the case at other interferometers. GRAVITY however implements off-axis fringe tracking where separate targets are observed by the science combiner and fringe tracker, it is then possible to observe targets as faint as K = 17th magnitude but this places strict constraints on what areas of the sky are observable as the second fringe tracking star must be within 2" of the science target. Work is currently under way, however, to increase this off-axis angle (Haubois et al. 2020). In this discussion I use the single field mode limiting magnitudes for a fair comparison.

Such limiting magnitudes restrict the number of targets which can be observed for a given class of objects. Figure 1.5 shows the cumulative distribution of magnitudes of Herbig and AGN targets with the limiting magnitude of the beam combiners in table 1.1 overplotted. The scale along the y axis is normalised such that the last bin of each distribution equals one. This is appropriate as we are interested simply in what fraction of a population of targets would be observable for a given beam combiner. The data in figure 1.5 has not been corrected for what targets will actually be observable at each interferometer. The GRAVITY beam combiner does not operate in the H band but its K band limiting magnitude is displayed for completeness.

The sample of Herbig stars is taken from the targets listed in the online accompanying data of Wichittanakom et al. (2020) which is a spectroscopic study. From this target list H band magnitudes are retrieved via Simbad (Wenger et al. 2000). AGN magnitudes are taken from the known AGN candidates presented in the online data of Kouzuma & Yamaoka (2010). Note that Kouzuma & Yamaoka (2010) cut their catalogue to only include targets fainter than 10th

magnitude in the K band as they assume targets brighter are probably stars within our own galaxy. This cut is not expected to have a large impact on the distribution of AGN magnitudes as figure 1.5 shows there are few AGN between $10^{\text{th}}$ and $12^{\text{th}}$ magnitude so even fewer are likely to be brighter than $10^{\text{th}}$ magnitude.

Figure 1.5 highlights the need for fainter limiting magnitudes in optical interferometry. Significant progress is being made in the number of galactic targets such as Herbig stars which can be observed with surveys of moderate sample size being carried out in recent years, 51 and 27 for Lazareff et al. (2017) and Gravity Collaboration et al. (2019) respectively. However a significant fraction of targets are still out of reach. By modelling the MROI beam train and FOURIER beam combiner as discussed in section 5.7 FOURIER is expected to reach a limiting magnitude of 13.2 in the H band, putting 99% of Herbig targets within reach. The case is even more compelling when AGN astrophysics is considered, by the data presented in figure 1.5 no AGN are within reach of current generation optical interferometers. This is a pessimistic view as some dozen or so AGN have been observed with optical interferometery (Buscher et al. 2013), however figure 1.5 shows that significant sample sizes will not be reached until limiting magnitudes of at least $12^{\text{th}}$ are possible. Figure 1.5 shows FOURIER will be able to observe 238 AGN or 8% of the sample. In practice this number will be smaller as not all will be observable from the MROI site and likely more will be inappropriate due to other observational constraints, however, even being able to observe a fraction of those 238 AGN will be a significant gain.

### 1.6.2   UV plane coverage

The goal of an optical interferometer is to measure visibilities (and ideally closure phases) at different on-sky spatial frequencies pointing along different position angles and use these observations to recover spatial information about the intensity distribution of a source on-sky. The best approach is to perform direct model-independent image reconstruction. As the name suggests this is when no prior model of the intensity distribution is assumed and an "image" is reconstructed from the data alone. This method requires significant number of observations to be made, as a rule of thumb for an image to be reconstructed that contains N resels then N independent visibility measurements must be made (Buscher et al. 2013). Therefore to produce a 5×5 pixel image 25 visibilities must be measured, as the number of baselines goes as:
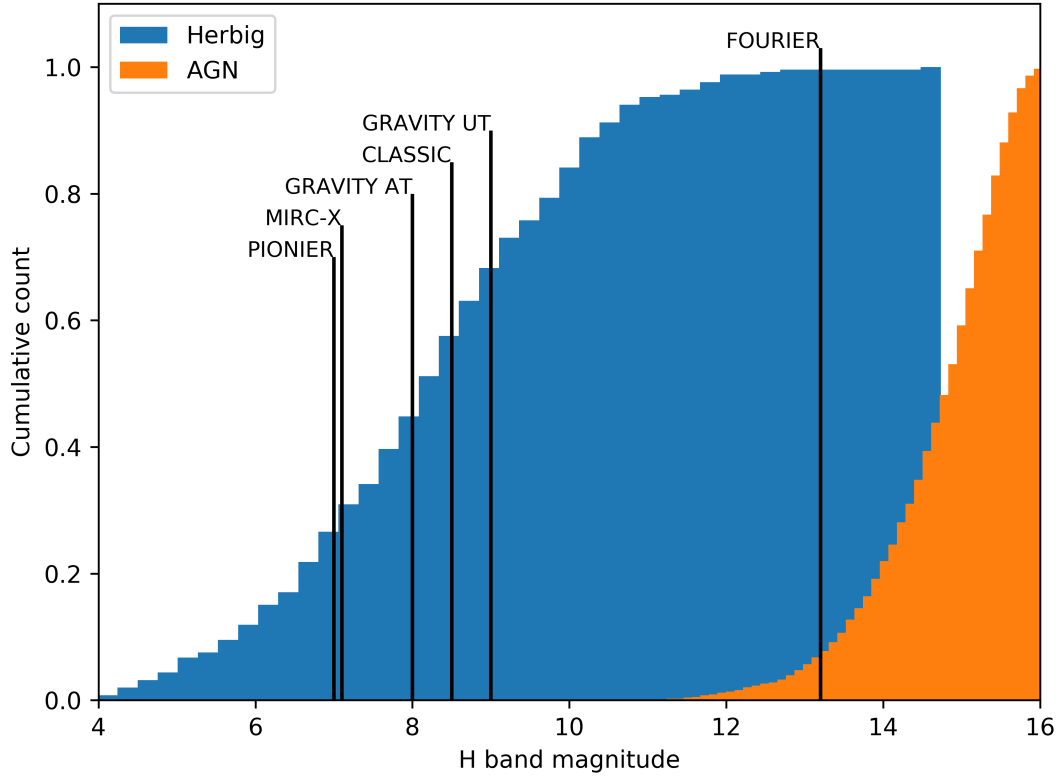
**Figure 1.5:** The H band magnitude of Herbig targets available online for Kouzuma & Yamaoka (2010) and AGN targets taken from the sample presented in Kouzuma & Yamaoka (2010). The limiting magnitude of current generation near-infrared beam combiners are denoted by solid vertical lines. This figure shows that a significant fraction of Herbig and all AGN targets presented here are beyond the reach of current generation instruments, highlighting the need for fainter limiting magnitudes in optical interferometry.

$$N_b = \frac{n^2 - n}{2}. \tag{1.13}$$

Where $n$ is the number of telescopes being combined. Reconstructing such an image in a "snapshot" (with the data collected at once without relying on the Earth's rotation or relocating telescopes to sample additional visibilities) an array of around 8 telescopes is required (the exact number depends on the morphology of the source). This is compared to the maximum of 4 and 6 telescopes which can be combined in a snapshot at the VLTI and CHARA arrays respectively.

As mentioned above it is possible to obtain more interferometric measurements by both using the Earth's rotation and telescope relocation. The former takes advantage of the fact that as the Earth rotates the baseline as projected onto the sky between a pair of telescopes

changes and thus the telescope pair samples similar but different spatial frequencies on-sky. The drawback to this technique is that the same target must be returned to multiple times throughout the night, limiting the total number of targets that can be observed on a given night and hence the amount of science that can be carried out. The latter method requires one or more of the telescopes to be physically relocated which is typically done during the day when scheduling permits, meaning data can be taken weeks apart which can be a problem when observing objects which vary on timescales of weeks, such as for the inner few au of protoplanetary disks (Kobus et al. 2020).

These difficulties have significantly limited the amount of model independent imaging science carried out with optical interferometry. A basic search on the NASA astrophysics data system for papers published in the last five years which contain the phrase "optical interferometry" and are tagged in the astronomy collection reveal 2,100 papers, the same search but for papers which also contain the phrase "model independent" returns only 106 papers, suggesting as few as 5% of papers published in the field utilise model independent image reconstruction.

Instead most papers opt for fitting the visibilities to some predefined model, the most simple example being that of a circular, uniform disk on-sky representing a resolved stellar disk. In this model the diameter of the stellar disk is a free variable for which the best fit to the data is found and requires only one visibility measurement.

In the next chapter I will discuss how the MROI is designed to tackle these problems, in turn laying out the case for the beam combiner developed for this PhD thesis.

# THE MROI

## 2.1  Introduction

The Magdalena Ridge Observatory Interferometer (MROI) is an ambitious next generation long baseline optical interferometer currently under construction in New Mexico, USA. When completed it will be a 10 telescope interferometer operating on baselines from 7.8-347 m in both the visible and near-infrared ($\lambda$ = 0.6–2.4 μm). The project is currently working towards operating three telescopes in the near-infrared ($\lambda$ = 1.1–2.4 μm).

In this chapter I briefly discuss how the design of the interferometer is optimised to reach the science goals discussed in section 1.6. As mentioned in the declaration the information presented in this chapter is mainly taken from Buscher et al. (2013).

## 2.2  Design of the MROI

### 2.2.1  Limiting magnitude

A top priority for the design of the MROI is to reach as faint a limiting magnitude as possible. As discussed in section 1.6.1 it is not possible to simply use larger telescopes than those currently deployed at Centre for High Angular Resolution Astronomy (CHARA) or the Very Large Telescope Interferometers (VLTIs) auxiliary telescopes to collect more light without
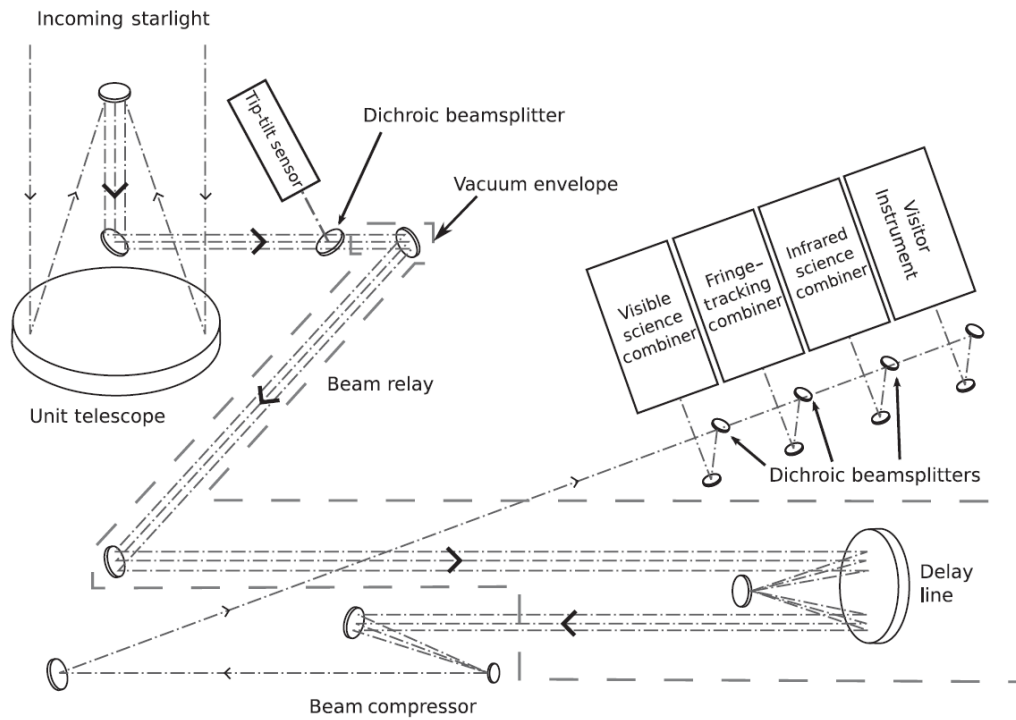
**Figure 2.1:** A diagram of the MROI beam train for a single arm of the interferometer. There are only 13 reflections from the UT primary to the entrance of each beam combiner. This highlights how the MROI has been optimised for sensitivity by maximising the throughput and minimising sources of fringe contrast loss of the array. Taken from figure 4.1 of Buscher (2015). © David F Buscher, Practical Optical Interferometry: Imaging at Visible and Infrared Wavelengths, 1st ed 2015, reproduced with permission of the licensor through PLSclear.

purchasing expensive high order adaptive optics systems for each telescope. Instead the MROI is optimised to achieve its goal of reaching fainter limiting magnitudes by optimising the lossy interferometric beam train to maximise throughput and fringe contrast. How this is achieved is discussed in more depth in sections 5.5.1 and 5.6.1 respectively. To summarise here, the throughput is maximised in large part by simplifying the beam train as much as possible, and fringe contrast is maximised by maintaining a strict error budget of tolerable losses to each source of loss. Figure 2.1 depicts the optical path along one arm of the MROI from incoming starlight to the entrance of the beam combiner. In total there are only 13 reflections from the primary of the Unit Telescope (UT) to the entrance of each beam combiner. This is less than half the number of reflections at the VLTI as discussed in section 1.6.1.

The above will improve the limiting magnitude of any beam combiner used at the MROI. The limiting magnitude of the science combiner however is additionally restricted by the performance of the fringe tracker for two reasons. Firstly as the science combiner and fringe

tracker typically observe the same target, if the target is too faint for the fringe tracker then atmospheric piston cannot be corrected and science observations cannot be made even if the target is bright enough for the science combiner. The second reason is that the type of fringe tracking impacts how long the science beam combiner can expose for which affects its limiting magnitude.

The MROI fringe tracker, the Infrared Coherencing Nearest Neighbor tracker (ICONN), is designed to fringe track at $14^{th}$ magnitude (Creech-Eakman et al. 2020) and so will be able to fringe track at the limiting magnitude of the Free-space Optical multi-apertUre combineR for IntERferometry (FOURIER). ICONN is designed as a coherencing beam combiner meaning it does not "freeze" the interference fringes on the science combiner as a cophasing fringe tracker would but instead maintains the optical path difference to within the coherence envelope. This means FOURIER cannot expose for longer than a few tens of milliseconds. Many of these short exposure frames can be combined to improve the Signal to Noise Ratio (SNR) however this comes at the cost of increased read noise from successive reads rather than one longer integration. This will affect the limiting magnitude of the science beam combiner and so must be taken into account when modelling its limiting magnitude.

### 2.2.2 Array configuration

When completed the MROI will consist of 10 telescopes with 28 relocation stations giving a wide range of baselines from 7.8-347 m. This provides 45 visibility measurements in a single snapshot, sufficient to produce a model independent image of up to 45 resels with data taken only over a few minutes.

Such a rapid increase in the rate at which enough data to produce a model independent image can be acquired will lead to significant increase in productivity of the MROI over other interferometric arrays, with up to 50 images per night being produced Buscher et al. (2019).

## 2.3 Summary

The design of the MROI has been presented in this chapter to highlight how the beam train itself is optimised for the scientific motivation presented in section 1.6. This will help with understanding the motivation behind the optical design of the Free-space Optical multi-apertUre

combineR for IntERferometry (FOURIER) (chapter 4), which is based on the same core principle of minimising the number of optics to maximise both throughput and fringe contrast and hence improve the limiting magnitude of the system.

# DESIGN REQUIREMENTS OF THE

# FOURIER BEAM COMBINER

## 3.1   Introduction

In this chapter I outline the role of the Free-space Optical multi-apertUre combineR for IntER-ferometry (FOURIER) beam combiner at the Magdalena Ridge Observatory Interferometer (MROI) and the requirements which affect the design of the instrument.  As mentioned in the declaration this work is the result of a collaboration with the instrument scientist of the interferometer.

## 3.2   The need for FOURIER

The MROI is currently progressing towards operating three telescopes in the near-infrared and FOURIER is to be the science beam combiner during this phase of the project.  During this phase of the project there will be a second beam combiner, the Infrared Coherencing Nearest Neighbor (ICONN) (McCracken et al. 2014), which will provide fringe tracking. The need for FOURIER as a separate, dedicated science beam combiner is two fold.  Firstly, ICONN operates in a pairwise beam combination scheme, producing a unique set of interference fringes for each baseline.  In addition to this ICONN only generates interference fringes for baselines formed

by "nearest-neighbour" telescope pairs, i.e. baselines formed by telescopes that are adjacent to each other along one of the arms of the MROI. This means ICONN is unable to measure closure phases and so a separate all-in-one beam combiner which multiplexes all three baselines simultaneously is needed. Secondly, ICONN is designed to measure the interference fringes and perform fringe tracking rapidly which leads to a different set of design requirements such as a lower spectral resolution to maximise the number of photons and hence Signal to Noise Ratio (SNR) on each spectral channel. FOURIER on the other hand is designed for science operations leading to a different set of requirements.

These factors point to the need for an all-in-one beam combiner optimised specifically for science operations and FOURIER fills this role. In the following parts of this chapter I discuss the specific requirements which constrain the design of FOURIER further.

## 3.3   Functional Requirements

### Limiting magnitude

FOURIER should be designed with a top level goal to reach as faint a limiting magnitude as possible. The specific requirement is that observations with FOURIER should reach a SNR of two on unresolved $10^{th}$ magnitude targets within five minutes of incoherent integration at the MROI with seeing conditions at $\lambda = 500$ nm of Fried parameter 14 cm and atmospheric coherence time 4.4 ms. The goal is to reach this performance on $11^{th}$ magnitude targets.

The scientific motivation for this goal has been outlined in section 1.6.1 and is essentially that many more targets of a given population of objects can be observed allowing statistical studies of the morphology of objects at high angular resolution to be carried out.

FOURIER is designed to meet this goal by maximising the throughput while minimising any visibility loss due to the design of the instrument. A detailed discussion of the design and performance of FOURIER towards meeting this goal is given in chapters 4 and 5 respectively. As this is a top level goal for FOURIER extensive modelling of the limiting magnitude is discussed in section 5.7.

**Spectral coverage**

FOURIER is designed to operate in the near-infrared. The requirement is that it must be able to form interference fringes over the whole of either the J, H or K bands, with the band of choice being selectable. FOURIER was designed to meet this requirement in the simplest way possible by having all three bands observable on the detector without the need for any reconfiguration as discussed in section 5.4.

**Spectral Resolution**

As discussed in section 4.8 the ability to study the interferometric observables as a function of wavelength can be very advantageous. The requirement placed on FOURIER is that it should have a minimum resolving power $R = 70$ in all of the J, H and K bands. Where $R$ is defined as $R = \lambda/\Delta\lambda$, where $\lambda$ is the wavelength of observation and $\Delta\lambda$ the smallest difference in wavelengths that can be distinguished at $\lambda$. The term "smallest difference in wavelengths that can be distinguished" is taken here to be the difference in wavelengths (which are dispersed along the detector) that just satisfy the Rayleigh criterion, such that the Airy disks of the two wavelengths are separated so the maximum of the Airy disk of one overlaps with the first minimum of the other along the detector. An example of this calculation is given in section 5.4. How the design of FOURIER was set to meet this requirement is discussed in section 4.8. Laboratory measurements of the spectral resolving power of FOURIER are presented in section 7.6.

**Configurability**

As mentioned FOURIER is designed to operate during the three telescope phase of the project and as such it has been designed as a three telescope beam combiner. It can also work with both two and three beams as discussed in section 4.4.

## 3.4 Performance requirements

**Dynamic Range**

Some targets of interest in optical interferometry are very bright. For example α Ori (Betelgeuse) in Orion has a K band magnitude of -4.05 (Ducati 2002). For this reason FOURIER should be

capable of observing targets of -3$^{rd}$ magnitude in the K band without saturating the detector. This requirement does not place tight constraints on the design of FOURIER as it can be met by selecting an appropriate high quality neutral density filter, to be placed into the path of the starlight for observations of bright targets.

## Observable Calibration

The two observables FOURIER will measure are visibility and closure phase. It is of course desirable to calibrate these data products accurately to reduce the error on results produced with data from FOURIER. As an example Gordon (2013) states that the maximum flux ratio which can be detected when observing binary star systems is proportional to the precision on the closure phase, showing that a difference of around four magnitudes can be measured for closure phase precision around 1°. For this reason the goal of calibrating visibilities to the 5% level and closure phases to within 0.5° has been set for FOURIER. This requirement does not place a tight constraint on the design of the instrument but on the subsequent data calibration routine which is not within the scope of the work presented in this thesis.

## Crosstalk

Crosstalk is a systematic error on the visibility measurements which affects all-in-one beam combiners such as FOURIER. It is the process by which a signal from one baseline being measured "leaks" into another, altering the measured visibility. The requirement of reducing crosstalk below 1% was set for FOURIER. This affects the configuration of the input beams which is discussed in section 4.3. A detailed simulation of crosstalk arising from previously unexplored affects and their impact on FOURIER is presented in chapter 8.

## Wavelength calibration

The light in FOURIER will be spectrally dispersed to allow for spectro-interferometry, the study of objects as a function of wavelength. It is of course required that the spectrally dispersed light be calibrated to know what wavelengths are present on a given spectral channel. For this reason the ability to perform wavelength calibration at a known level is set as a requirement. The ability to do this calibration with FOURIER is demonstrated in section 7.6.

**Polarisation Fidelity**

Keeping the diattenuation (the difference in throughput for different polarisation states) low reduces visibility losses and helps boost the SNR. For this reason the entire MROI beam train has a goal of keeping diattenuation below 2%. The goal of minimising diattenuation is set on FOURIER (though no requirement for it to be below a certain limit). FOURIER is hence designed to reduce the Angles of Incidence (AoI) on any optic, as large AoI can cause large diattenuation. Where this is not possible diattenuation is considered in the design of the anti-reflection coating to minimise the difference in throughput as discussed in chapter 4.

**Footprint**

FOURIER must be designed to fit on a 2×1 m table to be integrated at the observatory. Thus I also had a requirement on size when designing FOURIER.

**Cryostat hold time**

The SAPHIRA detector FOURIER uses, and the fact the instrument operates in the K band ($\lambda = 2$–$2.4\,\mu m$) means the instrument must operate within a Liquid Nitrogen (LN2) cryostat. As there will be no system to automatically refill the cryostat, and as operators cannot enter the beam combining area during observations to minimise atmospheric disturbances, the requirement that the cryostat must be able to hold its temperature for 24 hours with a goal of 30 hours was set. This informed the size of the LN2 reserve the cryostat can hold at any one time based on assumptions about the thermal dissipation within the cryostat.

## 3.5 Summary

The requirements discussed above do not significantly constrain the design of FOURIER. For example they make no comment on the kind of beam combination scheme FOURIER should use. A variety of possible combination schemes are discussed in section 1.5. An image plane beam combination scheme was selected for FOURIER as it was seen as the scheme which could achieve the highest throughput using bulk optics and as few optics as possible. The goal of the work carried out and presented in this PhD thesis then was to design, simulate, build and

test as faint a limiting magnitude science beam combiner as possible which satisfied the above requirements.

# 4

# THE OPTICAL DESIGN OF FOURIER

## 4.1  Introduction

In this chapter I outline the optical design of the Free-space Optical multi-apertUre combineR for IntERferometry (FOURIER) as motivated by the instrument requirements discussed in chapter 3. This chapter focuses on the function and design of each optic/subsystem only. A discussion of the simulated performance of the instrument and the optomechanics are reserved for chapters 5 and 6 respectively.

The detailed manufacturing drawing for each optic can be found in Appendix-A.

## 4.2  Design Overview

Figure 4.1 shows a overview of the optical design of FOURIER, where the optics are shown floating in free space, with no optomechanics supporting them. The beam path is as follows: the three beams travel from right to left towards the initial focusing mirror M1, from here they are reflected towards the cryogenic optics, passing through the cryostat window. The beams continue to the focal plane of M1 at which the pinhole spatial filter is located. After the spatial filter the beams begin to diverge until they reach the cylindrical mirror M2. After reflection at M2 the beams begin to slowly converge along one axis, the interference fringe axis, but

continue to diverge along the perpendicular, spectral axis. After M2 the beams are spectrally dispersed via the prism before passing through L1 which focuses the beams in the spectral axis onto the SAPHIRA detector. The system is designed such that the focal planes of M2 and L1 are coincident at the location of the SAPHIRA detector.

FOURIER is designed to maximise both throughput and fringe contrast by minimising the number of optical surfaces. The throughput is additionally maximised via the use of high throughput, coated bulk optics. As a result the complete instrument contains only five optical surfaces. Detailed discussions of the simulated and measured throughput of the instrument are given in sections 5.5.2 and 7.4 respectively.

The resulting pattern on the detector of FOURIER comprises spatially modulated interference fringes which run along one axis of the detector, with these interference fringes being spectrally dispersed along the perpendicular axis. These are referred to as the interference fringe and spectral axes respectively. A simulated detector readout is shown in figure 5.18.

## 4.3   Input beam configuration

Here I discuss the configuration of the starlight beams used at the entrance of the FOURIER beam combiner as the size of this layout influences the size of the FOURIER instrument's optics.

In image plane beam combination a pair of beams from any two telescopes (a baseline) produces interference fringes in the image plane. The physical size on the detector of one interference fringe cycle (and hence the spatial frequency at which the interference fringes are seen to oscillate on the detector) is determined by

$$w_s = \frac{\lambda l}{d},$$  (4.1)

where $w_s$ is the width of one fringe cycle, $\lambda$ the wavelength of observation, $l$ the distance from the focusing optic to the image plane and $d$ the spacing of the incoming beams.

For image plane beam combiners it is possible to sample multiple baselines simultaneously, with interference fringes from each baseline overlapping on the detector. However, the spatial frequency of each set of interference fringes must be sufficiently unique such that each baseline
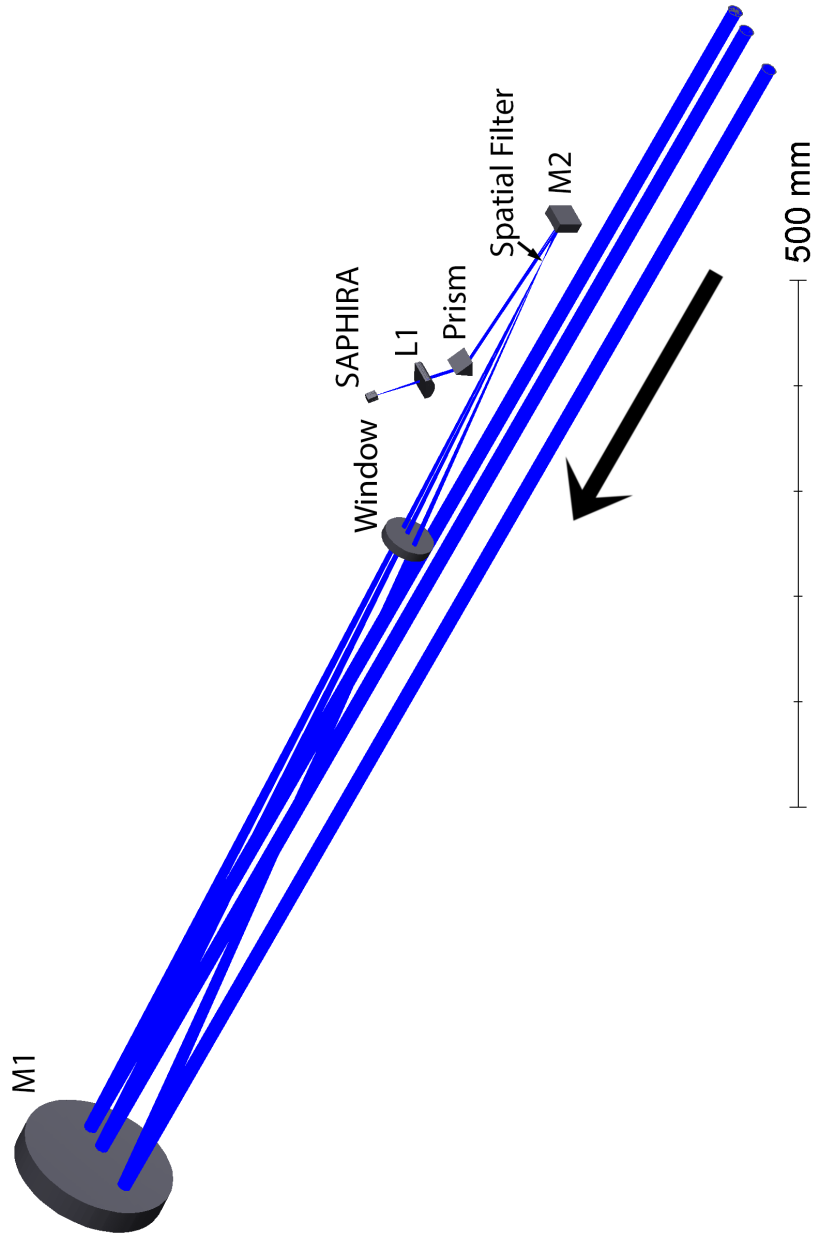
**Figure 4.1:** A 3D shaded model of the optical components of the FOURIER instrument. The three beams of starlight shown initially travel right to left before reflecting off M1 and passing through the cold optics. A detailed description of the beam path is given in the text. Reproduced from Mortimer et al. (2020).

can be measured independently from the others.  If they are not, a phenomenon known as crosstalk can occur.

As can be seen from equation 4.1 for a set of beams being combined by the same beam combiner optics the only free variable to distinguish the spatial frequency of different baselines is $d$, the beam spacing.  Hence when multiple baselines are multiplexed into spatially modulated interference fringes, the spacing of the beams at the entrance of the beam combiner is used to ensure each set of interference fringes are sampled at a unique spatial frequency.

The visibilities in image plane beam combination can then be extracted by taking the Fourier transform of the resulting interference fringes recorded on the detector.  This generates a power spectrum in which the signal of each baseline is recorded at the spatial frequency of the interference fringes on the detector.

The nominal diameter of the beams of starlight in the I-BCA of the Magdalena Ridge Observatory Interferometer (MROI) is 13 mm.  Where the nominal diameter is the expected beam diameter if only geometric optical effects are considered, i.e. ignoring the effects of atmospheric seeing and diffraction which would cause the intensity pattern of the pupil to vary with time.  To minimise the risk of crosstalk a $2d$, $4d$, $6d$ beam configuration is adopted where d is the 13 mm diameter of the beams, producing a power spectrum shown in figure 4.2.  In the resulting power spectrum there are four terms: the zero spatial frequency (or DC term), and three peaks corresponding to the three baselines sampled by FOURIER.  The dashed vertical lines represent the spatial frequencies of the interference fringes, for the input beam configuration used, as given by equation 4.1.  Figure 4.2 shows the three baselines to be well separated and easily distinguishable from each other for the $2d$, $4d$, $6d$ arrangement used here.

Here I have derived the required pupil spacing for FOURIER, however the system at the MROI which arranges the beams onto the required non-redundant spacing, known as the switchyard (Buscher & Wilson 2018), is independent of FOURIER and as such is not a part of this work.  Instead the $2d$, $4d$, $6d$ beam spacing is set as a requirement on the design of the switchyard.

This is a quick overview of the reasoning behind the beam spacing configuration utilised within FOURIER. A more thorough discussion of the shape of the power spectrum and the impact of crosstalk is presented in chapter 8.
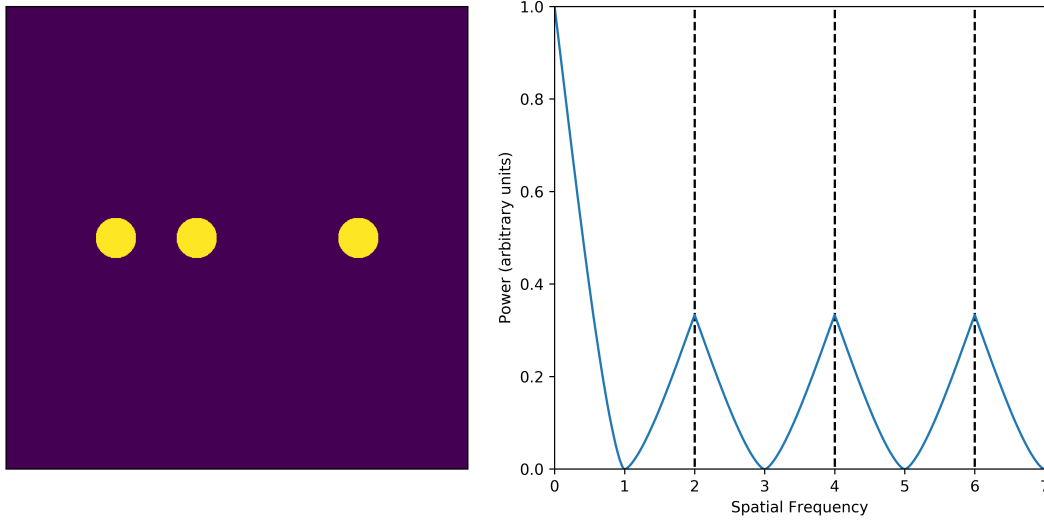
**Figure 4.2:** Left: the pupil spacing utilised at the entrance of the FOURIER beam combiner. Here the beams of starlight are spaced at $2d$, $4d$, $6d$ from each other where d is the 13 mm diameter of the beams. Right: the power spectrum of the multiplexed interference fringes produced by this pupil spacing pattern. The DC term and the three interference peaks (one per baseline) are well separated to minimise crosstalk.

## 4.4   Initial focusing mirror M1

M1 is the first optic along the FOURIER beam train and is a 6" diameter gold coated mirror with a focal length of 1.203 m. Its function is to both redirect the beams into the cryostat as well as act as the focusing optic for the spatial filtering system.

The diameter of M1 is set by the input beam spacing mentioned in section 4.3 where the total width of the incoming starlight beam pattern is 91 mm, or 3.6 inches for the 13 mm beams spaced up to 78 mm apart.

Because M1 acts as the focusing optic for the pinhole spatial filter, the optical axis of M1 must pass through the spatial filter. The incoming beams are, however, vertically displaced by 95.2 mm from the location of the spatial filter so they do not collide with the cryostat they pass underneath, as shown in figure 6.1. One solution would be to place the centre of M1 level with the spatial filter and make M1 large enough such that the beams would be contained within the clear aperture of the optic when they strike M1 95.2 mm below the optic's centre. Such an approach would require an optic with a clear aperture of at least 8", likely making the optic itself 10" in diameter.

An alternative scheme is to use three small off-axis parabolas, one for each beam. In this

scheme the vertical displacement between the height of the incoming beams and the height of the spatial filter would not alter the diameter of the initial focusing optic as the parabolas would be the effective cut out from a parent parabola with its optical axis aligned with the spatial filter. One disadvantage with this scheme is that each parabola would have to be aligned individually, increasing the complexity of the alignment procedure. While it is possible to mount all the parabolas on a common mount, fine adjustment would be needed for each parabola due to the tight alignment tolerance between the optical axis of the initial focusing mirror and the spatial filter as well as the tight tolerance on the overlap of the Point Spread Functions (PSFs) of each beam at the image plane of the instrument, see section 5.6.1.4.

Hence an advantage of using a monolithic optic compared to three small individual optics for each beam is that the focal plane of the initial focusing optics for the three beams cannot go out of alignment with respect to each other as all three beams reflect off a common optic.

The solution implemented for FOURIER is to use a monolithic, "off-axis" spherical mirror. By using a spherical mirror it is possible to tilt and decentre the mirror along the surface of the parent sphere until it is centred on the incoming beams without introducing any additional aberrations. This reduces the required clear aperture of the optic and so M1 is only 6" while maintaining the benefits of a monolithic mirror.

The use of a spherical mirror instead of a parabolic one does introduce additional aberrations to the instrument. However due to the long focal length of M1 it is effectively a f/92 system for a single 13 mm beam, meaning these aberrations are minimal. A geometric spot diagram is shown in figure 4.3 along with the diameter of the first null of the diffraction limited Airy disk shown as a black ring, showing that the system is diffraction limited as the geometric spot diagram is significantly smaller than the Airy disk itself.

A final advantage of the monolithic mirror approach is that the beam spacing into FOURIER can be altered without any need to reconfigure M1 as there is a continuous clear aperture. Due to the simple bulk optics layout of FOURIER this means the instrument can be used as a "crosstalk resilient" two beam combiner or even a four beam combiner with no adjustments required to the beam combiner itself.

**Figure 4.3:** The geometric spot diagram for one 13 mm beam at the focus of M1 produced in Zemax. The corresponding Airy disk is shown as a black ring

## 4.5 Cryostat window

The next optic along the beam train after M1 is the cryostat window. This is a plano-plano 2" diameter optic which enables the beams to enter the cryostat while maintaining the vacuum levels and cryogenic temperatures within. It is coated with a single layer of magnesium fluoride ($MgF_2$) on both surfaces, optimised at a wavelength of $\lambda = 1.75\,\mu m$ (the centre of the FOURIER passband) as an anti-reflection coating. The window is 10 mm thick to avoid warping due to the differential atmospheric pressure on either side of the optic. The maximum displacement of a simply supported circular window under differential pressure can be calculated via

$$d = \frac{0.696pr^4}{Et^3}, \tag{4.2}$$

where $d$ is the deflection at the centre of the optic, $p$ the uniform load applied to the optic (assumed to be one atmosphere, or 101,325 Pa), $r$ the radius of the optic (25.4 mm), $E$ Young's
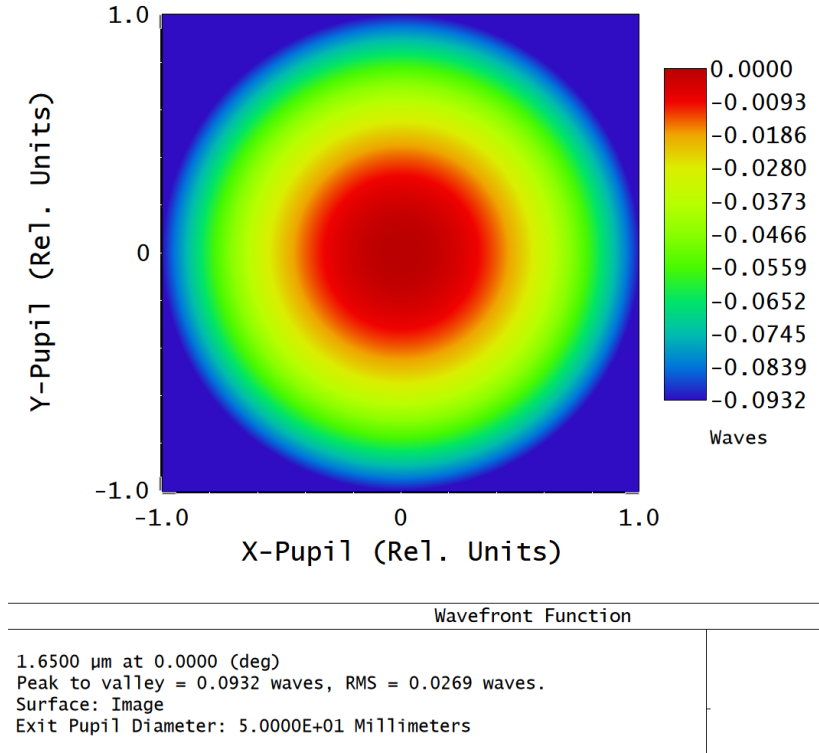
**Figure 4.4:** The WFE of the cryostat window when the cryostat is under vacuum. Here the peak to valley WFE at $\lambda = 1.65\,\mu\text{m}$ is $\approx \lambda/10$ and so minimal. This is compared to a ideal cryostat window which would show no WFE.

modulus (72 GPa) and $t$ the thickness of the optic (10 mm). This gives a very small deflection of $0.4\,\mu\text{m}$ at the optics centre.

To asses the impact of this deformation I modelled the cyostat window in zemax as a concave-plano optic (compared to its nominal plano-plano form) where the front surface is modelled to have a sag value of $0.4\,\mu\text{m}$ over its aperture. The Wavefront error (WFE) over the window's 2" aperture is show in figure 4.4. As the figure shows the peak to valley WFE at $\lambda = 1.65\,\mu\text{m}$ is $\approx \lambda/10$ and so minimal.

## 4.6   Spatial filter

Spatial filtering is a form of "passive adaptive optics" which ultimately increases the fringe contrast by removing some amount of atmospherically induced perturbations from the wavefront, at the cost of reducing throughput. This can be crucial depending on what regime the beam combiner is observing in. For example, Buscher (2015) states that if observations are being

carried out in a photon noise dominated regime (i.e. there is sufficient flux that detector read noise is negligible) then the Signal to Noise Ratio (SNR) for a single detector read goes as

$$\text{SNR} = \frac{1}{2}|V|\sqrt{N_{\text{phot}}}, \tag{4.3}$$

where $V$ is the fringe visibility and $N_{\text{phot}}$ is the intensity summed over all pixels (number of photons).

In the read noise dominated regime the SNR goes as:

$$\text{SNR} = \frac{V N_{\text{phot}}}{2\sigma_{\text{read}}\sqrt{N_{\text{pix}}}}, \tag{4.4}$$

where $\sigma_{\text{read}}$ is the read noise per pixel, $N_{\text{pix}}$ the number of pixels read out and the other terms have the same meaning as in equation (4.3). In the read noise dominated case of equation (4.4) the SNR goes linearly with both visibility and photon count and so any fractional gain in fringe contrast must exceed the fractional loss of photons for spatial filtering to be advantageous. With the recent development of sub-electron read noise detectors in the near-infrared such as the SAPHIRA detector used in FOURIER, observations are rarely read noise limited. So instead the SNR is linear with visibility but goes with the square root of the number of photons. As a result maximising fringe contrast at the expense of photons can result in a higher SNR overall.

Figure 3 of Keen et al. (2001) shows the significant gain in fringe contrast that can result from a pinhole spatial filter. As an example here I calculate the gain in SNR from implementing spatial filtering in the H band for FOURIER. Assuming a value of $D/r_0 = 2.4$, where $D$ is the telescope diameter and $r_0$ the Fried parameter, Keen et al. (2001) gives that a pinhole spatial filtering system results in a boost to fringe visibility by a factor of 1.64× (as the simulated RMS visibility for a point source is 0.95 with the pinhole spatial filtered system and 0.58 for a system without spatial filtering). To calculate the loss in throughput due to spatial filtering I use figure 3.14 of Buscher (2015) which shows that 48% of light is coupled into a single mode fibre for an atmospherically perturbed beam of starlight which has undergone tip-tilt correction, this is assumed to be approximately equal to the coupling through a pinhole. The ratio of the SNR in the photon noise limited case between a filtered system (V=0.95, throughput=0.48) and the unfiltered system (V=0.58, throughput=1) is 1.13× and so spatial filtering does result in a gain in SNR. In the read noise limited case however spatial filtering results in a loss in SNR, with the ratio of the SNR in the filtered and unfiltered system being 0.79.

As discussed in section 5.7.1 there is an additional advantage to implementing a spatial filter. A spatial filter reduces the number of thermal photons reaching the detector which is crucial in the K band where thermal effects are significant.

While a single mode fibre system provides better spatial filtering than a pinhole system, I opted for a pinhole in FOURIER as a single mode fibre system would require three initial focusing optics coupling light into three path matched optical fibres (as for example is done for six beams in the MIRC-X instrument (Anugu et al. 2020)) increasing the complexity and cost of the design. Using a pinhole also avoids the challenge of selecting a optical fibre with high performance across the wide FOURIER passband of $\lambda = 1.1$–$2.4\,\mu m$.

In addition to this, a pinhole affords much greater flexibility. The pinhole in FOURIER is actually a slit, performing spatial filtering in hardware along the spectrally dispersed axis only while passing the whole beam along the perpendicular, interference fringe axis. The advantage of such a system is that spatial filtering can be carried out in software along the interference fringe axis (by simply not including pixels which sample the outer parts of the PSF). This means that the effective width of the digital spatial filter can be adjusted for each spectral channel, scaling with size of the PSF as a function of wavelength. Keen et al. (2001) finds that the optimally sized pinhole is just slightly less than the width of the first Airy disk nulls.

## 4.7 Anamorphic optics

A common technique in image plane beam combination is to reshape the PSF such that it is much larger along the interference fringe axis than the spectral axis. The advantage of such a design comes down to two constraints which I work through in the case of FOURIER below.

Along the interference fringe axis it is necessary that the interference fringes are sampled well enough to accurately recover them. An extreme example to demonstrate this is if one considers sampling the fringes at one pixel per cycle. In this case the flux from both the peak and the trough of the fringe would be summed on a single pixel resulting in the same constant flux value for all pixels and no interference being recorded at all. Sampling three pixels per fringe cycle is often seen as a good compromise between sampling the interference fringes well enough while minimising the number of pixels to be read out. In the case of FOURIER I opted to sample four pixels per cycle on the highest spatial frequency interference fringe pattern, the same number of samples is used in some wave-guided optics beam combiners such as

GRAVITY (Gillessen et al. 2010). Figure 7.26 plots the maximum fringe contrast as a function of how well sampled the interference fringes are.

The physical width (diameter of the first null of the Airy disk) of a PSF produced by a focusing optic such as M1 is given by

$$x = \frac{2.44\lambda l}{D},$$ (4.5)

where $\lambda$ is the wavelength of observation, $l$ the distance from the focusing optic to the image plane and $D$ the diameter of the beam. By substitution with equation (4.1) we get

$$x = \frac{2.44 w_s d}{D}.$$ (4.6)

With this I can now determine how large the PSF must be along the interference fringe axis. I wish to sample four pixels per cycle, meaning the fringes must be 96 µm wide per cycle for the SAPHIRA's 24 µm pixels for the highest spatial frequency interference fringes at the shortest wavelength of $\lambda = 1.1$ µm (as this is the wavelength where the PSF is smallest). The highest spatial frequency fringes occur for the largest separation of two beams at the entrance of the beam combiner, d = 6×13 mm beam diameters for FOURIER. From equation (4.6) the PSF along the interference fringe axis then must be 1405 µm, or 59 pixels in diameter at $\lambda = 1.1$ µm.

The requirement of the beam size along the perpendicular spectral axis is just that I must sample two pixels (48 µm) across the PSF (again at $\lambda = 1.1$ µm) to ensure Nyquist sampling. Minimising the number of pixels read out along the spectral axis is desirable as this minimises the effects of any read noise present, as well as potentially increasing the frame rate of the detector. If only a fraction of the total number of pixels are utilised the frame rate can often be increased.

These two conditions along the interference fringe and spectral axes are significantly different by a factor of 29 times. In order to satisfy both of these conditions the PSF at the focal plane of FOURIER must be 29 times larger along the interference fringe axis than the spectral axis. This is dubbed the anamorphic factor, which would be hard to achieve by magnifying or demagnifying the image along one axis only. Instead, in FOURIER the anamorphic factor is shared between the two axes, by magnifying the image of the M1 focal plane by a factor of 5.4 along the interference fringe axis and demagnifying it by a factor of 5.4 along the spectral
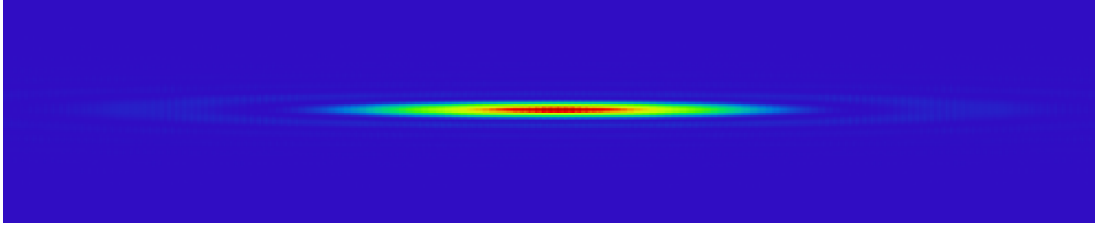
**Figure 4.5:** A simulated monochromatic PSF at the SAPHIRA detector for a single beam in FOURIER showing the high anamorphic factor. When multiple beams are combined the PSF is modulated by interference fringes along the elongated axis and when polychromatic light is used the light is dispersed along the perpendicular axis. Reproduced from Mortimer et al. (2020).

axis. Hence the same anamorphic factor of 29 times is achieved with a significantly reduced magnification/demagnification requirement along any one axis.

This approach required the diameter of the PSF at the focal plane of M1 to be exactly in between the 1405 μm and 48 μm Airy disk sizes, at 258.5 μm, which from equation (4.5) constrained the focal length of M1 to be 1.25 m. The focal length of M1 was later changed to 1.203 m due to a manufacturing error.

This high anamorphic factor reshapes the circular PSF at the focal plane of M1 to the PSF shown in figure 4.5 at the SAPHIRA detector. The PSF is simulated in Zemax using the Physical Optics Propagation (POP) routine for a single monochromatic beam. When multiple beams are combined the elongated axis is modulated by interference fringes and when polychromatic light is used the light is spectrally dispersed along the perpendicular axis. A simulation of this is shown in figure 5.18.

The magnification/demagnification required was achieved with two cylindrical optics of the same focal length which reimaged the M1 focal plane onto the SAPHIRA detector along perpendicular axes and were placed at complementary spacings. The first cylindrical optic, M2, shown in figure 4.1, is a gold coated cylindrical mirror with a focal length of 44 mm along its powered axis. It is placed at a distance of 52.5 mm from the focal plane of M1 and 296.2 mm from the SAPHIRA detector. A mirror rather than a lens for this first cylindrical optic was chosen so it did not introduce any chromatic aberrations and, continuing in the design style of FOURIER in minimising the number of optics where possible, it acts as a fold mirror which minimises the length of the cold space envelope required for the cryogenic optics.

The second curved optic is a cylindrical lens made of calcium fluoride ($CaF_2$) and coated with a single layer of magnesium fluoride ($MgF_2$) optimised for a wavelength of 1.75 μm on

both surfaces as an anti-reflection coating. L1 is a convex plano cylindrical lens and has a radius of curvature of 18.7 mm along its powered axis, from the lens makers equation

$$\frac{1}{f} = (n-1)\left(\frac{1}{R_1} - \frac{1}{R_2} + \frac{(n-1)d}{nR_1R_2}\right), \tag{4.7}$$

where $f$ is the focal length, $n$ the refractive index of the substrate, $R_1$ and $R_2$ the radii of curvature of the two surfaces and $d$ the thickness of the lens (Hecht 2017), the focal length of L1 can be calculated. At a wavelength of $\lambda = 1.75\,\mu m$ (the centre of the FOURIER passband) Zemax gives the refractive index of $CaF_2$ to be $n = 1.425$ (at 25 °C and 1 atm of pressure). From this the focal length of L1 is also 44 mm.

A lens was chosen for the second anamorphic optic due to its proximity to the SAPHIRA detector (approximately 50 mm). To prevent the SAPHIRA detector mounting from obstructing the incoming starlight, a mirror at the location of L1 would have to be used at an angle of 45°, leading to intolerable levels of optical aberration.

I chose $CaF_2$ as the substrate for L1 due to its low chromatic dispersion to minimise chromatic aberrations, this is particularly important in FOURIER due to its wide bandpass ($\lambda = 1.1$–$2.4\,\mu m$). The dispersion ($dn/d\lambda$) of $CaF_2$ along with three other commonly used near-infrared glasses is shown in figure 4.6, demonstrating that the chromatic dispersion of calcium fluoride is up to 4.8 times less compared to the other glasses.

Figure 4.7 shows the geometric spot diagram at the SAPHIRA detector at a wavelength of $\lambda = 1.1\,\mu m$ with the anamorphically reshaped Airy disk overlaid. The diffraction limited performance indicates that this novel design does not introduce significant levels of aberration which could degrade the quality of the interference fringes, borne out by the laboratory measurements of visibility in section 7.5.

As L1 is a singlet there is still some chromatic dispersion. To reduce this, the SAPHIRA detector is tilted by 6.4° in order to better reach the focal points at all wavelengths. A more complex design such as a doublet or triplet could have been pursued for L1 however the diffraction limited performance indicated by figure 4.7 suggested this was not necessary. As L1 is subject to cryogenic temperatures such a design would have a significantly higher risk of damage due to thermal contraction/expansion as the cryostat temperature is cycled between room temperature and 77k. For these reasons I decided to keep L1 a simple singlet.

The 44 mm focal length used for M2 and L1 was selected as a compromise between the cold space envelope required to enclose the cryogenic optics and the optical aberrations as well
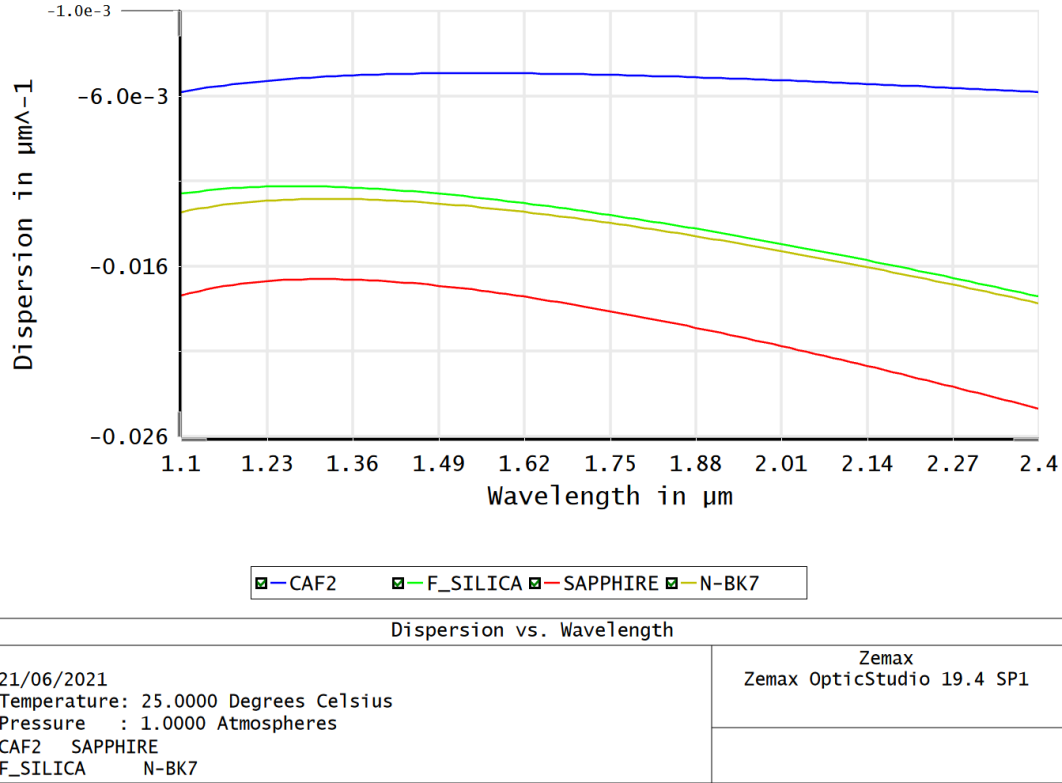
**Figure 4.6:** The dispersion ($dn/d\lambda$) of the calcium fluoride substrate used for L1 and three other commonly used near-infrared glasses from Zemax. Calcium fluoride has significantly less chromatic dispersion compared to the other glasses.

as alignment tolerances. By considering the following equations for linear magnification of a thin lens:

$$d_o = f - \frac{f}{M}, \tag{4.8}$$

$$d_i = Mf + f, \tag{4.9}$$

where $d_o$ is the distance from lens to the object, $d_i$ the distance from the lens to the image, $f$ the focal length of the lens and $M$ the magnification of the image produced by the lens, it can be seen that reducing the focal length for a given magnification reduces both $d_o$ and $d_i$. This would in turn reduce the total distance required between the focal plane of M1 and the SAPHIRA detector to achieve the same magnification/demagnification, minimising the volume of the cold space envelope, reducing both the manufacturing and operating costs of the instrument. However, $d_o$ and $d_i$ must be large enough that the optics are sufficiently spaced to
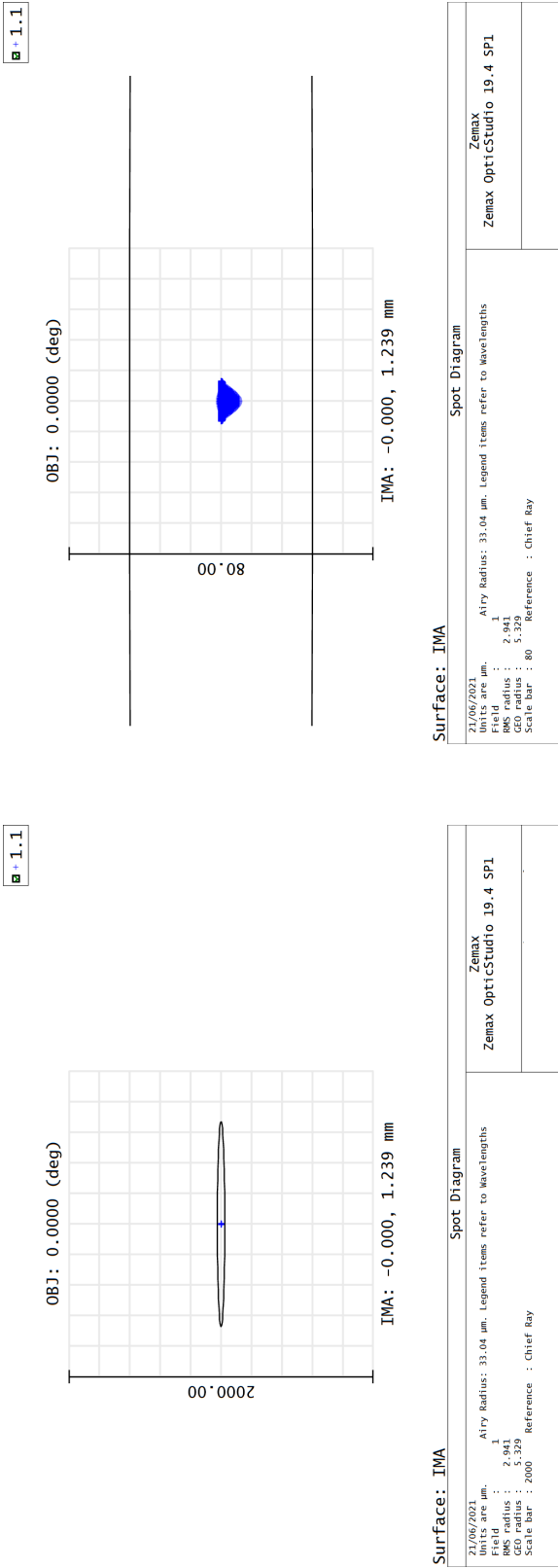
**(a)** A zoomed out view highlighting the size of the total Airy disk.

**(b)** A magnified view highlighting the geometric optical aberrations.

**Figure 4.7:** The geometric spot diagram at the SAPHIRA detector with the anamorphically reshaped Airy disk overplotted by the black solid curve.

enable the optomechanics to fit around them. In addition to this, increasing $d_o$ and $d_i$ relaxes the alignment tolerance of the instrument. The larger $d_o$ and $d_i$ are, the larger the physical spacing allowed under the tolerance error budget to keep the system aligned to say within 1% of the nominal spacing between it and the focal plane of M1.

## 4.8   Dispersing optic

Spectrally dispersing the starlight has advantages both for optimising the instrumentation and for science. For instrumentation, spectral dispersion reduces the bandwidth present in a spectral channel, both increasing the coherence length, making interference fringes easier to find, as well as reducing bandwidth smearing, allowing images with a wider Field of View (FoV) be recovered (Buscher 2015). The scientific advantages are numerous as it enables the object under study to be analysed as a function of wavelength. For example, in the near-infrared observations of Young Stellar Objects (YSOs) trace the thermal emission from hot dust in the circumstellar disk (Lazareff et al. 2017; Gravity Collaboration et al. 2019). As the disk temperature varies with distance from the star observations, different wavelengths probe different regions of the circumstellar disks. If the spectral resolution is sufficiently high the object can be studied across a spectral line and images of the emitting gas can even be resolved as a function of blueshift and redshift (Hone et al. 2017).

The design of FOURIER fits the J, H and K bands onto the detector simultaneously as this means the instrument does not need to be reconfigured in any way to change bands when observing. This does however limit how high a spectral resolution the instrument can achieve while fitting the light on the small $320 \times 256$ pixel detector. A design with a $R$ value of order $R \approx 100$ was reached, with $R$ given by $R = \lambda/\Delta\lambda$, where $\Delta\lambda$ is the smallest difference in wavelength resolvable at a wavelength of $\lambda$.

A simple way to implement spectral dispersion with high throughput is with a prism. Many beam combiners implement this method for their low dispersion mode (Mérand et al. 2010; Gravity Collaboration et al. 2017; Anugu et al. 2020; Pannetier et al. 2020) and this was the option selected for FOURIER.

In order to reach a high spectral resolution with a simple prism a high dispersion glass was required. Looking at the glass map shown in figure 4.8 a prism made of N-SF11 glass was selected due to its low Abbe number (high dispersion) and wide availability as an off-the-shelf
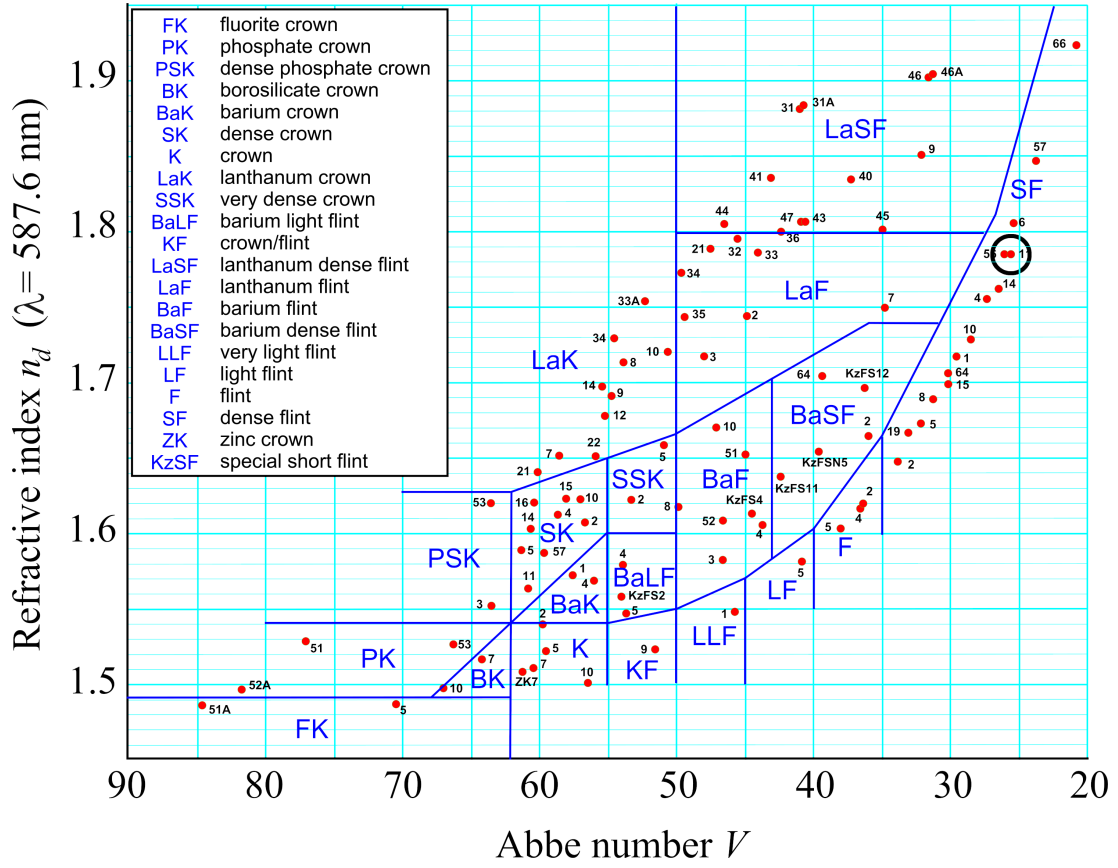
**Figure 4.8:** An Abbe diagram or glass map of many commonly available glasses. The location of the N-SF11 substrate selected for the FOURIER prism is circled, highlighting its low Abbe number (high dispersion) compared to other available glasses. From Mellish & Bajart (2010) with adaptation to highlight the location of the N-SF11 glass.

component. As figure 4.8 shows, such a low Abbe number however requires a relatively high index of refraction from the available glasses. An equilateral prism is typically used at angle of minimum deviation, giving the maximum clear aperture through the prism. The angle of minimum deviation is given by:

$$D_m = 2\arcsin\left(n\sin\left(\frac{A}{2}\right)\right) - A, \tag{4.10}$$

where $n$ is the refractive index of the prism substrate and $A$ the apex angle of the prism ($60°$ for an equilateral prism). From equation (4.10) it can be seen that the angle of minimum deviation increases with increasing refractive index of the substrate. As the Angle of Incidence (AoI) at the angle of minimum deviation is given by $i = (A + D_m)/2$ an increase in the angle of minimum deviation results in an increase of the AoI. For N-SF11 glass at a wavelength of

$\lambda = 1.75\,\mu$m n = 1.74 this equates to an angle of minimum deviation of $D_m = 60.9°$ and a corresponding AoI of $i = 60.45°$.

While such an AoI is manageable it must be carefully designed around, in particular with regards to the clear aperture and reflection losses at the surface of the prism.

At high AoI the clear aperture is reduced due to the projection of the beam onto a tilted surface. This is simple enough to compensate for by selecting a prism with large enough faces, however, the larger the faces of the equilateral prism, the thicker the substrate the light travels through. This is a concern as N-SF11 glass has substantial internal transmission losses in the K band, as figure 4.9 shows for a 10 mm thick slab of N-SF11 glass transmission losses are at around 10% at the centre of the K band (while only 0.25% and 1.37% at the centres of the J and H bands respectively). The off-the-shelf prism, with the minimum clear aperture to pass a 22 mm input beam (the maximum clear aperture expected at the MROI for diffracted starlight beams), was selected which was a prism with 20 mm sides (Thorlabs PS859). The footprint diagram showing the geometric beam size on the surface of the prism for a 22 mm input beam is shown in figure 4.10.

The second consideration when using a prism at such a high AoI is reflection losses. Fortunately, the AoI at the angle of minimum deviation of an equilateral N-SF11 prism of 60.45° is very close to Brewster's angle, the angle at which 100% of light is transmitted through the glass for P polarised light. Brewster's angle is given by:

$$\theta_B = \arctan\left(\frac{n_2}{n_1}\right), \tag{4.11}$$

where $n_2$ is the refractive index of the prism and $n_1$ the initial medium (either vacuum or air). For N-SF11 glass $\theta_B$ is 60.11°, resulting in excellent transmission of the P polarisation state as shown in figure 4.11. However, a significant (around 25.7%) amount of S polarised light is reflected and so lost if the prism is uncoated, giving a total reflection loss of around 12.8% for unpolarised light. For an instrument designed to maximise throughput this is significant and so the prism will be coated with an anti-reflection coating. Due to the tough requirements placed on the coating, namely that it must work across a wide spectral bandpass ($\lambda = 1.1$–$2.4\,\mu$m), at a high AoI (60.45°) and at liquid nitrogen temperatures (77K), a multi-layer custom coating is being designed by an external manufacturer. So far theoretical reflection curves have been produced which suggest throughput losses could be reduced to as low as 3.5% for unpolarised
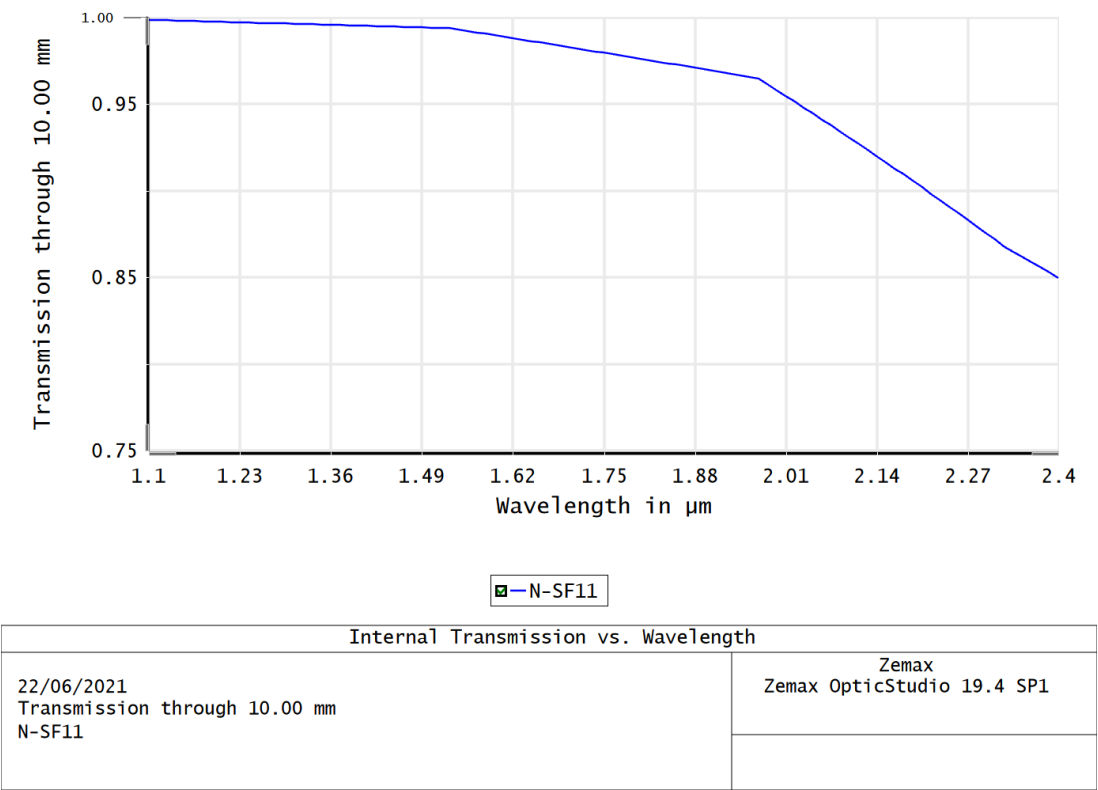
**Figure 4.9:** The internal transmission loss through a 10 mm substrate of N-SF11 glass, showing substantial loses in the K band.

light on the incident surface. At the time of writing however, the prism remains uncoated.

## 4.9   Cold stop

Room temperature objects emit a significant number of thermal photons in the K band (see section 5.7.1 for a detailed calculation). In order to limit the number of thermal photons reaching the detector a cold stop is necessary. The cold stop is designed to limit the number of thermal photons reaching the detector while passing all stellar photons. This is achieved by limiting the height of on-axis rays above the optical axis reaching the detector to the diameter of the aperture stop. The aperture stop in this case is the clear aperture of an optic before FOURIER along the MROI beam train. To limit the height of on-axis rays above the optical axis (typically) a liquid nitrogen cooled metal sheet with a circular hole is placed at the image location of the aperture stop produced by the intervening optics.

An example of a simplified cold stop system is shown in figure 4.12. Here the first surface is

☑ + 1.75



```
Aperture Full X Width : 20.0000
Aperture Full Y Height: 17.3200                          % rays through = 100.00%
                                    Footprint Diagram
22/06/2021                                                              Zemax
Surface 13: Prism                                          Zemax OpticStudio 19.4 SP1
Ray X Min =   -0.1587 Ray X Max =    0.1587
Ray Y Min =   -3.7945 Ray Y Max =    4.0008
Max Radius=    4.0008 Wavelength=    1.7500
Legend items refer to Wavelengths
```
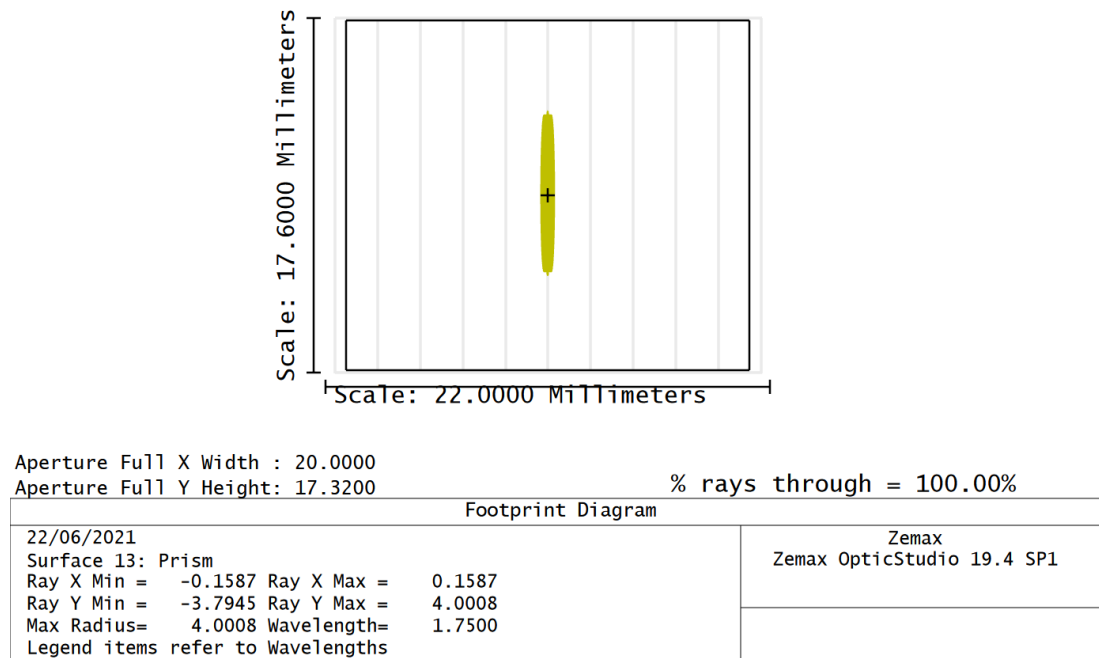
**Figure 4.10:** A footprint diagram of the geometric beam size for a 22 mm beam as it is projected onto the surface of the prism, showing the clear aperture of the prism is sufficient.

the aperture stop which limits the height of the on-axis rays of starlight the system can pass (as demonstrated by the rays that terminate at the surface). The remaining rays are then imaged by the focusing optic. While starlight is limited to the extent of the aperture stop, thermal photons emitted by the surfaces around the aperture stop would still reach a detector in this system, this is why a cold stop is needed. The cold stop (shown on the far right of figure figure 4.12) is at the location of the image of the aperture stop produced by the focusing optic. By placing a circular hole equal to the size of the image of the aperture stop at this location a detector at a subsequent image plane will only "see" the extent of the aperture stop, immediately surrounded by the cold stop. As the cold stop is cold, it will emit significantly fewer thermal photons than the surfaces around the aperture stop that the detector would "see" without the cold stop.

To find the location of the exit pupil I must first consider which surface to take as the aperture stop. Given the complex beam train of the MROI (see figure 2.1) this is not a simple task. The obvious surface to consider is the primary mirror of the Unit Telescope (UT) itself, however,
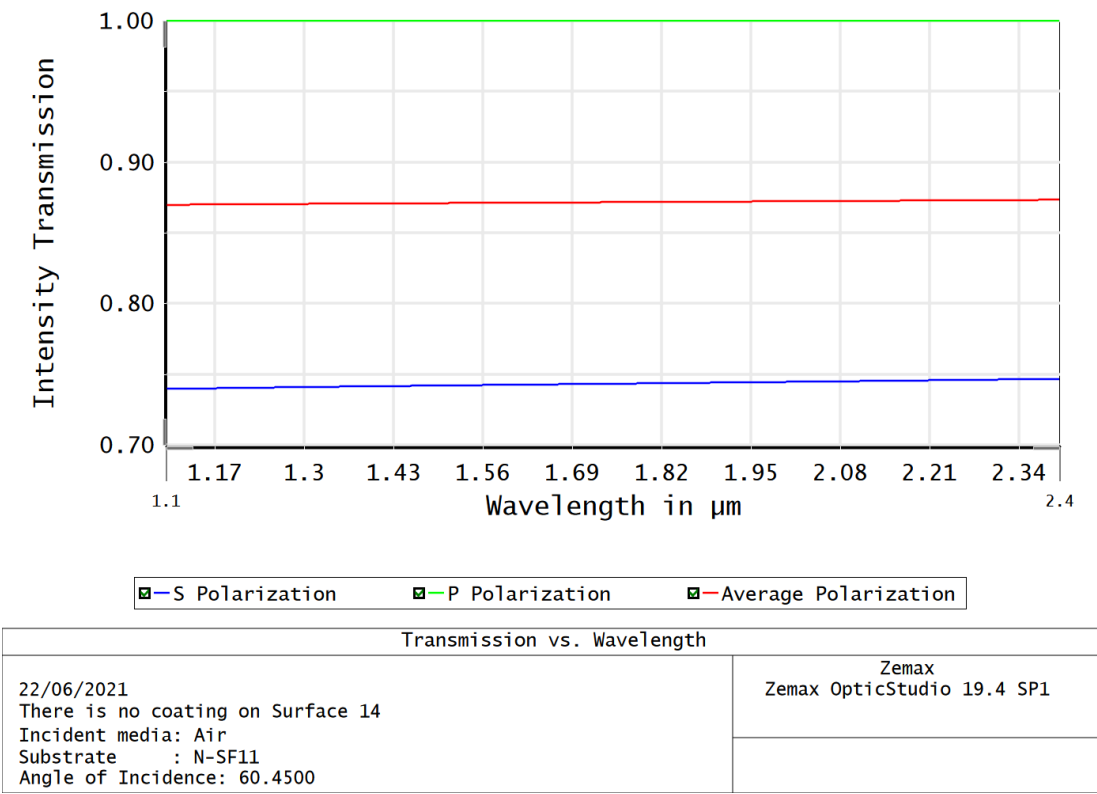
**Figure 4.11:** Transmission vs wavelength for an uncoated N-SF11 prism used at the angle of minimum deviation. As the angle of minimum deviation is close to the Brewster's angle of the glass, transmission is excellent for P polarised light but far from ideal for the S polarised light.
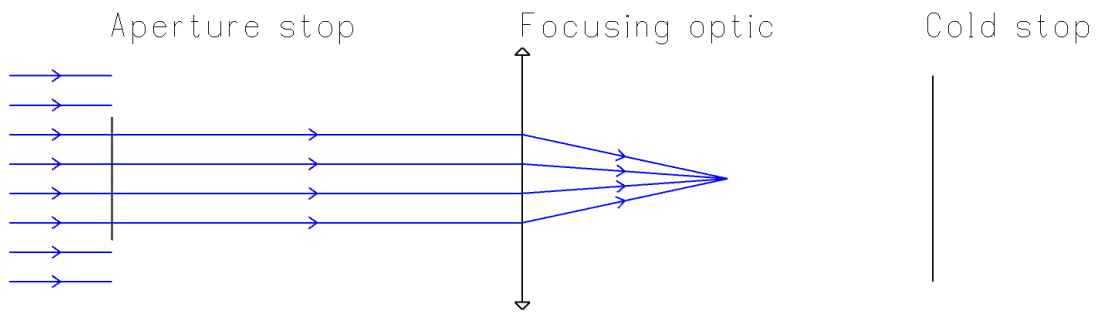


**Figure 4.12:** A simplified example of a cold stop system. Here the aperture stop (far left) limits the height of the on-axis rays of starlight above the optical axis to the diameter of the aperture stop (as demonstrated by the rays that terminate at that surface). These rays are then imaged by the focusing optic. The extent of the on-axis rays of starlight is limited by the aperture stop, however, the surface around the aperture stop will emit thermal photons which will pass through the system. To remove these thermal photons a circular hole equal to the size of the image of the aperture stop is placed at the location of the image of the aperture stop produced by the focusing optic. A detector placed at a subsequent image plane will then "see" the extent of the aperture stop immediately surrounded by the cold stop which will emit far fewer thermal photons as it is cooled.

as the distance from the UT to the FOURIER beam combiner varies significantly (from tens to hundreds of meters) depending on the baseline it would not be possible to select one fixed location for the cold stop. I therefore only consider surfaces after the delay line exit as these then have a fixed distance from FOURIER. The exit pupil must be both within the cryostat and before the dispersing optic. Considering the exit pupil produced by the M1 optic alone I find that as the distance between the aperture stop and FOURIER increases, the location of the exit pupil tends towards the focal length of M1. I therefore select the optic at the greatest distance from FOURIER which remains at a fixed distance with respect to FOURIER, as its exit pupil is least likely to be after the dispersing optic along the FOURIER beam train. This is the exit of the Beam compressor, taken to be a 1" diameter aperture located 14.19 m from M1.

Modelling the system in Zemax the exit pupil is 112 mm along the optical axis behind the location of the spatial filter and is 2.35 mm in diameter. This places the exit pupil between M2 and the prism as M2 is 52.5 mm along the optical axis behind the location of the spatial filter and the prism is 240 mm behind.

While this location is accessible, because the light reflects off M2 first it is unsuitable to be used as the exit pupil along the interference fringe axis as the effects of both M1 and M2 must be considered. As mentioned this is only an issue along the interference fringe axis, as M2 acts simply as a fold mirror along the perpendicular, spectral axis, the properties of the exit pupil are unchanged. This therefore leads to the idea much like the spatial filter (section 4.6) of two cold stops, one for the for the interference fringe axis and one for the spectral axis.

The location of the cold stop along the interference fringe axis is then at the image of the aperture stop created by both M1 and M2. Modelling this in Zemax again the exit pupil is located 78 mm along the optical axis behind the location of the spatial filter, placing it 25 mm after M2. It is 1 mm in diameter.

The solution implemented is to place two sets of rectangular apertures, one at the location of each stop, of height equal to the applicable exit pupil diameter at that location and width many times larger to ensure all light is passed along the axis it is not acting as the cold stop for. Because of the difference in magnification if M2 is or isn't considered the detector will then "see" a square cold stop which limits the on-axis FoV to the 1" clear aperture at the beam compressor.

Figure 4.13 shows the location of the cold stops with respect to M2 in a 3D shaded model.
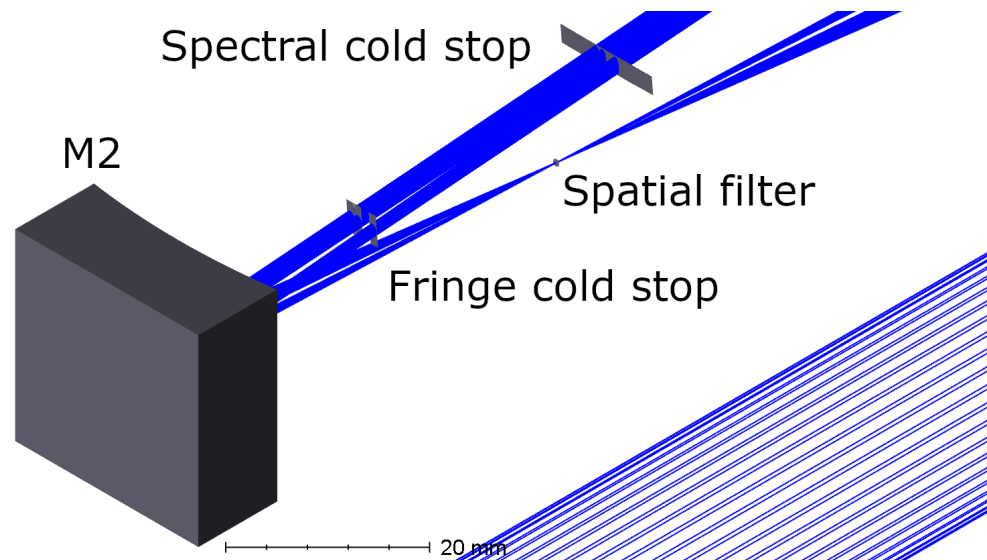
**Figure 4.13:** A 3D shaded model showing the two sets of cold stops implemented within FOURIER. The fringe cold stops are three independent apertures (one for each beam) restricting the light along the interference fringe axis. The spectral cold stop is a single long slit which restricts the light along the perpendicular, spectral axis. What is shown here is the extent of the apertures themselves, this will be implemented by a sheet of metal with holes cut out where the apertures are shown here.

It shows the fringe cold stops as three independent apertures (one for each beam) restricting the light along the interference fringe axis. The spectral cold stop is a single long slit which restricts the light along the perpendicular, spectral axis. What is shown in the figure is the extent of the apertures themselves, the design will be implemented by a sheet of metal with holes cut out where the apertures are shown in the figure, at the location of each set of stops.

## 4.10 Summary

In this chapter I have presented the proposed optical design for the FOURIER beam combiner, highlighting the motivation for the various design choices. In the next chapter I will quantify the performance of this design, demonstrating it is both feasible to build and satisfies the performance requirements.

CHAPTER

# 5

## Simulated performance of FOURIER

### 5.1 Introduction

In the previous chapter I discussed the motivation behind the optical design of the Free-space Optical multi-apertUre combineR for IntERferometry (FOURIER). In this chapter I take that optical design and quantify the performance of it against various metrics both verify that it satisfies the design requirements discussed in chapter 3, and that the design is practical to build when considering alignment tolerancing (section 5.2) and thermal cooldown (section 5.3).

As mentioned in the declaration the throughput (section 5.5) and visibility loss (section 5.6) of the Magdalena Ridge Observatory Interferometer (MROI) beam train for the H and K bands is taken from a model developed by David Buscher. This was extended to the J band by myself.

### 5.2 System tolerancing

In the previous chapter I discussed the optical design of FOURIER for an ideal system with perfect optics held exactly in place floating in free space. Unfortunately actual hardware development is much more complex than this and a design which appears to work under ideal conditions can quickly deteriorate in performance with imperfect optics and alignment. In this section I outline the work that went into developing the alignment error budget to study how

practical the design of FOURIER was to build.

I computed the alignment error budget for FOURIER using the tolerancing tools contained within Zemax. There are two categories of tolerancing errors that have to be considered when developing a tolerancing budget, manufacturing and alignment errors. A list of tolerances considered for each optical element and their Zemax command names are listed in table 5.1.

**Table 5.1:** The Zemax operand name and description of the tolerance parameters used to simulate the performance of FOURIER. They are split into alignment errors and manufacturing errors associated with the optics.

| Operand | Tolerance |
|---|---|
| Alignment errors | |
| TEDX | element decentre x axis |
| TEDX | element decentre y axis |
| TTHI | element decentre z axis |
| TETX | element tilt about x axis |
| TETY | element tilt about y axis |
| TETZ | element tilt about z axis |
| Manufacturing errors | |
| TRAD | surface radius of curvature |
| TEZI | surface irregularity |
| TIND | substrate refractive index |

In Zemax the tilt and decentre alignment errors are calculated by inserting a coordinate break on both sides of the optical element with the origin of the coordinate break being coincident with the centre of the optical element. In practice this means each optic is rotated and decentred about the centre of the first surface the incoming light strikes. This, and the alignment operands are shown in figure 5.1. The result of this is that each optical element toleranced has its own origin about which the tolerancing is conducted. As FOURIER has a complex 3D geometry not only are the x, y and z axes offset from each other but also rotated as the z axis typically points along the beam propagation direction. This means that tolerances do not correspond to tilts about the same axes for a given operand.

Tilts and decenters of each optical element are self-explanatory, however it is worth discussing the manufacturing errors modelled. The error in the surface radius of curvature, TRAD,
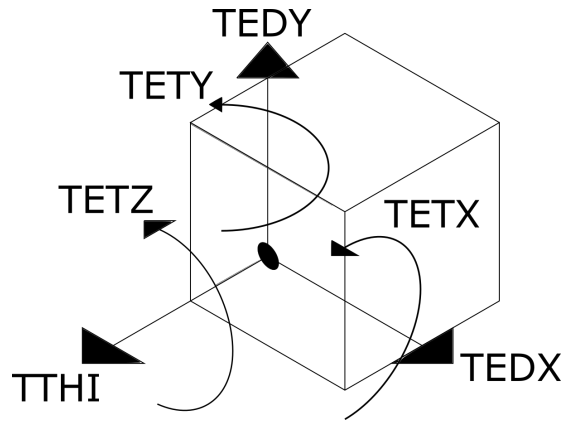
**Figure 5.1:** A sketch showing the vertex about which each optical element is tilted and decentred during the tolerancing process. The black disk represents the centre of the first surface of the optical element along the beam train.

is implemented here such that it alters the radius of curvature of the optical element by a percentage of its nominal value. The TEZI parameter, a measure of the surface irregularity is more complex. TEZI uses Zernike polynomials to model optics which deviate from the ideal surface. Zernike terms between 2nd (ignoring piston) and 231st can be simulated, though for the tolerancing carried out here only terms up to the 50th are used. The coefficients of all Zernike terms used are then set so that they yield the Root Mean Square (RMS) surface error specified by the user in lens units. The lens unit is set to mm in the Zemax model so needs to be converted a meaningful criterion. For example by assigning the surfaces a $\lambda/4$ peak to valley (P2V) surface error at $\lambda = 633$ nm, giving a P2V surface error of $1.6 \times 10^{-4}$ mm. The P2V surface error is divided by a factor of 5 to convert from P2V to RMS, which is a conservative value estimated from the average factor of 5.5 between P2V and RMS wavefront error values found by Porro et al. (1999).

The TIND parameter tolerances the index of refraction of the glass by taking a user input minimum and maximum variation on the refractive index at the Fraunhofer spectral D line ($\lambda = 589.3$ nm), with the refractive index at other wavelengths being estimated based on this change and the model of refractive index as a function of wavelength within Zemax.

When setting up the tolerance operands it is possible to implement an compensator, a operand which will optimise a parameter of the Zemax model (such as the tilt of an optic) against a metric defined by the user (such as geometric RMS spot size) after the system has been perturbed from the ideal alignment. An example of where a compensator would be

useful is in adjusting the distance between the last element and the image plane in a lens system, simulating someone adjusting the focus distance of a real misaligned lens system. The tolerance error budget I have built does not utilise any compensators as FOURIER has no motorised controls within the cryostat and so it will not be possible to correct any random perturbation in the alignment after cooldown of the cryostat as the optics will be inaccessible.

Tolerancing in Zemax is carried out by two complementary techniques. Common between the two, however, is that they report the performance of the toleranced design against a user defined metric such as the geometric RMS spot size. In the analysis I conducted I input a maximum and minimum value each tolerance operand can take, which is then used differently by the two techniques. The first technique, known as sensitivity analysis, perturbs the system by one parameter at a time to the extreme deviations (both the minimum and maximum value) allowed by the tolerance error budget, repeating the process for each parameter. The user defined metric is calculated and stored for each unique perturbation. The TEZI operand is a special case as there are many different arrangements of the coefficients of the Zernike polynomials which would result in the same RMS surface error. For this operand each Zernike polynomial in use is assigned the same coefficient value, which is set such that the square root of the sum of the squares of the coefficients results in the user defined RMS surface error. From the stored user defined metric measured for each perturbation the Root Sum Square (RSS) value of the change from the nominal is calculated by summing over $i$, the unique tolerance operands with

$$C = \sqrt{\sum_i \frac{\Delta_{i,min}^2 + \Delta_{i,max}^2}{2}}, \tag{5.1}$$

where $\Delta_{i,min}^2$ and $\Delta_{i,max}^2$ represent the difference between the nominal value and value from the perturbed system of the user defined metric at the minimum and maximum tolerance values respectively. By this method, while the change in the user defined metric is calculated at both the minimum and maximum deviation, only the average is used in the estimation of the performance for the system as a whole. This is because both the minimum and maximum deviation from the nominal value of each tolerance operand cannot occur simultaneously and so including both as separate terms, inflating $C$ by doubling the number of terms, would lead to an underestimation of the performance of the toleranced system as a whole.

The estimated performance of the toleranced system against the user defined metric is then reported as $F = \sqrt{N^2 + C^2}$ where $F$ is the estimated RSS user defined metric, $N$ the value of

```
Worst offenders:
Type                              Value        Criterion        Change
TEZI     3                     -3.1650E-05     0.00685117     0.00275431
TEDX    10       10             0.15000000     0.00677973     0.00268287
TEDX    10       10            -0.15000000     0.00651912     0.00242226
TRAD    10        1            -0.30867000     0.00599148     0.00189462
TTHI     9       10            -0.15000000     0.00551515     0.00141830
TRAD    16        1             0.30900000     0.00530635     0.00120949
TETY    10       10             0.05700000     0.00521035     0.00111349
TETY    10       10            -0.05700000     0.00501249     0.00091564
TETX    10       10             0.05729578     0.00493825     0.00084139
TTHI    15       17             0.15000000     0.00490872     0.00081186


Estimated Performance Changes based upon Root-Sum-Square method:
Nominal RMS Spot Radius    :      0.00409686
Estimated change           :      0.00430243
Estimated RMS Spot Radius  :      0.00839928
```

**Figure 5.2:** An example output from the RSS statistical approach of Zemax tolerancing. From left to right, the operand and the surface it is applied to is listed, followed by the value of the tolerance applied (deviation from the nominal value). The "Criterion" column lists the value of the user defined metric when that tolerance alone is applied, with the change column reporting the change in the user defined metric from the nominal value. Each tolerance is listed by its impact on the user defined metric, making it easy to identify which tolerances need tightening. Estimated performance of the whole system via RSS statistics is given below.

the metric for the nominal system and $C$ as defined in equation (5.1).

The benefit of this sensitivity analysis approach is that the impact of each tolerance can be assessed independently, highlighting which tolerances have the greatest impact on system performance and identifying the ones which have a minimal impact. A example of this is shown in figure 5.2.

The methodology I used for developing the tolerance error budget was to build a basic budget and adjust it, tightening the tolerances on the worst offenders first and relaxing tolerances which had no or minimal impact on the performance of the system. These were adjusted until the metric I measured against (discussed in section 5.2.1) was at a desired level.

While an advantage for identifying the worst offenders, the fact that with RSS statistics each tolerance is considered in isolation is also a limitation. This is fine if the tolerances are truly independent of each other, but this is not necessarily the case in optical tolerancing. For example, considering a tilt error on a pair of mirrors, the two tilt errors could combine to deviate the beam more than each tilt error would individually. To investigate the effect of all tolerances being applied to the system simultaneously, Zemax provides a Monte Carlo analysis tool. In this

approach all tolerances are perturbed at the same time, with the value of the perturbation being chosen at random by assuming that the probability of a value within the permitted tolerance range occurring follows a normal distribution (other distributions are also available). In this case for symmetrical tolerances (same allowed range +/- the nominal value) the nominal value is the mean of the normal distribution and the standard deviation 1/4 the maximum/minimum tolerance value. The Gaussian is slightly modified in that the distribution is cut off at $n$ times the standard deviation (where $n = 2$ by default) to ensure that (while unlikely) values outside the specified tolerance range are not drawn. A random draw is made for each perturbation from the normal distributions and each tolerance operand is perturbed by that value. The user defined criterion is then measured for the randomly perturbed system and this process is repeated many times, typically a couple of thousand times in the runs I performed. These thousands of randomly perturbed systems build up a distribution of the user defined metric for the defined tolerance error budget, to which a Gaussian is fitted, extracting a standard deviation and a mean from which the quality of the misaligned system can be assessed. An example run from a Monte Carlo tolerance error budget is shown in figure 5.3.

### 5.2.1   Measurement metrics

To assess if a tolerance budget is appropriate I must first associate the performance of the instrument to a metric which can be quantified within Zemax. Zemax offers many criteria that can be used such as RMS geometric spot size, wavefront error or a user defined merit function. As discussed in section 4.7 the instrument is designed for two very different specifications, along the spectral axis the PSF is compressed to just two pixels across the Airy disk at $\lambda = 1.1\,\mu m$. Along the perpendicular interference fringe axis the Airy disk is 59 pixels across at $\lambda = 1.1\,\mu m$.

The spectral axis criterion for tolerancing is simple to define: I placed the criterion to be that the RMS spot size should be no more than 20% the width of the Airy disk to keep the system diffraction limited. Defining a criterion along the interference fringe axis is more complex. Here I wish to maximise the visibility, or fringe contrast, however measuring the visibility in Zemax requires a Physical Optics Propagation (POP) simulation to be run through the system and then a Fast Fourier Transform (FFT) to be calculated from the resulting interference fringes. This cannot be done within Zemax and so cannot be directly used as a criterion in the tolerance analysis.
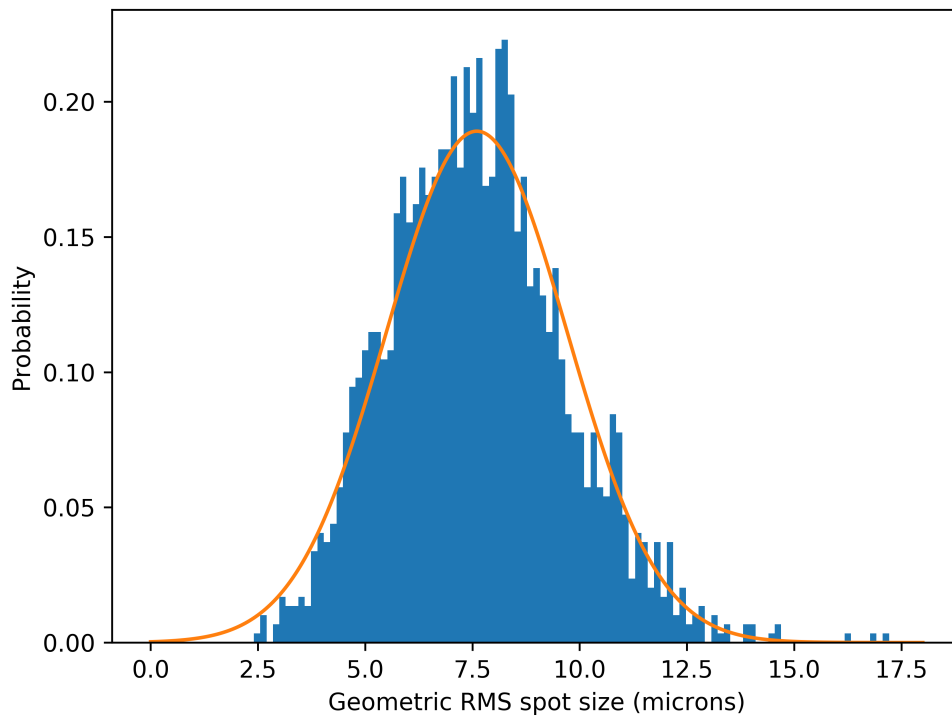
**Figure 5.3:** An example result of running Monte Carlo tolerancing. The 2,000 runs are split into 100 bins in this normalised histogram with the extracted mean and standard deviation used to plot the fitted histogram curve in orange, showing the distribution of the tolerance runs to be Gaussian like.

Instead, I developed a proxy for the fringe contrast by linking fringe contrast to the RMS geometric spot size. To do this I adjusted the distance between M2 (the mirror which refocuses the light along the interference fringe axis) and the subsequent optics (prism, L1, SAPHIRA) and detector in Zemax, essentially defocusing the light along the interference fringe axis. I increased the level of defocus in incremental steps, running the POP routine and extracting the simulated visibility as well as recording the RMS spot size along the interference fringe axis at each step. Figure 5.4 plots the resulting relationship between geometric RMS spot size along the interference fringe axis and the percentage visibility loss, i.e. how many percent from the idealised system the resulting fringe contrast is. This is measured for all three baselines sampled by FOURIER where "Baseline 1" represents the shortest separation between two beams and "Baseline 3" the largest. There are two samples per position here as I took measurements at both sides of the nominal position of M2 to test how robust this metric was. As figure 5.4 shows the metric does not give complete repeatability, for example for spot sizes of around 85 μm on
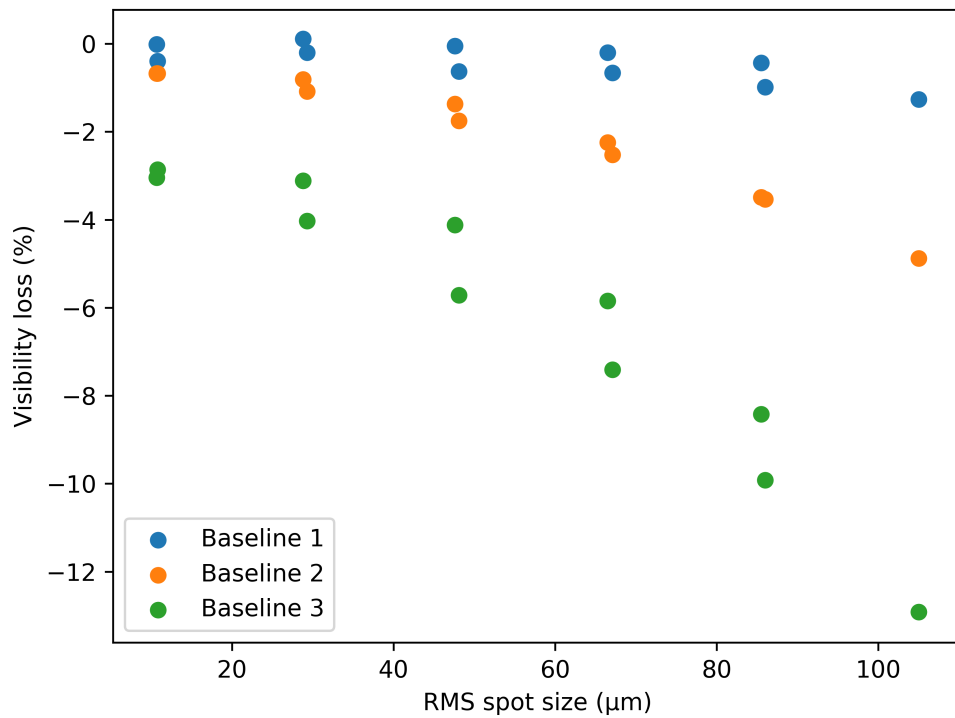
**Figure 5.4:** The RMS geometric spot size, calculated along the interference fringe axis, against the resulting visibility loss along all three baselines sampled by FOURIER. This relation was generated by adjusting the distance between M2 and the subsequent optics either side of the nominal focus, hence there are two measurements at approximately the same spot size. This established a loose correlation, which was used to inform the tolerance error budget along the interference fringe axis.

baseline 3 there is a difference of around 2% in visibility loss between measurements made at the same distance on opposite sides of the nominal position of M2. Though as the RMS spot size is not the same value either side of the nominal focus, this could in part be explained by the system being more sensitive to defocus one side of the nominal position compared to the other. However, this correlation does not need to be exact as it is designed only to aid in developing a quick estimate of system performance along the interference fringe axis that can be evaluated within Zemax. Verification of the error budget on the visibility was carried out later by directly measuring the visibility for a small sample of individual files from the Monte Carlo runs to verify this relation held.

By adopting the criterion that the visibility must not drop by more than 4% on any baseline due to both alignment and manufacturing errors, from figure 5.4 I can see that the geometric

RMS spot size must not exceed 30 μm along the interference fringe axis and so this was the criterion the tolerance error budget developed to not exceed. The ideal system has a geometric RMS spot size of 5.5 μm along the interference fringe axis.

## 5.2.2 FOURIER tolerancing results

With the error budget against quantifiable metrics and the parameters that would be toleranced defined, I generated the alignment error budget for all optics by starting with a loose set of tolerances, running the analysis and adjusting the budget, using the sensitivity analysis to identify tolerances which needed tightening while simultaneously loosening errors which had little impact on the system performance. This iterative process led to the final error budget, given in table 5.2.

**Table 5.2:** The tolerance error budget for FOURIER ensuring that when both alignment and manufacturing errors are taken into account the system performance is within the criterion set out in section 5.2.1 for both the spectral and interference fringe axes. Surface quality is referenced as a P2V wavefront error at $\lambda = 633$ nm.

| Component | $\Delta$X (μm) | $\Delta$Y (μm) | $\Delta$Z (μm) | $\Delta\Theta_X$ (mrad) | $\Delta\Theta_Y$ (mrad) | $\Delta\Theta_Z$ (mrad) | $\Delta$rad (%) | Surf Quality | $\Delta$n |
|---|---|---|---|---|---|---|---|---|---|
| M1 | ±10 | ±10 | ±50 | $\pm 3 \times 10^{-3}$ | $\pm 3 \times 10^{-3}$ | $\pm 3 \times 10^{-3}$ | $\pm 2 \times 10^{-2}\%$ | $\lambda/4$ | NA |
| Window | 300 | 300 | 300 | 2 | 2 | 2 | NA | $\lambda/4$ | ±0.001% |
| M2 | 150 | 300 | 150 | 1 | 1 | 2 | ±0.3% | $\lambda/4$ | NA |
| Prism | 300 | 300 | 300 | 1 | 2 | 2 | NA | $\lambda/4$ | ±0.001% |
| L1 | 300 | 300 | 150 | 2 | 2 | 2 | ±0.3% | $\lambda/4$ | ±0.001% |
| SAPHIRA | NA | NA | 150 | NA | NA | NA | NA | NA | NA |

Evaluating the RSS statistics for the final error budget at a test wavelength of $\lambda = 1.75\,\mu m$ results in an increase from an RMS spot size along the interference fringe axis from $4\,\mu m$ to $10.7\,\mu m$. From figure 5.4 this equates to a visibility loss of no more than a couple of percent along any of the baselines, well within the desired level of 4% or less. The RMS spot size along the spectral axis increases from $1.8\,\mu m$ to $4.8\,\mu m$, again this is well within our criterion of keeping the RMS spot size below 20% the diameter of the first Airy disk null of $76\,\mu m$ in diameter at $\lambda = 1.75\,\mu m$. Simulating 2,000 runs of the Monte Carlo analysis I find similar results. Figure 5.5 and 5.6 show the distribution of the RMS spot size along the interference and spectral axes respectively from the Monte Carlo tolerancing with the Gaussian of mean and standard deviation as calculated by Zemax for the 2,000 runs overplotted in orange.

The distributions are far from Gaussian in shape implying that the mean and associated standard deviation cannot be directly relied upon to estimate the system performance. However, by inspection one can see that nearly all of the 2,000 systems generated are within the tolerance error budget along both the interference fringe axis (spot size of $30\,\mu m$ to ensure a visibility drop of 4% or less) and spectral axis (smaller than the 20% $76\,\mu m$ diffraction Airy disk size at the test wavelength of $\lambda = 1.75\,\mu m$). In fact the analysis of the distribution shows that 98% of the Monte Carlo generated systems have a RMS spot size of $20\,\mu m$ or less along the interference fringe axis and $5.4\,\mu m$ or less along the spectral axis.

The alignment tolerances placed on M1 are significantly tighter than for the other optics. This is not due to it producing high levels of aberration in the tolerance error budget, but instead to ensure that the image plane of M1 coincides with the location of the narrow spatial filter to maximise the amount of light coupled through the spatial filter. A $10\,\mu m$ decentre coupled with a $3 \times 10^{-3}$ mrad tilt error were selected as the error budget as they would result in a shift of the PSF at the M1 focal plane of $14\,\mu m$, or 18% of the slit width for a slit $76\,\mu m$ in width (the width of a diffraction limited beam at $\lambda = 1.75\,\mu m$). The tolerancing analysis did reveal the need for a tight error on the radius of curvature of M1, set to $\pm 2 \times 10^{-2}\%$ its nominal value. However for manufacturing purposes it can be much looser as I only need to know the radius of curvature of M1 to within $\pm 2 \times 10^{-2}\%$, not have it manufactured to within $\pm 2 \times 10^{-2}\%$ of its nominal value. This is because I am able to compensate for any manufacturing error above $\pm 2 \times 10^{-2}\%$ by adjusting the spacing between M1 and the spatial filter which has no impact on the optical performance of the subsequent optics which only serve to reimage the
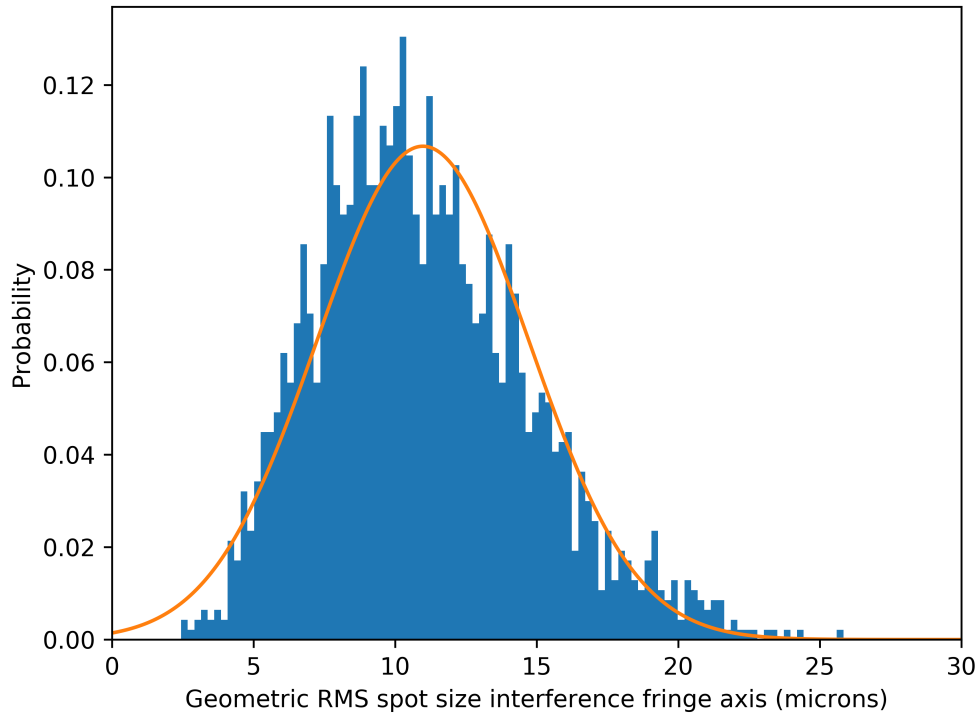
**Figure 5.5:** The RMS geometric spot size along the interference fringe axis for 2,000 randomly perturbed realisations of FOURIER. All toleranced elements were randomly perturbed by the method described in the text to the error budget given in table 5.2. The vast majority of the systems are below the 30 μm RMS spot size required to keep visibility losses at 4% or less.

M1 focal plane. The tolerance error budget for the rest of the system is moderately relaxed which is expected as the system was designed with long focal lengths resulting in "slow" beams. For example considering the 13 mm beams on M1, with a focal length of 1.203 m the system has an effective f ratio of f/92. With this alignment error budget the system does not require complex optomechanics to align it and does not require any motorised parts within the cryostat, significantly reducing the cost and complexity of the optomechanics.

## 5.3   Thermal Modelling

In the previous section I demonstrated the degree to which FOURIER has to be aligned in order to maintain good system performance. Such loose tolerances of hundreds of microns in position and milliradians in tilt are moderately easy to achieve on an optical bench, however,
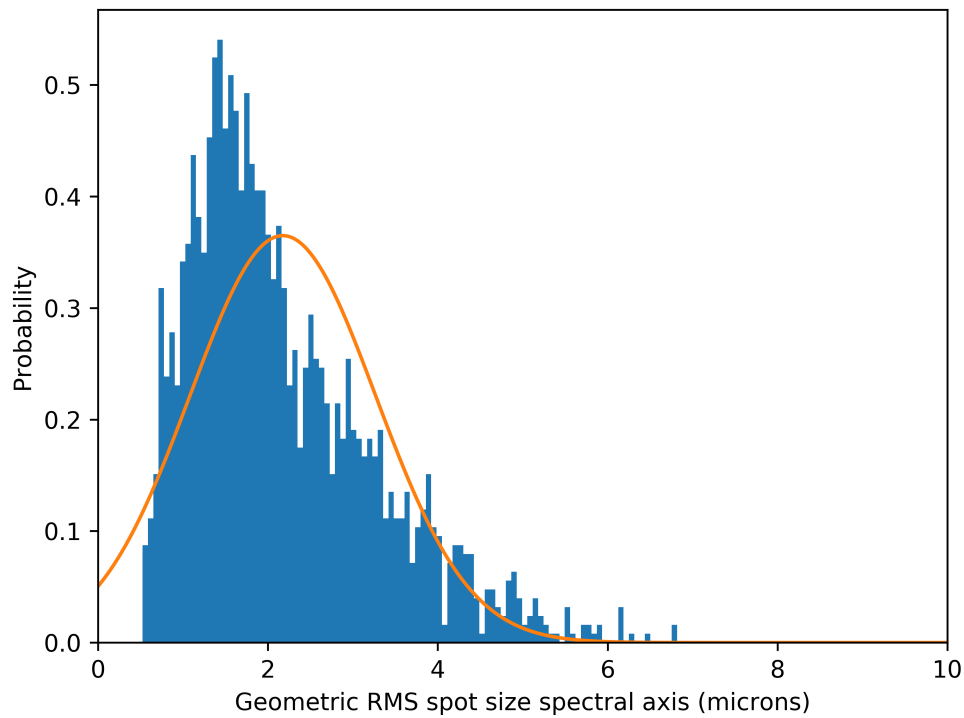
**Figure 5.6:** The RMS geometric spot size along the spectral axis for 2,000 randomly perturbed realisations of FOURIER. All toleranced elements were randomly perturbed by the method described in the text to the error budget given in table 5.2. The vast majority of the systems are below the 15 μm criterion which is 20% of the diffraction limited PSF at the test wavelength of $\lambda = 1.75$ μm.

this alignment would be done when the system is at room temperature whereas observations will be carried out with the instrument at liquid nitrogen cooled temperatures. In cooling the system the optomechanics will shrink, moving out of alignment. It is therefore necessary to model how the alignment will change on cooldown to ensure it does not exceed the alignment tolerance error budget, and if it does, to generate a plan to purposefully misalign the system at room temperature such that it comes into alignment (within the tolerance error budget) on cooldown.

This work was carried out with the thermal modelling tools within Zemax which simulate both the variation of refractive index, as well as thermal expansion/contraction of the glass types modelled. Between optical surfaces it can also simulate the variation in spacing with temperature based on a user input Coefficient of Thermal Expansion (CTE) for the spacing surface.

### 5.3.1   Cold plate CTE

I first consider how the optics move as the system is cooled from room temperature to 100K (it is assumed that the system will not reach the 77k of LN2 due to thermal inefficiencies). The model used is relatively simple as all the optics are mounted to a common cold plate made of aluminium cast MIC-6 and so the system is modelled as point sources that move on an expanding and contracting 2D plane.

First it is important to know what CTE to use. As the system is cooling over such a wide temperature range (293-100K) the typical linear CTE cannot be assumed to be constant with temperature. I was unable to find cryogenic CTE measurements for aluminium cast MIC-6, however, Bradley et al. (2013) provide such measurements for aluminium 6061-T6. As the CTE for the two alloys are the same at room temperature and the other aluminium alloys listed in Bradley et al. (2013) have the same CTE at all measured temperatures I expect this to be a good enough approximation for the CTE of aluminium cast MIC-6. Bradley et al. (2013) provide a polynomial to extract the linear expansion coefficient of aluminium 6061-T6 from room temperature (293K) to the desired temperature down to 18K which is given by

$$\frac{\varDelta L}{L} \times 10^{-5} = -4.1277 \times 10^2 - 3.0389 \times 10^{-1}T + 8.7696E \times 10^{-3}T^2 - 9.9821 \times 10^{-6}T^3, \quad (5.2)$$

where $L$ is the length of a section of aluminium and $T$ the temperature of the aluminium. Evaluating equation (5.2) at 288K (a 5K temperature difference) gives a $\varDelta L/L$ of $11.35 \times 10^{-5}$ m/m or $113.5\,\mu m/m$. Dividing this by a factor of five to give the CTE per degree kelvin then gives the more traditional CTE to be $22.7 \times 10^{-6}$ /°C expected for room temperature aluminium. So the CTE is the gradient, or differential of equation (5.2). Figure 5.7 plots the polynomial of equation (5.2) alongside an estimate of the thermal expansion if the room temperature CTE of $22.7 \times 10^{-6}$ / °C is assumed to be valid at all temperatures, it shows that the constant CTE approximation deviates at temperatures below around 200K, with a large difference in the final expansions at the operating temperature of 100K. Assuming a constant CTE is then unsuitable for this work. Assuming a constant CTE and evaluating it at 100K would overestimate the contraction of the aluminium by $594\,\mu m/m$ compared with the polynomial fit.

Figure 5.8 looks at the change in CTE as a function of temperature, plotting the differential of figure 5.7, which is only approximately constant for temperatures above 200K. This presents
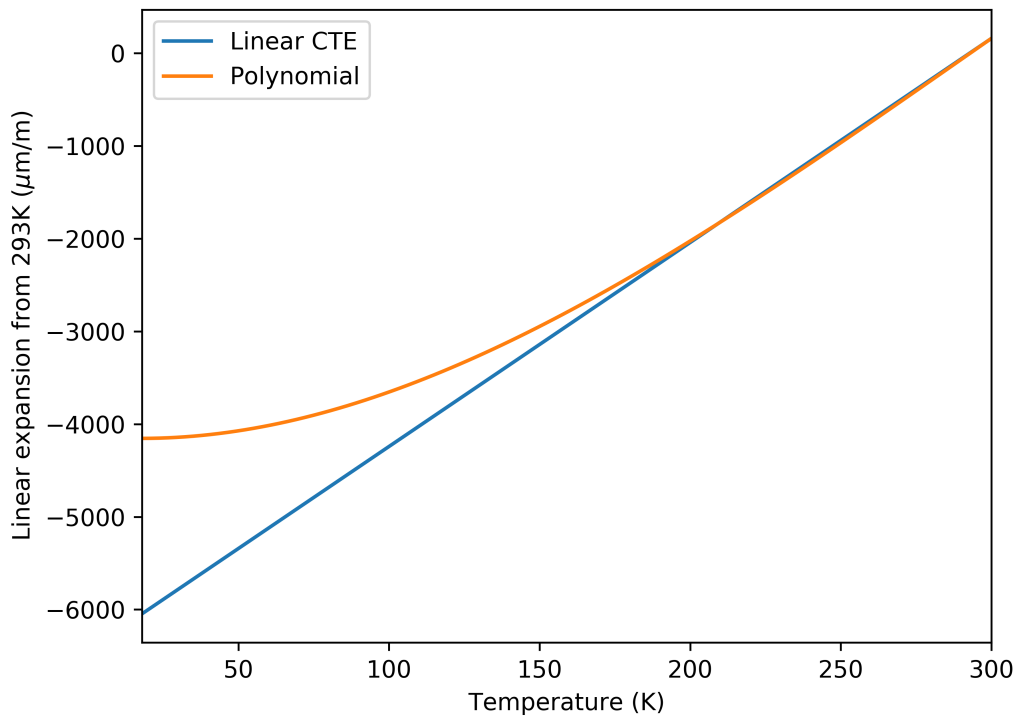
**Figure 5.7:** The linear expansion of 6061-T6 Aluminium from 293K as a function of temperature using equation (5.2) from Bradley et al. (2013).

a problem as Zemax only accepts a constant CTE for the spacing of surfaces between optics. This can be overcome by inputting a value of the constant CTE which would result in the contraction expected from the polynomial CTE at a temperature of 100K though this would make evaluating the system at any temperatures other than 293 and 100K invalid. This is fine for the work presented here as I only evaluate the system at room temperature and its 100K operating temperature. The polynomial expansion of figure 5.7 gives the expansion between 293 and 100K to be 3655 μm/m so an effective CTE of $18.9 \times 10^{-6}$ / °C is used.

### 5.3.2 Optics motion on cooldown

With the rate at which the cold plate will contract on cooling established, it is now possible to model how the optics will move on cooldown. Zemax does this by modelling mounting spacers as infinitesimally thin cylindrical shells with their axes pointing along the z axis of the local coordinate system (typically the direction the beam is travelling). The motivation for this
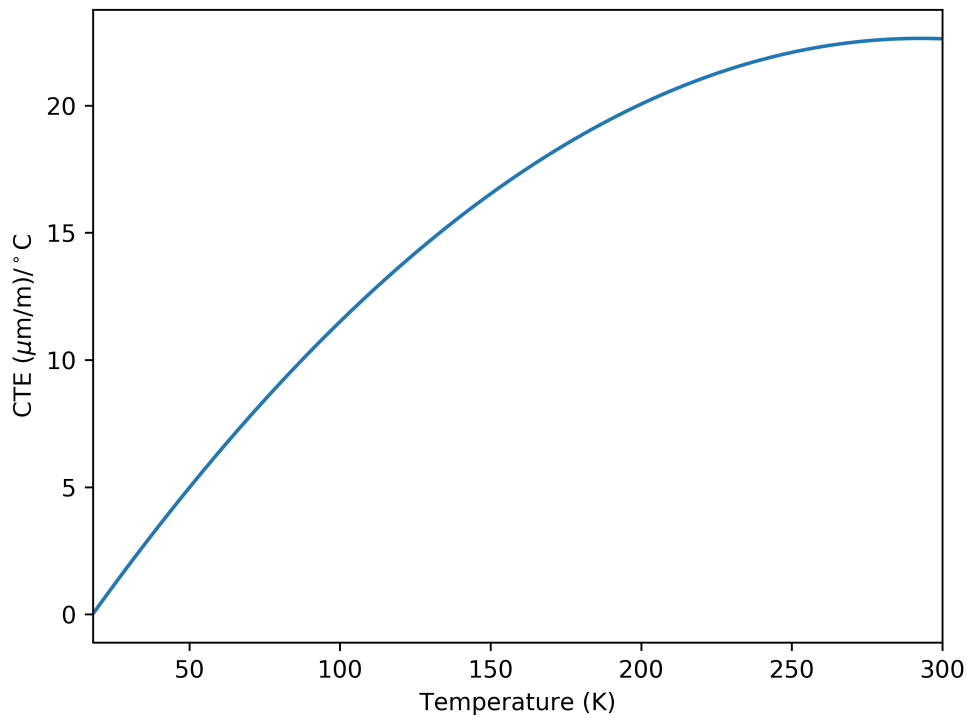
**Figure 5.8:** The CTE of aluminum 6061-T6 as a function of temperature using differential of equation (5.2) from Bradley et al. (2013).

model can be understood for the case of two curved optics with their optical axes pointing along the z axis, separated by a cylindrical rod acting as a spacer. A diagram of this arrangement is shown in figure 5.9. As the temperature is reduced the mounting spacer compresses along the z axis (bringing the optics closer together) but also shrinks radially. In addition, the radius of curvature of the optics will also change with temperature. This will mean that the spacer will contact the two lenses at different heights above the optical axis and so the spacer will contact the lenses at a different sag value, changing the spacing of the lenses in addition to the compression of the mount along the optical axis. This model is not appropriate for the FOURIER system, however, as the Zemax documentation warns, the accuracy is not guaranteed for systems with tilts and decenters (i.e. where the optics are not placed along the same axis like a traditional camera lens) or where the clear apertures are not regionally symmetric, as the sag is only calculated along the positive y axis. Both of these are true for the FOURIER model so the accuracy of the simulated linear motions of the optics must be verified, which is done by
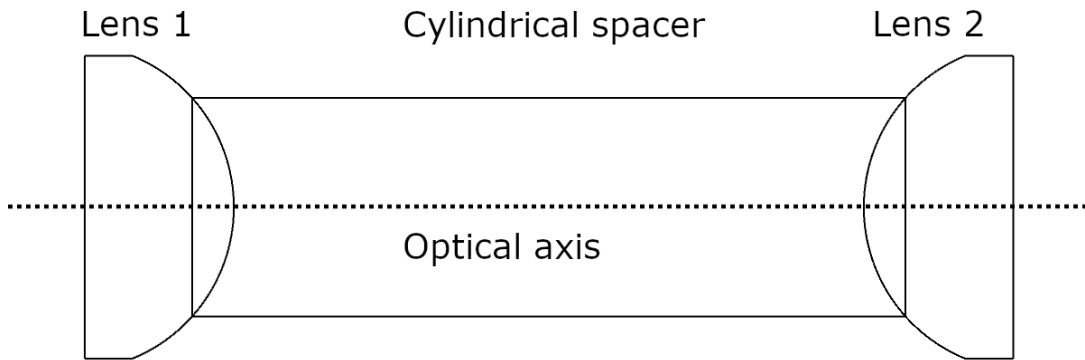
**Figure 5.9:** A diagram of two lenses with a common optical axis in contact with, and separated by, a cylindrical spacer. This arrangement highlights the motivation for the thermal expansion model implemented by Zemax as described in the text.

calculating the motion of the optics manually.

To calculate the motion of the optics I first need to know their positions. Using the global coordinate positioning data of each optic from the Zemax prescription report I can extract the location of the optics with respect to a defined global reference point. For the work presented here the reference point was chosen to be the focal plane of M1 (where the spatial filter is located) as this location is set by the warm optic M1, its position does not change during cooldown so this is the reference point about which the optics contract towards as the cold plate they are attached to contracts. With these locations referenced to the spatial filter I used equation (5.2) to calculate the motion of each optic on cooldown which depended on its distance from the spatial filter. The result of this motion is plotted in figure 5.10 as the "Cold location analytical".

In Zemax the model was set up by using the "make thermal" tool which places thermal solves on all appropriate surfaces, particularly in this case on the spacing between optics. The motion of the optics in the Zemax model can then be extracted by comparing the global coordinate position of the optics at room temperature and 100K. The cold location of the optics are displayed in figure 5.10 as "Cold location Zemax".

As figure 5.10 shows, the displacement between the warm and cold positions can be significant, the SAPHIRA detector for example is displaced by 0.75 mm. The figure also shows that the Zemax and analytical model are in good agreement, again considering the SAPHIRA detector the distance between the two estimated cold locations is 0.021 mm, giving an estimate
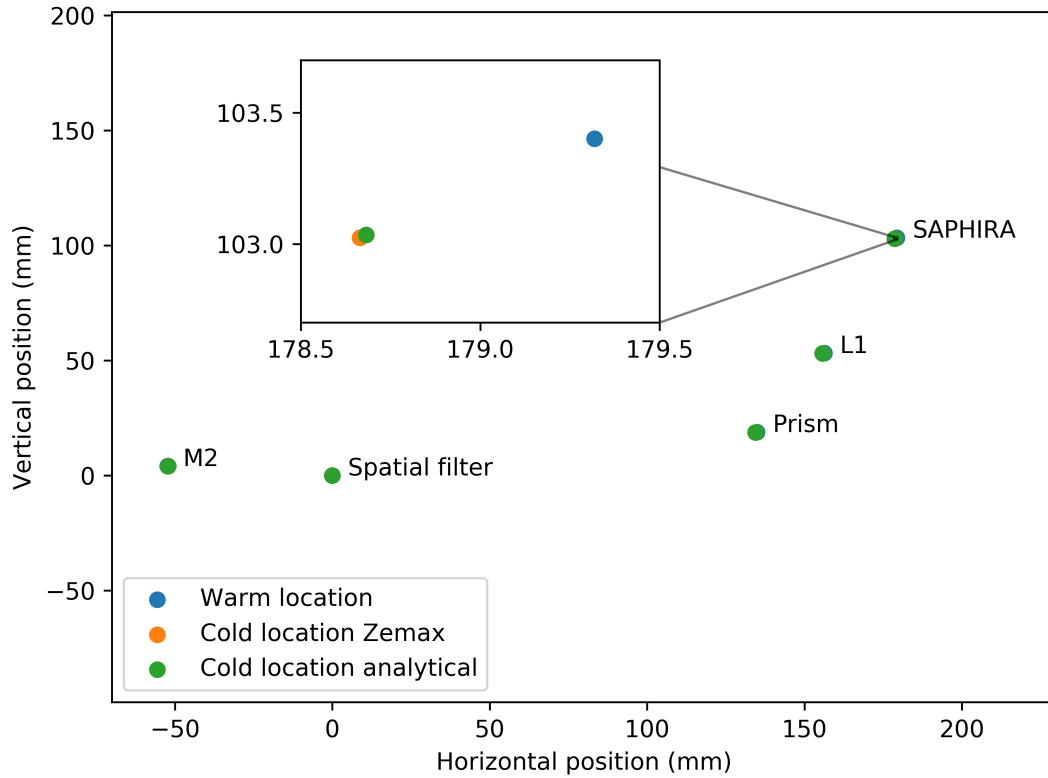
**Figure 5.10:** The position of the optics at the warm nominal focus and the location after cooldown, according to both the Zemax model and my independent analytical estimation. The insert shows the location of the SAPHIRA detector where the motion from the warm location to the cold location is in good agreement between the Zemax and analytical model.

for uncertainty to be 3% the distance the optics move in the worst case. Having confirmed the validity of the Zemax model for the contraction of the cold plate I now consider the second half of the thermal modelling: the effects on the optics themselves.

### 5.3.3   Thermal effects on the optics

For the optics there are two unique parameters of interest. The first is the CTE of the glasses, which is used by Zemax to calculate the change in thickness, as well as change in radius of curvature of powered optics. As before, Zemax only accepts a linear CTE in its optics catalogue and the values provided by the manufacturers are often only valid at around room temperature. For example Schott Glass Technologies provide the linear CTE of N-SF11 glass to be $8.5 \times 10^{-6}$ over a temperature range of -30-+70°C. However, as FOURIER utilises small, 1" sized optics, the absolute change in thickness of the optics is small and so any deviation from the linear

CTE value and a more complete model will be smaller still, so the linear CTEs are used for the thermal modelling here. The second parameter of interest is the variation in refractive index with temperature. As the system is assumed to be in a vacuum once cold, calculating the refractive index of the surrounding "air" is trivial and is simply assumed to be a perfect vacuum. Modelling the glass change in refractive index is more complex. Zemax uses the following equation developed by Schott:

$$\Delta n = \frac{n^2 - 1}{2n} \left( D_0 \Delta T + D_1 \Delta T^2 + D_2 \Delta T^3 + \frac{E_0 \Delta T + E_1 \Delta T^2}{\lambda^2 - \lambda_{tk}^2} \right). \tag{5.3}$$

$D_0$, $D_1$, $D_2$, $E_0$, $E_1$, and $\lambda_{tk}^2$ are constants available in glass data sheets. Zemax only provides the the $D_0$ parameter (which provides a linear estimate for the change in refractive index with temperature) for the fused silica glass of which M2 is made. However, this is sufficient as M2 is a reflective optic I am not concerned with the variation of refractive index. A full set of parameters are provided in Zemax for the N-SF11 glass. The CaF$_2$ glass of L1 only has a $D_0$ value provided, however, Daimon & Masumura (2002) provide values of $D_0$, $E_0$ and $\lambda_{tk}^2$, which are used to model a new glass and provide a more accurate value of the change in refractive index than the linear model alone. This change is not found to be significant, with the refractive index of the linear model provided by Zemax at 100K being $n$ = 1.4274223577 and with the non-linear model of Daimon & Masumura (2002) being $n$ = 1.4275376064. A summary of the parameters used for modelling the thermal properties of the glass is given in table 5.3.

**Table 5.3:** The parameters used in equation (5.3) for each glass modelled in FOURIER.

| Optics/glass | TCE | $D_0$ | $D_1$ | $D_2$ | $E_0$ | $E_1$ | $\lambda_{tk}$ |
|---|---|---|---|---|---|---|---|
| M2/fused silica | 0.51 | $2.24 \times 10^{-5}$ | 0 | 0 | 0 | 0 | 0 |
| Prism/N-SF11 | 8.52 | $-3.65 \times 10^{-6}$ | $9.2 \times 10^{-9}$ | $-2.1 \times 10^{-11}$ | $9.65 \times 10^{-7}$ | $1.44 \times 10^{-9}$ | $2.94 \times 10^{-1}$ |
| L1/CaF$_2$ | 18.9 | $-2.84 \times 10^{-5}$ | 0 | 0 | $4.69 \times 10^{-7}$ | 0 | $1.16 \times 10^{-1}$ |

### 5.3.4 Model results

With the thermal properties of both the cold plate and glasses defined I now analyse the effects of thermal cooldown on the system. To quantify the system performance I use the geometric

spot diagram. Figure 5.11 shows the effect of taking a system under perfect alignment at room temperature to cryogenic temperatures, applying the thermal effects of both the cold plates and glasses. The effects of thermal misalignment are clearly seen, however even without any compensation the system is still diffraction limited. The size of the PSF at the SAPHIRA detector at $\lambda = 1.75\,\mu m$ is $2.235\,\mu m \times 76\,\mu m$ (scaling it linearly with wavelength from the PSF size at $\lambda = 1.1\,\mu m$) and the geometric spot diameter of the cooled system is shown to be $73\,\mu m \times 13.5\,\mu m$, with the RMS spot size being $28.8\,\mu m \times 2.56\,\mu m$.

As both the system tolerances discussed in section 5.2 and the thermal misalignments will occur simultaneously however, these results must be considered together. To do this I combine the RMS spot size due to thermal misalignment and the RMS spot size due to system tolerances via the root sum square method as the two errors can be assumed to be independent. Along the spectral axis the requirement is that the RMS spot size be 20% or less the diffraction limited $76\,\mu m$ PSF diameter. The RMS spot size is taken to be $5\,\mu m$ due to tolerance/manufacturing errors from figure 5.6, combined with the $2.56\,\mu m$ value for the thermally misaligned system I derive a estimated RMS spot size along the spectral axis to be $5.62\,\mu m$, significantly diffraction limited without any compensation. For the interference fringe axis the criterion is to maintain a RMS spot size of $30\,\mu m$ or less, to keep visibility losses below 4%. This is not met when considering a $15\,\mu m$ RMS spot size from tolerance/manufacturing errors (figure 5.5) and $28.8\,\mu m$ given above resulting in a RSS estimated spot size of $32.5\,\mu m$ when both system tolerances and thermal modelling are considered. Referring back to figure 5.4 such a spot size would still produce a visibility loss of only around 4%, however this can be improved.

While not a significant loss in performance, the spot size along the interference fringe axis can be improved by adjusting the location of M2 after warm alignment, purposefully misaligning it, such that the location M2 moves to after cooldown provides better performance than if the system were cooled directly from the warm alignment configuration. Using the visual optimiser tool in Zemax, the spot size is minimised by applying a $190\,\mu m$ displacement of M2 along its optical axis, moving it further away from the SAPHIRA detector, this results in a geometric spot diameter of $26.6\,\mu m$ and a RMS spot diameter of $12\,\mu m$. The resulting cooled system spot diagram is shown in figure 5.12. This is a significant improvement on the $73\,\mu m$ geometric spot diameter and $28.8\,\mu m$ RMS spot diameter for the uncompensated, cooled system. The compensated alignment reduces the RSS predicted RMS spot size to $19\,\mu m$, once again well

**(a)** Spot diagram warm aligned system



**(b)** Spot diagram of the system when cooled to 100K with no compensators. The spots of the three individual beams are separated but the system is still diffraction limited.
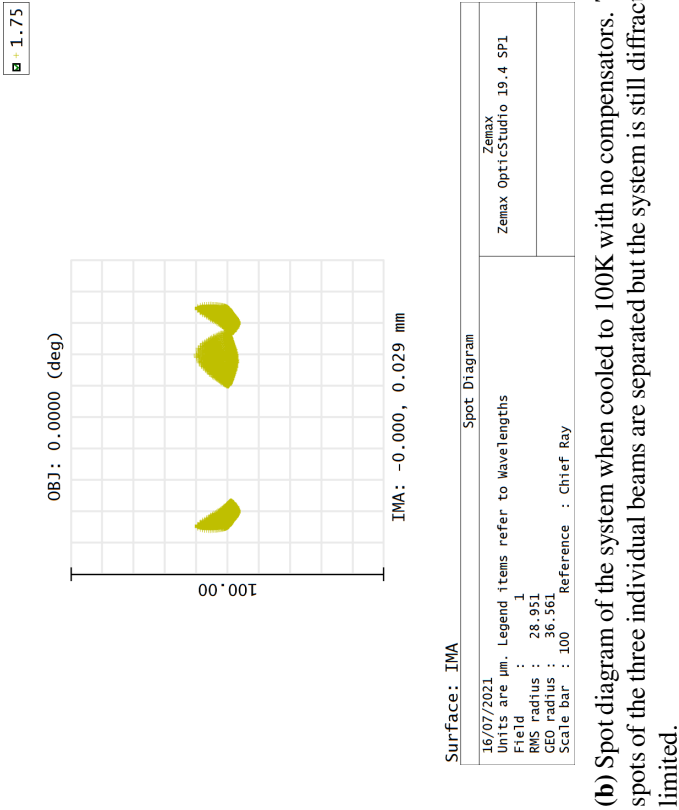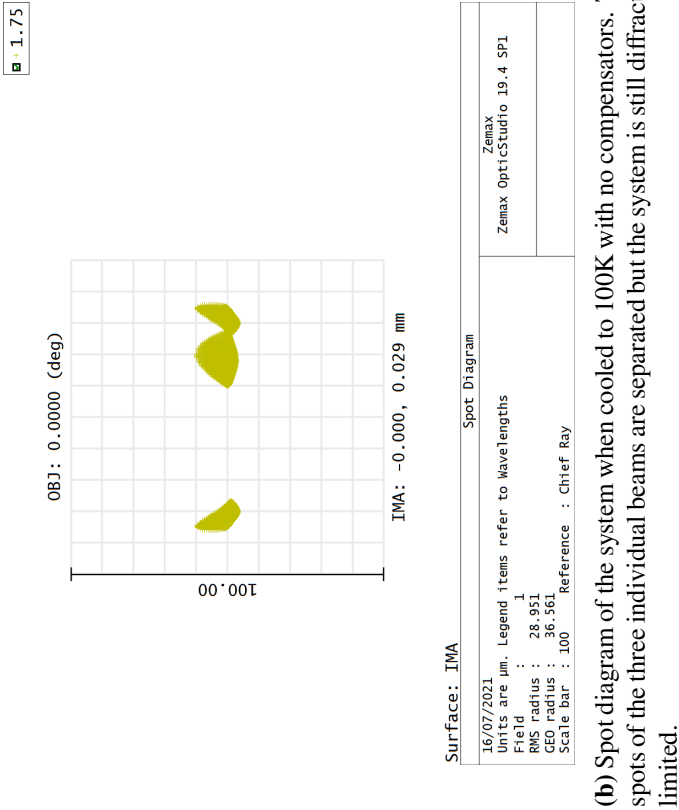
**Figure 5.11:** The geometric spot diagram at the SAPHIRA detector for a aligned warm system and the spot if the system is cooled to 100K without any compensation.
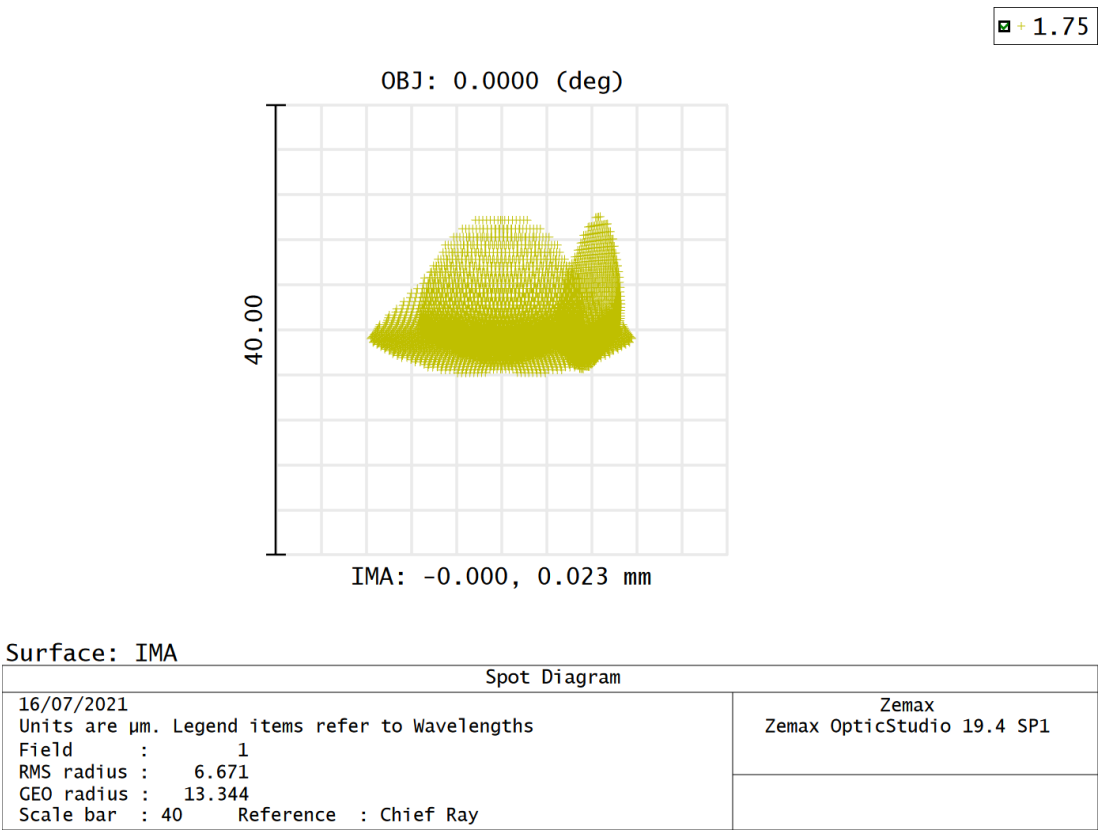
**Figure 5.12:** The geometric spot of the system after cooldown but with the position of M2 compensated to minimise spot diameter.

below the 30 μm criterion required to keep visibility loss at the level of 4% on the worst baseline. The spot size along the spectral axis is not affected by this compensation and is still worse than the nominal warm alignment however this is well within acceptable limits and so no further compensations are implemented. This increase in spot size along the spectral axis could be compensated by moving the SAPHIRA detector 232 μm closer to L1 (along L1's optical axis) which would recover a RMS spot size along the spectral axis of 1.4 μm, however adding such a compensation would unnecessarily increase the complexity of the detector mounting and so is not implemented.

## 5.4  Spectral Resolution

I estimated the spectral resolution of FOURIER using the Zemax model. Figure 5.13 shows the landing positions of the edges and centres of the J, H and K bands on the active area of the SAPHIRA detector, showing that all three bands can be sampled on the detector in the same
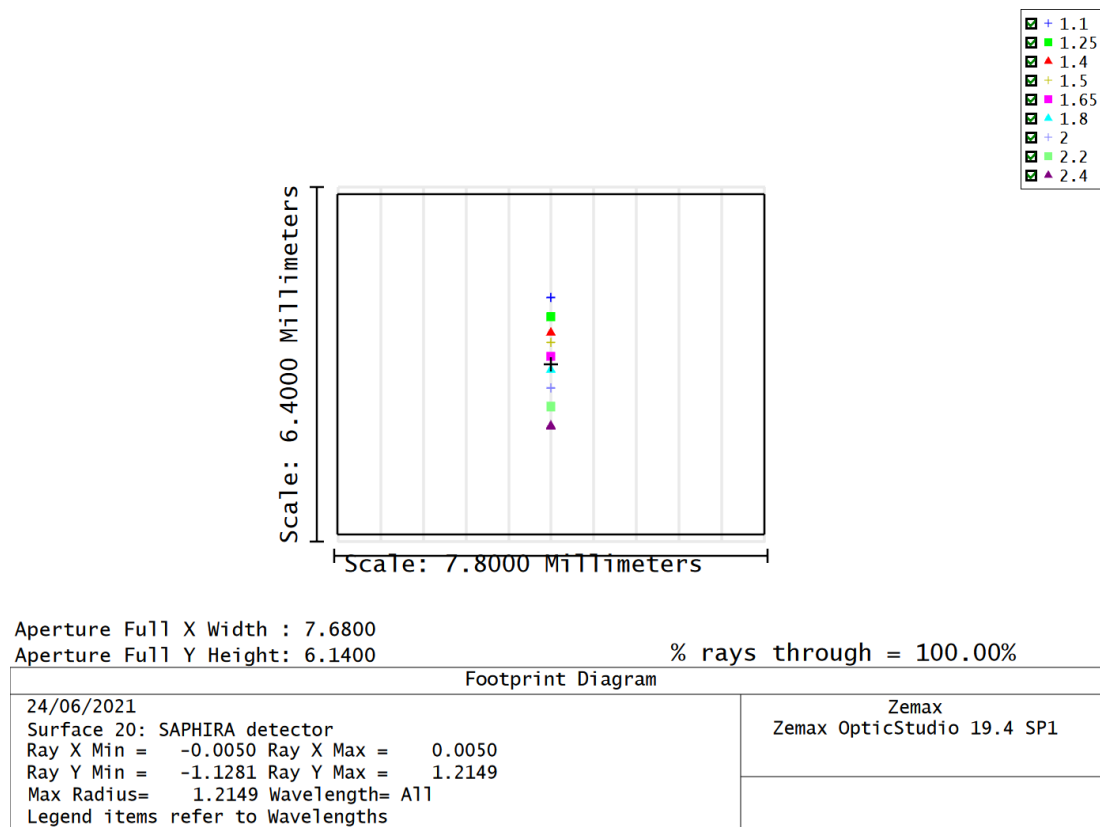
**Figure 5.13:** The landing positions of the edges and centres of the J, H and K bands bounded by the active area of the SAPHIRA detector at the focal plane of FOURIER. This shows that the J, H and K bands can fit on the detector simultaneously at the spectral resolution used.

configuration.

The ray landing locations can also be used to estimate the spectral resolution of FOURIER. Spectral resolution is defined to be

$$R = \frac{\lambda}{\Delta\lambda}, \tag{5.4}$$

where $\Delta\lambda$ is the smallest difference in wavelength that can be distinguished at a wavelength of $\lambda$. Here I take the smallest difference in wavelength to be given by the Rayleigh criterion, which is met when the null of the Airy disk of one wavelength overlaps with the maximum of the Airy disk of another. To quantify the spectral resolution by this criterion I first modelled the width of the Airy disk, including system aberrations, using the POP routine in Zemax. I then used the centroids of the geometric spot diagrams to find the wavelength which satisfies the Rayleigh criterion, the wavelength whose centroid is one Airy radius away from the centroid of

**Figure 5.14:** The geometric spot at $\lambda = 1.65\,\mu$m and its geometric Airy disk, traced by the solid black lines, along with the wavelength which just satisfies the Rayleigh criterion.

the wavelength of interest.

I performed centroiding of the geometric spot landing positions by eye, this is sufficient as the geometric spot radius is typically around $10\,\mu$m so centroiding to an accuracy of around $1\,\mu$m was easily achieved. Figure 5.14 shows an example of this calculation, here the spot diagrams of the centre of the H band, $\lambda = 1.65\,\mu$m, and the wavelength that is just resolved by the Rayleigh criterion, $\lambda = 1.628\,\mu$m, are shown along with the geometric Airy disk size at $\lambda = 1.65\,\mu$m. The centroids are shown to just satisfy the Rayleigh criterion. Note that the radius of the geometric Airy disk shown in figure 5.14 is $1.16\,\mu$m smaller than that predicted by the POP routine. The larger radius is used for calculating the spectral resolution.

This process is repeated for the centres of the J and K bands giving a spectral resolution of 89, 75 and 81 in the J, H and K bands respectively. This is a moderately high spectral resolution for a simple equilateral prism.

## 5.5 Throughput

The aim of the remainder of this chapter is to estimate the limiting magnitude of FOURIER at the MROI. As reaching faint limiting magnitudes is a top priority of FOURIER I discuss how I derive this value in detail.

To do this I must quantify both the throughput and visibility loss (how much the fringe contrast is reduced due to instrumental effects) for both the MROI beam train and the FOURIER beam combiner.

In this section I present the throughput of the MROI and FOURIER, in section 5.6 the visibility losses and in section 5.7 I bring these together to calculate the limiting magnitude itself.

### 5.5.1 MROI throughput

A core design feature of the MROI beam train is to minimise the number of optics to maximise throughput. Here I estimate the throughput of the MROI beam train, calculating losses from the top of the atmosphere to the entrance of the beam combiner.

The first term to consider is atmospheric absorption and scattering. Using the atmospheric transmission curves generated for Mauna Kea with Lord (1992) at a 1.6 mm column of water vapour and an air mass 1.5, the transmission is taken to be 1, 0.99956 and 0.8713 in the J, H and K bands, respectively.

The largest loss of throughput is due to the optical components themselves, table 5.4 lists the throughput of all optical components along the MROI beam train. The throughput is reduced from its theoretical value by 1% for optics exposed to air to account for ageing. This is with the exception of the Unit Telescope (UT) primary mirror which is expected to age worse due to it being exposed to the open air and pointing upwards. For the primary the throughput has been reduced from its theoretical value of 97% to 93%. The central obstruction of the UT blocks 5% of the aperture of the primary however this has been doubled to 10% to account for diffraction effects of this obscuration along the long optical path of the interferometer. The throughput for all components is assumed to be the same across the J, H and K bands. This gives a throughput of 45.8% for the MROI beam train considering optical losses alone.

The next loss in throughput to consider is due to diffraction effects. This can cause a loss in throughput if light from the beam diffracts out beyond the clear aperture of the optics further

**Table 5.4:** The estimated throughput of the optical components along the MROI beam train from the UT primary to the entrance of the FOURIER beam combiner. A total throughput of 45.8% is achieved, which is taken to be the same across the J, H and K bands.

| Subsystem | Assembly | Component | Type | Coating | Throughput |
|---|---|---|---|---|---|
| **UT** | Telescope | M1 | Mirror | Aluminium | 93% |
| | | M2 | Mirror | Silver | 97% |
| | | M3 | Mirror | Silver | 97% |
| | | Central obstruction | | | 90% |
| | ADC | Prism 1 | Surface | AR | 98% |
| | | | Substrate | Infrasil 20 mm | 99% |
| | | Glue | Surface | Internal contact | 99.5% |
| | | Prism 2 | Substrate | Infrasil 20 mm | 99% |
| | | Oil | Surface | Internal contact | 99.5% |
| | | Prism 3 | Substrate | Infrasil 20 mm | 99% |
| | | Glue | Surface | Internal contact | 99.5% |
| | | Prism 4 | Substrate | Infrasil 20 mm | 99% |
| | | | Surface | AR | 98% |
| | FTT pickoff | Dichroic | Surface | Dichroic | 98% |
| | | | Substrate | Infrasil 20 mm | 99% |
| | | | Surface | AR | 98% |
| **Beam relay** | Vacuum Window | Window | Surface | AR | 98% |
| | | | Substrate | Infrasil 20 mm | 99% |
| | | | Surface | AR | 98% |
| | Relay mirrors | M4 | Mirror | Silver | 97% |
| | | M5 | Mirror | Silver | 97% |
| **Delay line** | Catseye | M6 | Mirror | Silver | 97% |
| | | M7 | Mirror | Silver | 97% |
| | | M6 | Mirror | Silver | 97% |
| | Exit window | Window | Surface | AR | 98% |
| | | | Substrate | Infrasil 20 mm | 99% |
| | | | Surface | AR | 98% |
| **Beam relay 2** | Beam compressor | M8 | Mirror | Silver | 97% |
| | | M9 | Mirror | Silver | 97% |
| | Beam turning | M10 | Mirror | Silver | 97% |
| **Switchyard** | | Dichroic | Surface | Dichroic | 98% |
| | | M11 | Mirror | Silver | 97% |
| | | | | **Total:** | **45.8%** |

along the beam train. The first effect to consider is that the MROI propagates a finite sized beam, 95 mm in diameter, for most of the beam train. Beyond a distance $D_r$, given by

$$D_r = \frac{\pi d^2}{4\lambda}, \tag{5.5}$$

where $D_r$ is the Rayleigh distance, $d$ the diameter of the beam being propagated and $\lambda$ the wavelength of the light, the beam will diverge due to diffraction, tending towards diffracting by the Fraunhofer diffraction angle of $1.22\lambda/d$ (Buscher 2015). $D_r$ for the 95 mm beam is 4.3 km in the H band. This implies that diffraction due to the finite beam width will not be significant over the few hundred meters of propagation, indeed this is the reason for using a large beam diameter along the beam relay system.

Unfortunately, the system is subject to additional diffraction losses due to atmospheric seeing inducing phase perturbations which occur on scales smaller than the beam diameter if the telescope aperture is larger than the Fried parameter, which is the case for the MROI with the telescope aperture being 2.4× the expected Fried parameter in the H band (the telescopes are 3.3× and 1.7× the Fried parameter in the J and K bands). In this case the effective Rayleigh distance for the atmospheric perturbations is less than the beam itself and so diffraction effects matter. This will cause the beam to become speckled in appearance and expand, with light falling outside the clear aperture of optics further along the beam train. Worse still, as the atmospheric perturbations change randomly with time, the amount of flux landing within the clear aperture, and in turn, the amount reaching the beam combiner, will also vary with time.

As these fluctuations vary as a function of time a statistical approach must be taken to find the average throughput over time. Applying the results of Horton et al. (2001) the mean throughput of the MROI beam train due to diffraction effects can be estimated from their figure 4, by assuming a value of $\alpha$ (the ratio of telescope diameter to Fried parameter) of 3 in the J and H bands and 1.5 in the K band, a value of $\beta$ (the ratio of initial beam width to clear aperture of optic further down the beam train) of 1.4, and a $\delta$ (a measure of how significantly the beam is affected by diffraction) of 0.16, 0.22 and 0.29 for the J, H and K bands respectively. These $\delta$ values are calculated as worst case scenarios based on the propagation path length along the MROI beam train. A detailed calculation of $\delta$ is given in section 8.8.1. This results in a diffraction throughput of 87%, 82% and 85% in the J, H and K bands respectively.

Combining all the effects mentioned above gives a final expected throughput from the top

of the atmosphere to the entrance of the FOURIER beam combiner of 38%, 37% and 34% in the J, H and K bands respectively.

### 5.5.2   FOURIER Throughput

The main throughput loss considered for FOURIER is from the optics themselves. The majority of the optical elements in FOURIER where throughput losses can occur are easy to calculate as the optics are simple bulk optics. I calculated the losses at each surface using the reflection vs wavelength tool in Zemax, and internal transmission losses via the internal transmission tool. With these tools I was able to extract a theoretical throughput curve across the FOURIER passband which accounted for anti-reflection coatings, Angles of Incidence (AoI) and the thickness of substrates for transmissive optics. The throughput at the surface of the N-SF11 prism is taken from preliminary theoretical throughput curves provided by Thin Films Inc for a custom multi-layer anti-reflection coating designed for FOURIER. The Quantum Efficiency (QE) of the SAPHIRA detector was estimated from the QE curve in Finger et al. (2016) for a Mark14 SAPHIRA array with an APD gain of 1. I interpolated this data onto a common set of sample points in wavelength using cubic 1D interpolation from the scipy interpolate package (Virtanen et al. 2020).

Calculating the throughput of the spatial filter was more complicated. The throughput of a pinhole aperture for light subject to atmospheric seeing was estimated based on the calculation shown in figure 3.17 of Buscher (2015), which calculates the mean coupling into a single mode optical fibre for a tip-tilt corrected atmospherically perturbed beam as a function of $D/r_0$ where $D$ is the diameter of the UT and $r_0$ the Fried parameter. Taking $r_0$ at $\lambda = 500$ nm to be 14 cm at the MROI site it is possible to scale this $r_0$ as a function of wavelength using the relation

$$r_{0\lambda} = r_{0_{\lambda=500\,\text{nm}}} \left( \frac{\lambda}{\lambda_{500\,\text{nm}}} \right)^{6/5}, \qquad (5.6)$$

where $r_{0_\lambda}$ is the Fried parameter at the wavelength of interest and $r_{0_{\lambda\,=\,500\,\text{nm}}}$ the Fried parameter at $\lambda = 500$ nm. Calculating $D/r_0$ is then a case of simply dividing the 1.4 m UT diameter by the value of $r_0$ at each wavelength. The throughput at each wavelength is calculated by retrieving the value at the $D/r_0$ corresponding to each wavelength from figure 3.17 of Buscher (2015).
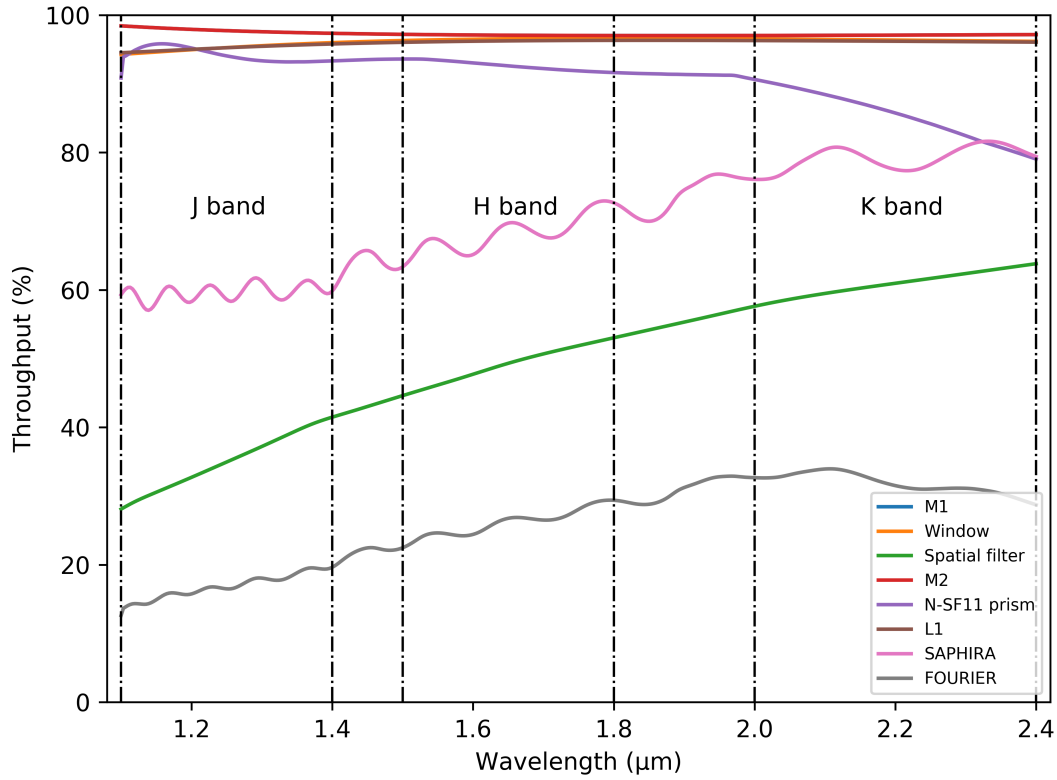
**Figure 5.15:** The total throughput of FOURIER considering anti-reflection coating, AoI, substrate thicknesses, atmospheric induced coupling losses of the spatial filter and the SAPHIRA detector's QE.

The throughput of the system considering bulk optics losses, detector QE and spatial filtering coupling losses is shown in figure 5.15. The throughput of the optics (M1, Window, M2, N-SF11 prism and L1) is excellent, with only the N-SF11 prism showing any substantial loss, particularly in the K band where there is partial internal absorption as discussed in section 4.8. The spatial filter shows a steady increase in throughput towards longer wavelengths as $D/r_0$ decreases where the atmosphere is more stable and so $r_0$ increases. This increase in throughput must be considered alongside a reduced effectiveness in spatial filtering, which is discussed in section 5.6.

Considering the throughput of the bulk optics only, i.e. not including the coupling losses of the spatial filter or the SAPHIRA detector QE, neither of which can be optimised in the work I have carried out, the throughput is then given by figure 5.16. M1 has a near identical throughput to M2 as they are both gold coated mirrors. Here the benefits of using high throughput bulk optics and reducing the number of optics wherever possible is evident, with a throughput of 80.5%, 78% and 66.5% at the centres of the J, H and K bands respectively.
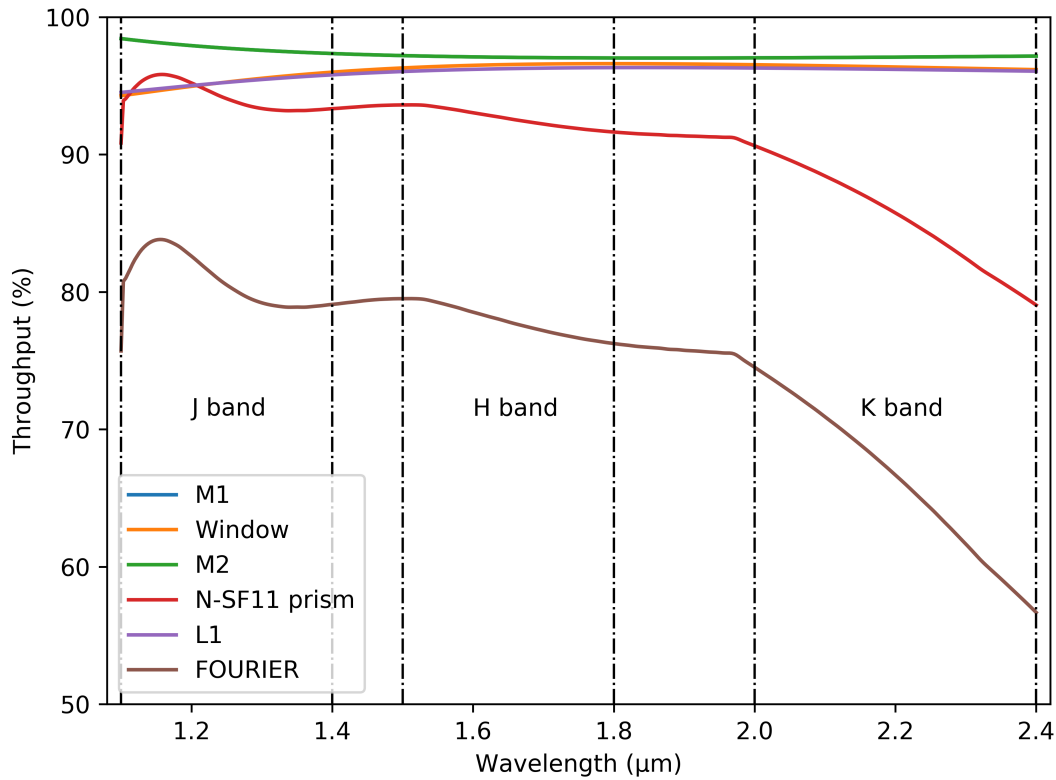
**Figure 5.16:** The throughput of the FOURIER bulk optics considering anti-reflection coating, AoI and substrate thicknesses.

## 5.6   Visibility loss

As I will discuss in section 5.7, in interferometry the amount of light arriving at the detector is not the only factor which has to be considered when calculating the limiting magnitude of a beam combiner at an interferometric array. The visibility or fringe contrast of the interference fringes is also a significant factor.

The visibility of a object varies as a function of how well resolved it is, with the highest contrast interference fringes being produced for an object which is completely unresolved, i.e. appears as a point source at the baseline the interferometer is sampling. The Signal to Noise Ratio (SNR) of an observation drops for lower fringe contrast.

In addition to the intrinsic visibility of the object on-sky, there are many instrumental effects that can reduce the fringe contrast. Minimising these will improve the limiting magnitude of the instrument. The first source has already been discussed at length in section 5.2 where I developed a manufacturing and alignment error budget and studied the effects of instrument

cooldown (section 5.3) to keep visibility losses due to these instrumentation effects below 4%
for the FOURIER instrument itself. In this section I calculate other visibility losses for both
the MROI beam train and FOURIER.

The model used to estimate visibility losses follows that of Porro et al. (1999) where the
observed visibility is assumed to be

$$V_{\text{obs}} = S_{\text{atm}} S_{\text{inst}} V_{\text{obj}}, \tag{5.7}$$

where $V_{\text{obs}}$ is the fringe contrast measured by the beam combiner, $S_{\text{atm}}$ the Strehl ratio
due to atmospheric seeing effects, $S_{\text{inst}}$ the Strehl ratio due to instrumental effects and $V_{\text{obj}}$ the
intrinsic visibility of the object being observed (always assumed to be unity, that of a point
source, for these calculations). Modelling the observed visibility is then a matter of estimating
the atmospheric and instrumental Strehl ratios, achieved by approximating them with

$$S \approx \exp\left(-\left(\frac{2\pi\delta}{\lambda}\right)^2\right), \tag{5.8}$$

where $\delta$ is the RMS wavefront error and $\lambda$ the wavelength of observation. This method
has been shown to be valid to within $\pm 10\%$ for $s \geq 0.3$ (Mahajan 1982). Note that this model
assumes wavefront errors are uncorrelated but of equal magnitude for each of the two arms of
the interferometer which combine generate the interference fringes. The task then is to estimate
the RMS wavefront error for all aberrations introduced by the atmosphere, interferometer and
beam combiner, which is done in the subsections below.

## 5.6.1 MROI visibility losses

### 5.6.1.1 Static wavefront error

This term encapsulates the visibility loss due to optical surface aberrations, mounting induced
aberrations and misalignments along the beam train.

Each optic along the beam train was assigned an optical surface WaveFront Error (WFE)
of either $\lambda/10$ or $\lambda/20$ P2V at a wavelength of $\lambda = 633$ nm with large and/or curved surfaces
being assigned the looser $\lambda/10$ tolerance on the WFE. Assuming RMS WFE is a factor of 5×
smaller than the P2V (Porro et al. (1999) found the value ratio to be around 5.5 but I am being
conservative here) this corresponds to a 26 nm or 13 nm RMS WFE for the $\lambda/10$ and $\lambda/20$

surfaces, respectively. This is with the exception of the UT optics, which have a requirement of
a RMS WFE of 42 nm for the primary and secondary combined with the tertiary being assigned
a standard $\lambda/20$ WFE.

In addition to the WFE from surface quality, WFEs induced due to the optic mounting must
also be considered and are given in column 5 of table 5.5. The values assigned are assumptions
with higher mounting WFEs for larger and/or curved optics.

The values derived for column 6 in table 5.5, the alignment tab, are more complex to
calculate and are based on the analytic equations given by Porro et al. (1999) for various system
misalignments. As an example, the defocus of the secondary mirror is assigned to be 2.2 µm
for the UT at the MROI. Equation 14 of Porro et al. (1999) then gives the resulting RMS WFE
for secondary defocus to be

$$\delta = \frac{z_s}{16\sqrt{3}f_\#^2}, \tag{5.9}$$

where $z_s$ is the axial defocus and $f_\#^2$ the f ratio of the UT, 2.25 in the case of the MROI
UTs. As a result the defocus error is assigned a RMS WFE of 15.7 nm. As before, these
misalignments are calculated individually and then combined with RSS statistics to calculate
the RMS WFE for the misalignments of the subsystem as a whole. This process is repeated for
the delay lines and "beam relay 2", the beam compressors.

The RMS static WFE of the interferometer as a whole is then simply the RSS of all
the calculated RMS WFEs giving a final value of 99 nm RMS static wavefront error for the
interferometer optics. This is another benefit to minimising the number of optical surfaces along
an interferometer's beam train, improving not only throughput but also reducing wavefront
errors and in turn increasing system visibility and limiting magnitude in the process.

Using equation (5.8) I convert this 99 nm RMS WFE into a Strehl ratio of 0.78, 0.86 and 0.92
at wavelengths of $\lambda = 1.25$ µm, $\lambda = 1.65$ µm and $\lambda = 2.2$ µm (J, H and K bands), respectively.
This implies that if static WFEs along the beam train alone were to degrade the visibility I
would expect the visibility to drop by 22% in the J band, even with these stringent surface
and alignment requirements, showing how demanding building an interferometer designed for
observations at faint limiting magnitudes is.

**Table 5.5:** The estimated RMS static WFE for all the optics along the MROI beam train. The polishing column accounts for WFE, originating from surface errors of the optics, support WFE induced by the optics mounting and alignment WFE induced by misalignments of the optics.

| Subsystem | Assembly | Component | Static WFE nm | Mounting WFE nm | Alignment WFE nm | RMS WFE nm |
|---|---|---|---|---|---|---|
| **UT** | Telescope | M1 | 42 | 20 | 0 | 46.5 |
| | | M2 | 0 | 5 | 0 | 5 |
| | | M3 | 13 | 5 | 0 | 13.9 |
| | | UT alignment | 0 | 0 | 40.1 | 40.1 |
| | ADC | Prism 1 | 13 | 10 | 0 | 16.4 |
| | | Prism 2 | 13 | 10 | 0 | 16.4 |
| | | Prism 3 | 13 | 10 | 0 | 16.4 |
| | | Prism 4 | 13 | 10 | 0 | 16.4 |
| | FTT pickoff | Dichroic | 13 | 10 | 0 | 16.4 |
| **Beam relay** | Vacuum Window | Window | 13 | 10 | 0 | 16.4 |
| | Relay mirrors | M4 | 13 | 5 | 0 | 13.9 |
| | | M5 | 13 | 5 | 0 | 13.9 |
| **Delay line** | Catseye | M6 | 26 | 10 | 0 | 27.9 |
| | | M7 | 13 | 0 | 0 | 13 |
| | | M6 | 26 | 10 | 0 | 27.9 |
| | | DL alignment | 0 | 0 | 11 | 11 |
| | Exit window | Window | 13 | 10 | 0 | 16.4 |
| **Beam relay 2** | Beam compressor | M8 | 26 | 10 | 0 | 27.9 |
| | | M9 | 13 | 0 | 0 | 13 |
| | | BC alignment | 0 | 0 | 10.1 | 10.1 |
| | Beam turning | M10 | 13 | 0 | 0 | 13 |
| **Switchyard** | | Dichroic | 13 | 0 | 0 | 13 |
| | | M11 | 13 | 0 | 0 | 13 |
| | | | | | **Total:** | **98.2** |

### 5.6.1.2   Atmospheric high order WFE

The UTs at the MROI are equipped with a Fast Tip-Tilt (FTT) system, however, higher order atmospheric WFE are not removed at the MROI. These remaining perturbations reduce the Strehl ratio by

$$s = \exp(\sigma^2), \tag{5.10}$$

where $\sigma$ is the RMS WFE in radians of each beam. The value of $\sigma$ is assumed to be equal in magnitude but uncorrelated between the two beams. For a tip-tilt corrected wavefront the WFE goes as $0.134(D/r_0)^{5/3}$ (Porro et al. 1999), where $D$ is the telescope diameter and $r_0$ the Fried parameter. This leads to a maximum theoretical visibility of 0.37, 0.56 and 0.72 in the J, H and K bands respectively, a significant source of visibility loss.

### 5.6.1.3 Fresnel filtering gain

Contrary to most effects discussed in this section, there is one which improves the system visibility. Known as Fresnel spatial filtering it is the effect whereby as the beam is propagated along the arms of the interferometer, high order atmospheric perturbations in the wavefront, caused by atmospheric seeing on scales smaller than the diameter of the UT primary mirror will diffract out of the pupil faster than the pupil itself diffracts. When the beam is subsequently cropped by finite sized optics along the beam train the higher spatial frequency perturbations are disproportionately removed, leaving the starlight partially spatially filtered. This is the same effect which leads to a loss in throughput as discussed in section 5.5.1. This effect is shown in figure 2 of Horton et al. (2001). Using the same diffraction parameters as discussed in section 5.5.1 with additionally $\gamma = 1$ (meaning the path of the two beams in the interferometer are equal in length, the condition for objects observed at the zenith) figure 5 of Horton et al. (2001) provides estimates for the gain in visibility from Fresnel spatial filtering by comparing the RMS visibility with no propagation ($\delta = 0$) to the visibility at the $\delta$ values stated in section 5.5.1. This results in a visibility gain of 1.08, 1.14, 1.06 times in the J, H and K bands respectively. Note that this gain is an underestimate in the J band and an overestimate in the H band as while both bands are assumed to be at a $D/r_0 = 3$ to match up with the data available from Horton et al. (2001), in reality $D/r_0$ is 3.3 and 2.4 in the J and H bands respectively (as Fresnel spatial filtering provides a higher gain at worse seeing). For this reason I take the Fresnel filtering visibility gain factor to be 1.14 in both the J and H bands as a rough estimate.

### 5.6.1.4 Beam tilt

If the two beams being combined are not perfectly overlapped there will be a loss in fringe contrast. Again using the work of Porro et al. (1999) this loss can be quantified by

$$S_{\text{tilt}} \approx 1 - \frac{1}{8} \left( \frac{\pi D \theta}{\lambda} \right)^2 , \tag{5.11}$$

where $D$ is the beam diameter, $\theta$ the misalignment angle between the wavefronts projected on-sky and $\lambda$ the wavelength of observation. The beam along the MROI beam train is effectively compressed twice, once by the telescope itself from 1.4 m collected by the primary to the 95 mm collimated beam which exits the telescope, and again from 95 mm to 13 mm within the beam combining array. Tilt errors in a demagnified beam are also demagnified on-sky by the ratio

of the beam compression. For example, a tilt error of 807 mas ($2.2 \times 10^{-4}°$) in the beam combining area must be divided by the ratio of the original beam to the compressed beam diameter, 1.4 m/13 mm = 108, so the 807 mas tilt error corresponds to a 7.5 mas tilt error on-sky.

Fortunately, the MROI will employ the Automated Alignment System (AAS) (Luis et al. 2020) designed to aid with alignment of the beam train at the start of the night and carry out intra-night alignment corrections. As a result of this, tilt error budgets can be rather tight for the array while still allowing for "jitter" terms, essentially vibrations that cannot be corrected for by the AAS, as well as drifts between AAS alignment corrections. Table 5.6 shows the tilt errors assigned for the MROI beam train. Note that as the switchyard optics are after the AAS system in the beam train drifts cannot be corrected during the night and so the switchyards have their own error budget. Transmissive optics are not expected to contribute to instrumentation beam tilt.

**Table 5.6:** The tilt errors budgeted for along the MROI beam train covering jitter terms arising from vibrations, as well as alignment errors from the AAS. Note that as the switchyard optics are after the AAS system in the beam train drifts cannot be corrected during the night and the switchyards have their own error budget.

| Item | Wavefront tilt (mas) | Beam diameter (m) | RMS tilt (mas on-sky) |
|------|------|------|------|
| Telescope jitter | 36 | 1.4 | 36 |
| M4 jitter | 221 | 0.095 | 15 |
| M5 jitter | 221 | 0.095 | 15 |
| DL tilt jitter | 147.4 | 0.095 | 10 |
| BC jitter | 147.4 | 0.095 | 10 |
| M10 jitter | 807.7 | 0.013 | 7.5 |
| Start-of-night alignment error | 1615.4 | 0.013 | 15 |
| Intra-night alignment drift | 1615.4 | 0.013 | 15 |
| Switchyard dichroic drift | 1615.4 | 0.013 | 15 |
| Switchyard mirror drift | 1615.4 | 0.013 | 15 |
| | | **Total:** | **53.8** |

Combining the RMS tilt terms for the beam train with RSS statistics, the resulting expected tilt error for each beam line is given as 53.9 mas. As the $\theta$ term in equation (5.11) corresponds to the tilt error between the two beam being combined, this tilt error per beam is doubled, under

the assumption that the two tilt errors are uncorrelated.

Applying these tilts to equation (5.11) I derive a maximum theoretical visibility of 0.79, 0.88, 0.93 for the centres of the J, H and K bands respectively, if visibility was only reduced because of tilt errors.

In addition to instrumentation tilt, the turbulent atmosphere will also introduce tilt errors in the beams. All the UTs are equipped with a FTT designed to remove the majority of atmospheric tilt, however, some residual tilt will remain. Here I assume the angle of the uncorrected tilt is such that it causes a 10% reduction in visibility in the H band. Rearranging equation (5.11) gives a value of differential tilt, $\theta$, at which this 10% loss occurs, by

$$\theta = \frac{0.284}{\sqrt{2}} \frac{\lambda}{D},$$

(5.12)

where $\lambda$ is the wavelength of observation ($\lambda = 1.65$ μm for the H band) and $D$ the diameter of the telescope primary. This angle is then 0.048". With this tilt the visibility loss for uncorrected atmospheric tilt in the J and K bands is calculated from equation (5.11) to be 0.829 and 0.94 in the J and K bands respectively.

### 5.6.1.5   Pupil shear

Pupil shear is another factor which can degrade the system visibility. A 1% differential pupil shear is assigned to each beam as a start-of-night alignment error, intra-night alignment drift and switchyard drifts for the two beams being combined. The RSS differential pupil shear is then 1.7%. Assuming visibility drops linearly with pupil shear, i.e. it is a maximum for perfectly aligned beams and zero at the point the beams no longer overlap, this corresponds to a maximum visibility of 0.983.

### 5.6.1.6   Instrumental piston jitter

In addition to vibrations causing tilt errors, vibrations also cause piston errors. The reduction in fringe contrast due to fast piston vibrations, jitter, is calculated using equation (5.8) with the $\delta$ term being the overall RMS piston vibration expected in each arm of the interferometer. The error budget for the various subsystems which may contribute to instrumental piston vibration are given in table 5.7. This term degrades the maximum visibility of the system to 0.77, 0.86 and 0.97 for the J, H and K bands, respectively.

**Table 5.7:** The estimated RMS piston vibrations for the various subsystems in each arm of the interferometer. The RSS combined piston vibration is used with equation (5.8) to calculate the reduction in fringe contrast due to this term.

| Item | RMS piston vibrations (nm) |
|---|---|
| UT vibrations | 57 |
| UT tilt-piston coupling | 57 |
| M4 | 20 |
| M5 | 20 |
| DL | 41 |
| M10 | 20 |
| Switchyard dichroic | 20 |
| Switchyard mirror | 20 |
| FOURIER | 20 |
| **Total:** | **275** |

#### 5.6.1.7   Atmospheric piston jitter

A finite exposure time of $2t_0$ (where $t_0$ is the atmospheric coherence time) is assumed for this limiting magnitude model. During this exposure time the atmosphere will introduce path length errors between the two beams, changing the phase and so causing the interference fringes to move on the detector, causing fringe smearing. The amount by which this fringe smearing will reduce the system visibility has been calculated by Buscher (1988). For an exposure time of $2t_0$, Buscher (1988) found the maximum visibility would be 79% (or a 21% loss).

Note this value is the same for all wavelengths as $t_0$ (and hence the exposure time) scales with wavelength by $t_{0_\lambda} \propto (\lambda)^{6/5}$. Therefore while the atmosphere is more turbulent at shorter wavelengths this is compensated for by shorter exposure times, giving the same loss in visibility at all wavelengths.

In practice, FOURIER is designed such that it can detect light from the J, H and K bands simultaneously on the same detector. Only one exposure time can be used however, so if multiband observations are used the ideal exposure time of $2t_0$ cannot be applied to all wavelengths, giving a different visibility loss. For this limiting magnitude model however, I assume that the observations have been optimised for a single band, i.e. for the limiting magnitude in the H band that the detector has been set to an exposure time of $2t_0$ for the value of $t_0$ in the H band.

This model is reasonable as FOURIER will not observe all three bands simultaneously (though the instrument is configured such that all three bands can be measured on the detector in the same configuration) as either the H or K bands will be sent to the Infrared Coherencing Nearest Neighbor tracker (ICONN) for fringe tracking.

This value does not take into account any effects of the MROI fringe tracker as it will not provide path length corrections of the timescale of $2t_0$.

### 5.6.1.8   High order dispersion effects

Differential optical dispersion between the two beams can also contribute to visibility loss. A differential path can be introduced by different glass thickness or by propagation of the beam through different amounts or quality of air. While the delay lines are set to equalise the path length between beam lines, this is done at a specific wavelength and so this correction will not be exact for other wavelengths, reducing visibility. This effect is not expected to be large and so is assigned a 1% visibility loss for all wavelengths.

### 5.6.1.9   Differential polarisation effects

Differential polarisation between the two beams being combined can also reduce the system visibility (Traub 1988; Buscher et al. 2009). One way to minimise this effect is to design the arms of the interferometer to be symmetrical such that the starlight from different arms experiences the same number of reflections of the same type of surfaces at the same AoI. This is what is implemented at the MROI and so visibility losses due to differential polarisation effects are expected to be low. As a result I again assign a 1% visibility loss to all wavelengths for this term.

### 5.6.1.10   Differential Throughput

Visibility will be reduced if the two beams being interfered are of different intensity. This can occur if the two arms of the interferometer have a different throughput either by the optical components along the arms having a differential throughput or by differential diffraction throughput losses if the two beams travel significantly different distances through the beam relay system.

The visibility of two beams of different intensity being combined is given by

$$V = \frac{2\sqrt{I_1 I_2}}{I_1 + I_2}, \tag{5.13}$$

where $I_1$ and $I_2$ are the intensities of the two beams being combined. Rewriting the intensity of one of the beams as a fraction of the other $I_2 = \alpha I_1$ equation (5.13) becomes $V = 2\sqrt{\alpha}/(1 + \alpha)$.

Losses due to differential throughput of optical components are expected to be small, both because there are few components (20, including the 13 reflections, tip-tilt dichroic, Atmospheric Dispersion Correctors (ADCs) and the two windows as the beam enters and exits the vacuum envelope along the beam relay and delay line) and the fact that the components for each arm of the interferometer will be housed in the same environment so will be expected to age at the same rate. Even assuming a conservative estimate that the throughput may differ by 10% between the arms of the interferometer the theoretical visibility will be as high as V = 0.9986.

**Table 5.8:** The maximum theoretical visibilities in the J, H and K bands, along with the maximum theoretical fringe contrast due to losses along the MROI beam train.

| Factor | Value | Units | J | H | K |
|---|---|---|---|---|---|
| Atmospheric high order WFE | | | 0.37 | 0.57 | 0.73 |
| Diffraction Fresnel filtering | | | 1.14 | 1.14 | 1.08 |
| Instrumental high order static WFE | 98 | nm | 0.78 | 0.87 | 0.92 |
| Uncorrected atmospheric tilt | 0.048 | arcseconds on-sky | 0.83 | 0.9 | 0.92 |
| Instrumental tilt | 0.054 | arcseconds on-sky | 0.79 | 0.89 | 0.93 |
| Fractional pupil shear | 0.017 | | 0.98 | 0.98 | 0.98 |
| Instrumental piston jitter | 102 | nm | 0.76 | 0.85 | 0.91 |
| Atmospheric piston jitter | | | 0.79 | 0.79 | 0.79 |
| High order dispersion effects | | | 0.99 | 0.99 | 0.99 |
| Differential polarisation effects | | | 0.99 | 0.99 | 0.99 |
| | | **Total:** | **0.13** | **0.29** | **0.45** |

### 5.6.1.11   Summary

The visibility loss along the MROI beam train due to the terms mentioned in this section may be individually small but combining them via RSS results in a maximum theoretical visibility of 0.13, 0.29 and 0.45 in the J, H and K bands respectively (as shown in table 5.8). Most effects are compounded at shorter wavelengths leading to a significantly reduced system visibility in the J band.

## 5.6.2   FOURIER visibility losses

In addition to the visibility losses along the MROI beam train, potential visibility losses of the FOURIER instrument itself must be taken into account.

### 5.6.2.1   Static WFE

Contrary to how the static WFE is calculated for the MROI beam train in section 5.6.1.1 the visibility loss due to surface WFE, alignment and thermal system cooldown have already been estimated numerically in section 5.2. Here the visibility loss was predicted to be 4% for both effects.

An interesting comparison is between the visibility loss predicted by the analytical model used in section 5.6.1.1 and the numerical Monte Carlo approach used in section 5.2.

All surfaces of FOURIER are specified to have a surface quality of $\lambda/4$ P2V at $\lambda = 633$ nm. Again reducing the P2V by a factor of 5 the RMS surface error suggests a surface error of 31.65 nm. For the reflective surfaces, M1 and M2, a wavefront error of 63.3 nm RMS will be imparted as reflective surfaces are double pass. Transmissive surfaces will also impart a 63.3 nm RMS wavefront error as the wavefront passes through two surfaces. Combining the wavefront errors via RSS I arrive at an imparted wavefront error of 118 nm, larger than what the MROI beam train imparts. This is not surprising as the FOURIER has roughly half the optics of the beam train but much looser surface tolerances on each optic. Converting this WFE into a visibility loss at the J, H and K bands, the visibility is estimated to be 0.70, 0.82 and 0.89 in the J, H and K bands respectively.

This is a significant level of loss, however performing Monte Carlo analysis of the FOURIER instrument with the above surface quality, tolerancing only the surface quality, produces the distribution of RMS spot size along the interference fringe axis shown in figure 5.17. The

mean of this distribution is only marginally lower than for the distribution generated by the entire tolerance error budget (10.2 µm compared to 11 µm), suggesting that surface quality is the dominant contribution to the alignment error budget along the interference fringe axis. This is not the case along the spectral axis, where the contribution to the error budget from surface quality is negligible, highlighting the importance of separating the metrics between the spectral and interference fringe axes in section 5.2. This result is to be expected as I apply a compensator to correct for misalignments in the interference fringe axis (by adjusting the position of M2) but not along the spectral axis. Converting this toleranced geometric spot size of 10.2 µm due to optic WFE into a visibility loss using figure 5.4 I conservatively adopt a 4% visibility loss, i.e. a maximum theoretical visibility of 0.96%.

This is significantly higher than the value stated for the analytical model, however the discrepancy can be explained by a number of factors. Firstly, the surface area of the optics the individual beams occupy is often a small fraction of the total optics surface, meaning that while globally the surface error may be as large as $\lambda/4$ if the whole aperture was used, within a small section of the optic it is likely much better. In addition to this, equation (5.8) assumes that the two beams being interfered have uncorrelated wavefront errors. This assumption will partially break down as all beams passing through FOURIER travel along a common path, though they do strike different parts of the optics so this assumption may not break down entirely. These reasons highlight the need for a more realistic numerical simulation of the system, rather than relying on the analytical approach. This appears to be proven correct with the high visibility values measured in laboratory experiments presented in section 7.5. These assumptions are expected to hold better for the MROI beam train, where the starlight fills a larger fraction of the aperture of each optic and the beams do not pass through the same optics.

### 5.6.2.2 Misalignment losses

The error budget for FOURIER derived in section 5.2.1 gave a 4% visibility loss for surface error, system misalignment and thermal cooldown effects. This is the value I use in this section as well, assigning a 4% visibility loss due to these effects. From figure 5.4 I note that it is only the beam pair spaced furthest apart, "Baseline 3" which is likely to suffer a 4% drop in visibility. Assigning this one value to all baselines will not affect the limiting magnitude calculations as the limiting magnitude is calculated for the worst performing baseline in section 5.7, which is
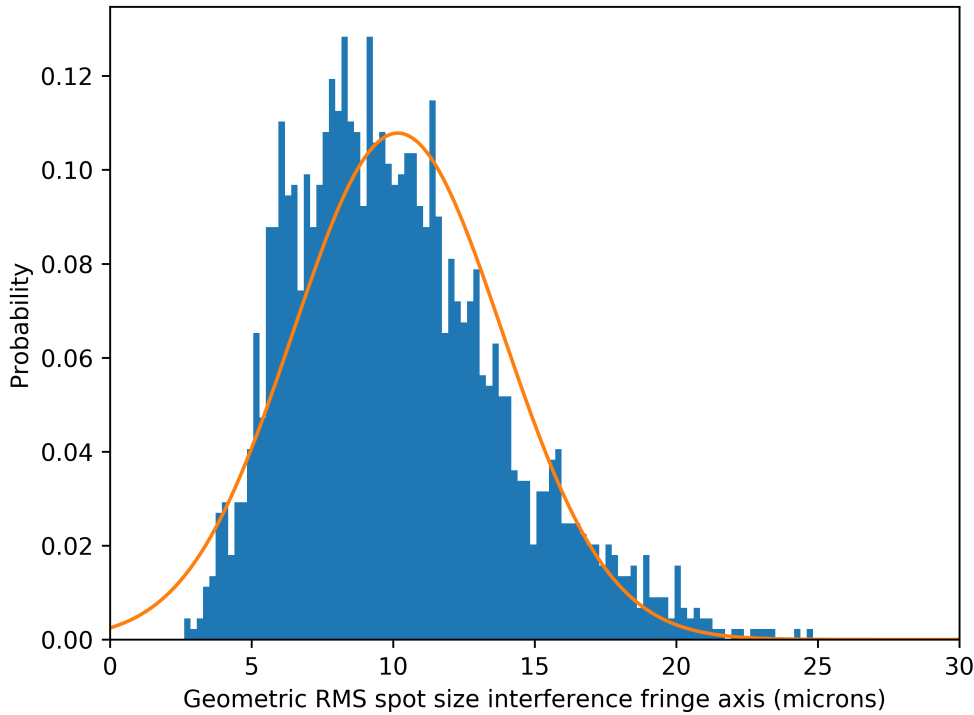
**Figure 5.17:** This RMS spot size distribution along the interference fringe axis for 2,000 simulated systems where only the surface error for each surface is considered and randomly perturbed for each simulation. This produces only a marginally lower mean than the distribution presented in figure 5.5, suggesting surface quality is the dominant term in the error budget along the interference fringe axis.

baseline 3.

### 5.6.2.3  Vibrations

A benefit of all the beams within FOURIER propagating through the same optics is that any tilts of the optics will introduce the same tilt in all beams and so no differential tilt between the beams will be introduced, meaning the effects of equation (5.11) are not expected to contribute. This reduces the impact of both misalignments and vibrations. One effect which will still be present, however, is if vibrations shake the interference fringes with respect to the detector during an exposure the fringe contrast can be reduced. This is minimised in FOURIER, both by placing the instrument on an isolated optical table and by not using any active vacuum pumping or LN2 delivery system during observations. Instead, the instrument will be evacuated and loaded with LN2 during the day. Nevertheless, to be conservative I assign a 1% visibility

loss due to vibrations in the system. In addition to this there is a 20 nm RMS piston vibration assigned to FOURIER in table 5.7.

### 5.6.2.4 Differential polarisation

Traub (1988) show that a phase difference between the polarisation states can lead to a reduction in fringe contrast but this is not expected to be an issue in FOURIER as the optics experience a common path. I assign a 1% loss in visibility at all wavelengths for this effect.

### 5.6.2.5 Spatial filtering gain

FOURIER contains a dedicated pinhole spatial filter in the form of a slit along the spectral axis at the focal plane of M1. Spatial filtering along the interference fringe axis is carried out in software by applying a virtual pinhole (setting pixel value to zero outside a window). As with Fresnel spatial filtering discussed in section 5.6.1.3 this spatial filter boosts the fringe contrast lost due to high order atmospheric WFE. The gain factor used here is taken from figure 3 of Keen et al. (2001) by comparing the visibility in their simulation with a pinhole spatial filter to that without one, at $D/r_0$ values estimated at the MROI observatory of 3.3, 2.4, 1.7 in the J, H and K bands respectively. These give visibility gain factors of 2.2388, 1.66437 and 1.3596 in the J, H and K bands, respectively. This means that the maximum fringe contrast of 0.369 in the J band due to high order atmospheric WFE given in table 5.8 is improved to 0.82. This is a significant gain in visibility, though of course this comes at the cost of a loss of throughput as discussed in section 5.5.2.

### 5.6.2.6 Polychromatic simulation

In addition to the visibility losses discussed above, there are additional terms such as the effects of finite sized pixels used to sample the interference fringes, optical aberrations (these are different to surface WFE, optical aberrations are present even with perfect optics) and polychromatic bandpasses on each spectral channel.

To quantify visibility losses due to these effects I developed python code which produced a simulated SAPHIRA detector readout, showing spectrally dispersed interference fringes sampled at the resolution of the SAPHIRA detector's 24 µm pixels.

To achieve this I utilised the POP routine in Zemax, which propagates coherent, monochromatic light through a Zemax model. By generating a large beam which was immediately cropped by three circular apertures, I replicated the three coherent beams of starlight at the entrance of FOURIER, which propagated through the model and produced interference fringes at the image plane. However, interacting with the POP routine via the Zemax GUI presented a couple of problems. Firstly, the monochromatic wavelength the simulation was run at had to be manually changed for every wavelength sampled. Secondly, it is not possible to combine the monochromatic results within Zemax to produce a polychromatic simulation.

It is worth noting that the Huygens PSF routine within Zemax offers an alternative to POP and can simulate polychromatic light, however, it is much slower as it relies on direct integration. There is also a limit of 24 wavelengths which can be defined within the GUI of Zemax and so it would not be possible to accurately simulate the image plane of FOURIER over a wide wavelength range of $\lambda$ = 1.1-2.4 μm with this approach.

To overcome these issues I developed a script using the python package PYZDDE (Sinharoy 2016) to retrieve the POP runs from Zemax within python. With this I was able to automatically generate a POP file for an arbitrary number of wavelengths and incoherently sum each wavelength onto a single 2D array. The individual beam files were sampled at a high resolution to avoid inaccuracies in the propagation routine and the polychromatic image was subsequently downsampled via interpolation onto an array with the resolution of the SAPHIRA detector 24 μm pixels. An example output of this simulation is shown in figure 5.18.

With this simulated detector readout it was then possible to measure the fringe contrast on all three baselines by taking the Fourier transform of the interference fringes along the spectral axis of the image. As the simulation stores the information about which wavelength files are summed on each spectral channel, visibility losses as a function of wavelength can be extracted as shown in figure 5.19. This shows that the visibility losses from optical aberrations, polychromatic fringes and finite detector sampling are moderate, decreasing towards longer wavelengths, likely due to the larger PSF resulting in better sampling of the interference fringes. What is clear is that visibility losses are a strong function of baseline, with higher spatial frequency interference fringes more susceptible to a loss in fringe contrast.
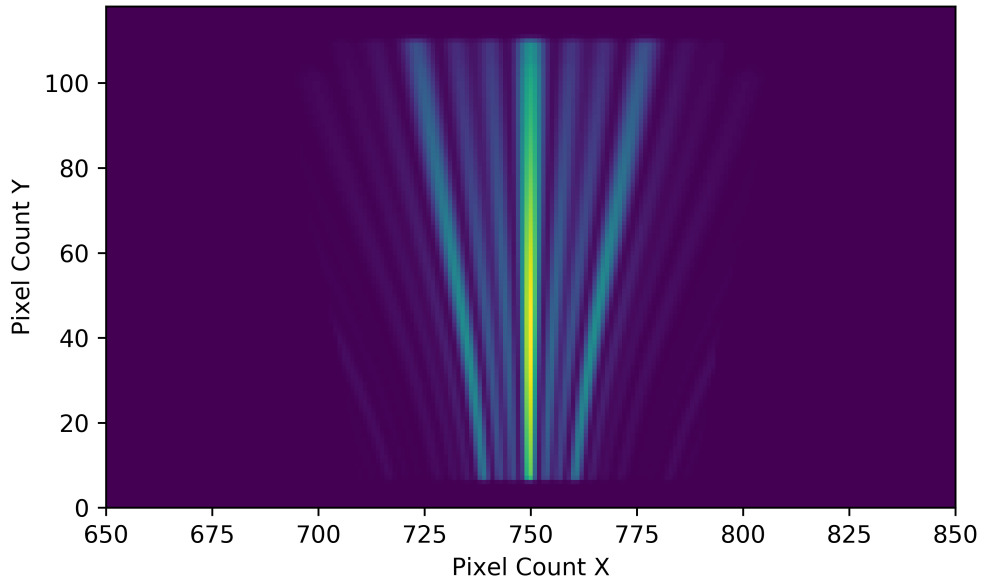
**Figure 5.18:** An example output of the polychromatic physical optics simulation showing dispersed interference fringes sampled at the resolution of the SAPHIRA detector.

### 5.6.2.7 Summary

Combining the visibility losses estimated for FOURIER in the previous sections, the estimated maximum visibility of fringes combined by the FOURIER beam combiner is given in table 5.9. Note that this does not include the gain in visibility due to the spatial filter as this is applied to the high order atmospheric WFE terms which are not considered in this section. The resulting visibility is a strong function of the beam spacing being considered, ranging from a 6% loss in the J band on the lowest spatial frequency fringes to 18% loss on the highest spatial frequency fringes. An 18% loss (i.e. a maximum theoretical visibility of 82%) is quite low, considering a loss of up to 80% is expected in the J band for the MROI beam train (table 5.8).
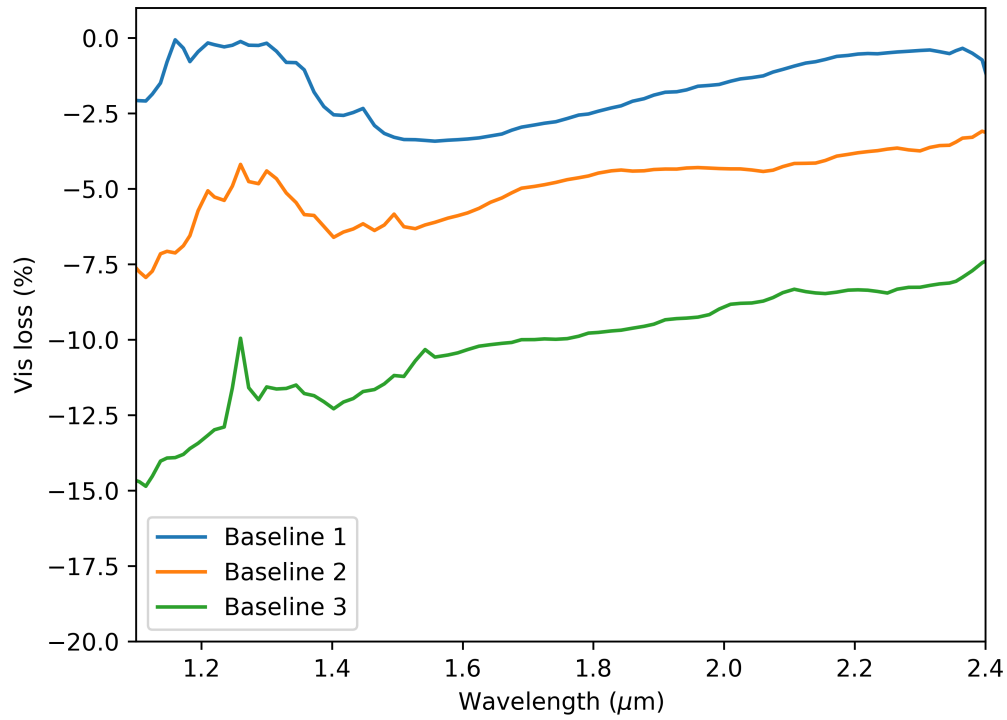
**Figure 5.19:** The visibility loss as a function of wavelength on the three baselines sampled by FOURIER. Baseline 1 represents the lowest spatial frequencies interference fringes and baseline 3 the highest.

**Table 5.9:** The theoretical maximum visibility of the FOURIER instrument considering losses due to polychromatic effects, finite pixel sampling of the fringes, optical aberrations, misalignments, vibrations, and polarisation losses.

| FOURIER system visibility | J | H | K |
|---|---|---|---|
| Baseline 1 | 0.94 | 0.91 | 0.94 |
| Baseline 2 | 0.90 | 0.89 | 0.91 |
| Baseline 3 | 0.84 | 0.85 | 0.87 |

## 5.7   Limiting Magnitude

With the expected visibility and throughout defined for a point source observed with the MROI/FOURIER, these values can be used to estimate the limiting magnitude of the FOURIER beam combiner. Here limiting magnitude is defined as the magnitude at which it is possible to achieve a SNR of two or greater in a single spectral channel within five minutes of integration on the least sensitive input channel in the least sensitive spectral band. The spectral channels used to evaluate the limiting magnitudes given below are taken to be at the centres of the J, H and K bands at $\lambda = 1.25\,\mu m$, $1.65\,\mu m$ and $2.2\,\mu m$ respectively. The range of wavelengths in each spectral channel is set such that such that they match the spectral resolution of FOURIER simulated in section 5.4. For example, the H band spectral channel used here spans the wavelength range $\lambda = 1.639\,\mu m$–$1.661\,\mu m$, giving a $\Delta\lambda = 0.022\,\mu m$ and a central wavelength of $\lambda = 1.65\,\mu m$ resulting in a $R = 75$ by equation 5.4. The exposure time is taken to be $2t_0$ (where $t_0$ is the atmospheric coherence time) and seeing conditions to be $r_0 = 14\,cm$ and $t_0 = 4.4\,ms$ (where $r_0$ is the Fried parameter) at a wavelength of $\lambda = 500\,nm$.

Before calculating the limiting magnitude I must first convert this throughput into the number of stellar photons detected in each integration and quantify the number of noise photons per integration in each band. This is done in the following sections. To illustrate the process discussed below I work through an example of a 13th magnitude star in the H band at each stage.

### 5.7.1   Photon counts

To estimate the number of stellar photons I adopt the system of Campins et al. (1985), taking the flux of a magnitude zero star to be 1600, 1080 and 670 Janskys in the J, H and K bands, respectively. These flux values are scaled to fluxes at other magnitudes via

$$f_{m_1} = f_{m_0} \times 10^{-0.4(m_1 - m_0)}, \tag{5.14}$$

where $f_{m_0}$ is the above flux for a zero magnitude star and $f_{m_1}$ the flux of a star at magnitude $m_1$. Once the flux for the magnitude of the star I wish to calculate the SNR for has been calculated, the flux measurement is converted to photons per second via

$$N_{\text{phot}} = f A \frac{1 \times 10^{-26}}{h} \frac{d\lambda}{\lambda}, \tag{5.15}$$

where $f$ is the flux in Janskys, $A$ the collecting area (taken to be $1.46\text{m}^2$ for the 1.4 m UT primary, minus the 5% blocked aperture due to obstruction from the secondary, tertiary and spiders), $h$ Planck's constant and $d\lambda/\lambda$ the fractional bandwidth over which the observations are made (i.e. the range of wavelengths present on a single spectral channel divided by the mean wavelength).

Finally, to calculate the number of stellar photons per exposure I must account for the exposure time. The stated requirement for the limiting magnitude goal is an exposure time of $2t_0$. As $t_0$ is defined at $\lambda = 500\,\text{nm}$ it must be scaled to other wavelengths via

$$t_{0\lambda} = t_{0@500\,\text{nm}} \left( \frac{\lambda}{500\,\text{nm}} \right)^{6/5}. \tag{5.16}$$

For the example 13$^{\text{th}}$ magnitude star in the H band, I first scale from the 1080 Jy for a 0$^{\text{th}}$ magnitude star to $6.8\text{x}10^{-3}$ Jy for a 13$^{\text{th}}$ magnitude star with equation (5.14). Assuming a science channel spans the wavelength range $\lambda = 1.639\,\mu\text{m}$–$1.661\,\mu\text{m}$, and using the previously stated collecting area of the MROI UT of $1.46\text{m}^2$, the number of photons detected per second above the Earth's atmosphere is calculated to be 1998 via equation (5.15). By scaling $t_0$ via equation (5.16) and multiplying it by two the integration time of $2t_0$ in the H band is calculated to be 36 ms. This results in 72 stellar photons received per exposure. This is reduced by the throughput losses of the atmosphere, MROI beam train and FOURIER as discussed in section 5.5, giving a final 7 stellar photons detected per integration.

I now turn to calculating the number of photons from noise sources. The first is photons arising due to thermal emission from the sky. I take the sky brightness to be 15.50, 14.70, 13.50 magnitude per square arcseconds for the J, H and K bands respectively, based on values reported for observations at La Palma. Note that these values are independent of moon phase due to the minimal effect of the moon in the near-infrared. This is then converted to a flux per arcsecond square again via equation (5.14) (assuming again zeroth magnitude is equivalent to 1080 Jy in the H band etc.). It is next converted to the number of photons per second per arcsecond square in a single science channel with equation (5.15), again multiplying it by $2t_0$ to retrieve photons per arcsecond per exposure. Finally this is converted to photons per exposure under the assumption that the field of view is the diffraction limit of the telescope, i.e. $2.44\lambda/D = 0.57$ arcseconds in the H band for the 1.4 m MROI telescopes. Continuing the example of the 13$^{\text{th}}$ magnitude H band star, including the throughput losses of the MROI and

FOURIER, this translates to 0.52 sky photons detected per exposure.

The final photon source to consider is that of thermal background photons. The optics along the beam train are modelled as 300K black bodies, the number of photons arising from such a source at a wavelength $\lambda$ can be modelled via Planck's law expressed in photons/second/m$^2$/sr/m as

$$L_\lambda(\lambda, T) = \frac{2c}{\lambda^4 \left( \exp\left( \frac{hc}{\lambda KT} \right) - 1 \right)}, \tag{5.17}$$

where $c$ is the speed of light, $h$ Planck's constant, $\lambda$ the wavelength of observation, $K$ the Boltzmann constant and $T$ the temperature of the emitting body. This modified form of Planck's law is taking the standard form which expresses the energy emitted in Joule/second/m$^2$/sr/m by dividing by the energy of each photon of $E = hc/\lambda$.

Integrating this function over the range of wavelengths present on each science channel via $L = \int_{\lambda_2}^{\lambda_1} L_\lambda \, d\lambda$ gives the number of photons/second/sr/m$^2$. Continuing with the H band example, this gives $4.2 \times 10^{11}$ thermal photons/second/sr/m$^2$. This needs to be converted to thermal photons per second, which is done by considering the area and solid angle over which this thermal radiation is seen by the detector. To constrain the area, a cold stop of diameter D is used. The area over which thermal emission passes through the cryostat is then $\pi(D/2)^2$. In order to constrain the solid angle over which thermal photons pass through the system, I assume a pinhole (the spatial filter in FOURIER) is utilised which is matched to the angle subtended by the first null of the Airy disk the circular cold stop aperture would produce, i.e. $\pi(1.22\lambda/D)^2$. This model can be thought of as viewing a warm wall through a circular aperture of diameter D with the field of view being restricted to the diffraction limited "on-axis" bundle of rays. The product of the area and solid angle is then $(1.22\pi/2)^2\lambda^2$, where $\lambda$ is taken to be the centre wavelength of the passband in a scientific channel.

In the H band this results in 4.2 thermal photons/second entering the cryostat per cold stop, or 12.6 thermal photons in total as FOURIER combines three beams and so effectively has three cold stops. This number is reduced by the throughput of the optics after the cold stop/spatial filter (i.e. M2, N-SF11 prism, L1) and the detector's QE (59% throughput in the H band) to 7.434 thermal photons/second detected. Finally, adjusting this number for the integration time of $2t_0$ I arrive at 0.27 thermal photons detected per integration in the H band. The number of

thermal photons in the J band by this same model is estimated to be $1.8 \times 10^{-5}$ and 488 in the K band, demonstrating the rapid increase in thermal noise towards longer wavelengths in the near-infrared for room temperature objects.

The final noise term to be considered is read noise. This is caused by the imperfect electronics of the detector in converting the analogue signal recorded on each pixel to a digital value, meaning the signal count on each pixel will vary about a mean value between reads for a pixel under constant illumination levels. This number is typically quoted in electrons/pixel/read and for the SAPHIRA detector has been shown to be as low as 0.3 (or better) electrons (Lanthermann et al. 2019).

### 5.7.2   SNR calculation

Calculating the SNR of an interferometric observation is non-trivial, as it depends not only on the number of stellar photons to noise photons, but also on the visibility of the interference fringes (with lower contrast fringes reducing the SNR). In addition to this, simplified SNR equations like those given in section 4.6 depend on which observational regime you are in (photon noise or read noise dominated). If you are in an intermediate case where both of these terms are significant there are additional cross terms which arise. I must first discuss what it is I want to measure and in this case it is the fringe contrast or visibility of the object being observed. The first step is to extract the visibility from a single integration, which is done by applying a Fourier transform in the form of a FFT to a 1D slice of the interference fringes in a single science channel to obtain a power spectrum. The result of this is shown on the right in figure 4.2, which contains a component at the zero spatial frequency and three peaks at higher spatial frequencies, corresponding to the three baselines sampled by the beam combiner. The visibility along each baseline is then estimated by calculating the ratio of the power at the spatial frequency of each interference fringe, known as the coherent flux of $F_{ij}$, to the power of the zero spatial frequency term $F_0$, with a correction factor for the number of telescopes. $ij$ correspond to the interference fringes generated by combining telescopes $i$ and $j$. The visibility $V_{ij}$ on baseline $ij$ then takes the form of

$$V_{ij} = N_{\text{tel}} \frac{F_{ij}}{F_0}, \tag{5.18}$$

where $N_{\text{tel}}$ is the number of telescopes. Referring back to figure 4.2, for an ideal system

where the power spectrum has been normalised to $F_0 = 1$, the coherent flux $F_{ij}$ equals 1/3 on each baseline. Equation (5.18) then gives a visibility of unity along each baseline as expected. For objects near the limiting magnitude of the system, the SNR of an individual exposure of length $2t_0$ will be low. A first approach to improve SNR is to expose for a longer time as is done for example in photometry. However, this will result in the visibility tending towards zero in the presence of atmospheric turbulence, which cause the fringes to move randomly along the fringe axis due to random phase perturbations introduced between the beams. This leads to "fringe smearing" and eventually a visibility of zero (no interference fringes visible) for long exposure times.

$F_{ij}$ will also tend towards zero if it is calculated by averaging over a series of short exposures. Even if the visibility may be high in each individual exposure. This is again due to the random phase variations between exposures. I must instead use a metric which can be averaged over many exposures, leading to the concept of the power spectrum $P_{ij}$, described as

$$P_{ij} = |F_{ij}|^2 = \left(\frac{V_{ij}F_0}{N_{\text{tel}}}\right)^2, \tag{5.19}$$

which, as it is the modulus squared, is independent of phase and thus does not tend towards zero under atmospheric perturbations in contrast to the coherent flux. The SNR can then be calculated with

$$SNR = \frac{P_{ij}}{\sqrt{\sigma_{ij}^2}}, \tag{5.20}$$

where $\sigma_{ij}^2$ is the variance of the respective power spectrum. This equation does not include any other noise terms such as read noise, thermal or sky background photons which must also be taken into account. Fortunately an unbiased estimate of the power spectrum and its noise terms has been calculated by Gordon & Buscher (2012) and implemented in a SNR calculation by Mourard et al. (2017), resulting in

$$SNR = \frac{\left(\frac{V_{ij}F_0}{N_{\text{tel}}}\right)^2}{\sqrt{\text{PhotonNoise} + \text{ReadNoise} + \text{CoupledTerms}}}, \tag{5.21}$$

where PhotonNoise, ReadNoise and CoupledTerms represent the variance arising due to photon noise, read noise and coupling terms between the two noise sources respectively. The

PhotonNoise term is given by

$$\text{PhotonNoise} = 2N_{\text{ph}} \left( \frac{V_{ij}F_0}{N_{\text{tel}}} \right)^2 + N_{\text{ph}}^2, \tag{5.22}$$

the ReadNoise term by

$$\text{ReadNoise} = N_{\text{pix}}\sigma^2 + N_{\text{pix}}^2\sigma^4, \tag{5.23}$$

and finally, the CoupledTerms by

$$\text{CoupledTerms} = 2 \left( \frac{V_{ij}F_0}{N_{\text{tel}}} \right)^2 N_{\text{pix}}\sigma^2 + 2N_{\text{ph}}N_{\text{pix}}\sigma^2. \tag{5.24}$$

The parameter $N_{\text{ph}}$ is the total number of photons present in the interferogram (from the source, sky background and thermal photons), $N_{\text{pix}}$ the number of pixels the fringes were sampled over and $\sigma$ the read noise of each pixel. In the original Gordon & Buscher (2012) paper there is an additional term in the PhotonNoise term, which is concerned with the effects of interference fringes at twice the spatial frequency of the fringes the SNR is being calculated for. As the worst performing baseline, and so the one the SNR is calculated for here, corresponds to the highest spatial frequency interference fringes recorded by FOURIER, this term is equal to zero for the analysis carried out here and so is not included.

Applying this model for both the MROI beam train and the FOURIER beam combiner using the values derived in sections 5.5 and 5.6 I calculate that FOURIER will reach a limiting magnitude of 12.3, 13.2 and 11.7 in the J, H and K bands, respectively, by the above definition of limiting magnitude.

### 5.7.2.1 Dominant terms in the SNR calculations

It is worth taking a closer look at which (if any) terms are dominant in setting the limiting magnitude in each of the three bands. The first step is to compare the magnitudes of the PhotonNoise, ReadNoise and CoupledTerms noise terms given in table 5.10.

Table 5.10 matches expectations, for example in the J band where nearly all photons detected are from the source itself (12 photons from the object, $8 \times 10^{-2}$ from the sky background and $2 \times 10^{-5}$ thermal photons). Photon noise is minimal to the point that the low levels of read noise from the SAPHIRA detector of 0.3 electrons/pixel is almost equal in magnitude.

**Table 5.10:** The percentage contribution of each noise term to the overall noise in the J, H and K bands for the highest spatial frequency baselines sampled by FOURIER.

| Band | PhotonNoise | ReadNoise | CoupledTerms |
| --- | --- | --- | --- |
| J | 29% | 22% | 49% |
| H | 35% | 16% | 49% |
| K | 87.8% | 0.4% | 11.8% |

The coupled terms represent those in which both photon noise and read noise contribute significantly. Unsurprisingly, the opposite is true in the K band where the significant number of photons detected do not originate from the source (22 photons from the object, 3 from the sky background and 488 thermal photons), increasing the photon noise, while the read noise term remains the same order of magnitude. Hence the photon noise dominates in this regime. It is important to note that the read noise does increase significantly between the J and K bands due to the linear scaling of the PSF with wavelength, resulting in the number of pixels read out in a K band science channel being 3× that of the J band. However, this increase is insignificant compared to the increase in photon noise.

From this I conclude that while read noise is never the dominant term, as expected for the low read noise SAPHIRA detector, claiming the system to be photon noise dominated is only accurate in the K band. Hence it is important that both sources of noise are modelled simultaneously as is done here, rather than relying on simplified approximations for the SNR e.g. those given in equations (4.3) and (4.4).

The above limiting magnitudes only state at what magnitude the SNR goes to two. It is interesting to look at the SNR as a function of limiting magnitude as is shown in figure 5.20, using the analytical model discussed above.

Figure 5.20 shows that the performance on bright targets in the J band is significantly worse than the H and K bands. This is to be expected as the system visibility is roughly half in the J band compared to what it is in the H and K bands. This is primarily due to tilts and piston vibrations in the system, which are constant in magnitude at all wavelengths but have a larger impact in the J band due to its shorter wavelength such that, for example, any piston vibrations are a larger fraction of wavelength in the J band. Atmospheric effects are of course worse in the J band as well, but the Fresnel spatial filtering and spatial filter in FOURIER filter the beam
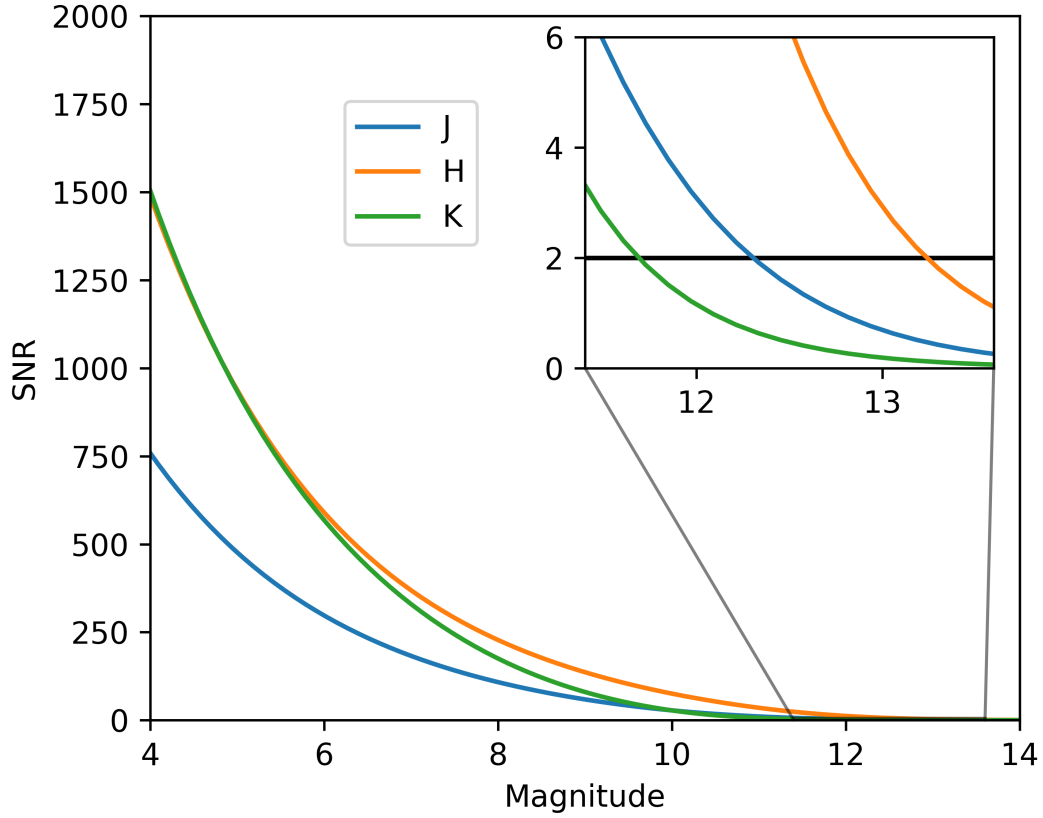
**Figure 5.20:** The SNR of the power spectrum as a function of magnitude for the MROI/FOURIER model for the worst performing baseline sampled in each of the J, H and K bands. The insert shows the SNR around the definition of limiting magnitude of SNR = 2.

well enough to remove the majority of these effects.

### 5.7.2.2 Model comparison

To understand figure 5.20 better, it is useful to study what regime the system can be considered to be in at each magnitude, i.e. photon noise dominated as is the case at high light levels or read noise dominated as is the case at low light levels. To assess this I take equation (5.21) and simplify it, firstly by assuming that photon noise dominates and hence the read noise and coupled terms can be ignored. This gives the SNR to be

$$\text{SNR} = \frac{\left(\frac{V_{ij}F_0}{N_{\text{tel}}}\right)^2}{\sqrt{2N_{\text{ph}}\left(\frac{V_{ij}F_0}{N_{\text{tel}}}\right)^2 + N_{\text{ph}}^2}}. \tag{5.25}$$

Simplifying this further by ignoring the contribution to $N_{\text{ph}}$ of the thermal background and sky background, i.e. that only stellar photons contribute so $N_{\text{ph}} = F_0$, equation (5.25) becomes

$$\text{SNR} = \frac{V_{ij}\sqrt{F_0}}{\sqrt{2}N_{\text{tel}}}. \tag{5.26}$$

Where the SNR goes linearly with the visibility but with the square root of flux, similar to the approximation given in equation 4.3.

Applying the same logic to the read noise dominated case, equation (5.21) can be written as

$$\text{SNR} = \frac{\left(\frac{V_{ij}F_0}{N_{\text{tel}}}\right)^2}{\sqrt{N_{\text{pix}}\sigma^2 + N_{\text{pix}}^2\sigma^4}}. \tag{5.27}$$

Here the SNR goes with the square of both the visibility and the number of photons. Taking equations (5.26) and (5.27), and calculating the SNR as a function of magnitude for both simplified cases, I can plot them alongside the full SNR model as is done in figure 5.21 for the H band.

As figure 5.21 shows, the photon noise only model is a good approximation, overestimating the SNR, as expected as it does not include the effects of read noise, thermal and sky background photons or coupled terms, which would only reduce the SNR. At a SNR of 50 at a magnitude of 11.7 the photon noise and read noise models cross, with the read noise subsequently being a better fit (closer in value to the full SNR calculation) and so the system can be considered read noise dominated at magnitudes fainter than this. The SNR of the photon noise only model does not drop below 2 until a magnitude of 18.7, compared to a magnitude of 13.2 for the full model, highlighting the importance not neglecting the effects of read noise even with sub-electron read noise detectors. Both the J and H bands exhibit the same behaviour of the photon noise model being a better fit on brighter targets and worse on faint targets.

In the K band, however, neither of the two simplified models are a good fit. In the photon noise dominated case the assumption that stellar photons are the only source of photons is not valid: at a magnitude of 11.7 there are 22 stellar photons to every 491 noise photons from the sky background and thermal emission so equation (5.26) is invalid. However, looking at the percentage contribution of the PhotonNoise, ReadNoise and CoupledTerms in the full SNR equation at magnitude 11.7, the photon noise terms contribute to 88% of the total noise (mainly
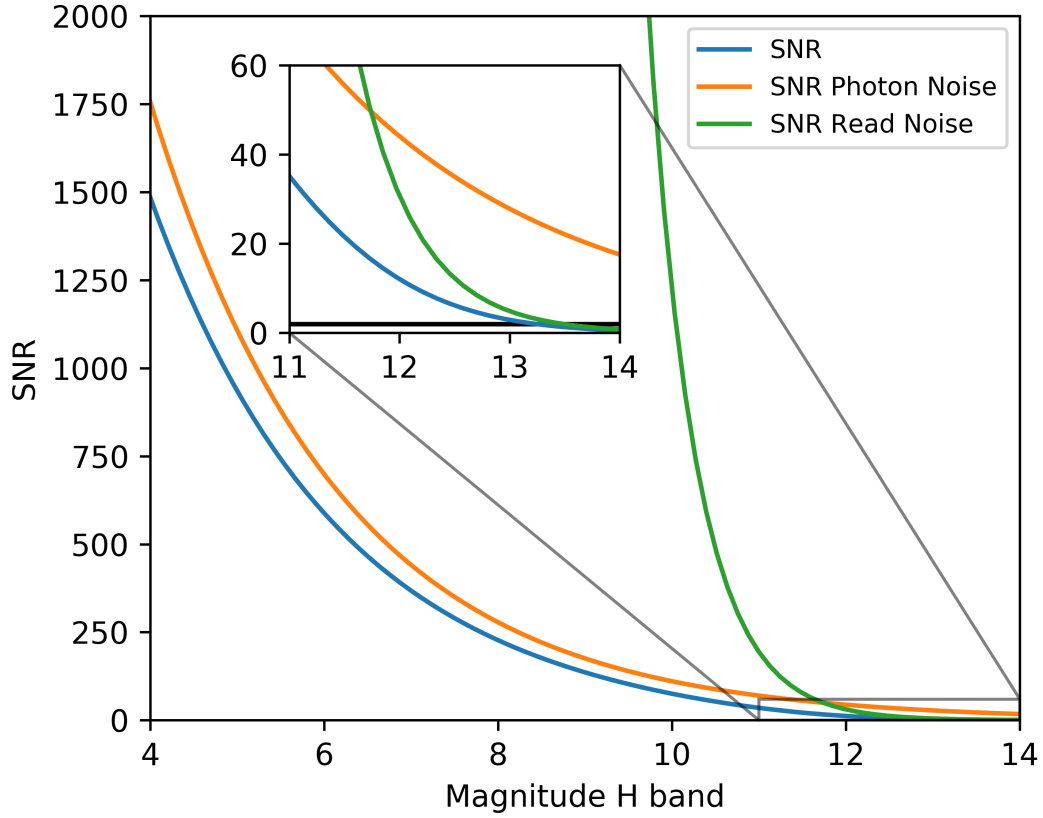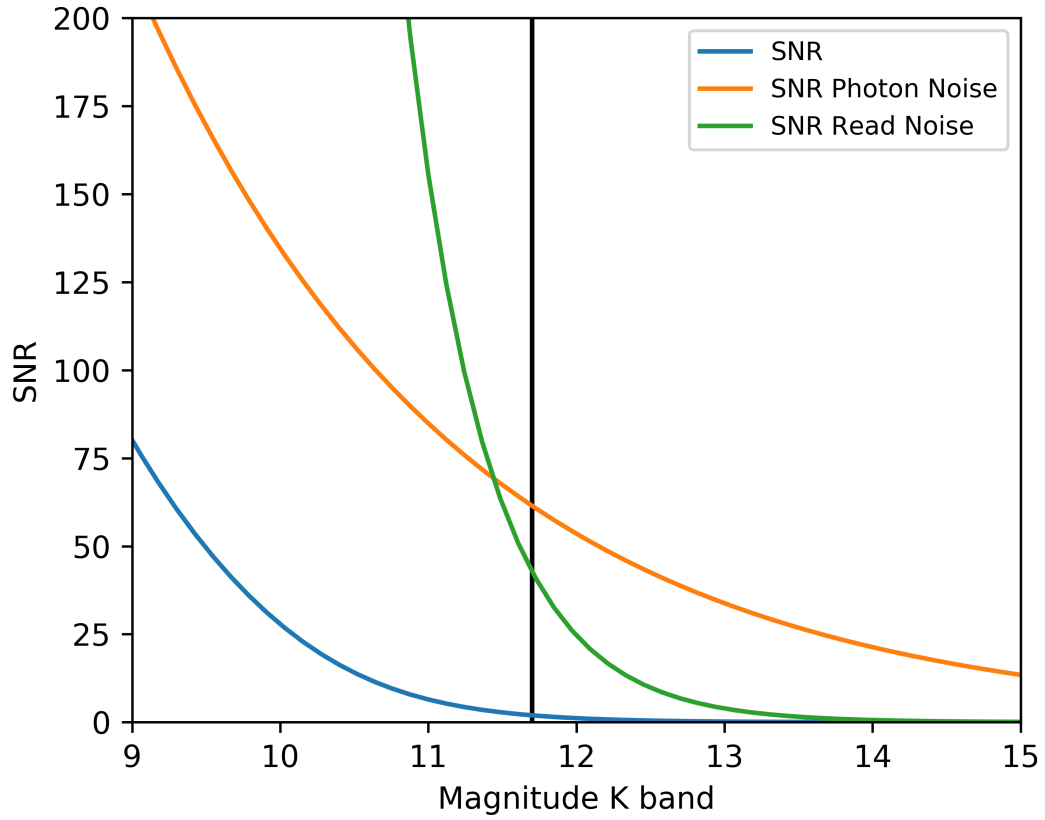
**Figure 5.21:** The SNR of the power spectrum as a function of stellar magnitude for the MROI/FOURIER model for the full SNR model, equation (5.21), the photon noise dominated model, equation (5.26), and the the read noise dominated model, equation (5.27). This shows that the system can be considered photon noise dominated down to a magnitude of 11.7, at which point the read noise model is a better fit.

due to sky background and thermal photons), with read noise only 0.4% and the rest in the coupled terms. Hence the read noise model neglects the vast majority of noise terms. As a result both simplified models significantly overestimate the SNR at the limiting magnitude as shown in figure 5.22, where the vertical line is at the magnitude which gives a SNR of 2 by the full model.

## 5.8   Summary

In this chapter I have demonstrated that the optical design presented in chapter 4 is feasible to build (based on the system tolerancing, section 5.2, and thermal modelling, section 5.3 carried out). That the proposed dispersing optic meets the spectral resolution requirements,

**Figure 5.22:** The SNR of the power spectrum as a function of magnitude for the MROI/FOURIER model for the full SNR model, equation (5.21), the photon noise model, equation 5.26, and the read noise model, equation 5.27. The vertical line is at the limiting magnitude of the system (determined by the full SNR model) and shows that both the simplified photon noise and read noise models significantly overestimate the SNR at this magnitude for reasons described in the text.

section 5.4, and finally that the combined performance of the MROI beam train and FOURIER beam combiner will enable a limiting magnitude of 12.3, 13.2 and 11.7 in the J, H and K bands, respectively.

# OPTOMECHANICAL DESIGN OF FOURIER

## 6.1  Introduction

In the previous chapters I have introduced the optical design of the Free-space Optical multi-apertUre combineR for IntERferometry (FOURIER) and quantified both its performance and the optical alignment requirements. As shown in section 5.2 the optical alignment criteria are moderately relaxed for FOURIER (positioning errors of order hundreds of microns and tilt errors of order 2 milliradians). This was intentionally designed for by developing a system with a high effective f ratio. The advantage of this loose alignment error budget is that it does not place tight constraints on the optomechanics, allowing FOURIER to use simple mounts which are placed at predetermined positions on the optical breadboard. This simple approach to alignment works so long as the optics and breadboard are manufactured to within the alignment error budget. As a result of this approach I do not need to use cryogenic motors to provide fine position adjustments to the optics. This significantly reduces the cost and complexity of the optomechanical design making it quicker to develop and less prone to failure when deployed at the observatory.

As in chapter 4 I will discuss the optomechanics of each optic in order of the optics position along the beam train, followed by a discussion on the design of the cryostat itself.

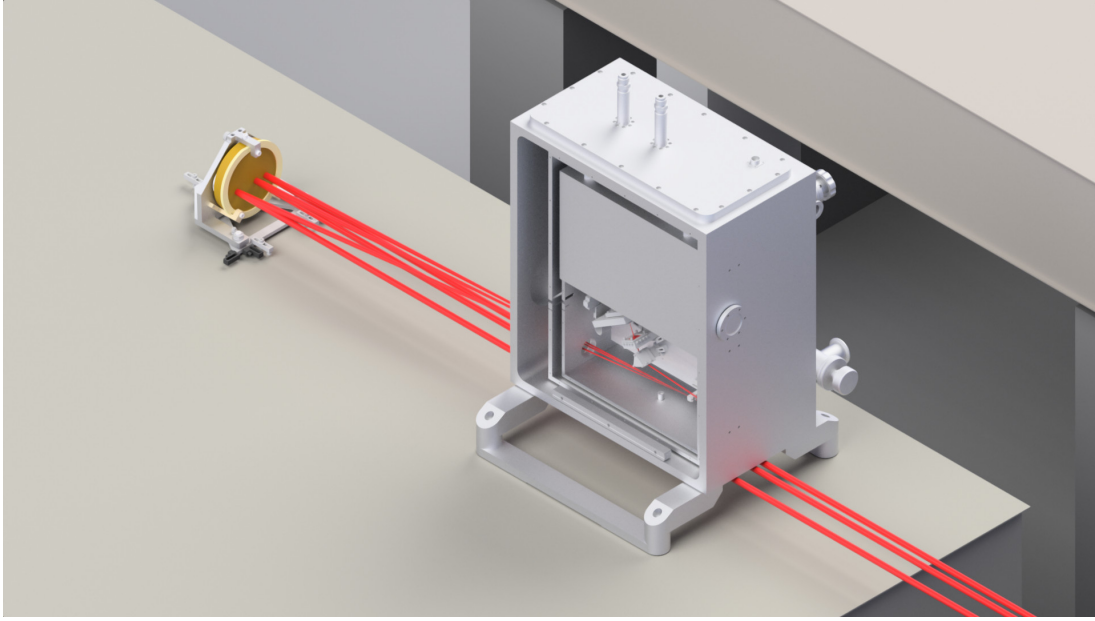As mentioned in the declaration the design of the optomechanical mounts of FOURIER was

**Figure 6.1:** A 3D render of the FOURIER instrument in the I-BCA at the MROI. The three beams of starlight are shown initially travelling from right to left towards M1 where they are reflected into the cryostat towards the cryogenic optics. Reproduced from Mortimer et al. (2020).

carried out by Xaiowei Sun based on my alignment requirements. The Cryostat was designed by Universal Cryogenics based on my design requirements.

## 6.2 System overview

Before discussing the optomechanics of each optic it is informative to look at an overview of where the optics are mounted. Figure 6.1 shows a 3D render of the FOURIER instrument in the Inner-Beam Combining Area (I-BCA) at the MROI. The beams travel initially right to left, passing underneath the cryostat and towards M1. They are then reflected up, through the cryostat window and into the cold optics before being recorded on the SAPHIRA detector. This render shows the cryostat with the door and the lids of the radiation shields removed so the path of the beams within the cryostat are visible.

Figure 6.2 shows a 3D closeup of the optics within the cryostat. The window is mounted into the outer wall of the cryostat itself, whereas the cryogenic optics and the SAPHIRA detector are mounted to the vertical and horizontal cold plates. The horizontal cold plate is attached to the underside of the liquid nitrogen tank and so is expected to reach the coldest temperatures. The vertical cold plate is attached to the horizontal cold plate and is the plate the optics are
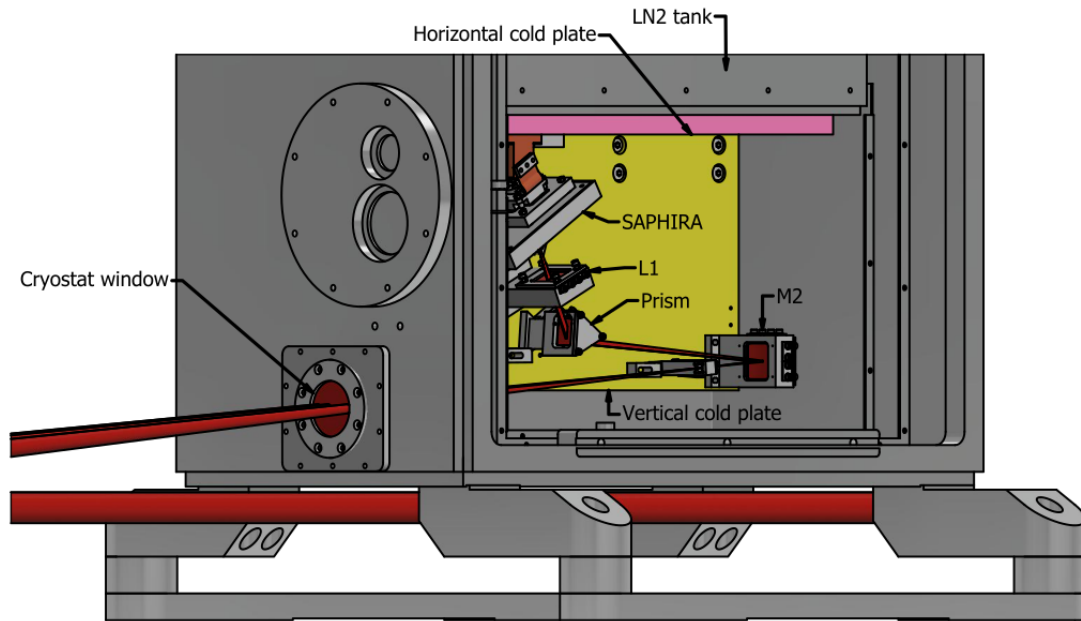
**Figure 6.2:** The optics of FOURIER (minus M1) as mounted in the cryostat, which is shown here with the door and radiation shield lids removed.

attached to.

## 6.3   M1 mount

As mentioned in the introduction, the optics within the cryostat are designed to not require adjustments after cooldown as they are inaccessible. This presents a problem as the focal plane of M1 and the spatial filter must be aligned to a tight tolerance (table 5.2) to maximise throughput as the spatial filter is set to be just wide enough to pass the PSF. In addition to this, the spatial filter will move on cooldown as the cold plate it is attached to contracts. A simpler solution than adjusting the location of the spatial filter after cooldown to the focal plane of M1 is to adjust the focal plane of M1 to that of the spatial filter. As M1 is kept at room temperature and can be adjusted manually after instrument cooldown. This is achieved by three spring loaded adjustment screws, which make contact with the back of the M1 mirror, shown in figure 6.3, counteracted by three spring loaded contact points on the front side of the mirror, which rest on a flat plate in contact with M1. These three adjustment screws allow for both piston and tip-tilt to be adjusted to realign the focal plane of M1 with the spatial filter after instrument cooldown.
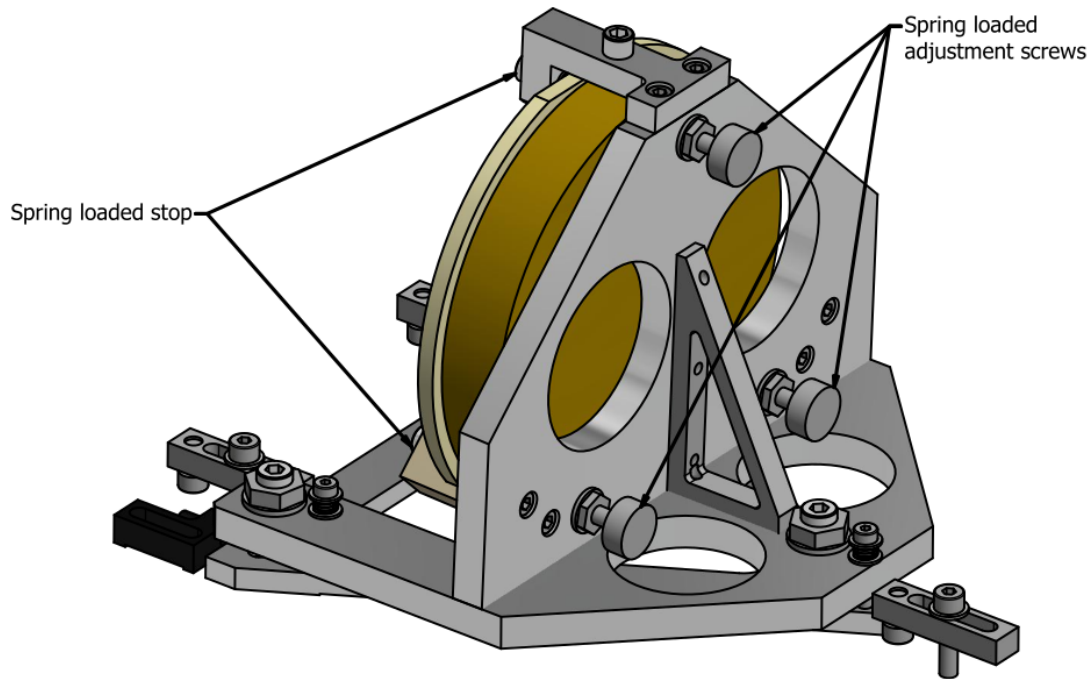
**Figure 6.3:** A back view of the M1 mount. The three spring loaded manual adjustment screws are visible which provide both piston and tip-tilt adjustment.

As discussed in section 4.4 M1 is used as an off-axis spherical mirror, meaning it has been tilted and decentered along the parent sphere. This requires a 2.031° tilt, which is built into the mount, as shown in figure 6.4. The correct tilt of M1 is achieved when the mirror is parallel to the vertical support plate of the mount.

An image of the M1 mirror in its mount during the warm laboratory tests in Cambridge is shown in figure 6.5, in which the three spring loaded contact points can be seen along the rim of the plate, resting on the front surface of the mirror.

## 6.4   Spatial filter

Spatial filtering is carried out in FOURIER via a pinhole spatial filter system. As discussed in section 4.6 spatial filtering is only done physically along the spectral axis and is done in software along the perpendicular, interference fringe axis (applying a digital filter on the SAPHIRA detector readouts by simply setting the pixel values to zero).

In practice this means the spatial filter is a slit rather than a pinhole aperture as shown in figure 6.6. The spatial filter consists of a hole with two knife edge plates forming the slit. The
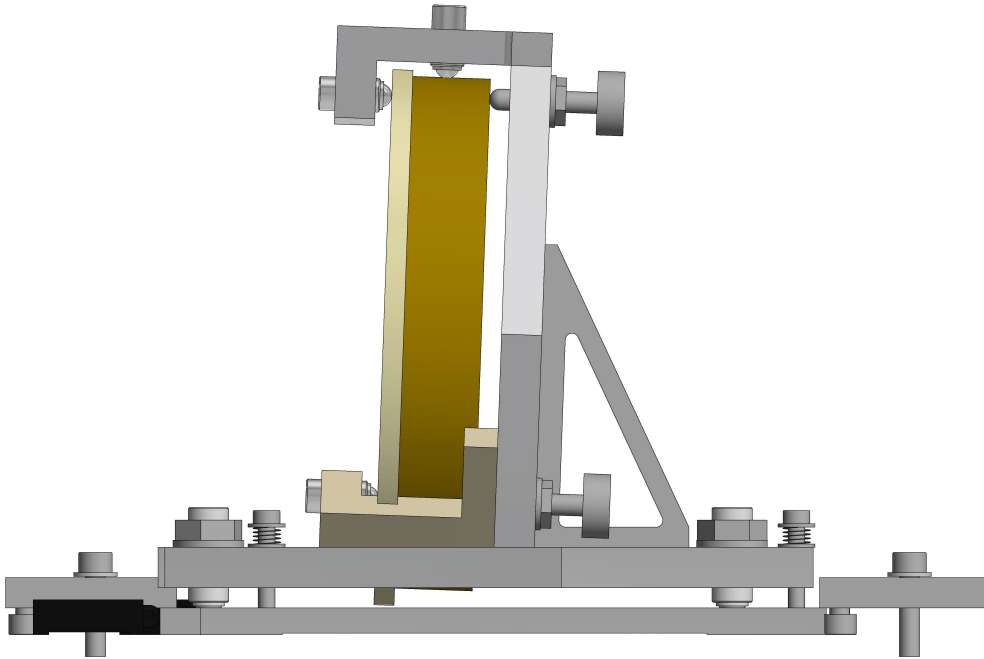
**Figure 6.4:** A side view of the M1 mount. The 2.031° tilt of the vertical supporting plate to aid in tilting the M1 mirror is visible here.

separation of these holes can be adjusted manually via the labelled adjustment screws, allowing the effective filter size to be best matched, for example, to the wavelength of observation if only one of the J, H or K bands is of interest. A future upgrade to the spatial filter could be to install a motorised slit, which can be adjusted during observations as with the current configuration the slit can only be adjusted when the instrument is undergoing warm alignment.

## 6.5   M2 mount

The mount for M2 (left figure 6.7) is simple in design as it does not incorporate any form of manual or motorised adjustment of the position/pointing of the M2 optic, to do this the whole mount assembly is moved.

The mount is designed to cope with the differential rate of expansion of the fused silica substrate of M2 and the aluminium that the mount itself is made of. The CTE of fused silica is approximately $0.48 \times 10^{-6}$/°C over the temperature range -100°C to 30°C, as established in section 5.3 the CTE of aluminium is $18.9 \times 10^{-6}$/°C over the cryogenic temperature range. As the system cools, the aluminium mount will shrink much more rapidly than the M2 optic itself,
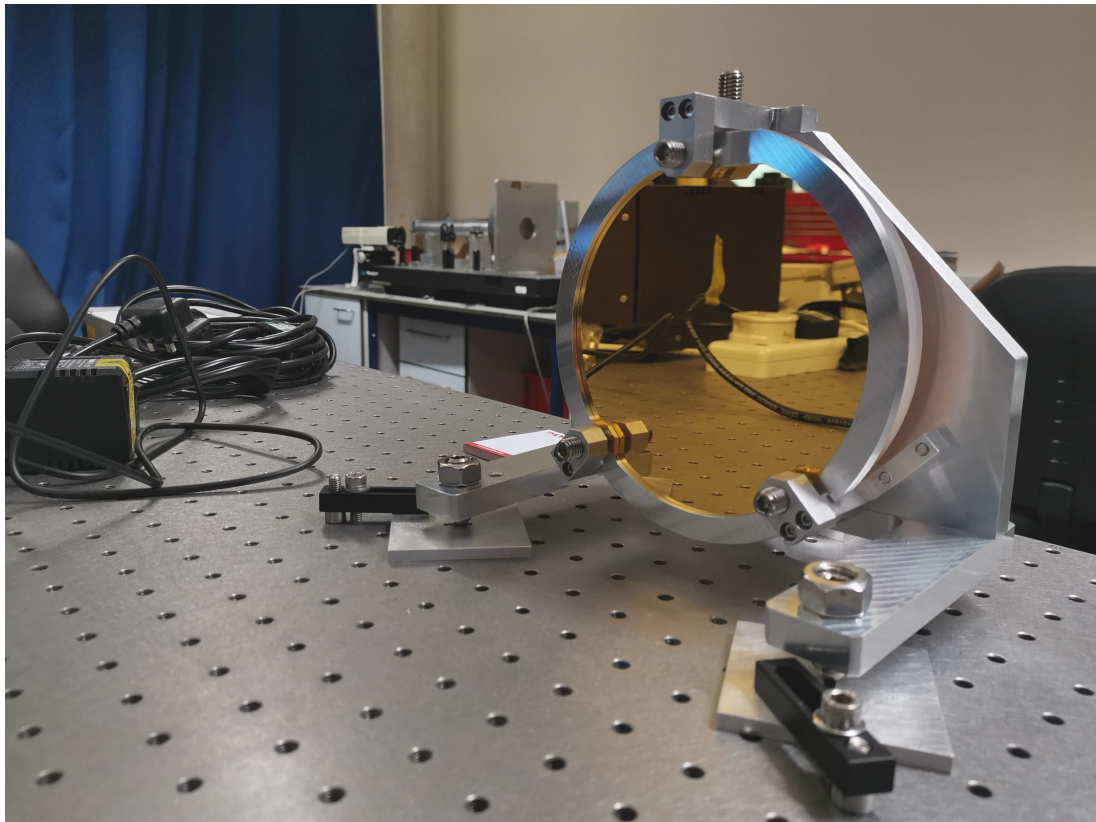
**Figure 6.5:** A front view of the M1 mirror mount taken during warm laboratory tests. The three fixed spring loaded contact points which counteract the spring loaded adjustment screws are visible along the perimeter of the front contact plate.
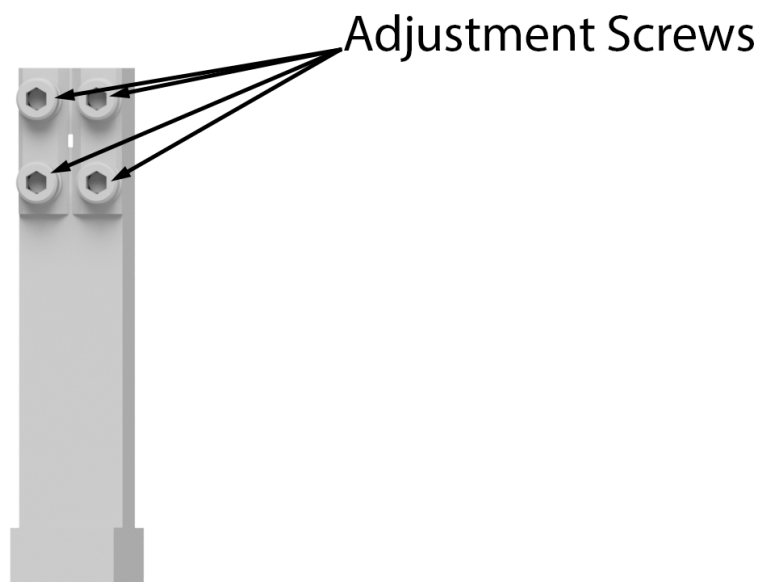


**Figure 6.6:** The spatial filter assembly. Two knife edge plates create a slit performing spatial filtering along the spectral axis. The adjustment screws can be used to manually adjust the width of the slit.
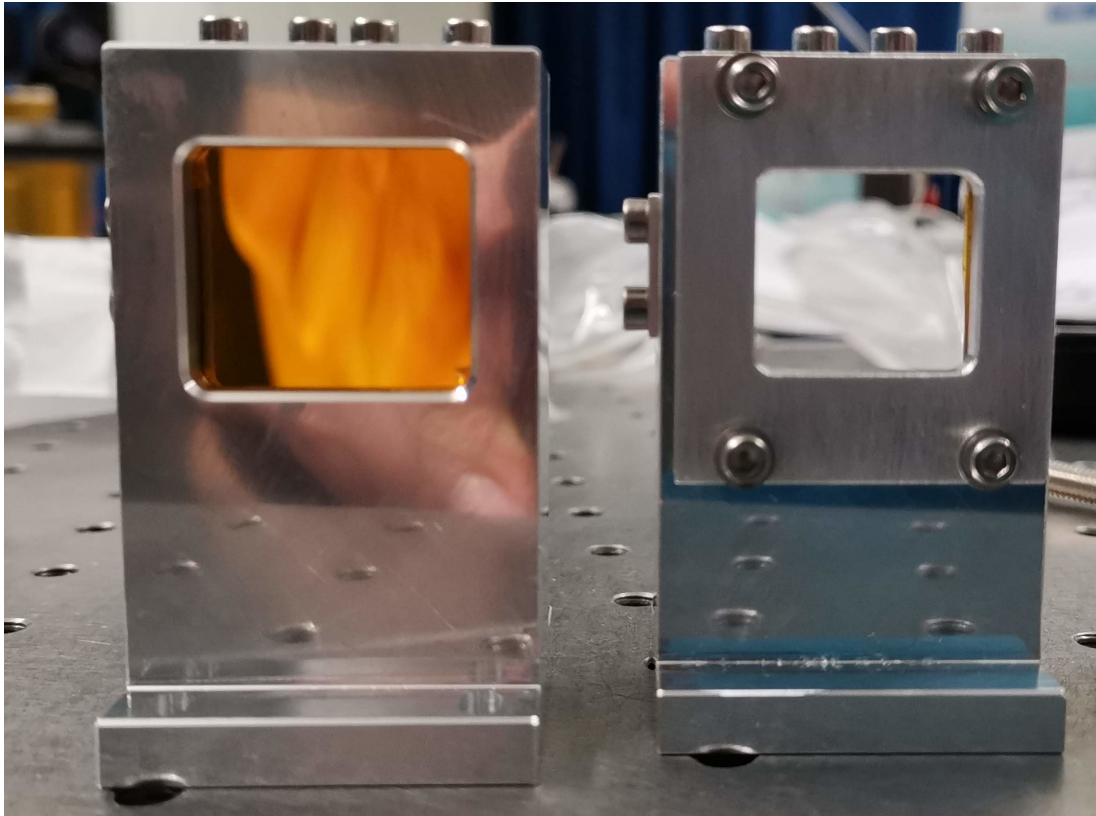
**Figure 6.7:** The M2 (left) and L1 (right) optics in their mounts during laboratory tests in Cambridge.

potentially placing pressure on the optic and cracking it. To overcome this problem a series of spring loaded contacts are placed on two sides and the back of the optic, with Teflon contacts on opposite sides. With this the springs can compress and the spacing between the optic and the mount can vary to avoid damaging the optic. These contact points are displayed in figure 6.8, which shows the optic and mount with the outer casing removed for clarity.

As discussed in section 5.3 the effects of thermal misalignment on cooldown can be counteracted by moving M2 190 μm closer to the SAPHIRA detector along M2's optical axis after the warm alignment of the system has been achieved. To enable this the four mounting holes for M2 are small tracks 5.6 mm long, which run parallel to the optical axis of M2 as shown in figure 6.9.
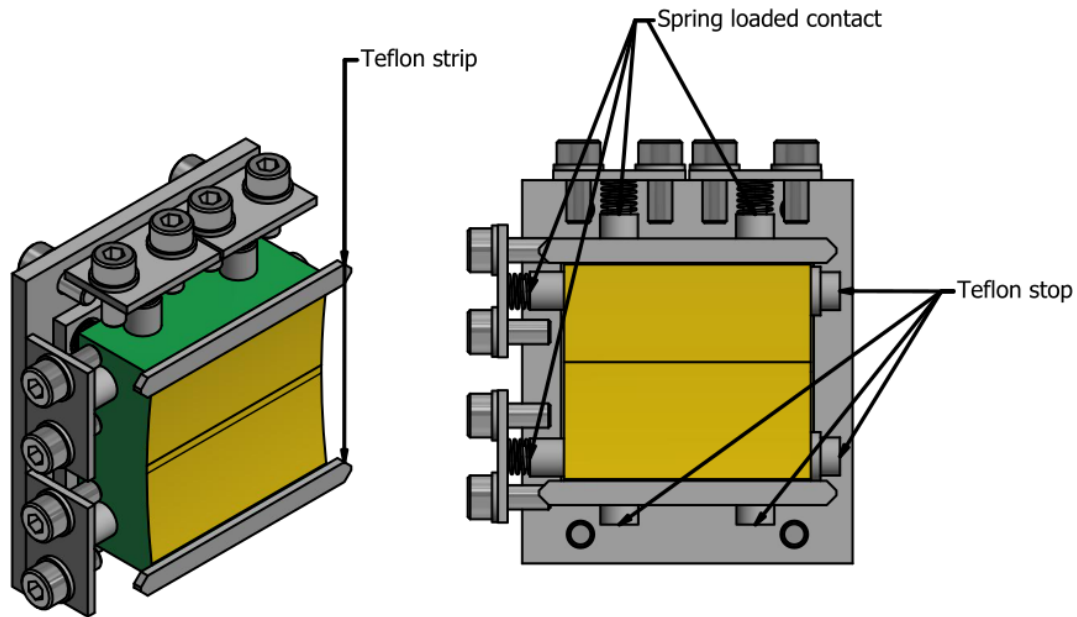
**Figure 6.8:** A view of the M2 optic mount with the outer casing removed, showing the spring loaded and Teflon contact points, designed to allow spacings to vary with the differential rate of expansion/contraction of the optic and mount without risking cracking the optic.
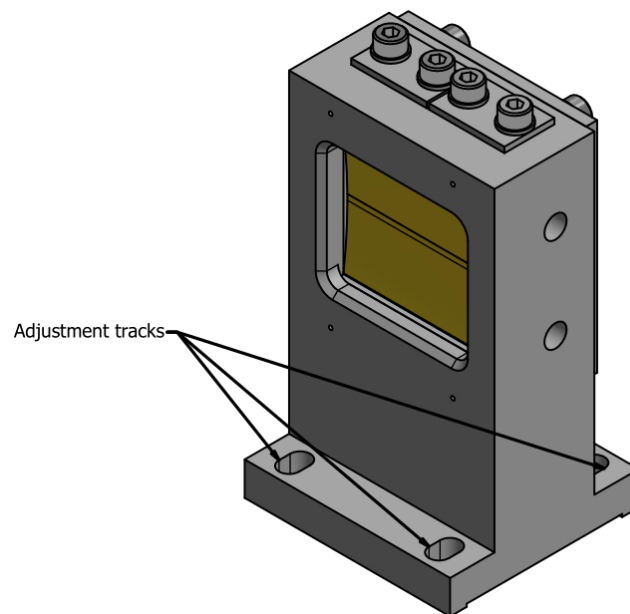


**Figure 6.9:** The M2 optic in its mount with the location of three of the four adjustment tracks highlighted. This allows for the 190 μm adjustment along the optical axis of M2 required between warm and cold alignment discussed in section 5.3.
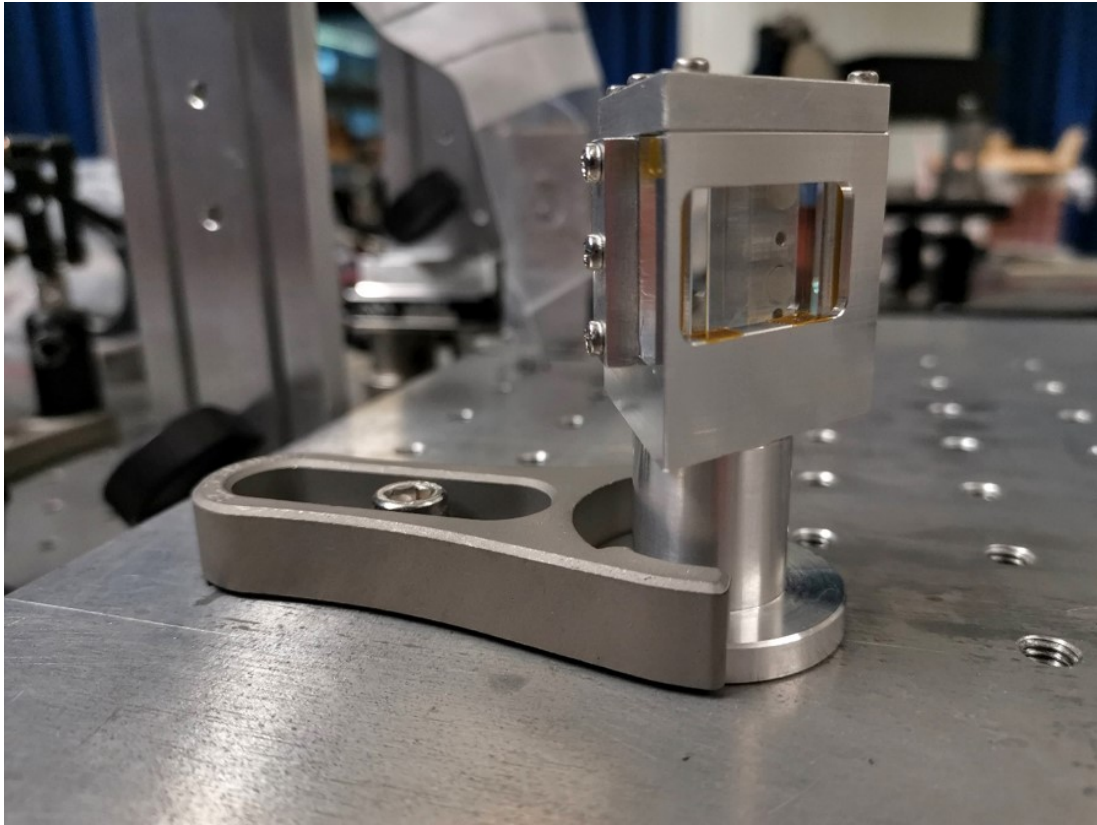
**Figure 6.10:** The prism and its mount during laboratory tests in Cambridge.

## 6.6   Prism mount

The prism mounting assembly in the laboratory is shown in figure 6.10. The mounting for the prism follows the same spring loaded contact points principle as M2. A grid of four spring loaded contact points are placed along the face of the prism the light does not pass through, with two Teflon contact points at the apex of the opposite side. The sides of the prism are supported by three spring loaded contacts and a large Teflon disk on the opposite side. A 3D model of the prism optic in its mount with parts removed to show the spring loaded and Teflon contact points is shown in figure 6.11.

## 6.7   L1 mount

The mount for L1 (right of figure 6.7) has the same spring loaded compensation design as the M2 optic. Two sides have spring loaded contacts and the two opposite sides, Teflon stoppers as shown in figure 6.12. The difference between this mount and M2's mount is that the back of
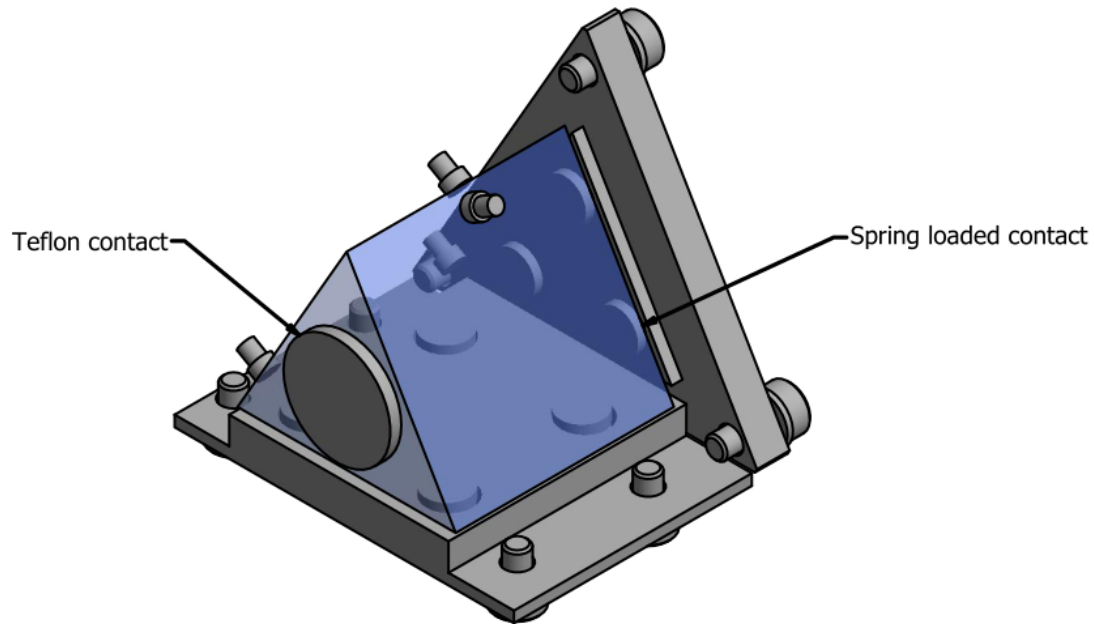
**Figure 6.11:** The prism mount with the outer casing removed. The prism is supported on two sides with four and three spring loaded contact points and fixed Teflon contacts on opposite sides to compensate for the differential rate of expansion of the glass and the aluminium mount.

the L1 optic cannot be obstructed as it is a transmissive optic. To ensure a clear aperture on the back surface Teflon strips are in contact with a spring loaded back-plate, which has a sufficient clear aperture to pass the starlight through L1 as shown in figure 6.13.

## 6.8   Cold stop

The optomechanical design of the cold stop is still under consideration. As discussed in section 4.9 the stops will likely be made from two separate thin sheets of metal (one at the location of the fringe and spectral cold stops respectively) with holes cut in them for each stop required. These sheets will be mounted to the vertical cold plate within the cryostat.

## 6.9   SAPHIRA detector mount

The SAPHIRA detector assembly is more complex than for the fixed optics mounted to the cold plate. It is typically operated at around 85K (Goebel et al. 2018), given the temperature of Liquid Nitrogen (LN2) is 77K, this means the cooling of the detector must be as efficient
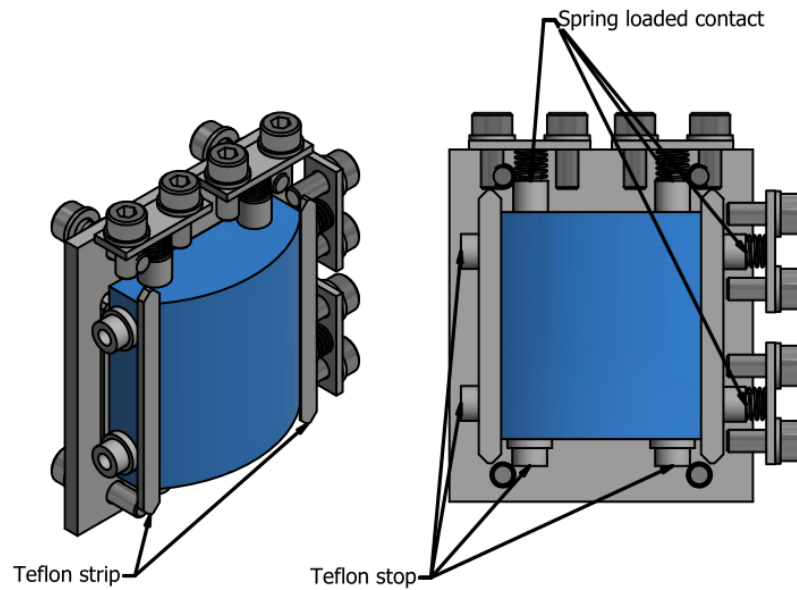
**Figure 6.12:** The L1 mount and optic with the outer casing removed, showing the spring loaded and Teflon contact points on the sides of the optic.
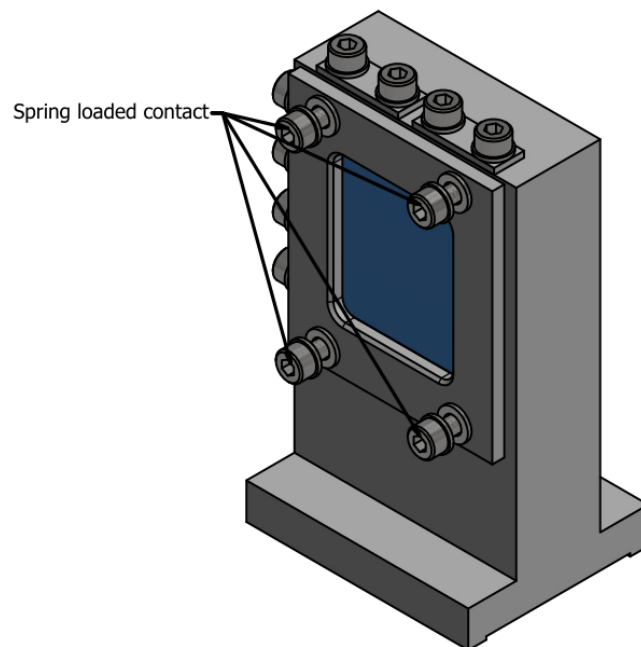


**Figure 6.13:** The rear surface of the L1 mount showing the spring loaded backplate, which compensates for the differential rate of expansion/contraction of the $CaF_2$ lens and the aluminium mount, while maintaining a clear aperture on both sides of the transmissive optic.
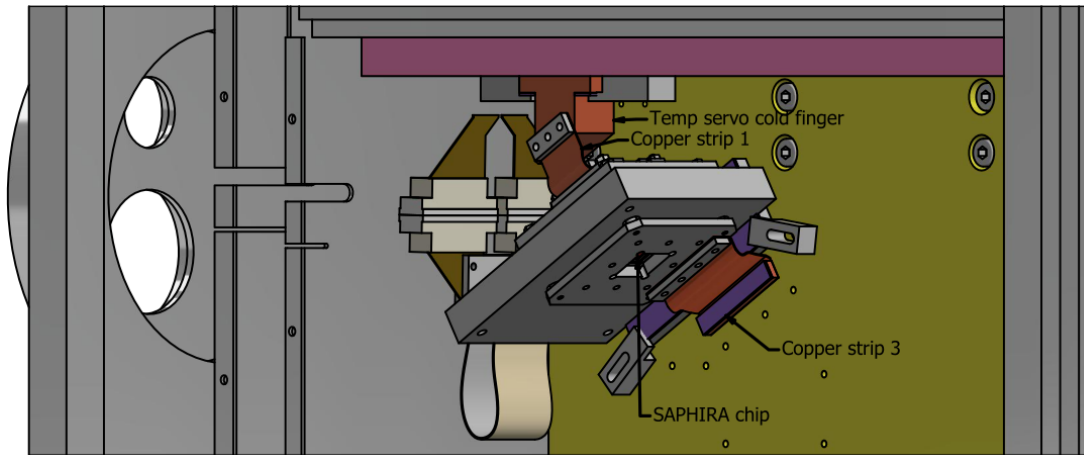
**Figure 6.14:** A 3D view of the SAPHIRA detector mounted within the cryostat. The cryogenic optics have been removed for clarity. The large copper cold finger is attached to the underside of the LN2 tank via a hole in the horizontal cold plate. The other end of the cold finger is attached to copper strip 1 shown in figure 6.15. In addition to this, copper strip 3 is shown connected to the vertical cold plate to provide cooling to the front plate of the detector housing.

as possible. For this reason a large copper cold finger (shown in figure 6.14) is attached to the underside of the LN2 tank via a hole in the horizontal cold plate.

The cold finger is attached to copper strip 1 of figure 6.15, which is in turn connected to copper strip 2, cooling the detector cold finger. The detector cold finger is spring loaded to ensure it does not apply too much pressure which could damage the detector as the system expands/contracts on warming/cooling.

The cold finger mounted to the underside of the LN2 tank will have both a temperature sensor and heater placed on it, which will be used as a servo loop to maintain a constant temperature of the cold finger to regulate the detector temperature. As this servo loop acts by heating the cold finger this necessitates that the cold finger must reach a temperature below 85K when not being heated. This is a further reason that the cold finger must be cooled to as close to the 77K LN2 temperatures as possible.

The front plate of the SAPHIRA detector housing is connected via copper strip 3 in figure 6.14 to the vertical cold plate to cool it, with the goal of minimising the number of thermal photons emitted directly in front of the SAPHIRA detector.
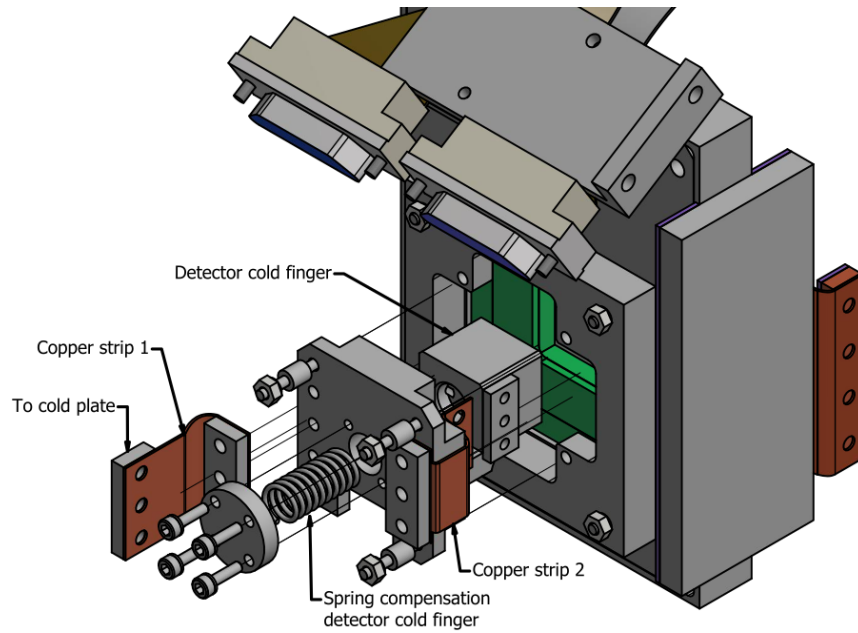
**Figure 6.15:** An exploded view of the rear surface of the SAPHIRA detector mounting. Copper strip 1 is connected to a cold finger (not shown) which connects with the underside of the LN2 tank. This thermal connection is transferred to the spring loaded detector cold finger which makes contact with the detector. This model has been rotated 180° around the axis the components are exploded along compared to figure 6.14 for clarity.

## 6.10  Cryostat

The cryostat was designed and manufactured by Universal Cryogenics in the USA to specifications I provided. It is 0.7×0.5×0.3 m in size and weighs ~130 kg. The interior is designed to provide a vacuum of $10^{-4}$ millibar (with a goal of $10^{-5}$ millibar), which must be maintained for a minimum hold time of 30 hours without any additional vacuum pumping after the initial evacuation, when the external pressure is 1 atmosphere. Tests performed by Universal Cryogenics demonstrated a vacuum level of $2 \times 10^{-4}$ millibar after pumping down the cryostat overnight.

Inside the evacuated area is a large assembly which is suspended from the top of the cryostat. At the top of this assembly is an 11 litre LN2 tank which is filled manually via a port on the top of the cryostat. Enclosing the tank and space beneath it is the first radiation shield which shields the tank and the cold space from the room temperature outer walls of the cryostat. Beneath the LN2 tank is a volume enclosed by another radiation shield. This second shield, enclosed by the first, is attached directly to the LN2 tank. This shield then encloses the cold space envelope, the volume where the cryogenic optics and SAPHIRA detector are contained. As discussed previously, the optics and detector are connected to a horizontal and vertical cold plate, with the
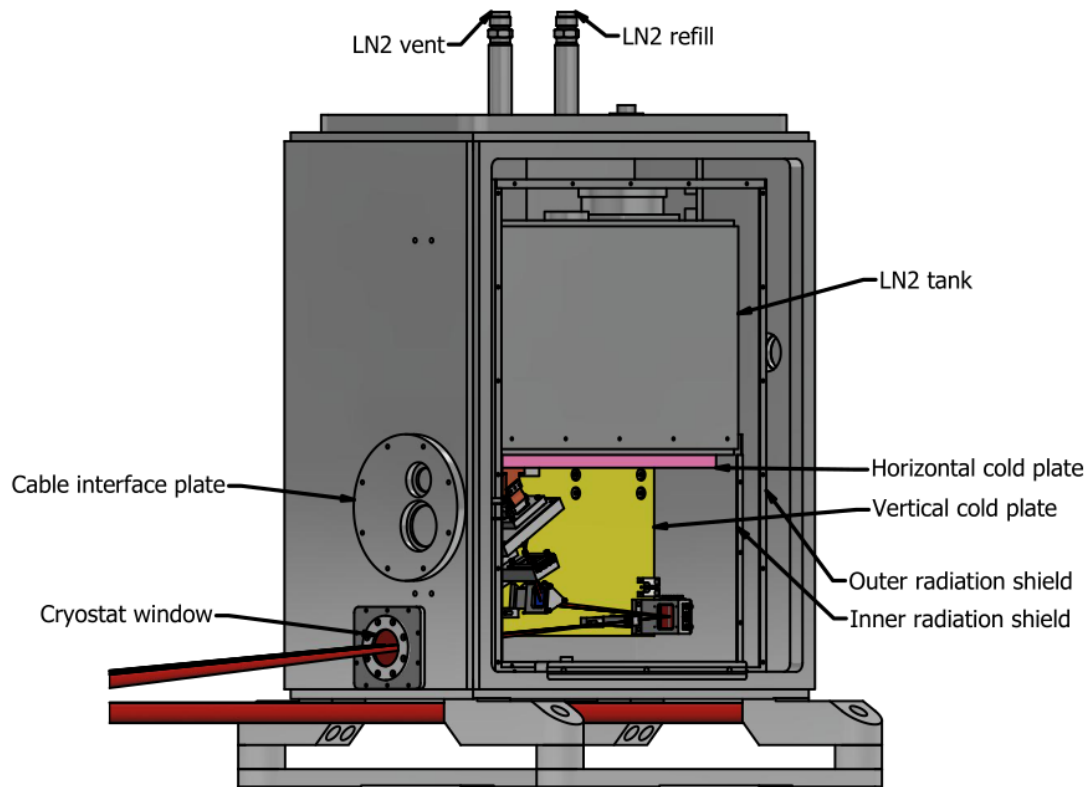
**Figure 6.16:** An annotated 3D view of the cryostat with labels highlighting features discussed in the text.

horizontal cold plate being connected directly to the underside of the LN2 tank. These features are labelled in figure 6.16

The cryostat is designed to be entirely passive such that during observations it is not connected to any systems such as a continuous vacuum pump or LN2 refilling mechanism. This is both to reduce complexity of the system and remove the risk of vibrations which could in turn reduce the visibility of the interference fringes.

## 6.11   Cabling

As the optical mounts do not have any motorised components the number of systems which require cabling are minimal. These are the connections to the SAPHIRA detector itself and temperature sensors/heaters within the cryostat.

For the SAPHIRA detector cabling I follow a design provided by the European Southern Observatory (ESO) (Accardo et al. 2013). In this design, all cabling related to controlling

and reading out the SAPHIRA detector is managed by a 130 mm long flex cable connected to the SAPHIRA detector pre-amp board. This splits into two arms, both of which terminate in individual 72 pin Micro-D connectors. These are then connected to two 450 mm flex cables which combine to terminate in a 128 pin HiRel 74000Y-25E-35PN-565N/R connector, enabling the interface from within the cryostat to the external world. During operations a HiRel 59000S-25-35PN connector is connected to the external wall of the cryostat and the warm cable bundle leading from the cryostat terminates in five separate connectors which plug into a ESO New General Controller (NGC), from which the detector can be controlled.

The pre-amp board also contains a silicon diode Lake Shore DT-670-CU temperature sensor which is monitored, the output of which is routed separately to the detector control/read cables though a 9 pin Micro D connector. This is in addition to the temperature sensor placed on the copper cold finger, which is used with a heater to regulate the temperature of the cold finger.

Finally, there are an additional two temperature sensors and one heater placed on the cold plates themselves. The temperature sensors are used for passive monitoring of the cryostat environment. The heater is placed on a cold plate and used for bringing the cryostat back up to room temperature while still under vacuum to ensure condensation does not form on the optics or detector when the vacuum is released and air is pumped in.

## 6.12 Summary

In this chapter I have presented an overview of the optomechanical mounts used by the FOURIER beam combiner. By designing an instrument with loose alignment tolerances the optomechanics can be simplified, requiring no moving parts within the cryostat. This reduces the cost, lead time and technical risk of the optomechanical design.

# WARM LABORATORY TESTS

## 7.1 Introduction

To verify the optical performance of the instrument I undertook a series of "warm", room temperature laboratory tests. These were particularly relevant because of the delay in delivery of the cryostat by a year due to the on-going COVID-19 pandemic.

These warm tests used the optics and optomechanics that will be deployed in the final instrument. The only difference from the final instrument was that the N-SF11 prism was uncoated due to constraints again imposed by the pandemic.

As mentioned in the declaration, the design of the light source was based on a system developed by James Luis however all work presented in section 7.2 are modifications I made myself. The Fourier Transform Spectroscopy (FTS) code for recovering spectra from the interferograms (section 7.6) was provided by James Luis. Parameter turning and analysis of the spectra was carried out by myself.

## 7.2   Laboratory setup

### 7.2.1   Overview

Before discussing the various subsystems used for the laboratory tests, it is useful to give a broad overview of the path the light takes through the setup overall. The light source designed and used for these warm laboratory tests is three sources in one. The first is a white light source generated by a Maglite filament bulb focused onto a pinhole to simulate an unresolved star, the second is a $\lambda = 633$ nm laser used for alignment purposes and the third is a $\lambda = 1.31\,\mu$m near-infrared laser (Thorlabs S3FC1310) fed by a single mode fibre (Thorlabs P1-SMF28E-FC-1). A top-down view of the path of the white light source showing only the optics it interacts with is given in figure 7.1. Here the light diverges from the pinhole (bottom left) before being collimated by the first mirror (bottom right), it is then reflected back and through an aperture stop, redirected by a 90:10 beam splitter to a pair of turning mirrors which then reflect it onto the Beam Splitter (BS) breadboard. Here the white light source is split into two beams as shown by the green and orange lines, which are reflected onto a two stage periscope subsystem. The first stage displaces the beams into the plane of the page and the second stage turns the beams so they point towards M1 and are vertically stacked. From here the beams propagate through the Free-space Optical multi-apertUre combineR for IntERferometry (FOURIER) instrument in the order discussed in section 4.2.

This beam path is superimposed on an image of the laboratory setup shown in figure 7.2 where the blue, green and orange beams represent the same beams as in figure 7.1. In addition to the path of the white light source, the path of the visible alignment laser and near-infrared laser are also shown in red and yellow respectively, up to the point they enter the 90:10 beam splitter as from there they follow the same path as the white light source.

It is worth noting that the laboratory setup used here has rotated the FOURIER optics by 90°, such that they are parallel to the horizontal optical table rather than vertical as they will be within the FOURIER cryostat as shown in figure 6.2.

### 7.2.2   Light source

In this section I discuss the design of the light source, in particular the white light source for which a considerable amount of time was devoted to designing a diffraction limited, achromatic
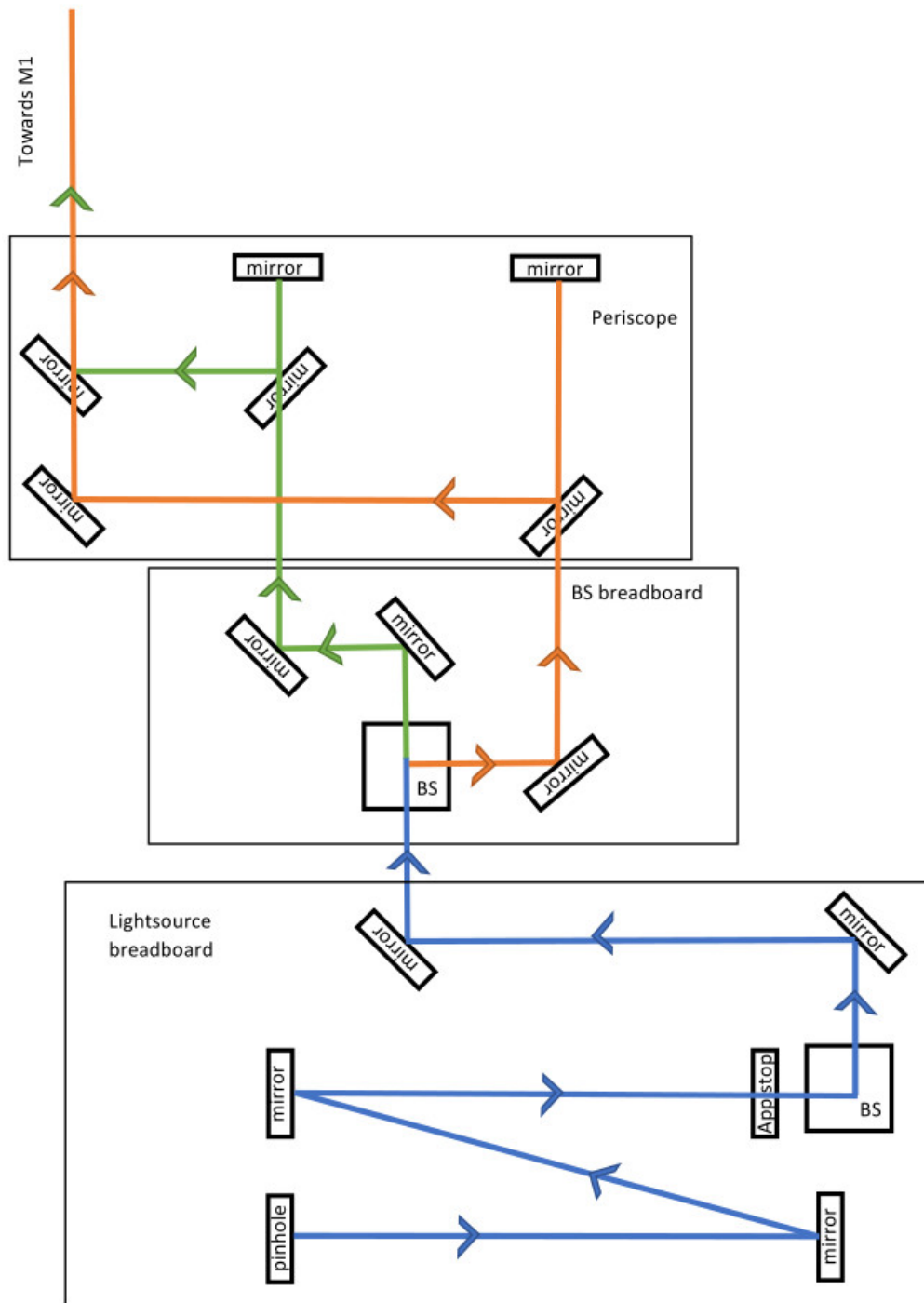
**Figure 7.1:** A top-down diagram of the path of the white light source through the warm laboratory setup towards the first optic of FOURIER, M1. The source is shown in blue until it is split into two beams by a beam splitter and is then represented by the green and orange beams. A description of the beam path is given in the text.
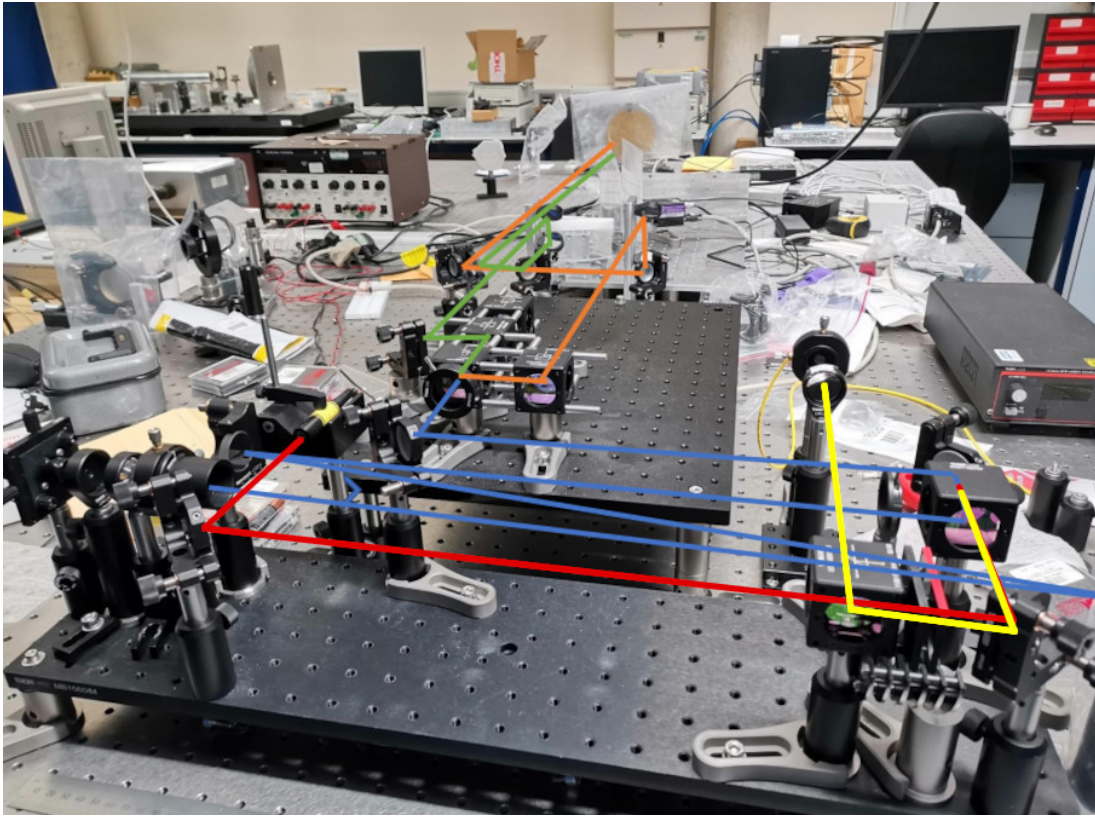
**Figure 7.2:** The path of the three light sources towards FOURIER in the configuration used during the warm laboratory tests. the white light source is shown in blue until it splits into two beams represented by the green and orange beams as shown in figure 7.1. The visible laser and near-infrared laser are shown in red and yellow, respectively, up to the point they combine at the 90:10 beam splitter with the white light at which point only the white light beam is drawn as all three sources follow the same path. M1 can be seen at the far end of the table where the beams terminate in this image.

and stable point source as these factors were crucial in minimising the light source's impact on the Point Spread Function (PSF) shaping, spectral resolution and throughput tests, respectively.

The goal of making the system achromatic was achieved by using a reflective optic as the collimator such that there was no axial shift in the focal point as a function of wavelength across the wide range of wavelengths under test ($\lambda = 1.1\text{-}1.8\,\mu\text{m}$), so the light would be equally well collimated at all wavelengths. The issue with a reflective optic is that the light is reflected back to the point source, this is typically overcome by using an Off-Axis Parabola (OAP), which is an off-axis section of a larger parent parabola. When the light source is then placed at the focal point of an OAP, the collimated beam is produced at an angle to the light source and so avoids the problem of the light reflecting back on itself.

One issue with OAPs, however, is the difficulty in aligning them due to both their non-
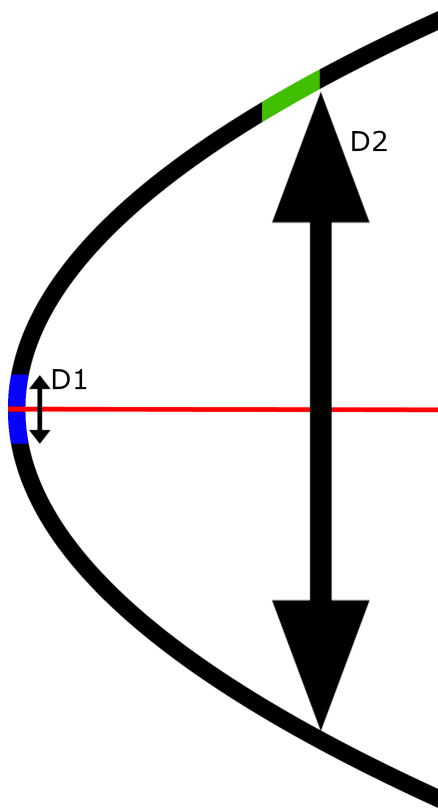
**Figure 7.3:** A parabolic curve representing a parent parabola from which the location of two smaller parabolas are highlighted. The blue section of the curve represents an on-axis parabola, where the diameter of the parent parabola (D1) is that of the on-axis parabola. The green section represents an OAP where the diameter of the parent parabola required to manufacture it (D2) is much larger making the effective f ratio of the system much smaller/faster and thus it harder to align.

rotational symmetry and the typically fast f ratio of the parent parabola that the OAP is cut from. In fact the f ratio of the parent parabola decreases the higher the off-axis angle of the OAP. Figure 7.3 demonstrates this, the black line represents the parent parabola and the red horizontal line its optical axis. The blue portion of the parabola represents an on-axis parabolic mirror, here the diameter of the parent parabola (D1) the on-axis parabola is cut from is equal to its diameter. The green portion of the parabola, however, represents a 90° OAP with the same clear aperture as the on-axis parabola. Here, in order to manufacture the OAP the parent parabola must be much larger in diameter (D2) and so for a given focal length the OAP will have a much faster effective f ratio (f#=f/D where f is the focal length of the optic and D the diameter) and faster f ratio systems are typically much more difficult to align. Therefore parabolas with larger off-axis angles will result in harder to align systems.

An alternative approach to an OAP is to use a spherical mirror tilted at an angle. This will

introduce astigmatism into the beam (whereas an OAP theoretically introduces no aberrations) but this can be reduced to a tolerable level by minimising the angle the mirror is tilted at with respect to the light source. This can be achieved by both reducing the transverse displacement of the collimated beam required for it to not land back on the light source, and by using a longer focal length mirror (the collimation mirror is placed one focal length away from the pinhole). The off-axis angle is then simply given by $\theta = s/r$ where $s$ is the transverse distance and $r$ the distance from the pinhole to the collimating mirror. I reduced the transverse distance to 1" by installing the mirror after the collimating optic in a clear-edge mount and placing it as close to the pinhole as possible. As a longer focal length was desired I selected the Thorlabs CM254-500-P01, a 1" spherical mirror with a 500 mm focal length. So for a 25.4 mm transverse distance over 500 mm the mirror had to be tilted to a 1.5° Angle of Incidence (AoI). With such a small AoI the system was shown to still be diffraction limited, figure 7.4 shows the spot diagram in the H band at the focal plane of M1, using the Thorlabs CM254-500-P01 mirror at a 1.5° AoI to collimate the light source M1 is fed with.

To highlight the advantage of a long focal length spherical mirror compared to an OAP mirror I carried out tolerance testing on the collimation optic itself considering displacements, tilts and rotations along all three axes. The criterion for acceptable alignment error was taken to be when the geometric RMS spot size was just smaller than the diffraction limited spot size or better for 98% of the Monte Carlo runs (see section 5.2 for a discussion on Zemax system tolerancing). The resulting tolerance error budget for the alignment of the 1" spherical mirror with a 500 mm focal length and a 45° OAP with a 86.614 mm parent focal length (Thorlabs MPD124-M01) are given in table 7.1. The analysis shows that the spherical mirror has significantly looser alignment tolerances. The tolerances of the spherical mirror are relaxed enough that alignment can be achieved with no special alignment tools and only a ruler.

The bulb used in the light source was powered by a bench-top DC power supply. Due to the age and unknown precision of the supply I opted to use a voltage regulator to regulate the current and stabilise the power supply, in turn stabilising the intensity of the light source. This was crucial for the throughput measurements, where the light source was assumed to be of constant intensity. To achieve this, I used a LM317T linear voltage regulator in the circuit shown in figure 7.5. The bulb was capable of operating at a current of 360 mA before overheating and failing. In the circuit configuration used, the current delivered to the bulb is given by
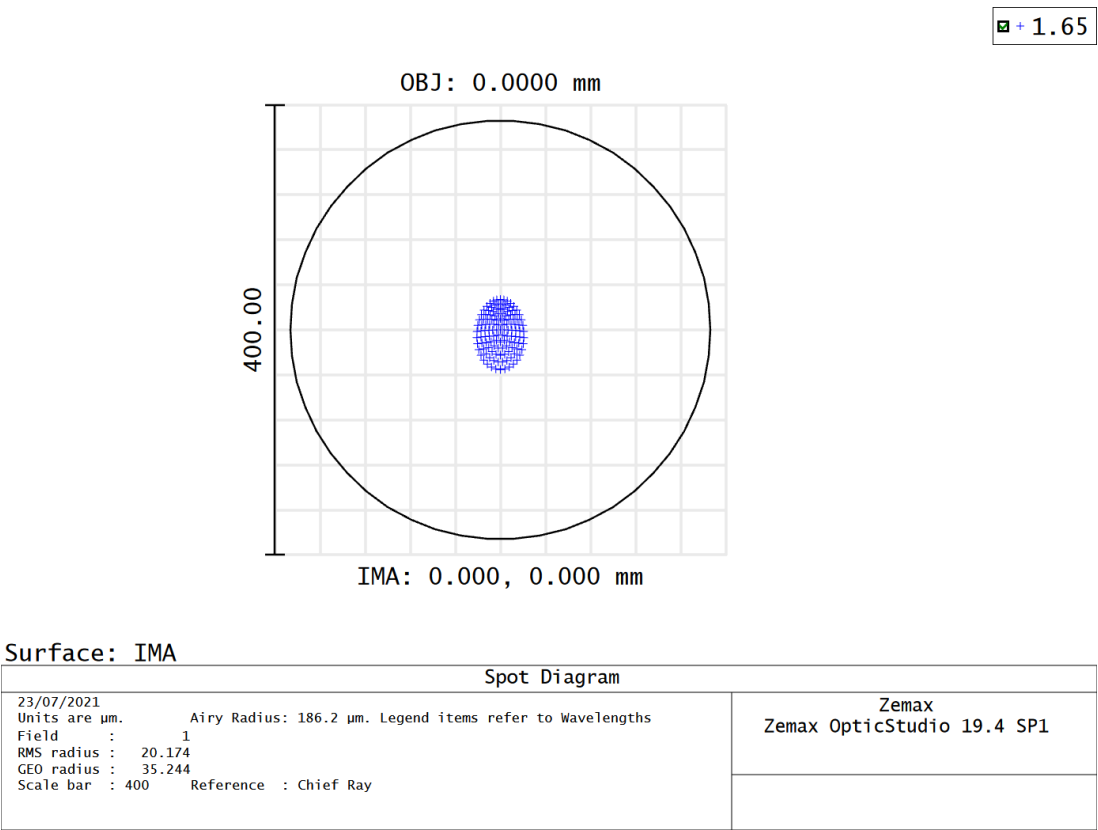
**Figure 7.4:** A geometric spot diagram at the focal plane of M1 for the simulated lab light source where a Thorlabs CM254-500-P01 500 mm focal length spherical mirror is used as the collimating optic at an AoI of 1.5°. The diffraction limited Airy disk for the H band is shown by the black ring.

$I_{\text{out}} = V_{\text{ref}}/R_1$ where $V_{\text{ref}}$ is a characteristic of the LM317T voltage regulator and is given to be 1.25±0.05 V by the data sheet. Hence a 3.57 Ω resistor gives a output current of 350 mA, maximising the intensity of the bulb while ensuring it does not overheat.

I quantified the improvement in stability this regulator provided by measuring a series of frames with and without the regulator and calculating the standard deviation of the intensity recorded on a detector for a given pixel. This data was taken at the FOURIER focal plane and so the light was spectrally dispersed. The stability of the light source was then examined as a function of wavelength by taking a 1D slice along the spectral axis, as shown in figure 7.6. At this point the spectral axis was not wavelength calibrated so it is presented as a function of pixels not wavelength.

Around 600 frames were taken with an exposure time of 20 ms and an image recorded every 100 ms. This setup provided frames with short enough exposures to detect any fast variations in the intensity while measuring for a long enough time period overall to capture any
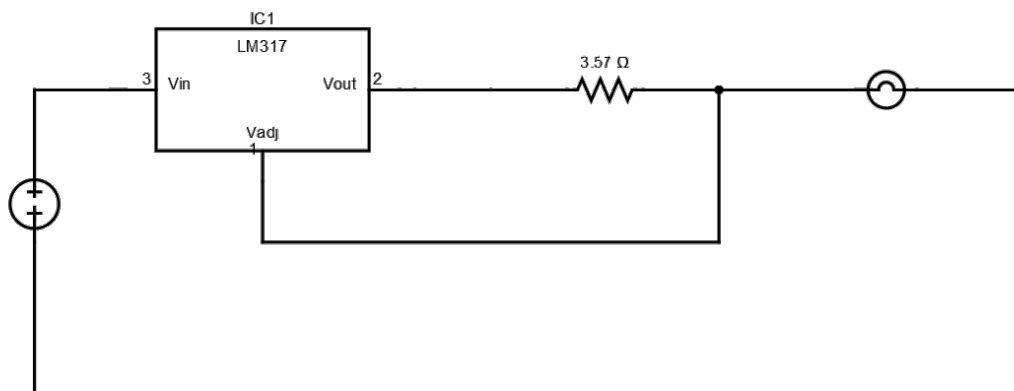
**Figure 7.5:** The LM317T linear voltage regulator circuit used to stabilise the bench-top DC power supply.
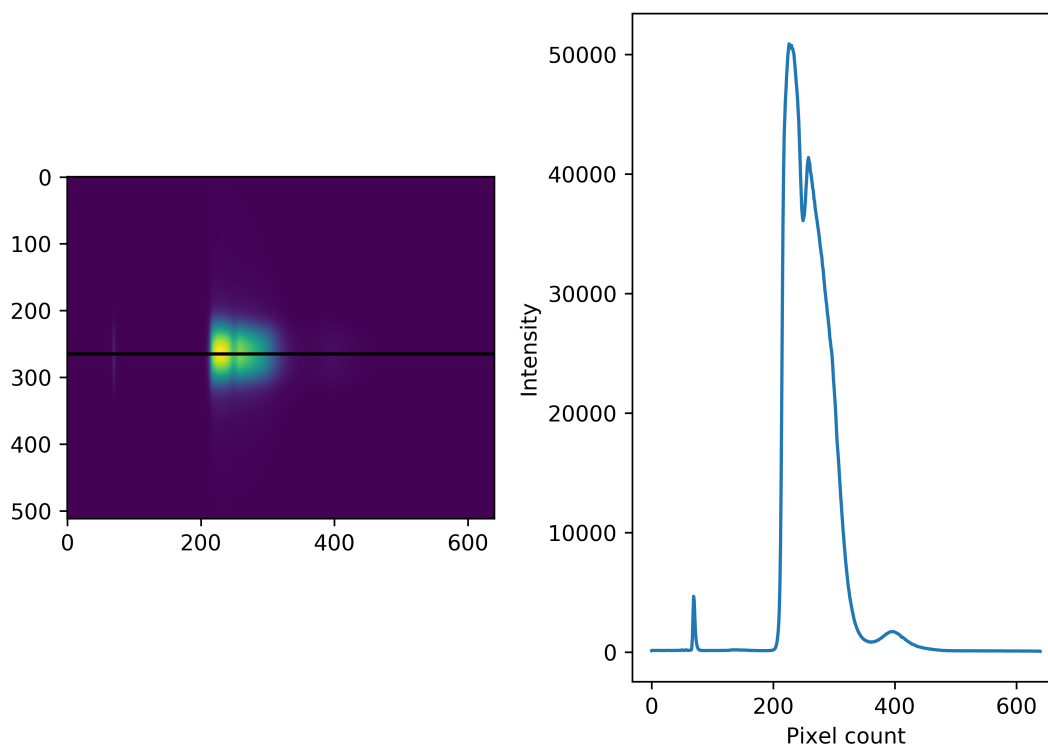


**Figure 7.6:** Left: a dark and bias subtracted frame. Right: a 1D slice of the intensity along the spectral axis used in the light source stability tests. Note the x axis is pixel count instead of wavelength as the instrument was not wavelength calibrated for these measurements.

**Table 7.1:** A comparison of the level of alignment required to achieve the same level of performance from a long focal length spherical mirror and a 45° OAP as the collimating optic in the light source. The criterion was taken to be when the geometric RMS spot size was just smaller than the diffraction limited spot size or better for 98% of the Monte Carlo runs. The table shows the significantly looser tolerances of the spherical mirror compared to the OAP. Positional alignments are give in mm and angular alignments in degrees.

| Optic | $\Delta X$ | $\Delta Y$ | $\Delta Z$ | $\Delta\Theta_x$ | $\Delta\Theta_y$ | $\Delta\Theta_z$ |
|---|---|---|---|---|---|---|
| Spherical mirror | 5 | 5 | 5 | 0.2 | 0.2 | 0.2 |
| 45° OAP | 0.05 | 0.05 | 0.05 | 0.05 | 0.05 | 0.05 |

slow changes. I performed a dark and bias subtraction on each frame and then computed the standard deviation of the intensity of each pixel over the 600 frames. The results are shown in figure 7.7. The configuration without the LM317T regulator, "Unstabilised power supply", shows that the background, where there is no light from the light source, is consistent across all pixels and stable with a standard deviation of around 30 counts. In the pixels where there is dispersed light, however, the standard deviation increases to around 500 counts at its peak, or 1% the average count for that pixel, implying that there is a significant variation in the light source intensity above the fluctuations of the background.

The result of the same experiment but with the LM317T regulator is labelled as "Stabilised power supply" in figure 7.7. Here the variation in intensity is shown to be much reduced for the pixels which contain light from the light source, to a maximum value of 165 counts, or ~0.3% the average count. This improves the stability of the light source by a factor of ~3×. Hence with the LM317T regulator I am able to produce a light source "stable" to ~0.3% in intensity with a simple torch bulb and a bench-top DC power supply.

The final design feature of the white light source worth highlighting is the size of the pinhole. In order to provide as close to a point source as possible the pinhole should be "unresolved" by M1, i.e. the image of the pinhole should be smaller than the PSF of the instrument.

In practise the PSF recorded at the focal plane of M1 is a convolution of the diffraction limited PSF and the image of the circular pinhole (ignoring any potential optical aberrations). Figure 7.8 shows the result of this convolution for various pinhole sizes, with the legend referring to the fractional width of the image of the pinhole to the first Airy dark ring of the system's Airy disk, the Airy disk here being the diffraction limited PSF for a circular beam. For example for
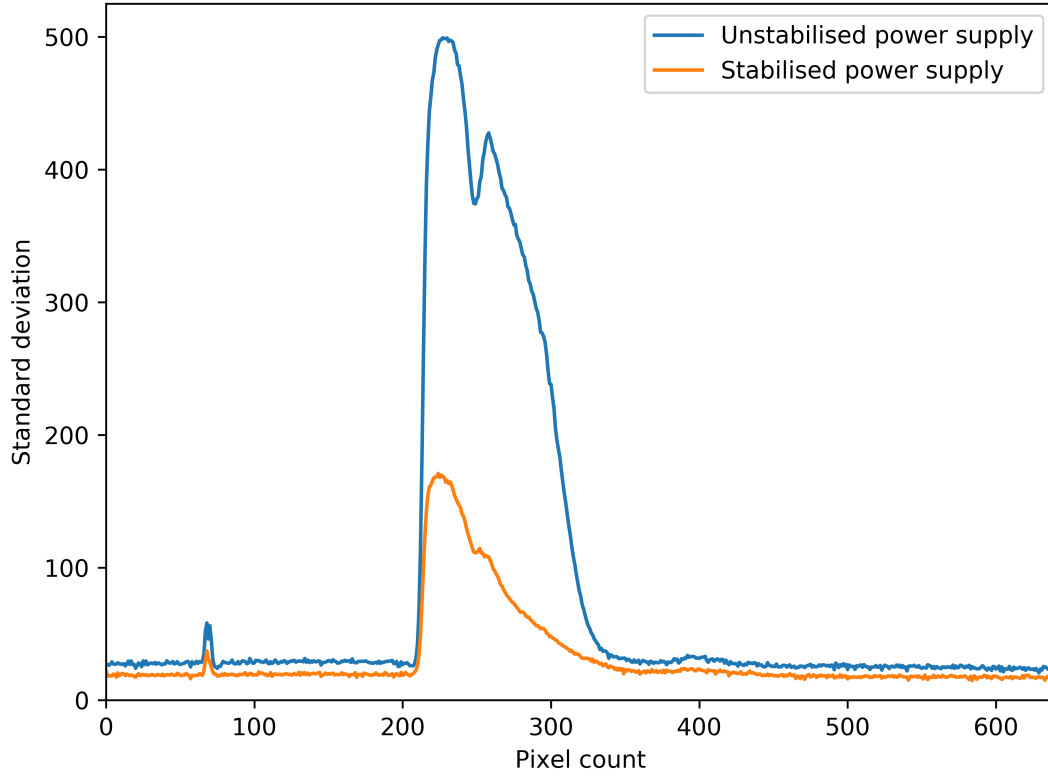
**Figure 7.7:** The standard deviation of 600 frames for a row of pixels along the spectral axis highlighted in figure 7.6. Here the standard deviation is ∼3× smaller when the LM317T regulator is used to stabilise the bench-top power supply.

the 0.1 curve the image of the pinhole at the focal plane of M1 is 0.1× the diameter of the Airy disk. Figure 7.8 shows that for pinhole images up to 0.3× the width of the Airy disk, the effect of a finite sized pinhole is minimal, however, the PSF broadens rapidly for larger pinholes.

For this reason the size of the image of the pinhole used should be kept below 0.3× the Airy disk diameter at the focal plane of M1, the initial focusing optic of FOURIER. The diameter of the Airy disk at the focal plane of M1 is given by

$$D_{\mathrm{AiryDisk}} = 2.44\lambda f_{\mathrm{M1}}/d, \tag{7.1}$$

where $\lambda$ is the wavelength of observation $f_{\mathrm{M1}}$ the focal length of M1 (1202.5 mm) and $d$ the diameter of the beam (13 mm). Therefore the image of the pinhole must be no larger than $0.3{\times}D_{\mathrm{AiryDisk}}$. As it is the image of the pinhole at the focal plane of M1, not the width of the pinhole itself that is convolved with the Airy disk of M1, I must consider that the collimator
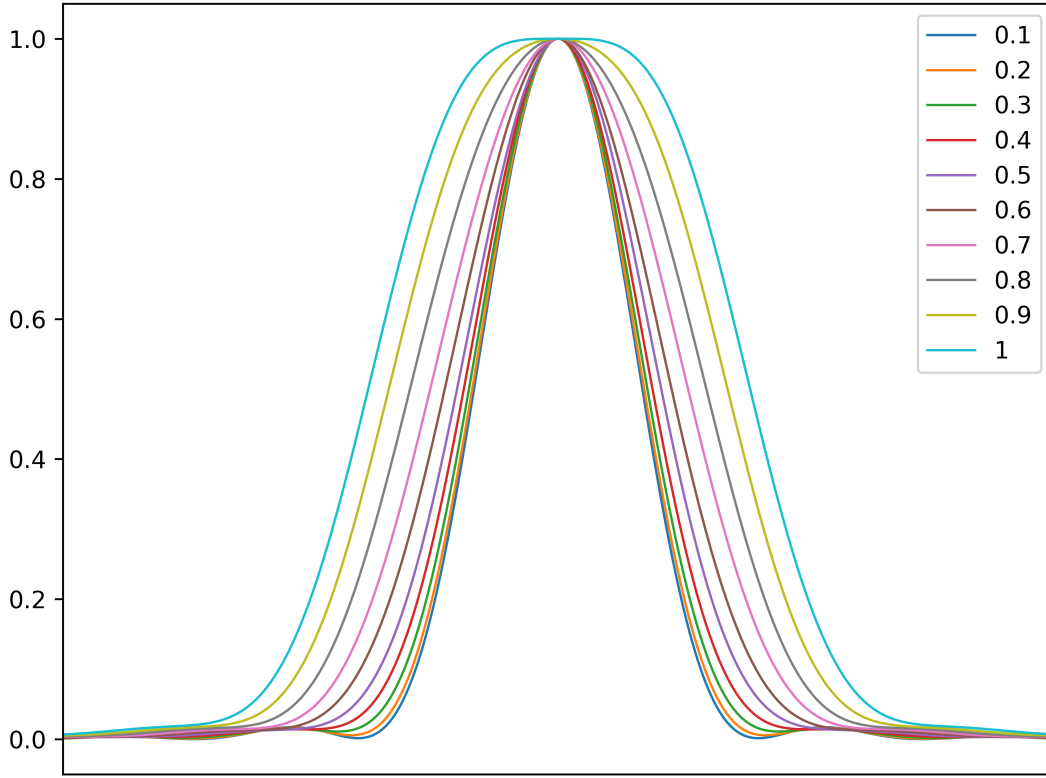
**Figure 7.8:** The convolution of the image of a finite sized pinhole and the diffraction limited PSF of a system. The legend refers to the fractional width of the pinhole to the diffraction limited PSF, i.e. the 0.1 curve is for a pinhole image 0.1× the width of the diffraction limited PSF.

and M1 act to reimage the pinhole at the focal plane of M1. The magnification of the pinhole at the focal plane of M1 is

$$M = f_{\mathrm{M1}}/f_{\mathrm{col}}, \tag{7.2}$$

where $f_{\mathrm{M1}}$ and $f_{\mathrm{col}}$ are the focal lengths of M1 and the collimating mirror respectively. For the system used here this gives a magnification of the pinhole of 2.405×. Combining equations (7.1) and (7.2) I can derive that the diameter of the pinhole should be no larger than

$$D_{\mathrm{pinhole}} <= \frac{0.3 \times 2.44\lambda f_{col}}{d}. \tag{7.3}$$

Note that the focal length of M1 cancels out and only the focal length of the collimator affects the diameter of the pinhole image here. Taking the worst case scenario (the shortest wavelength of $\lambda = 1.1\,\mu$m) this gives a limit on $D_{\mathrm{pinhole}}$ of 31 μm. Unfortunately, a pinhole of

this size was not available, with the closest being 10 μm and 50 μm. The 10 μm pinhole did not provide enough light and so the 50 μm pinhole was selected instead.

### 7.2.3   Beam splitter board

As figure 7.1 shows this board simply takes the output of the light source breadboard and splits it into two independent beams with a 50:50 Thorlabs BS015 beamsplitter and a pair of turning mirrors, which redirect the two beams so they travel in the same direction with a separation of 5" to feed the periscope system.

### 7.2.4   Periscope

The role of the Periscope was to take the two beams at the same height above the optical table and rearrange them to be vertically stacked, as well as to set the height difference between the two beams to match one of the beam pair separations used by FOURIER (see section 4.3). A 3D model of the periscope system used is shown in figure 7.9. The beams enter the top of the periscope and first reflect off a pair of vertically stacked mirrors referred to as the first stage of the periscope. The first stage displaces the beam by the vertical distance needed to replicate the input beam spacing of FOURIER. In addition to displacing the beams to an appropriate height, one of the periscope first stages has an Agilis piezo motor driven linear stage placed under the mounting to allow the optical path length to be modulated by up to 54 mm, in increments as small as 0.2 μm. This is necessary both to equalise the path length of the two beams to within the hundreds of microns as required to be within the coherence envelope and see interference fringes (discussed in section 7.6), but also to operate the system as a Fourier transform spectrometer for spectral resolution and wavelength calibration as discussed in section 7.6. The second stage of the periscope turns the beams to point them towards M1 as well as stacking them vertically. This stage features manual adjustment Thorlabs KM100 tip-tilt mounts for three of the mirrors and a AG-M100N motorised tip-tilt mount for the fourth, which allows for fine motorised control of the angle of one beam down to 1 μrad over a 2° range. This motorised adjustment is crucial to centroiding the two beams with respect to each other well enough to recover high contrast fringes as discussed in section 7.5.
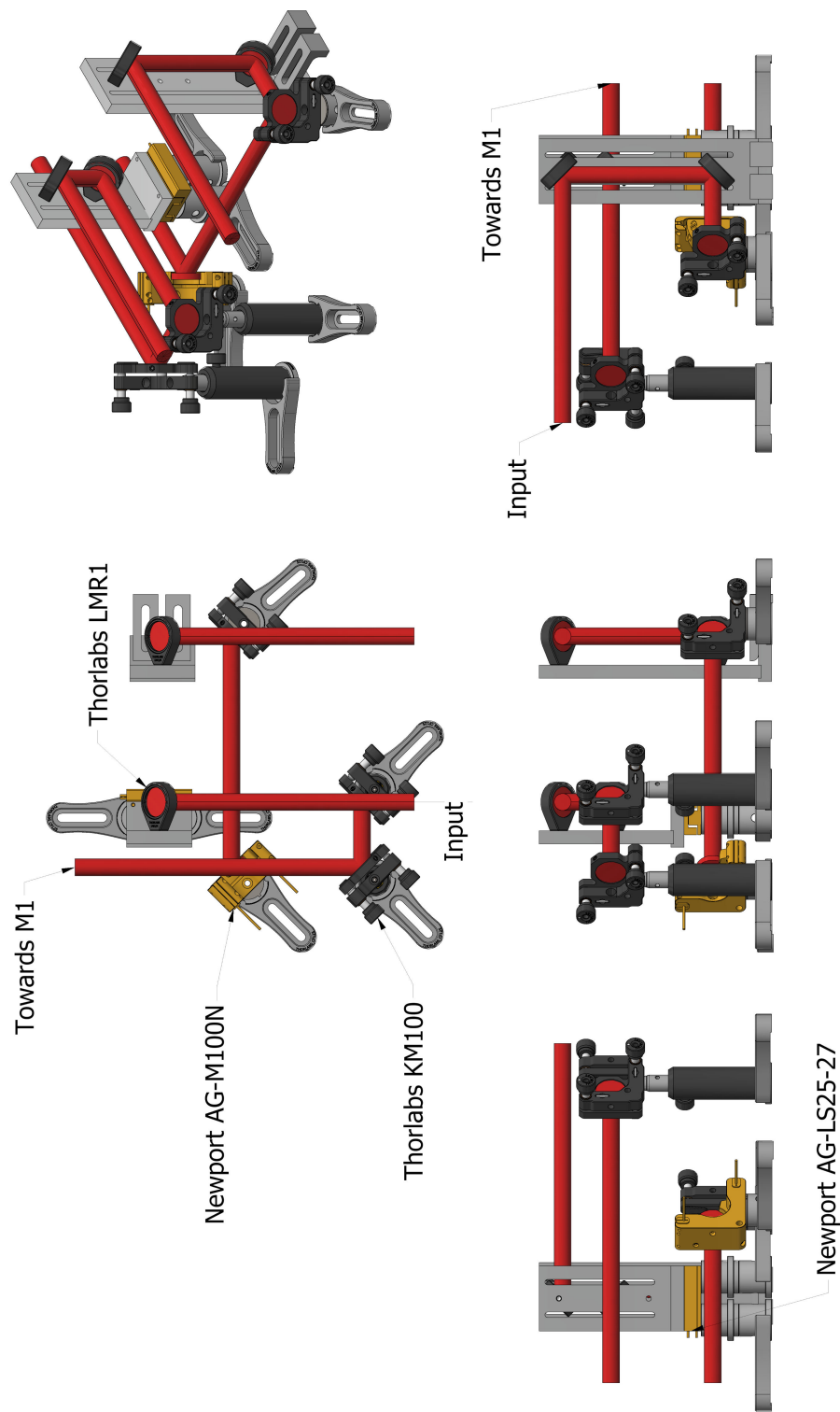
**Figure 7.9:** A 3D CAD model of the periscope system used in the laboratory tests. The first stage of the periscope alters the height of the input beams so that they are spaced vertically to match one of the beam pair separations sampled by FOURIER. One of the first stages also has a piezo linear stage for fine control of the path length. The second stage of the periscope redirects the beams towards M1, as well as stacking them vertically.

The periscope assembly is also designed to be symmetric for both beams, such that they are rotated in the same way. This is done in order to remove any instrumental losses in coherence of the two beams. The advantage of this is that if there are any asymmetries in the wavefront before the light source is split, those asymmetries are in the same orientation at the image plane of FOURIER.

### 7.2.5   Raptor Owl

The SAPHIRA detector is designed to operate at liquid nitrogen temperatures making its use inappropriate for these room temperature tests. I instead opted to use a Raptor OWL 640M, a compact camera sensitive to wavelengths from $\lambda = 0.6\,\mu$m-1.65$\,\mu$m. This means that the warm laboratory tests can only be conducted from the edge of the J band to the centre of the H band. There is a good reason the camera is not sensitive to longer wavelengths, as discussed in section 5.7.1, at wavelengths longer than $\lambda = 1.65\,\mu$m the thermal background rapidly increases for room temperature objects. A camera sensitive to these longer wavelengths would detect a significantly higher level of background noise from thermal photons. The Raptor also uses 15$\,\mu$m pixels, which are 1.6$\times$ smaller than the SAPHIRA detector's 24$\,\mu$m pixels. Though as the pixel sampling of the SAPHIRA was designed to not have an impact on the instrument's performance, finer sampling of the interference fringes will not degrade the results.

The final large difference between the Raptor Owl 640M and SAPHIRA is the read noise. While the SAPHIRA detector has sub-electron read noise, the Raptor Owl is quoted as typical read noise of 174 and 38 electrons in the low and high gain modes, respectively. This is not an issue, as I used an artificial light source and so was able to use a source bright enough to minimise the effects of read noise.

## 7.3   PSF profile

This first experiment verified the PSF reshaping by FOURIER and the quality of those PSFs. This test involved measuring the PSF profile of the two individual beams and comparing them to those predicted by the optical design discussed in section 4.7.

This measurement was performed with the white light source passing through the 50$\,\mu$m diameter pinhole and an aperture stop reducing the collimated beam diameter to 13 mm. The
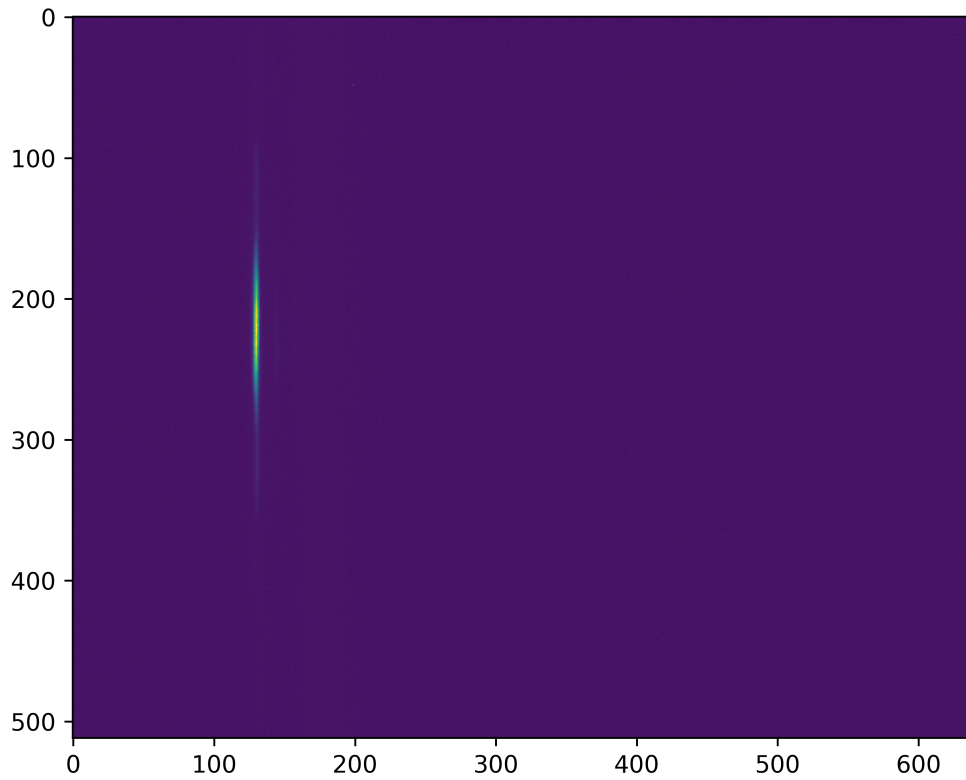
**Figure 7.10:** A single beam at the FOURIER focal plane with a $\lambda = 1.64\,\mu m$ narrowband filter in front of the CCD. This image has been averaged over 50 frames and dark frame subtracted. The high anamorphic shaping of the beam is clearly visible.

measurements were taken with a narrowband filter centred on $\lambda = 1.64\,\mu m$ with a Full Width Half Maximum (FWHM) of $\lambda = 15.5\,nm$ as a proxy for a monochromatic source. I took the data in the camera's high gain mode which provides greater sensitivity (due to its lower read noise) at the cost of a reduced dynamic range. This option was selected to reveal the fainter details such as the side lobes of the PSF. An example of one of the beams after averaging over 50 frames and performing a dark subtraction is given in figure 7.10, which clearly shows the high anamorphic reshaping of the PSF.

A more quantitative analysis of the beam profiles can be made by plotting the cross-section of the PSF along the elongated, interference fringe and compressed, spectral axes as shown in figure 7.11, where the cross-sections along the interference fringe and spectral axes have been overlaid. By inspection the diameter of the Airy disk is $\sim$180 by 6 pixels along the interference fringe and spectral axes respectively. This gives an anamorphic factor of $\sim$30$\times$, very close to the designed anamorphic factor of 29$\times$ (see section 4.7). This measured anamorphic factor has
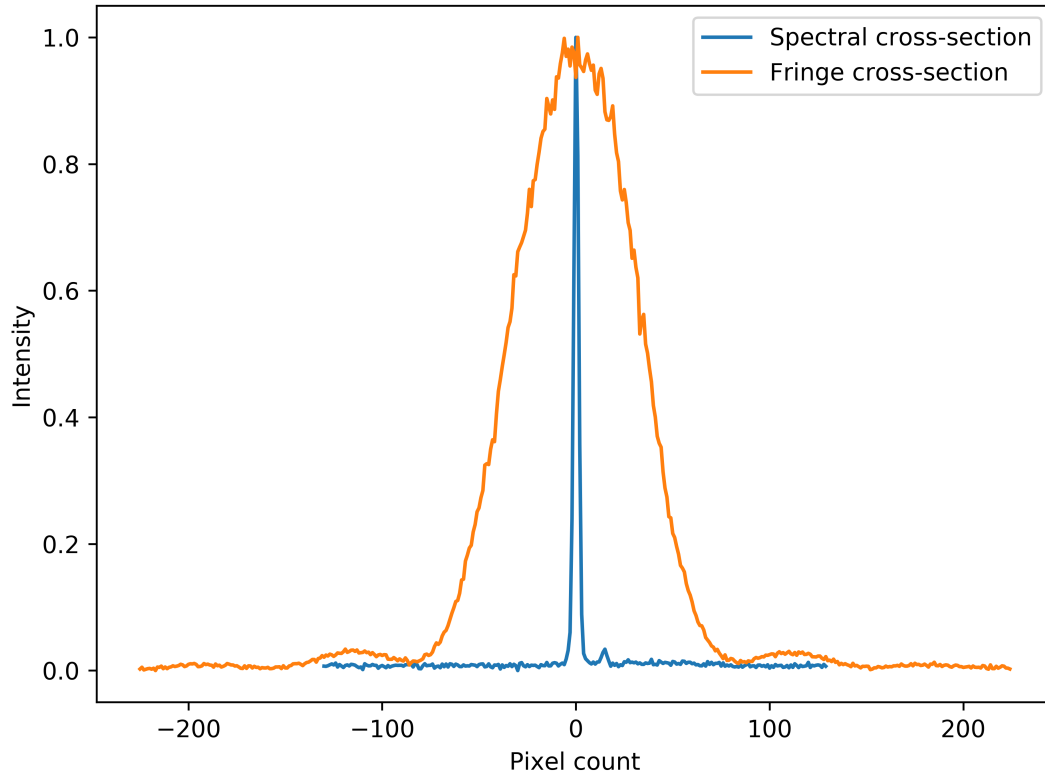
**Figure 7.11:** Cross-sections along the elongated interference fringe and compressed spectral axes of the image shown in figure 7.10. Here the high anamorphic reshaping is shown with the diameter of the first null of the Airy disk being ∼180 and 6 pixels along the interference fringe and spectral axes respectively, giving a measured anamorphic factor of ∼30×.

a moderate level of uncertainty around it, mainly because the PSF along the spectral axis is so poorly resolved (with an Airy disk radius of only three pixels) it cannot be precisely determined where the first null of the Airy disk is.

The anamorphic reshaping factor shows that the ratio of the size of the PSF along the two axes is correct, however it is important to also consider the absolute size of the PSF along each axis, comparing it to that expected from the design of FOURIER. I first consider the profile along the interference fringe axis, as shown in figure 7.12. Figure 7.12 displays the cross-section for both beams fed into FOURIER as well as the cross-section for the theoretical diffraction limited PSF, plotted as a perfect Airy disk scaled to the diameter to the first null of the Airy disk at the focal plane of M1 given by D=$2.44\lambda f_{M1}/d$, and magnified by a factor of 5.4× to replicate the magnification of the anamorphic optics (as discussed in section 4.7). In addition to the diffraction limited PSF, the convolved PSF profile when the effects of a finite
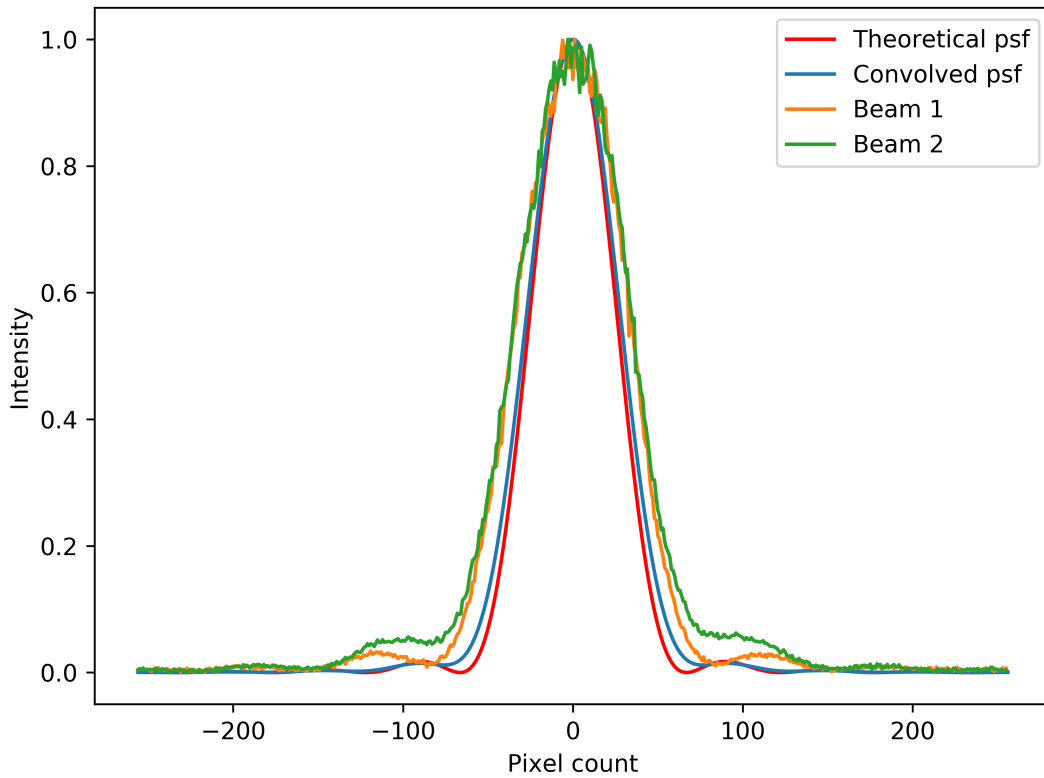
**Figure 7.12:** Cross-sections along the interference fringe axis for measured and simulated PSFs. Beam 1 and Beam 2 are the laboratory measured cross-sections of the two beams fed into FOURIER. The theoretical PSF is the diffraction limited PSF for a true point source and the convolved PSF is the diffraction limited PSF convolved with the image of the 50 μm diameter pinhole used for these measurements.

sized pinhole are considered (see section 7.2.2) is also plotted.

There are a few things worth commenting on. The first is that the two measured cross-sections (Beam 1 and Beam 2), while having the same FWHM of 74 pixels, do not have the same profile in the side lobes. This is believed to be due to a misalignment in the lab light source. For example the periscope first stage is restricted to a clear aperture of 23.7 mm which, when used with a 13 mm beam incident at a 45° angle, leaves a clear aperture of only 2.7 mm either side of the edge of the beam. Hence I believe the deviation in side lobes to be due to vignetting of beam 2. The difference in beam profile is unlikely to originate from FOURIER itself as both beams undergo a common path (so would have the same aberrations introduced) and are significantly undersized compared to the optics within the FOURIER instrument, which is designed to pass up to a 22 mm diameter input beam compared to the 13 mm input beams

used here.

The second point to consider is that the theoretical diffraction limited PSF and convolved PSF are both smaller than the measured beams, with FWHM of 56 and 61 pixels respectively, compared to the 74 pixel FWHM of the measured beams. This is a deviation of ~18% between the measured beams and what is predicted by the convolved PSF model. The difference is likely due to a error in the setup of the light source. For example, if the collimated input beam is reduced by 2.5 mm and assumed to be 10.5 mm in diameter in the convolved PSF model, it would have the same FWHM as the measured beams as shown in figure 7.13. The aperture is set by a manually adjustable iris diaphragm (Thorlabs ID25/M), using a ruler so a 2.5 mm error in setting the beam diameter is possible. The same effect can be achieved if the pinhole is not exactly 50 μm in diameter, but instead 80 μm. However, given the precision with which the pinholes can be manufactured (of order a few microns) such a large error is unlikely. In addition to this, as figure 7.14 shows a 80 μm diameter pinhole would remove the sidelobes when convolved with the ideal Airy disk, which is not seen in the laboratory data.

I can also analyse the PSF cross-section along the spectral axis as shown in figure 7.15. The same theoretical and convolved PSFs are plotted as done for the interference fringe axis. In the laboratory data the FWHM is broader by 22.6%, compared to the convolved PSF. As the FWHM are only ~3 pixels across, however, it is harder to compare the profile of the different beams as the differences are less than a pixel.

## 7.4   Throughput

In order to reach the goal of observations at faint limiting magnitudes, FOURIER is designed to have as high a throughput as possible. As the throughput is a core design feature of the instrument verifying it in the laboratory was a high priority.

This measurement was carried out as a differential measure of the flux at the M1 focal plane (with the cryostat window removed) and the detector focal plane of FOURIER. This measurement gave the throughput of all the optics except M1 simultaneously by simply calculating the ratio of flux between these two focal planes. I collected the data through a series of near-infrared narrowband filters, the properties of which are given in table 7.2. These filters cover the range from the edge of the J band to the centre of the H band, at which point the Raptor Owl 640M's Quantum Efficiency (QE) drops off.
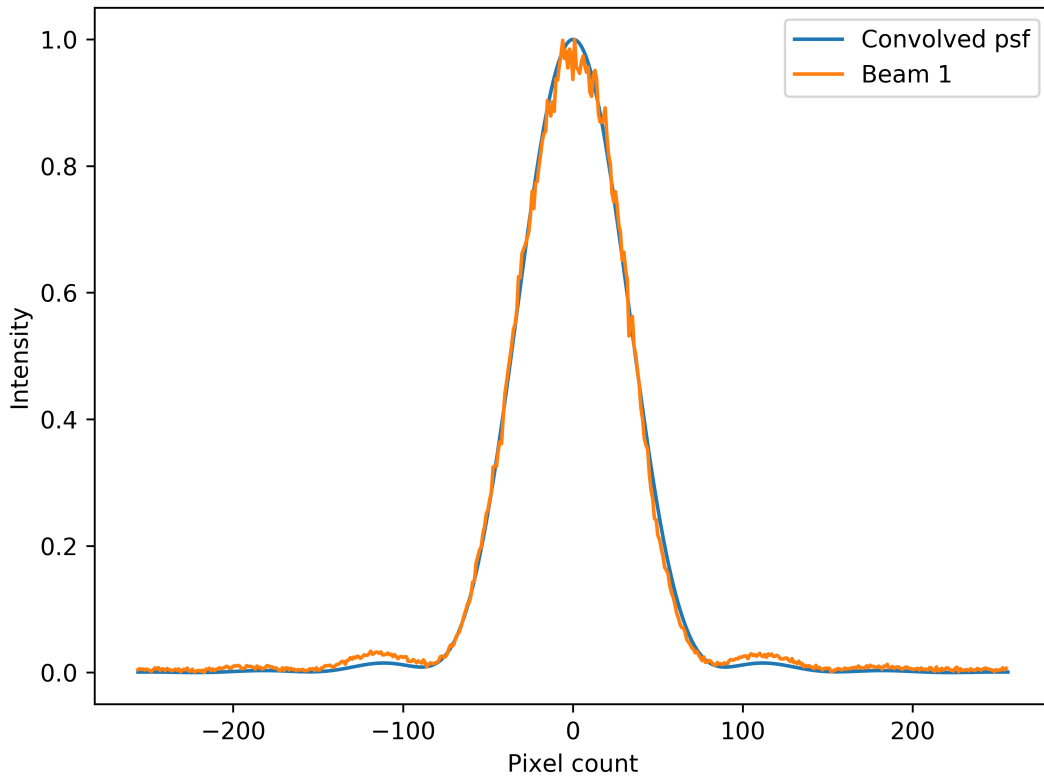
**Figure 7.13:** Beam 1 is the beam cross-section of figure 7.10 along the interference fringe axis. The convolved PSF is the diffraction limited PSF for a 10.5 mm diameter collimated beam convolved with a 50 μm diameter pinhole.

There were a number of steps undertaken to improve the accuracy of the data. The first was ensuring any automatic corrections applied by the camera processing software were turned off to avoid removing any measured flux from the light source (the Raptor provides in camera offset, gain and dark current corrections). The second was to ensure a single exposure time, at which the detector would not saturate at either of the focal plane, was selected. This was difficult to do as the light is spread out over many more pixels at the FOURIER focal plane due to the reshaping of the PSF. It is possible to correct for different exposure times under the assumption that detector counts scale linearly with exposure time, but the need for this assumption can be removed all together if an appropriate exposure time is chosen at the start. Secondly, the camera was operated in low gain mode, this provided multiple advantages, one of which being that the dynamic range of the camera was greater (79dB in low gain compared to 49dB in high gain), meaning the camera was able to measure light for a greater range of intensities. The low gain mode also necessitated a longer exposure time, reducing the risk of any artefacts from detector
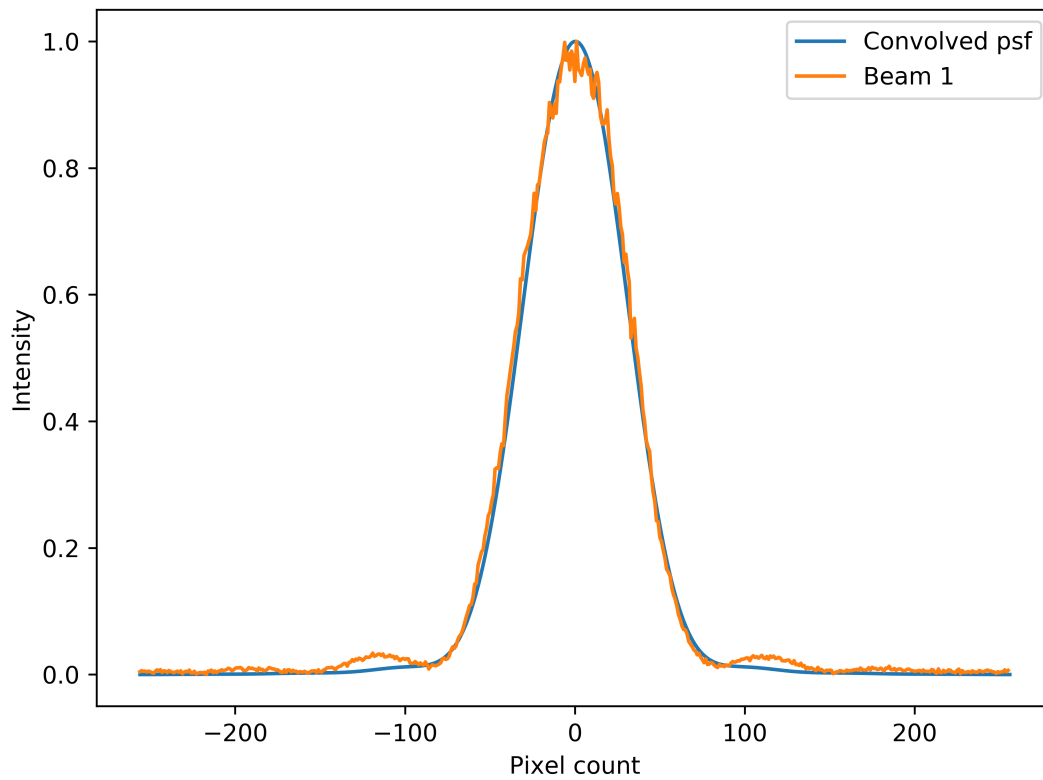
**Figure 7.14:** Beam 1 is the beam cross-section of figure 7.10 along the interference fringe axis. The convolved PSF is a simulated result for a diffraction limited PSF convolved with a 80 μm diameter pinhole. The figure shows that while the FWHM of the simulated data now matches the lab data, the convolution has removed the side lobes of the Airy disk which are clearly still seen in the laboratory data.

reads at high frame rates. The exposure time of the high gain frames was 5 ms whereas the exposure time of the low gain frames to reach the same detector count was 900 ms. Figure 7.16 shows that the flux measurements in the low gain mode were more "stable", having a lower standard deviation (as is evident by the lower scatter in low gain mode). This is due to the fact that while the low gain mode has a higher read noise (174 electrons typical) than the high gain mode (38 electrons typical) according to the manufacturers data sheet, the significantly longer exposure time in low gain mode means the read noise is a smaller fraction of the total camera readout.

A number of steps were taken to process the raw light frames into frames that could be used for photometric analysis. The first stage was to generate a master bias frame. For this 30 frames were taken in low gain mode with an exposure time of 1 ms, taking the median of all
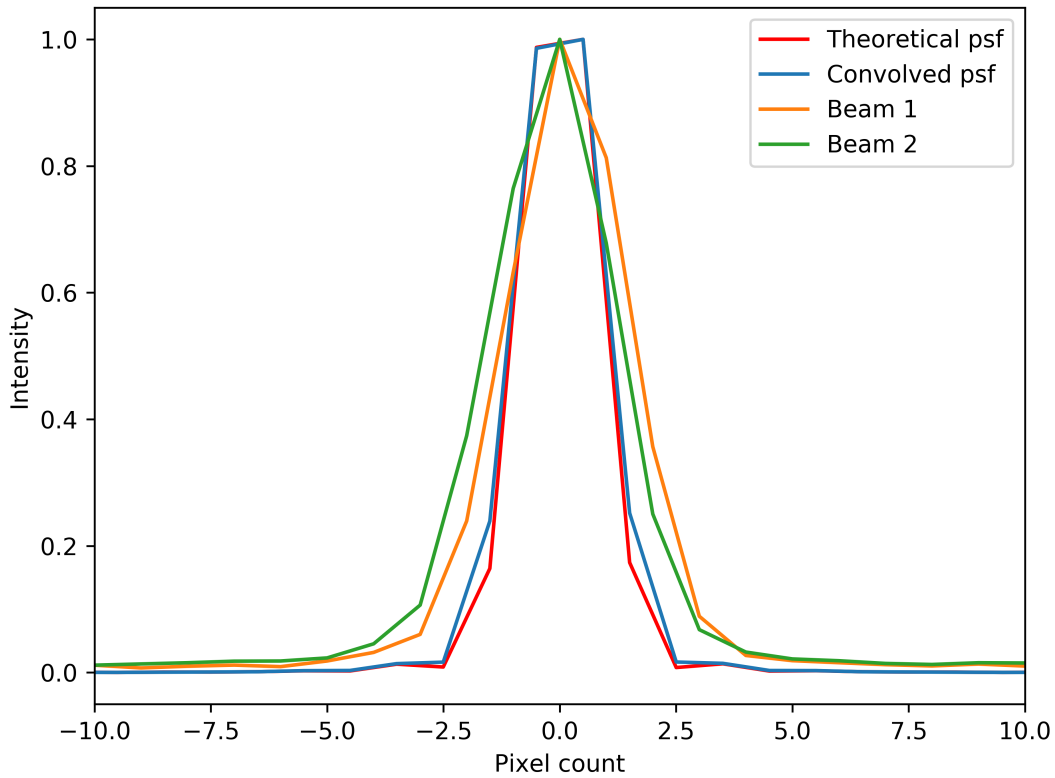
**Figure 7.15:** A cross-section along the spectral axis where the data have the same meanings as in figure 7.12.

the frames. The master bias is shown in figure 7.17.

Dark frames were recorded immediately after the light frames for each filter and consisted of 20 frames with the same 900 ms exposure time as the light frames. For these frames the light source was blocked but the camera was not covered. This allowed any stray light sources to be recorded on the dark frames and subsequently be removed during processing. The master bias was subtracted from each dark frame and the median of the bias corrected dark frames was calculated to generate the master dark. A unique master dark was created for each near-infrared filter as while the camera characteristics were expected to remain the same, the dark frames showed different levels of background flux between filters, as demonstrated in figure 7.18.

The final calibration frame was a flat field. It was not possible to access a uniformly illuminated light source bright enough to perform a traditional flat field by placing the light source at the entrance of the FOURIER lab test optical train. Instead a detector only flat was taken by placing a bulb in front of the camera with a cloth diffuser placed in between, at the

**Table 7.2:** The characteristics of the Comar narrowband near-infrared filters used in the throughput measurements.

| Wavelength | FWHM | Peak efficiency |
|---|---|---|
| $1.0\,\mu m$ | $12.8\,nm$ | 51% |
| $1.1\,\mu m$ | $16.6\,nm$ | 58% |
| $1.22\,\mu m$ | $12.7\,nm$ | 56% |
| $1.28\,\mu m$ | $17.2\,nm$ | 73% |
| $1.54\,\mu m$ | $15.1\,nm$ | 47% |
| $1.64\,\mu m$ | $15.5\,nm$ | 54% |

entrance of the camera to provide uniform illumination across the detector. As with the dark frames, multiple flat frames were taken and bias subtracted before being median combined to create a master flat. The master flat is shown in figure 7.19. In addition to the bias subtraction, the master flat has been divided by the average count in all the pixels to normalise it. The main use of this detector flat is to correct for different gain factors between pixels, leading to a different response from pixel to pixel for the same illumination. This is shown to be a minimal correction: selecting a 119×83 pixel box near the centre of the master flat, the mean is 1.04 with a standard deviation of 0.005. The mean is slightly higher than unity due to the drop off in flux towards the edges of the frame. This drop in flux is characteristic of vignetting and so is unlikely to be caused by pixel to pixel variations in gain. Such vignetting cannot be assumed to be characteristic of the detector when placed at the focal plane of FOURIER. This may lead to inaccurate calibration towards the edges of the frame, however, as the PSF is only recorded near the centre of the detector the measurements presented here will not be affected by such vignetting.

Finally, these calibration frames are applied to the individual light frames by subtracting the bias and dark frames and dividing by the flat frame. The result of this is shown in figure 7.20, where figure 7.20a shows a single raw uncalibrated light file and figure 7.20b the same frame after calibration, showing a uniform background with no hot pixels. It is worth highlighting here that the calibration makes the first Airy ring around the central lobe clearly visible at the M1 focal plane.

These individual calibrated light frames are median stacked to produce the final calibrated
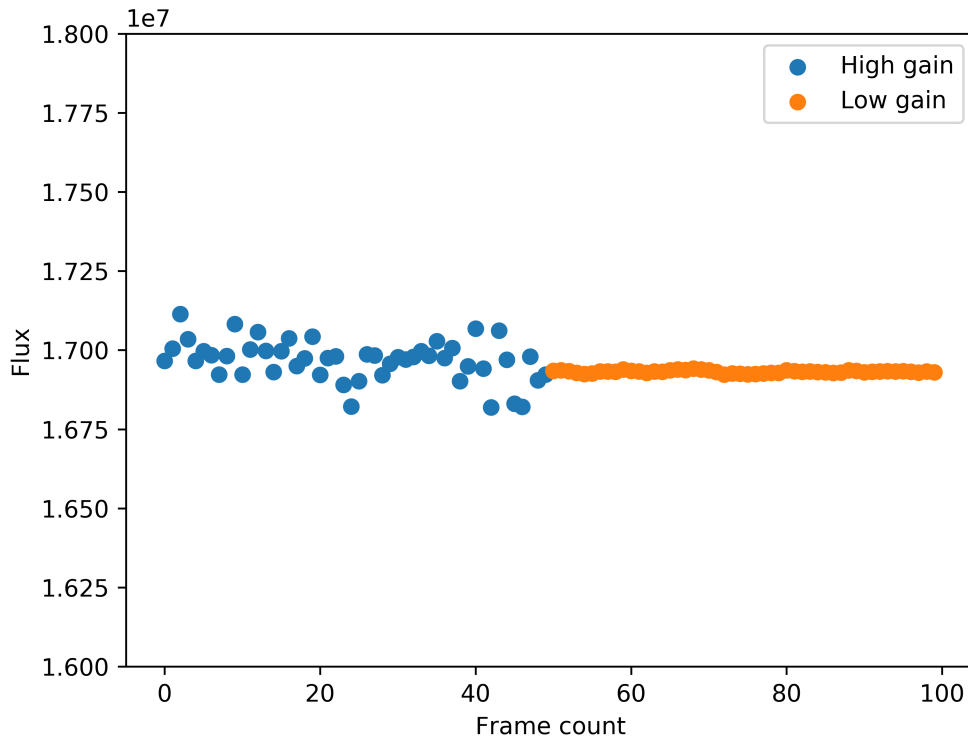
**Figure 7.16:** The flux count at the FOURIER focal plane through the $\lambda = 1.28\,\mu m$ filter for 50 frames in both the high and low gain mode of the Raptor Owl 640M camera. The low gain mode has a significantly lower scatter in the measured flux between frames.

light frame. The flux is then counted by simply drawing a box around the PSF and summing the detector count of all pixels within that box. This process is done for each filter at both the focal plane of M1 and the focal plane of FOURIER, from which the ratio of the flux at the two focal planes is used to calculate the throughput. However, the correct size for the flux counting box must be considered as taking the whole frame would include many pixels which are not illuminated by the light source, but would still contribute noise via, for example, read noise. On the other hand, selecting a box too small would exclude flux from the light source leading to inaccurate results.

It is important that the flux counting box be the same size at both focal planes to provide the most accurate data. For example if a hot pixel remains in the calibrated frame and is counted at one focal plane but not the other, this would introduce a systematic error on the throughput measurement. Whereas if the boxes are the same size, the hot pixel is counted in both frames and the additional flux of the hot pixel simply cancels out when calculating the throughput.
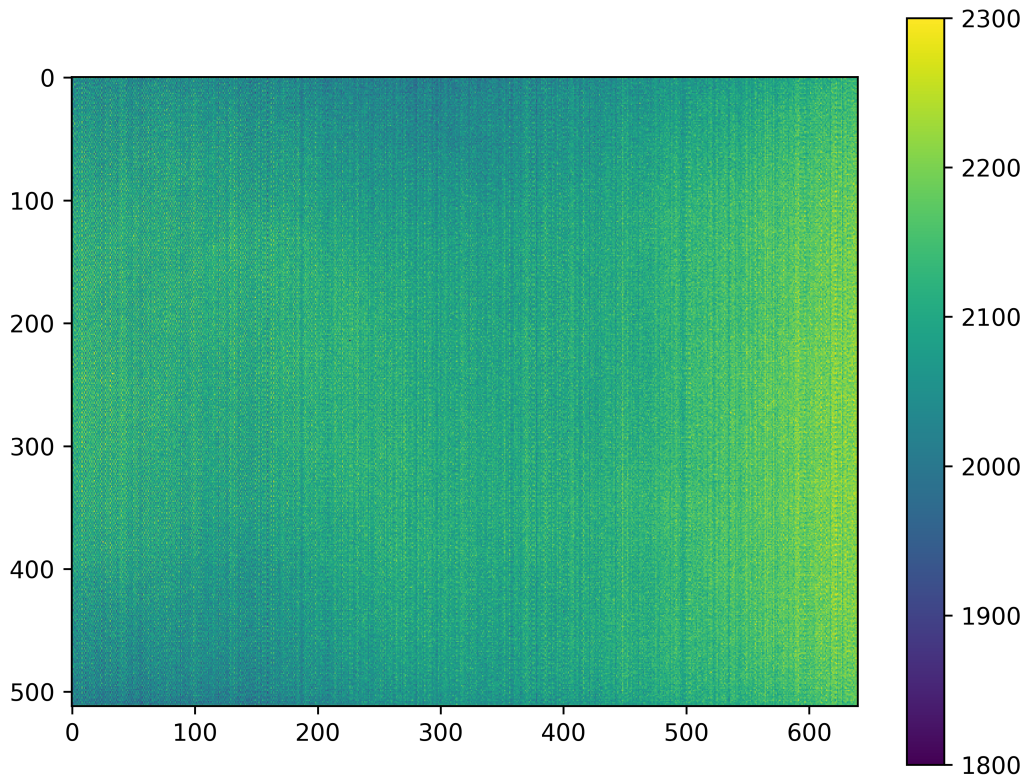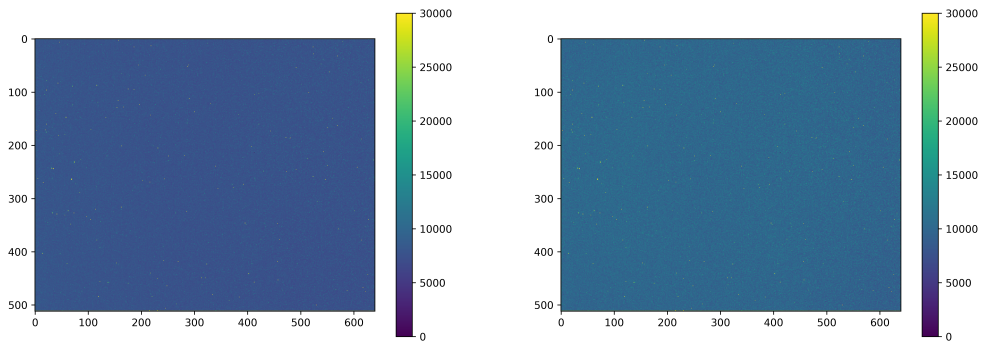
**Figure 7.17:** The master bias file used to calibrate light frames for throughput measurements. This was generated by computing the median of 30 frames taken with 1 ms exposure times in low gain mode.



**(a)** Dark frame with the $\lambda = 1.28\,\mu$m narrowband filter in place.



**(b)** Dark frame with the $\lambda = 1.54\,\mu$m narrowband filter in place.

**Figure 7.18:** Dark frames for the $\lambda = 1.28\,\mu$m and $\lambda = 1.54\,\mu$m narrowband filters. The camera was configured to a 900 ms exposure in low gain mode in both cases. The same hot pixel pattern is seen in both frames, however, the background flux is significantly different between the two, highlighting the need to take a unique set of darks for each filter.
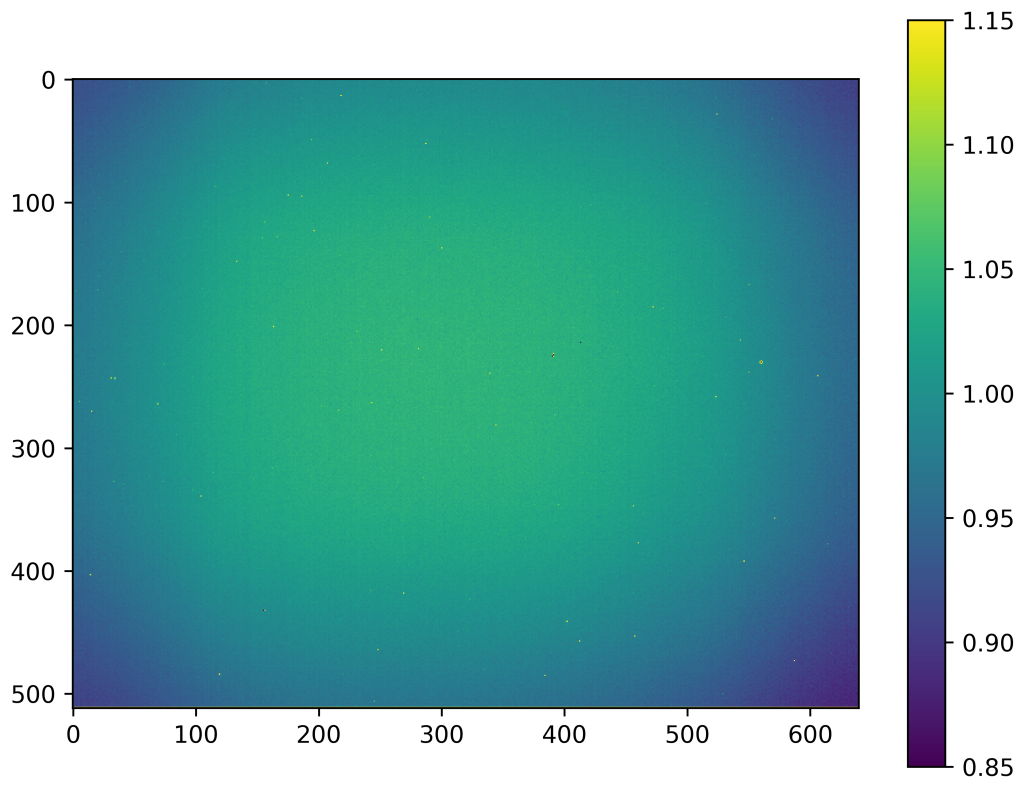
**Figure 7.19:** The master flat field. The pixel values have been divided by the average detector count over all the pixels to normalise the flat.



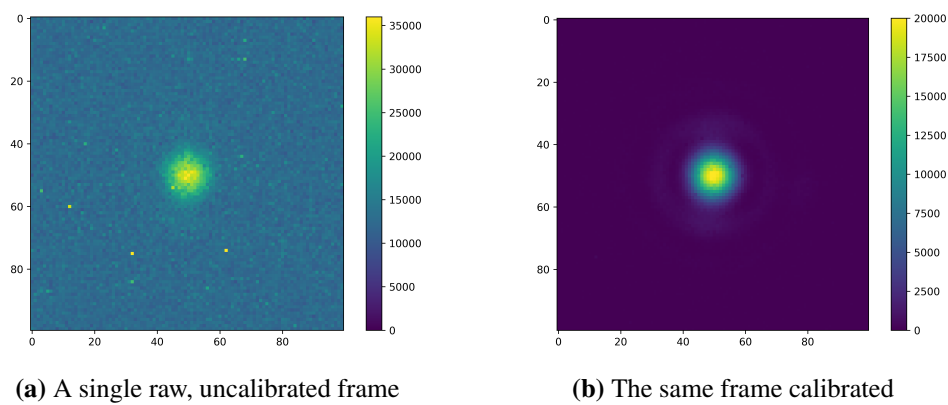**(a)** A single raw, uncalibrated frame

**(b)** The same frame calibrated

**Figure 7.20:** Left: a single raw light frame through the $\lambda = 1.54\,\mu$m filter at the focal plane of M1 showing significant background variation and numerous hot pixels. Right: the same frame after the master bias and dark has been subtracted and the master flat divided out.
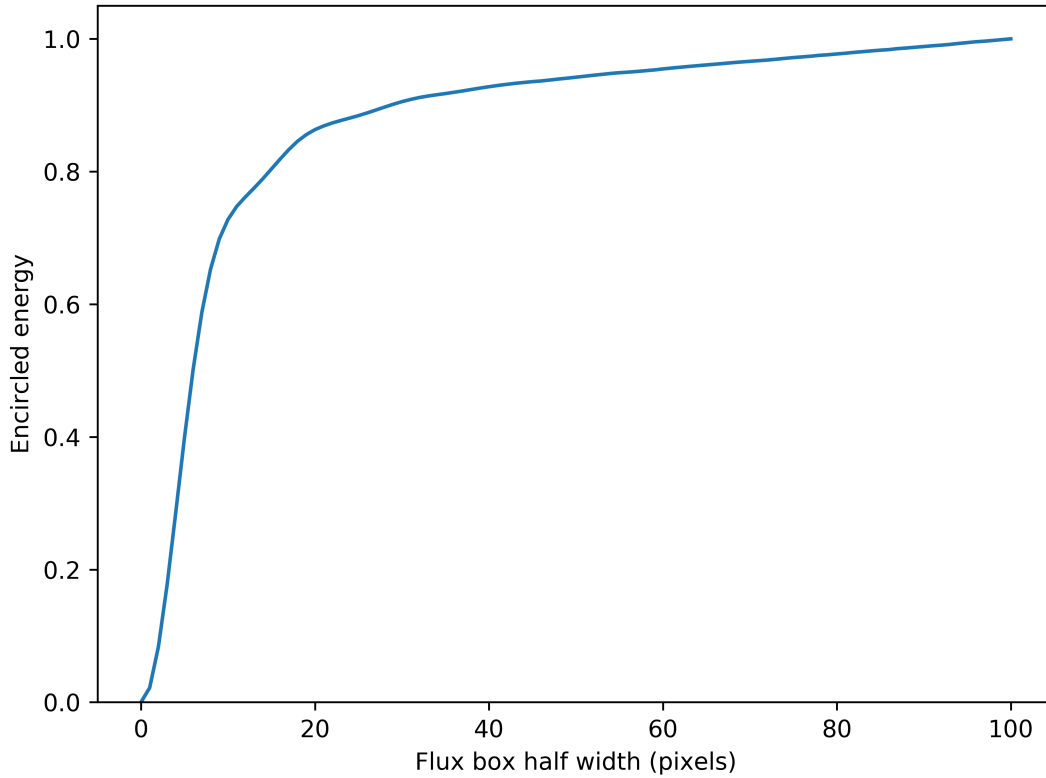
**Figure 7.21:** The encircled energy for the master light in the $\lambda = 1.54\,\mu$m narrowband filter. Note that the dip in flux at an encircled energy of 0.8 corresponds to the first null of the Airy disk. The encircled energy continues to rise approximately linearly beyond the extent of the PSF due to a non-zero background.

To assess the correct box size, the encircled energy at both focal planes is calculated. The encircled energy at the M1 focal plane for the master light in the $\lambda = 1.54\,\mu$m filter is shown in figure 7.21. The flux levels off with a box half width of around 40 pixels. The encircled energy continues to rise marginally beyond this due to imperfect background correction. A dip in the increasing encircled energy can be seen at around 15 pixels due to the first null of the Airy disk. This sets the box width along the spectral axis at both focal planes, as the beam is compressed along this axis at the FOURIER focal plane compared to the M1 focal plane. Hence any box wide enough to enclose the PSF at the M1 focal plane will enclose all the PSF at the FOURIER focal plane along this axis. As the PSF is magnified at the FOURIER focal plane along the perpendicular, interference fringe axis, however, the encircled energy along that axis must be calculated separately.

To calculate the appropriate flux box width along the interference fringe axis at the FOUR-
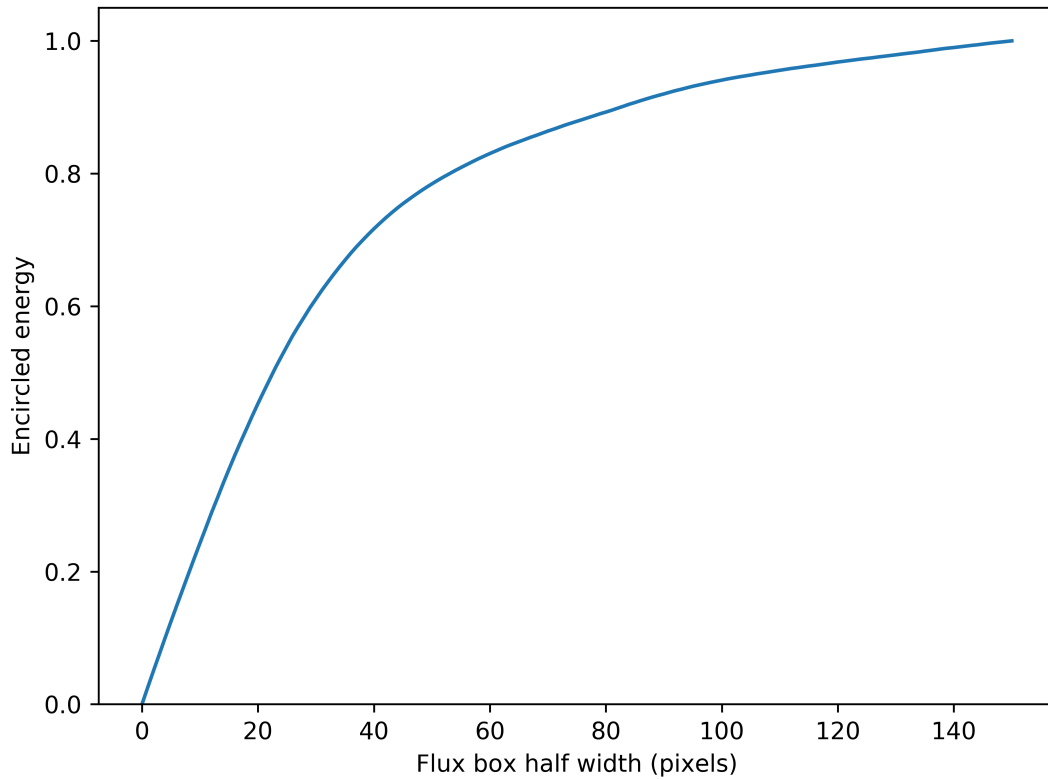
**Figure 7.22:** The encircled energy for the master light in the $\lambda = 1.54\,\mu$m narrowband filter at the FOURIER focal plane. This was calculated by fixing the box half width at 40 pixels along the spectral axis and increasing the box half width along the perpendicular, interference fringe axis. The encircled energy continues to rise approximately linearly beyond the extent of the PSF due to a non-zero background.

IER focal plane I fixed the 40 pixel half width along the spectral axis and then measured the enclosed energy as a function of width along the interference fringe axis. The result of this through the $\lambda = 1.54\,\mu$m narrowband filter is shown in figure 7.22. Based on this analysis I set the box half width to be 100 pixels along the interference fringe axis, giving a flux counting box 80×200 pixels along the spectral and interference fringe axes, respectively. This is then used for both focal planes and at all wavelengths.

As mentioned in both figures 7.21 and 7.22 the background correction is not perfect. The mean pixel count for a 500×200 pixel box (which does not contain light from the PSF) of the mean corrected light frame at the M1 focal plane is 115 counts. This average background pixel value is only 0.6% the count at the peak of the PSF but over hundreds of pixels it can become significant, hence the constant rise in encircled energy in figures figures 7.21 and 7.22. The same calculation for the same 500×200 pixel box at the FOURIER focal plane gives a mean

pixel count of 113. The cause of this offset after dark subtraction is unknown but as it is the same magnitude at both focal planes it will cancel out when the ratio of the detector counts at the two focal planes is taken and hence will not affect the final throughput values.

With the images corrected and the extent of the PSF known at both focal planes, calculating the throughput was simply a matter of taking the ratio of the flux within the box at the two focal planes. Doing so gives the measured throughput values in figure 7.23. The above discussion of the image calibration has only shown frames for beam 2 in the $\lambda = 1.54\,\mu m$ narrowband filter, however, the same process can be applied to the other beam (beam 1) passed by FOURIER, and for all narrowband filters. The measurements of the second beam were taken immediately after the first with the camera in the same configuration. This provides two measurements of the throughput at each wavelength, both of which are given in figure 7.23. In addition to the results for the two beams, the theoretical throughput is plotted which is calculated in the same way as discussed in section 5.5.2. The theoretical throughput presented here includes the cryostat window, M2, an uncoated N-SF11 prism and L1. The fact that the N-SF11 prism is uncoated is the reason both the predicted and measured throughput are lower compared to that given in figure 5.16 as, for example, the uncoated prism has a throughput of only 74.7% at $\lambda = 1.5\,\mu m$ compared with the 93.6% throughput for the coated prism.

The measured and theoretical throughputs are in good agreement, with an average difference of only 3.8% and a maximum difference of 10.2% for the $\lambda = 1.54\,\mu m$ filter. Error bars are plotted for the measured throughputs but are too small to be seen except for the $\lambda = 1.64\,\mu m$ filter value. They are calculated by binning the light frames into four bins of five frames, for each bin a master light frame is generated and the flux counted within the flux box. From these four mean values the mean and standard deviation are calculated with the standard deviation then divided by the square root of the number of bins to get the standard error of the mean, which is taken as the error on that flux count. This is repeated at the second focal plane and the two standard errors of the mean are combined via Gaussian error propagation to estimate the uncertainty on the throughput. This method captures errors which can vary the flux from frame to frame, such as read noise, but will not include systematic uncertainties which will offset the measured flux from its true value by the same amount in all frames.

I analysed this data further by calculating the mean flux and standard error of the mean flux for the light frames at the M1 focal plane, but shifting the flux counting box by 50 pixels
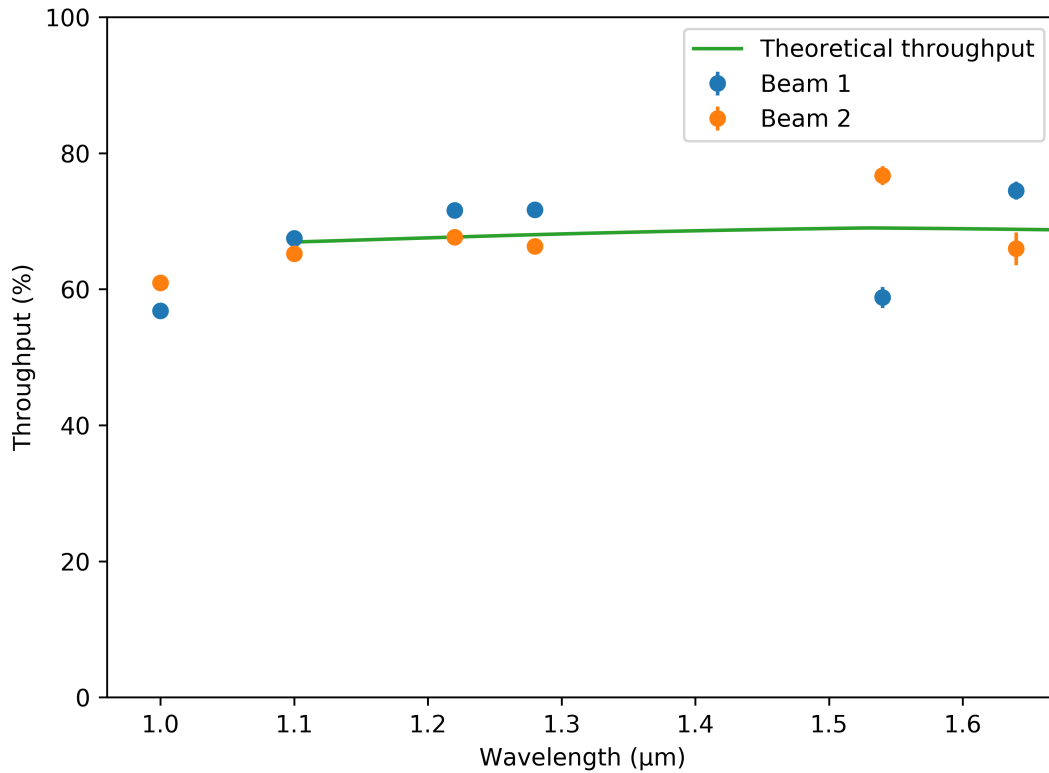
**Figure 7.23:** The throughput measured for FOURIER through the various narrowband filters for the two beams passed through FOURIER, in comparison to the simulated throughput. The error bars on the measured data represent the combined standard error of the mean flux at both focal planes. The simulated throughput is lower here than shown in figure 5.16 as the N-SF11 prism used was not coated with an anti-reflection coating for these tests.

along the spectral axis such that it counts only the background not the PSF. The error calculated from this was 5.5× larger at $\lambda = 1.64\,\mu$m compared to $\lambda = 1.1\,\mu$m, the same ratio as seen in figure 7.23, suggesting the uncertainties are largely due to variation in the background and not the light source.

## 7.5   Visibility loss

As I have discussed in section 5.6, throughput is not the only metric which must be considered when calculating an interferometer/beam combiner's limiting magnitude. Equally, and in the photon noise dominated regime, more importantly, is the maximum fringe contrast, or visibility the instrument can produce. To measure the visibility of FOURIER in the laboratory I combined the two beams from the white light source using the 50 $\mu$m pinhole to produce a near diffraction

limited image (see the discussion around figure 7.12). I also placed the $\lambda = 1.64\,\mu$m narrowband filter in front of the camera to isolate what wavelength of light the fringe contrast was being measured for. Different input beam separations were sampled by adjusting the vertical height the beams dropped in the first stage of the Periscope assembly.

The visibility was extracted by subtracting a dark and bias frame from the light frames and then averaging the 2D PSF along the spectral axis to reduce it down a 1D profile of the interference fringes. An example of which is shown in figure 7.24a. From this 1D profile the modulus of the FOURIER transform was taken to produce a power spectrum as shown in figure 7.24b. The power spectrum contains two distinct peaks, one at the origin of the spatial frequency axis, known as the DC term, and one at the spatial frequency corresponding to the frequency of oscillation of the interference fringes on the detector. The visibility was then measured by taking the ratio of the power at these two spatial frequencies via

$$V = 2\frac{X}{F}, \tag{7.4}$$

where $X$ is the power at the spatial frequency of the interference fringes and $F$ the power of the DC term. The visibility was measured for each frame individually with the subsequent list of visibilities averaged. An alternative method would be to average all frames and then take the visibility of the resulting average frame. This latter technique, however, is prone to fringe-smearing due to vibrations which may shift the position of the fringes from frame to frame.

A number of steps were taken with the laboratory setup to minimise any degradation of the visibility due to the experimental setup. The first of which was to minimise any loss due to tilt error between the two beams. To reduce the tilt error I blocked one of the beams, measured the centroid of the remaining beam and then, swapping the beams, adjusted the tilt of second to the centroid of the first so they overlapped. To increase the accuracy I performed a real-time dark frame correction in python and adjusted the second beam with the motorised Agilis tip-tilt AG-M100N mount for fine control. Fitting a Gaussian to both the beams, I find the difference between their centroids to be 0.02 pixels along the spectral axis and 0.25 pixels along the interference fringe axis, or 0.3% and 0.14% the FWHM of the beam profile along each axis, respectively.

In addition to beam alignment, the Raptor was set to low gain mode as the high gain
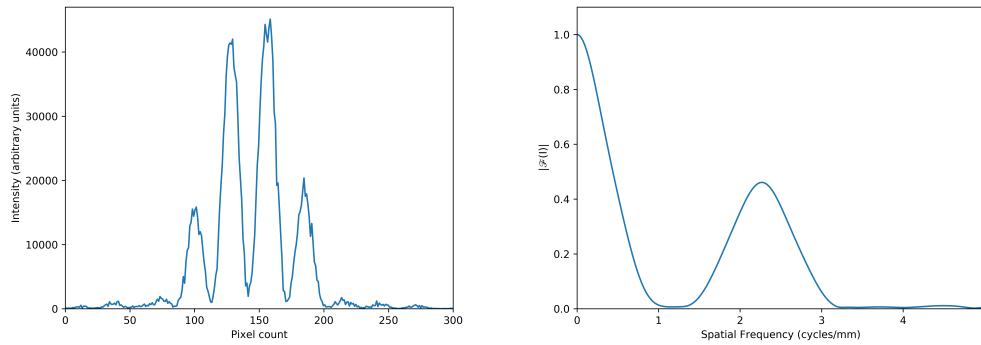
**(a)** The 1D intensity profile of the interference fringes after averaging along the spectral axis. **(b)** The normalised power spectrum of the 1D interference fringes.

**Figure 7.24:** Left: the 1D intensity profile of the interference fringes after averaging the PSF along the spectral axis for the shortest beam spacing of 26 mm with 13 mm beams. Right: the power spectrum of the 1D interference fringes showing two distinct peaks, one at the origin of the spatial frequency axis, the DC term, and one at the spatial frequency of the interference fringes. By taking the ratio of these peaks the visibility is extracted.

mode showed a greater scatter of the visibility values from frame to frame as demonstrated in figure 7.25. More significantly, when operated in high gain mode the measured visibility is 9% lower than in low gain for exactly the same setup (the high and low gain visibility measurements in figure 7.25 were taken immediately after each other). The reason for this could be due to a couple of factors, the first of which is the detector readout time. In the high gain mode the frames were only exposed for 18 ms to avoid saturating the detector whereas the exposure time was 1.5 s in low gain mode. The longer exposure time could reduce camera read out artefacts associated with fast frame rates. The second factor is that the Raptor Owl has a greater dynamic range in the low gain mode, meaning the interference fringes can be recorded with better fidelity as the ADC can take on a wider range of values allowing higher contrast fringes to be recorded. Either way, this is clearly a characteristic of the detector read out and not the FOURIER instrument. As the errors described above would both reduce the visibility in the high gain mode, I assume the visibility measured in the low gain mode is a better representation of the true system visibility. As such use the low gain mode throughout the rest of this section to measure the instrumental visibility.

## 7.5.1 26 mm beam separation

I first present the visibility for the shortest, 26 mm beam separation. The average visibility over 250 frames is 92% with a standard deviation of 0.06%. This is compared to the predicted value
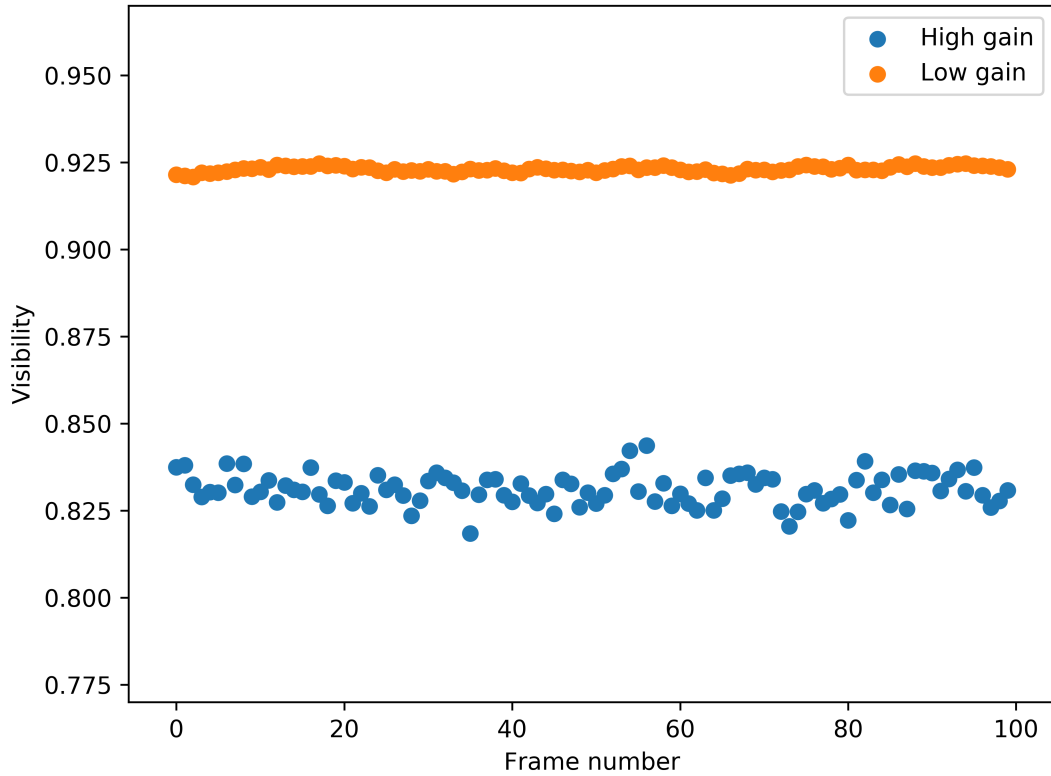
**Figure 7.25:** The visibility measured for a number of successive frames in both the high and low gain modes of the Raptor Owl 640M. The scatter in the visibility measurements is much smaller in the low gain mode. The mean fringe contrast is 9% lower for the high gain mode.

of 91% used in the limiting magnitude calculations (section 5.6.2), for this beam separation in the H band. The predicted value accounted for a 4% visibility loss due to misalignment, a 1% loss due to vibrations, a 1% loss due to differential polarisation effects and a 3% loss due to polychromatic effects, finite pixel sampling and optical aberrations.

From figure 5.4 I would not necessarily expect the maximum allowed 4% visibility loss due to misalignment of FOURIER as the shortest baseline is proven to be less sensitive to misalignments. However, one loss not captured by the predicted value is that the PSF of the two beams being combined on the 26 mm baseline have slightly different profiles (figure 7.12), likely originating from vignetting along the laboratory light source due to poor clear apertures as discussed in section 7.3. This profile difference will contribute to a reduction in fringe contrast. This is not expected to be an issue when FOURIER is deployed at the Magdalena Ridge Observatory Interferometer (MROI) as the system feeding FOURIER will be aligned to a higher degree of accuracy than the light source used for these warm laboratory tests.

Another difference between the visibility measurements made here and the model used to predict the visibility in section 5.6.2 is the visibility losses from finite detector pixel sampling. This is due to the measurements made here being on smaller pixels which will sample the interference fringes better. The visibility *V* expected from finite pixel sampling is given by

$$V = \text{sinc}(\pi f), \tag{7.5}$$

where *f* is the fringe frequency in pixels, i.e. cycles/pixel. This equation is graphed in figure 7.26. It can be understood by considering that as you sample fewer pixels/cycle you depart more from the theoretical system of a continuous interference fringe pattern until you reach one pixel/cycle, at which point both the peak and trough of the intensity are sampled by the same pixel which average out to give a constant intensity across all pixels and so no interference fringes are recorded. Note that figure 7.26 plots cycles/pixel along the x axis such that the closer to the origin of the x axis the better the sampling of the fringes. FOURIER is designed to sample four pixels/cycle at λ = 1.1 μm on the fastest frequency fringes. As the fringe frequency scales linearly with beam separation, for the shortest beam separation measured here the fringe sampling will be three times better (the beams are separated by two times their diameter for this separation as opposed to six times for the highest fringe frequency) i.e. the fringes would be sampled at 12 pixels/cycle on the SAPHIRA detector at λ = 1.1 μm.

The size of a fringe cycle also increases linearly with wavelength, meaning the sampling at λ = 1.64 μm is 17.8 pixels/cycle. At this level of sampling the maximum fringe contrast would be 99.5% on the SAPHIRA detector. The Raptor Owl 640M camera, however, has a pixel pitch of 15 μm as opposed to the SAPHIRA's 24 μm, giving 1.6× better sampling, or sampling 28.5 pixels/cycle (the fringe frequency recorded on the Raptor detector is in fact ~27.5 pixels/cycle). With this level of sampling the maximum theoretical visibility is increased to 99.8% for the Raptor owl 640M. Therefore the finite fringe sampling is not expected to contribute a significant visibility loss to either the 91% predicted visibility or 92% measured visibility for this configuration. For this reason the predicted and measured visibility losses due to finite pixel sampling are comparable, despite the better pixel sampling of the Raptor Owl 640M.

The final difference between the polychromatic simulation and the laboratory measurements which must be considered is the visibility loss associated with a finite range of wavelengths
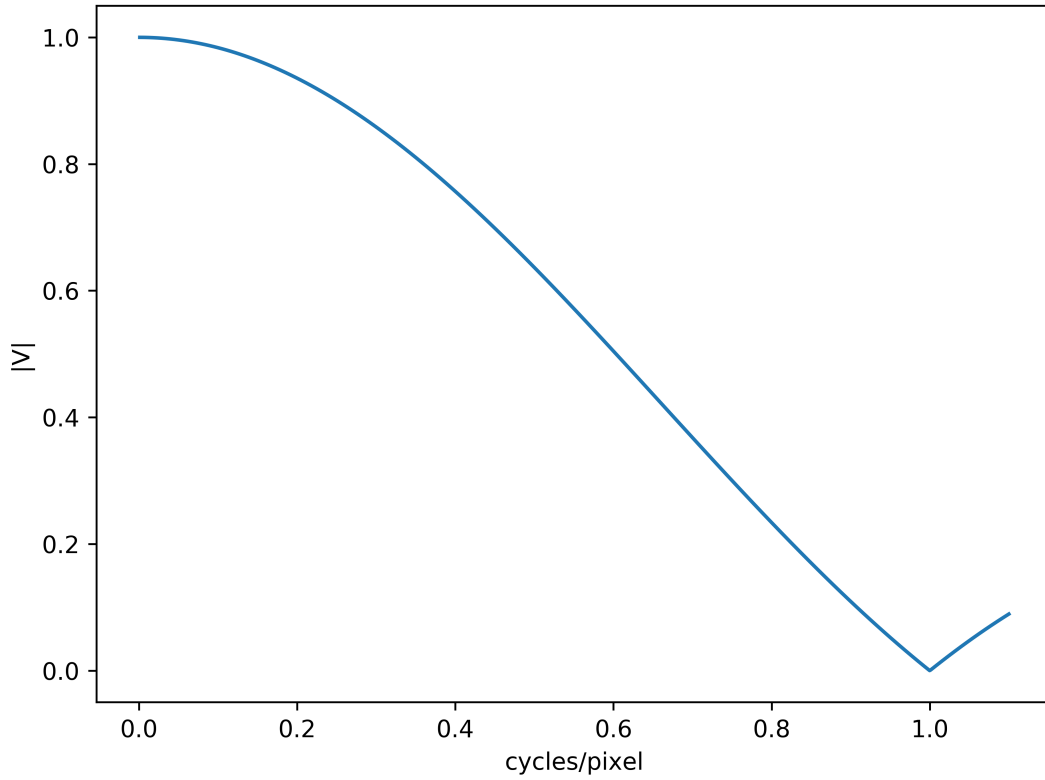
**Figure 7.26:** The maximum theoretical visibility for finite pixel sampling of the interference fringes. This is the modulus of the normalised sinc function given in equation (7.5) and passes through zero for a pixel sampling of one pixel/cycle.

sampled on each spectral channel. The range of wavelengths in a spectral channel of FOURIER is not necessarily the same for the measurements presented here where I used a narrowband filter which limited the bandpass. In the polychromatic simulation the range of wavelengths in a spectral channel is small as the light is spectrally dispersed. Thus the polychromatic simulation wavelengths range from $\lambda = 1.63\,\mu$m-1.65 $\mu$m on the spectral channel centred around $1.64\,\mu$m, giving a 20 nm range of wavelengths. This is comparable to the 15.5 nm FWHM of the $\lambda = 1.64\,\mu$m narrowband filter (see table 7.2). So again, I consider the impact of polychromatic effects to be same in both the polychromatic simulation and laboratory results presented here, making the results directly comparable.

The final estimate for the 26 mm beam separation is then a visibility of 91% compared to the laboratory measured value of 92%.
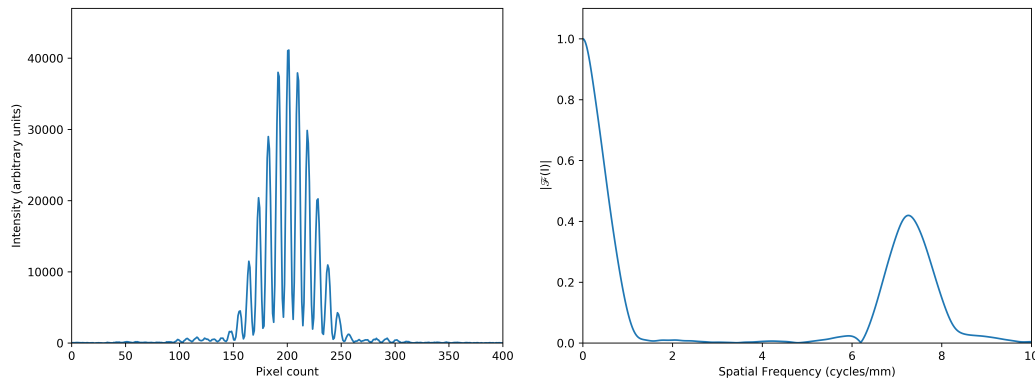
**(a)** The 1D intensity profile of the interference fringes after averaging along the spectral axis

**(b)** The normalised power spectrum of the 1D interference fringes

**Figure 7.27:** Left: the 1D intensity profile of the interference fringes after averaging along the PSF in the spectral axis for the longest beam spacing of 78 mm with 13 mm beams. Right: the power spectrum of the 1D interference fringes showing two distinct peaks, one at the origin of the spatial frequency axis, the DC term, and one at the spatial frequency of the interference fringes. By taking the ratio of these peaks the visibility is extracted. Note the higher fringe frequency than on the 26 mm beam separation.

## 7.5.2   78 mm beam separation

Next I consider the visibility on the largest beam separation of six times the beam diameter, 78 mm. As before, the 1D interference fringe pattern and its power spectrum are shown in figure 7.27. The lower fringe contrast is already evident from the increased intensity at the interference fringe nulls. Calculating the visibility for each frame as before the average visibility is 84%, 8% lower than what was measured on the 26 mm beam separation.

For this configuration the visibility is predicted to be 84.8% from the FOURIER visibility model. As before differences between the modelled visibility and configuration used in the laboratory tests must be considered. Scaling the 28.5 pixels/cycle expected for the laboratory measurements on the 26 mm beam separation separation, the 78 mm beam separation gives a sampling of 9.5 pixels/cycle (the measured fringe frequency is 9 pixels/cycle). Using equation (7.5) this gives a maximum theoretical fringe contrast of 98% for the Raptor Owl 640M pixel sampling. Scaling the pixel sampling for the SAPHIRA detector's 1.6× larger pixels, the maximum fringe contrast when considering only sampling losses is predicted to be 95.3%. This difference means the predicted visibility should be increased from 84.8% to 87.5% for the configuration used in the laboratory tests here.

As for the 26 mm beam discussed in section 7.5.1 I expect any visibility losses due to

polychromatic effects to be the same for the laboratory measured value and the modelled value due to a similar bandpass.

Unlike the 26 mm beam however, I would expect a 4% visibility loss due to misalignments as this 78 mm separation is the largest modelled in figure 5.4 and the most prone to suffering visibility losses from optical misalignment. For the shorter beam separation I assumed that the additional loss in visibility due to the difference in the PSF profiles of the two beams cancelled out the improvement from the lower impact of optical misalignment (i.e. the difference in beam profiles introduced a loss at the few percent level) so that the predicted and measured value were comparable. Here however I expect a 4% loss due to misalignment and a few percent loss due to the difference in beam profiles to both reduce the contrast, so the predicted visibility should be reduced back down from the 87.5% (when considering the gain due to the Raptor Owl 640M better pixel sampling) to 84%.

Therefore the measured visibility (84%) matches well to the predicted visibility of also 84%. There is some uncertainty in the predicted value as the loss due to the difference in PSF profiles has not been directly quantified. The differences between the measured and predicted visibility do not need to be known to a very high degree of accuracy anyway, reducing the FOURIER instrument's visibility by 3.5% only alters the limiting magnitude by 0.05 magnitudes which is ultimately the metric I am interested in.

## 7.6   Spectral Resolution

The final warm laboratory test conducted measured the spectral resolution of FOURIER via FTS. The FTS code was provided by group member James Luis however the parameter tuning and subsequent analysis of the recovered spectra is my own work.

At its simplest level, in this experiment the path length of one of the beams was adjusted using the Agilis AG-LS25-27 linear motor stage under the first stage of one of the periscopes, introducing a phase shift between the two beams and as a result causing the interference fringes to move on the detector.

A basic example of this technique is that for a fixed pixel on the detector with a monochromatic light source, the intensity on that pixel would vary sinusoidally as a function of path length modulation or phase shift, passing through one fringe cycle for one wavelength of phase shift. The wavelength of that monochromatic light could then be identified by taking the

Fourier transform of the pixel intensity as a function of path length modulation, producing a delta function at the wavelength of the source.

The experiment in practice is more complex. Firstly, the Agilis AG-LS25-27 does not provide information of how far it has moved with each step. This has to be calculated using the $\lambda = 1.31\,\mu m$ near-infrared laser (Thorlabs S3FC1310), which is part of the light source (see section 7.2.2). The laser is approximated as a monochromatic source and as such produces a sinusoidal variation of intensity as a function of path length difference. The $\lambda = 0.633\,\mu m$ visible alignment laser is not used here as its angle of deflection through the prism is too different to that of the near-infrared light under study. As the wavelength of the laser is known, the reverse of the above can be applied, i.e. for one cycle of the interference fringes passing over a fixed pixel the Agilis has moved one wavelength ($\lambda = 1.31\,\mu m$) in distance. This information can then be used to calibrate the step size between frames. This near-infrared laser is offset from the white light source by introducing a small angular tilt so that they do not overlap, as shown in figure 7.28. The second deviation from the monochromatic example is that in each row of pixels along the spectral axis there is a range of wavelengths present, and so the FTS produces a spectrum with the relative intensities of a range of wavelengths rather than a delta function.

Due to the polychromatic light on each spectral channel there is a finite range of path differences between the two beams for which the modulation of the light due to interference is large. Buscher (2015) shows that for a wavelength range $\lambda_0 \pm \Delta\lambda$, if the visibility is constant at all wavelengths, the path length over which high contrast inference fringes are seen, often called the coherence envelope, is given by

$$l \approx 2\frac{\lambda_0{}^2}{\Delta\lambda}. \qquad (7.6)$$

### 7.6.1 Data acquisition

Before the interferogram is measured it is important to consider how well it has to be sampled to produce quality results. The first consideration is the total Optical Path Difference (OPD) fringes need to be sampled over as this determines the effective spectral resolution of the FTS measurements. As the goal of this experiment is to quantify the spectral resolution of FOURIER, it is important that the resolution of the FTS measurement be higher than that of
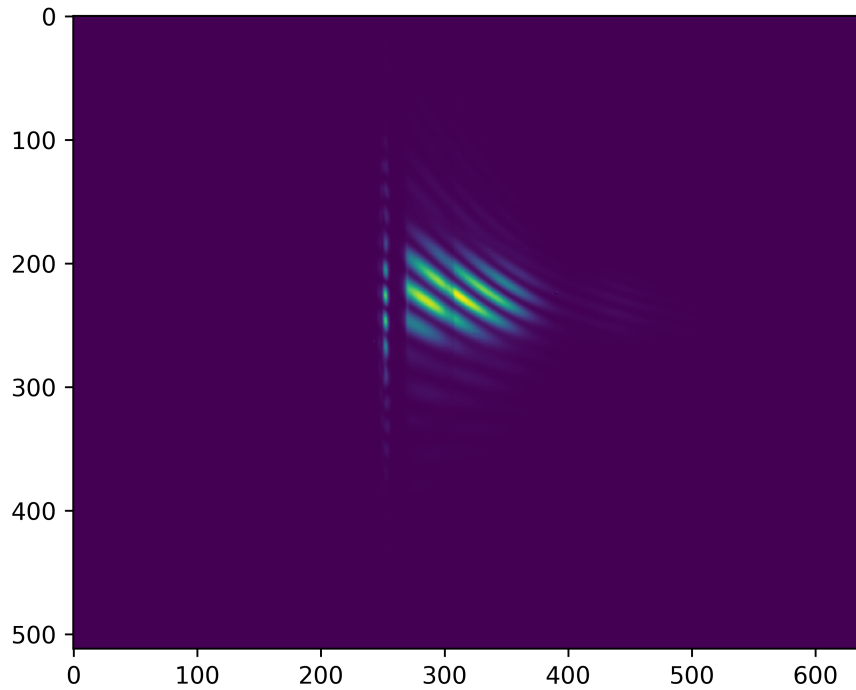
**Figure 7.28:** A dark subtracted frame recorded as part of the FTS data. The left interference fringes are the $\lambda = 1.31\,\mu m$ near-infrared laser, the light on the right is the spectrally dispersed white light source.

FOURIER itself. As Griffiths (2007) demonstrate in their section 2.3 the smallest difference in wavenumber (the inverse of wavelength) of two features that can be distinguished in a FTS spectra is equal to the inverse of the OPD from the centre of the interferogram to the end of the scan, i.e. $\Delta\nu = (\Delta_{max})^{-1}$. As mentioned, the spectral resolution only depends on the OPD from the centre of the interferogram to edge of scan. This point is important as in this work I sample an equal OPD either side of the centre of the interferogram but this does not increase the spectral resolution. This is because the interferogram is in theory symmetric about its peak and therefore sampling both sides does not provide any additional information. In practice, sampling both sides in a so called "double sided interferogram" improves the signal to noise ratio by a factor of $\sqrt{2}$ as the noise is reduced by repeating the measurement.

Given the formula for spectral resolution of $R = \nu/\Delta\nu$, this can be rewritten to give the spectral resolution of a FTS spectra of

$$R = \nu \Delta_{\max}, \tag{7.7}$$

where $\nu$ is the central wavenumber and $\Delta_{\max}$ the centre to edge OPD of the FTS scan. For the data used in this section the scan length of the single sided interferogram was 231 μm, giving a spectral resolution of $R$ = 150, in the $\lambda$ = 1.54 μm channel, above the expected resolution of the instrument of R ≈ 80 (section 5.4) at this wavelength. As the scan length is constant at all wavelengths the resolution of the FTS varies with wavelength, decreasing at longer wavelengths. At the edge of the J band, $\lambda$ = 1.1 μm, the spectral resolution of the FTS scan is $R$ = 210. In comparison, at the edge of the Raptor Owl 640M camera's QE, around $\lambda$ = 1.75 μm, the resolution drops to R = 136. This is still well above the expected resolution of the instrument.

The step size between measurements must also be considered. Here I wish to ensure Nyquist sampling of the data, i.e. sampling at least two measurements per fringe cycle on the shortest wavelength of interest, which is $\lambda$ = 1.0 μm, requiring a step size of 0.5 μm or less between frames. The data used here consists of 1,700 frames over a 469 μm scan giving an average step size of 0.27 μm, providing 3.7 measurements per cycle at the shortest wavelength so the data is adequately sampled.

This then explains the methodology of how the data was recorded. I will now discuss the software pipeline developed to turn the raw data into spectra.

### 7.6.2 Software pipeline

First the frames were opened and ordered by time of acquisition. Two pixels which did not show cosmic defects were selected, one within the PSF of the near-infrared laser and one along the spectral column of interest. The pixel count (intensity) was then recorded for both the laser and spectral column for all frames.

Next the pixel count for the laser pixel was converted to step size as a function of frame number. To do this the average value of the maximum and minimum of the laser fringe detector counts for all frames was found. The frame numbers for the first frames to pass the threshold set by this value, where the previous frame was below this threshold, were stored. This implemented a form of rising edge trigger which counts how many frames pass before the laser fringe returns to the same point in its cycle. For each oscillation cycle of the laser the
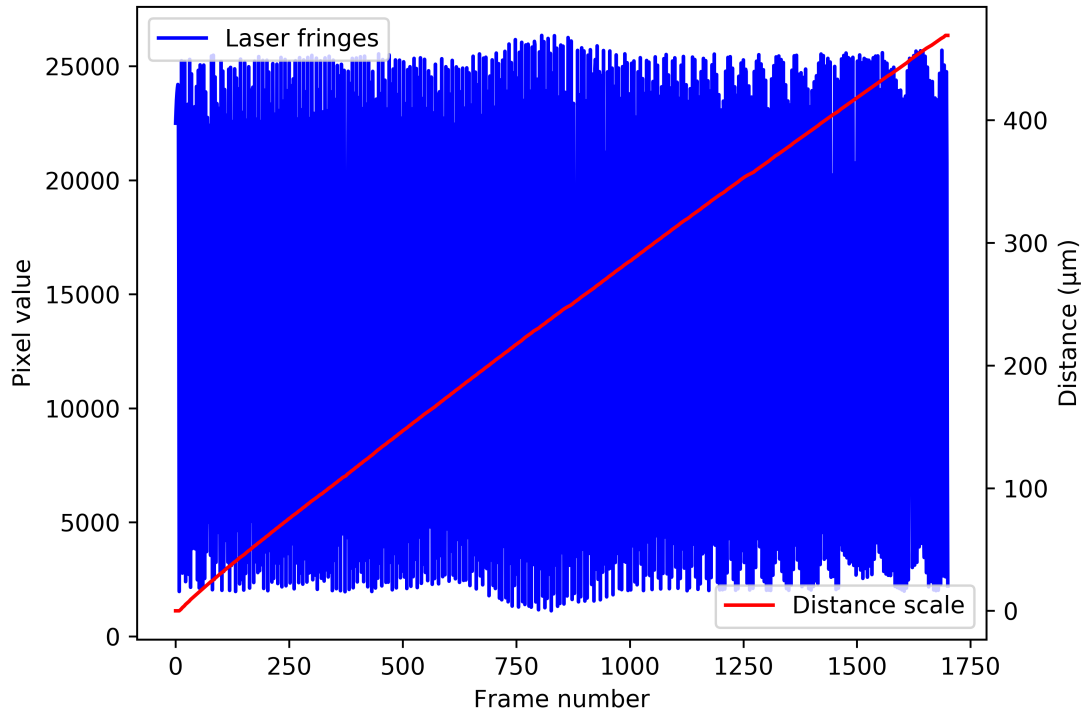
**Figure 7.29:** The pixel count of the laser fringe oscillation and the cumulative path length introduced as a function of frame number.

number of frames was then converted to an average step size per frame by dividing the laser wavelength by the number of frames. This average step size was then adopted as the step size for all frames within that oscillation cycle of the laser fringes. The mean step size of all frames was used to estimate the distance between frames for the first and last frames in the data set, which do not sample a complete oscillation of the laser and so may not trigger the rising edge trigger. The cumulative sum of these step sizes between frames was calculated to provide an array of distances from the first frame. The laser fringe oscillations and calculated cumulative scan distance are shown in figure 7.29.

With the frames calibrated for step size, the next step is to prepare the interferogram for Fourier transforming to produce a spectrum. First, the mean value of the interferogram across all frames is subtracted to centre the detector counts about zero. This is followed by a routine which shifts the data so that the nearest sample to the zero OPD is at the centre.

With the frames calibrated for step size and the interferogram centred, it can now be plotted
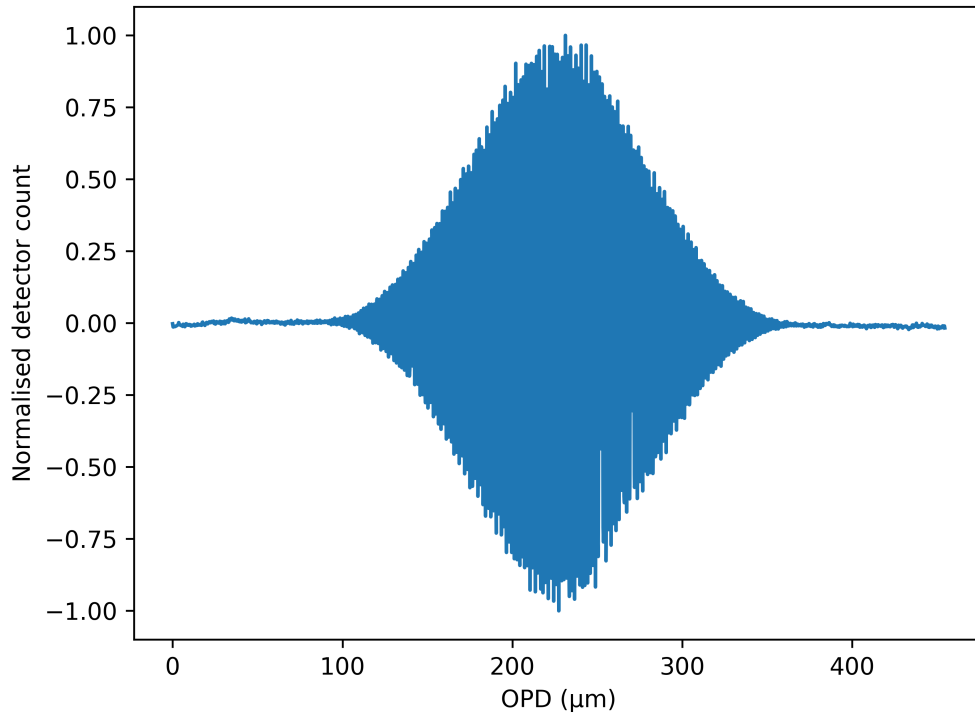
**Figure 7.30:** Normalised detector count as a function of OPD over the entire scan. The data here has been calibrated to give the OPD between frames along the x axis. The data has also been centred about zero and normalised to between 1 and -1.

with the OPD along the x axis as shown in figure 7.30 for the $\lambda = 1.54\,\mu\text{m}$ channel.

At this stage in FTS an apodization function is usually applied to the interferogram. This is particularly relevant when observing narrow spectral lines. Returning to the idealised case of a monochromatic light source, the interferogram would be a continuously oscillating sinusoidal function with fringes extending out to an infinite OPD from the zero OPD point. A finite scan length of the interferogram then would in effect truncate the interferogram, which can be thought of as the infinitely long interferogram multiplied by a tophat/rectangular function of width equal to the scan length. Recalling from the convolution theorem that the Fourier transform of the product of two functions is equal to the convolution of the two functions after they have been Fourier transformed individually, the effect of a finite scan length is to convolve what would be a delta function in the spectrum with the Fourier transform of a tophat/rectangular function (which is a sinc function). This has the unwanted effect both of lowering the resolution of the recovered spectra (hence the reason the resolution depends on the scan length by $\Delta v = (\Delta_{\text{max}})^{-1}$

from before) but also introducing side lobes which produce a signal at wavelengths different to the actual delta function spectral line.

Apodization is the process of multiplying the interferogram by a function, such as a Gaussian or triangular function, so that the spectra is no longer the convolution of the true spectrum with a sinc function but the true spectrum and the Fourier transform of the apodization function (a Gaussian and $\text{sinc}^2$ function in the case of a Gaussian and triangular apodization function). Convolving the true spectrum with a Gaussian for example has the effect of completely removing any sidelobes. The downside of applying an apodization function is that it will degrade the resolution of the recovered spectrum. For example, an unapodized spectrum which is only altered at the abrupt end of a scan will produce a sinc function response to a monochromatic light source with FWHM of $0.605/\Delta$, where $\Delta$ is the length of the scan. A spectrum convolved with a Gaussian apodization function which has a FWHM equal to the scan length will produce a Gaussian profile in the spectrum with FWHM of $1.015/\Delta$, i.e. a broader line (Griffiths 2007).

As mentioned, this process is most important for narrow features such as monochromatic light or narrow absorption lines in the spectrum. If, as is the case with the data presented here, the spectrum is a simple broadband light source with no spectral features the interferogram naturally tends towards very low amplitude within the scan length. Another way of thinking about this is that as the feature is so broad, the convolution of it with a narrow sinc function due to finite sampling produces a spectrum largely unaffected by the finite sampling length. Applying a strong apodization function will only degrade the spectral resolution of the instrument. To illustrate this, figure 7.31 shows the recovered spectrum for the case where no apodization function is applied and where a Gaussian apodization function with FWHM equal to the width of interferogram scan is applied. Figure 7.31 also displays the difference of the two spectra, which is shown to have a maximum amplitude of approximately 2% the amplitude of the spectrum itself. Note there is a very minor broadening of the spectrum when the apodization function is applied. For this reason I do not apply an apodization function to the interferogram.

The Fourier transform of the interferogram is then taken. The absolute value of the resulting complex spectrum is taken to produce the final spectrum. Griffiths (2007) state that this method of simply taking the absolute of the complex spectrum can suffer from noise nonlinearities which can be avoided by applying a phase correction. I implemented a phase correction but found that it did not change the recovered spectrum nor the final spectral resolution value. Given
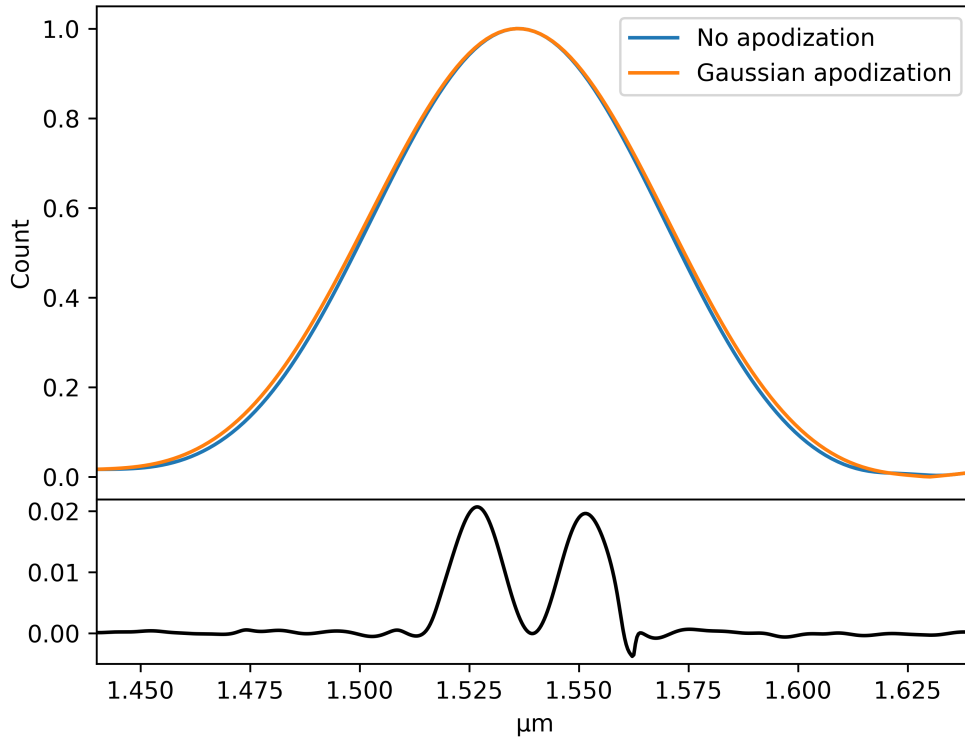
**Figure 7.31:** The recovered FTS spectrum for the case where no apodization function is applied and where a Gaussian apodization function, with FWHM equal to the width of interferogram scan is applied. The difference is plotted below. Note the minor broadening of the spectrum when the apodization function is applied.

this I take the absolute value of the complex spectrum for simplicity. Finally, the wavenumbers for the spectrum are computed using the numpy fftfreq routine (Harris et al. 2020) and are subsequently converted to wavelength by taking the inverse.

### 7.6.3   Data analysis

The final FTS spectrum for the $\lambda = 1.54\,\mu m$ channel is shown in figure 7.32, which shows a Gaussian-like distribution with a FWHM of 19 nm. Taking this as the $\Delta\lambda$, the R value for this channel is then R = 85 by R = $\lambda/\Delta\lambda$.

The spectrum in figure 7.32 has noise at around the 3% level, the origin of which is unknown, but is unlikely to be due to recorded light as the noise pattern continues at wavelengths longer than $\lambda = 1.75\,\mu m$ which the Raptor Owl 640M is not sensitive to due to its cutoff in QE.

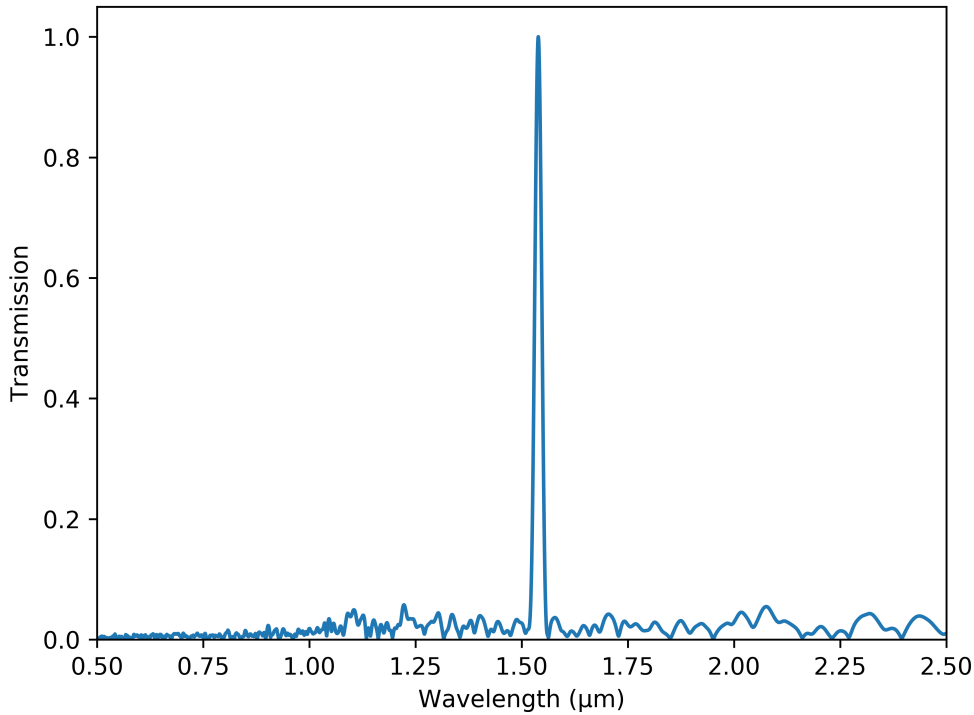To verify this result, as an order of magnitude calculation the scan for the $\lambda = 1.54\,\mu m$

**Figure 7.32:** The final FTS spectrum for the $\lambda = 1.54\,\mu m$ spectral channel, showing a Gaussian-like distribution from which the FWHM can be measured and hence the spectral resolution calculated.

channel shown in figure 7.30 can be used to estimate R directly. As the figure shows, the coherence envelope is approximately $250\,\mu m$ wide. From this an estimate for the spectral resolution of the data can be obtained by rearranging equation (7.6). $\varDelta\lambda$ can be found to be approximately 19 nm and R is then R $= \lambda/\varDelta\lambda \approx 85$.

So far I have focused on only one spectral channel, however, the same routine is applied to each column along the spectral axis, with a Gaussian function being fit to each resulting spectra via the scipy curve-fit routine (Virtanen et al. 2020). From this the mean ($\lambda$) and FWHM ($\varDelta\lambda$) are extracted and spectral resolution calculated for each channel. The resulting R value as a function of wavelength is shown in figure 7.33 and ranges from $80 <$ R $< 120$.

These results are in good agreement with the simulated spectral resolution from section 5.4, and reproduced alongside the FTS spectral resolution in table 7.3.

There are two regions in figure 7.33 which need looking into further due to their unusual response in R as a function of wavelength. The first is the one between $\lambda = 1.34\text{-}1.41\,\mu m$ and
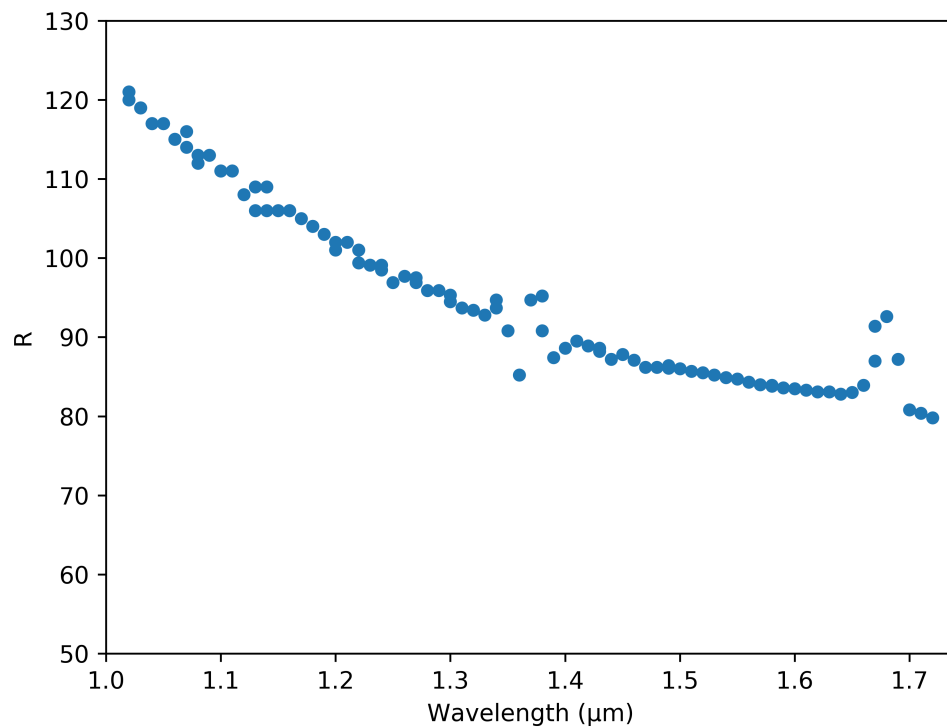
**Figure 7.33:** The spectral resolution as a function of wavelength. Each data point here is calculated from a spectrum recovered for a unique column of pixels along the spectral axis.

**Table 7.3:** The spectral resolution at the centres of the J and H bands simulated against the Rayleigh criterion and experimentally measured via the FTS method. A comparison of the two methods is given in the text.

| Wavelength (µm) | R simulated | R FTS |
|---|---|---|
| 1.25 | 89 | 97 |
| 1.65 | 75 | 83 |

the second is between $\lambda$ = 1.67-1.69 µm. To investigate the first region, in figure 7.34 I plot the detector count of one pixel for each column along the spectral axis for a single beam. The spectral column is converted to wavelength by taking the central wavelength of the Gaussian fitted to the spectrum recovered in each column. As the figure shows, the rapid variation of R in the region $\lambda$ = 1.34-1.41 µm is associated with a dip in the intensity of the light source. Separate analysis, which measured the spectrum of the light source without FOURIER, is also
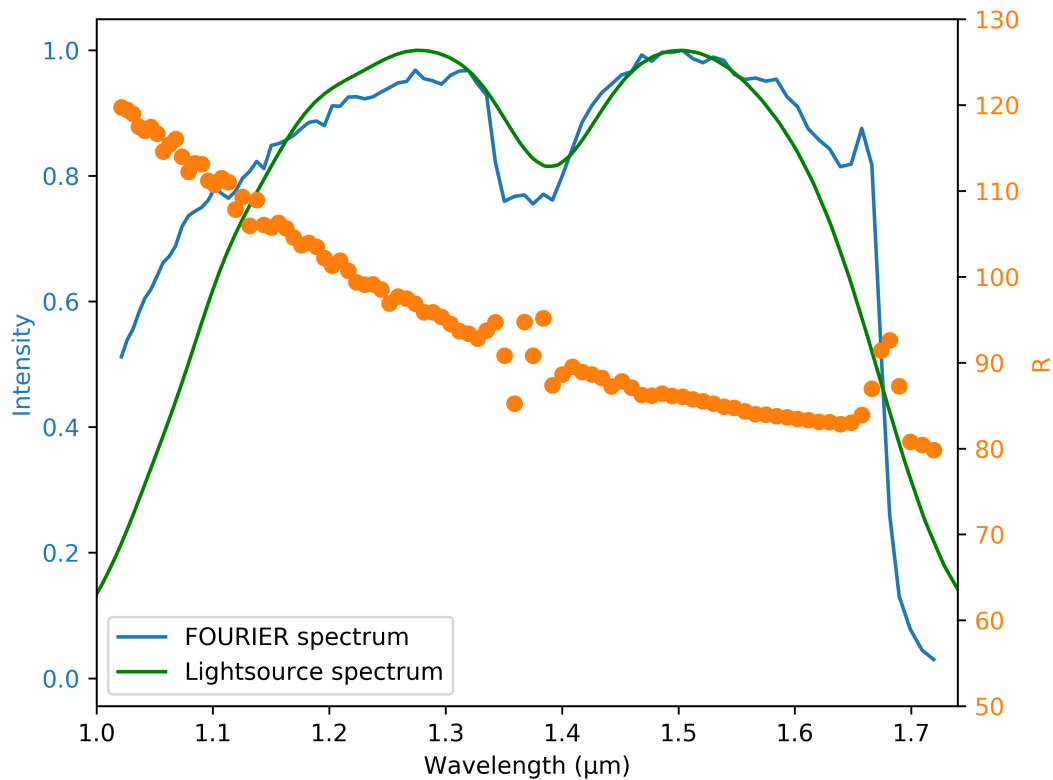
**Figure 7.34:** The spectrum for a single beam at the FOURIER focal plane (FOURIER spectra) and for the light source itself plotted alongside the measured spectral resolution as a function of wavelength. The rapid variation in R between $\lambda = 1.34\text{-}1.41\,\mu\text{m}$ appears to be associated with an artefact of the light source itself.

plotted in figure 7.34 and shows that this dip is a property of the light source itself, thus not induced by FOURIER. A rapid variation in intensity as a function of wavelength can misshape the Gaussian-like spectrum recovered for each spectral channel, altering the measured R value. This appears to be the case here as figure 7.35 shows for the $\lambda = 1.38\,\mu\text{m}$ channel.

The second unusual response in R as a function of wavelength is likely due to the cut off in the Raptor Owl 640M's QE. Figure 7.36 plots the QE of the camera (taken from the manufacturer's datasheet) and the measured spectral resolution against wavelength. As Figure 7.36 shows, the four measurements which spike in R correspond to the rapid cut off in QE of the camera. This has the effect of suppressing the amount of light measured at longer wavelengths within the spectral channel, thus reducing the FWHM and so increasing the R value. The three R value measurements at longer wavelengths are contained within a plateau in the QE curve, meaning, while not much light is measured, all wavelengths are suppressed equally and so the spectral
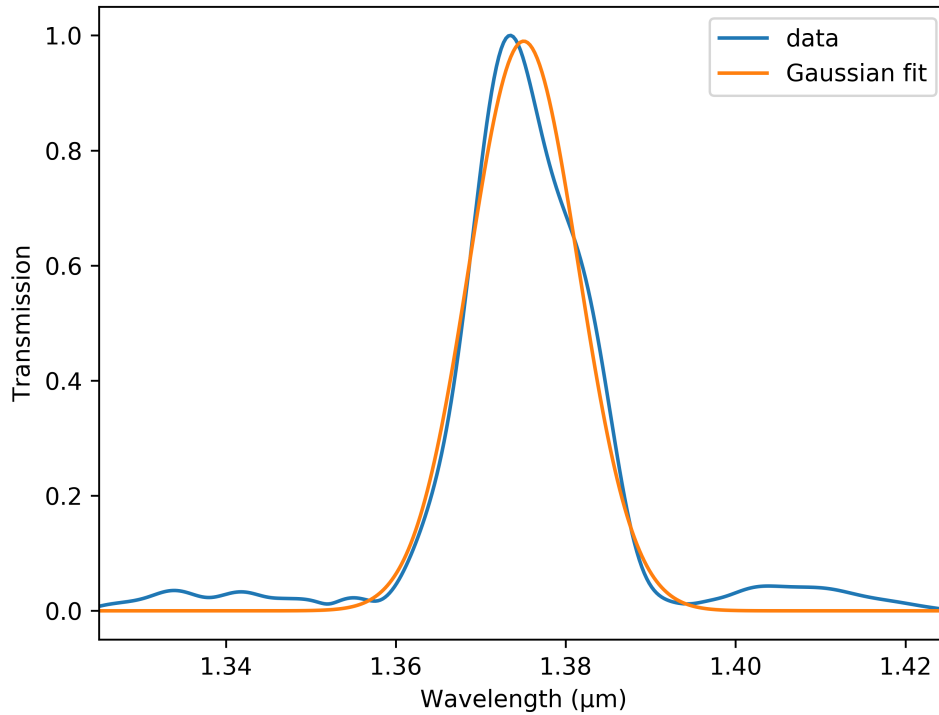
**Figure 7.35:** The recovered FTS spectrum and its associated Gaussian fit for the $\lambda = 1.38\,\mu m$ channel. The recovered spectrum is misshaped from the near Gaussian spectrum recovered in other channels, altering the measured R value.

resolution measurement is unaffected.

The simulated and measured spectral resolution values presented in table 7.3 both use the standard formula of $R = \lambda / \Delta\lambda$, however, the definition of their respective $\Delta\lambda$ is different. The simulated values use the Rayleigh criterion, where $\Delta\lambda$ is taken to be the difference in wavelength necessary, such that the first diffraction minimum of the PSF at wavelength $\lambda_1$ coincides with the maximum of another wavelength $\lambda_2$ as the light is dispersed along the spectral axis as a function of wavelength. The measured spectral resolution uses the definition that $\Delta\lambda$ is the range of wavelengths contained within the FWHM, i.e. the range of wavelengths on both sides of the peak where the integrated flux on the pixel being measured is half the flux of the central wavelength on that pixel. A loose comparison can be made, however, if a few assumptions are made.

The simplest comparison would be to measure the first wavelength at which the transmission goes to zero in the measured spectrum. If the pixel is assumed to have a small physical width,
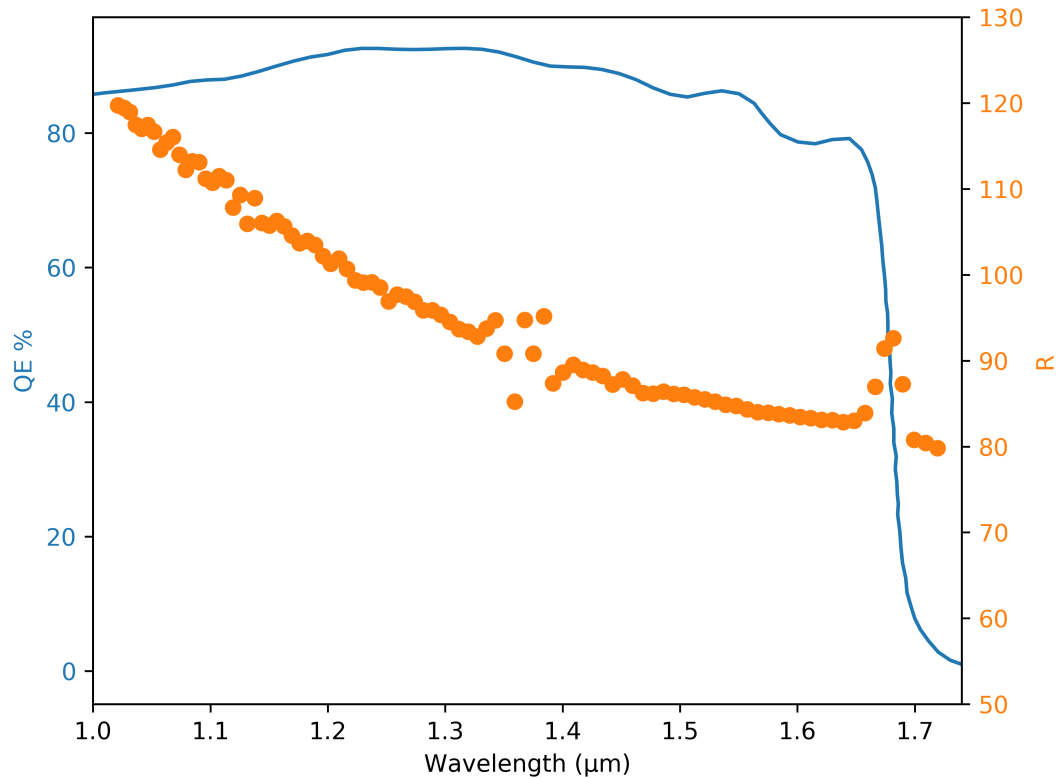
**Figure 7.36:** The Raptor Owl 640M QE from the manufacturers datasheet and the FTS measured spectral resolution as a function of wavelength. The spike in R value measurements between $\lambda$ = 1.67-1.69 $\mu$m are due to the rapid drop-off in QE at that wavelength range.

then by the Rayleigh criterion the wavelength whose null overlaps with the maximum of the central wavelength will contribute zero flux to the recovered spectrum. This is not a good measure in practice as there is noise associated with the data and so it is not feasible to say where the transmission goes to zero for the first time.

Instead, I find a conversation factor from the FWHM of the measured spectrum. Firstly, I assume that the shape of the monochromatic light falling on the detector is a perfect Airy disk PSF. Secondly, I assume that the pixel width is very small such that the instantaneous intensity of the Airy disk can be used instead of integrating the flux over a significant fraction of the Airy disk. The Half Width at Half Maximum (HWHM) of the measured spectrum now represents the difference in wavelength necessary, such that the flux landing on the pixel is half that of the wavelength centred on the pixel. This is demonstrated in figure 7.37, which plots two Airy disks offset from each other and shows that the flux from the second Airy disk is 0.5 at the peak of the first when the second disk is 42% of the way to satisfying the Rayleigh criterion. If I assume the
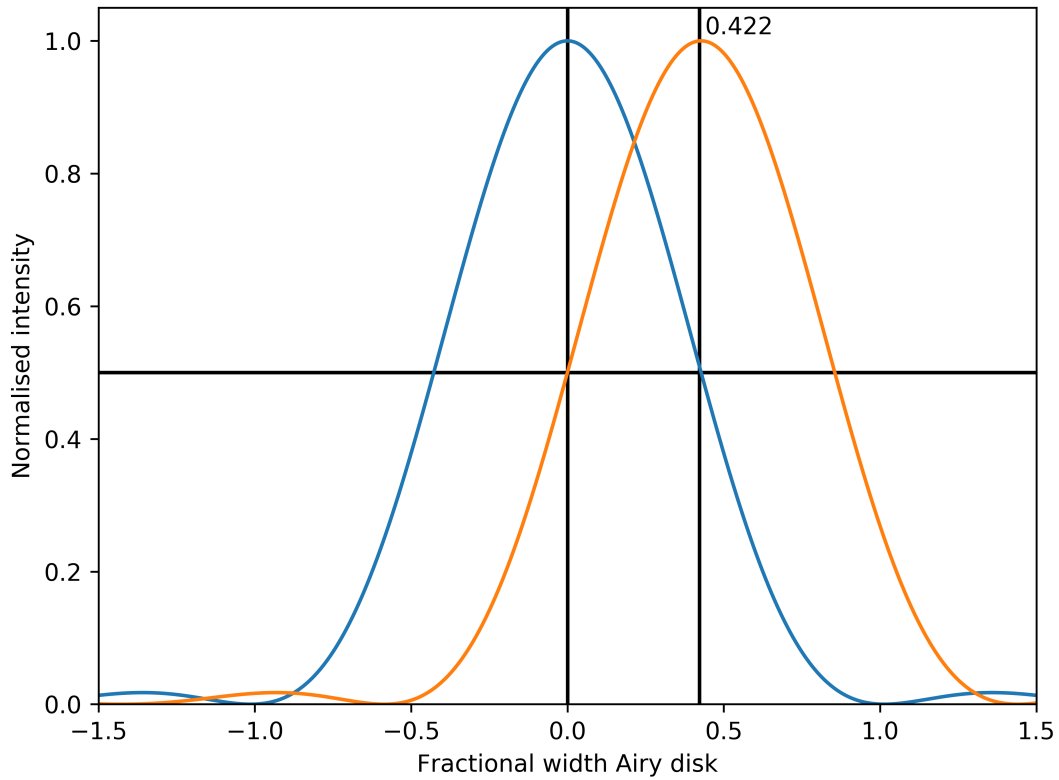
**Figure 7.37:** Two Airy disks offset from each other such that the intensity of one is a half the peak of the other. This criterion occurs when the two are offset by 42% the distance from the peak to the first null of the Airy disk. This information is used in deriving the relation between the FWHM spectral resolution value and that measured by the Rayleigh criterion.

dispersion is linear (which, as shown in figure 7.38 is a good approximation, particularly over the narrow range of wavelengths within one spectral channel) then the $\Delta\lambda$ which satisfies the Rayleigh criterion will be 2.38× the difference in wavelengths of the HWHM measured from the spectrum, which itself is $0.5 \times \Delta\lambda$ of the FWHM. Therefore $\Delta\lambda_{Rayleigh} = 0.5\times2.38 \, \Delta\lambda_{FWHM}$ = 1.19 $\Delta\lambda_{FWHM}$. The relation of the R values therefore follows as:

$$\frac{R_{\text{Rayleigh}}}{R_{\text{FWHM}}} = \frac{\lambda/1.19\Delta\lambda_{\text{FWHM}}}{\lambda/\Delta\lambda_{\text{FWHM}}} = \frac{1}{1.19}. \tag{7.8}$$

Therefore the *R* value by the Rayleigh criterion is a factor of 1.19× smaller than the *R* value by the FWHM. Given the number of approximations, this conversion factor cannot be used with a high degree of accuracy but it shows that the two R values are of the same order of magnitude.

In addition to quantifying the spectral resolution as a function of wavelength, I use the FTS data to measure the dispersion on the FOURIER focal plane. Figure 7.38 shows the distance

along the spectral axis of the detector from the $\lambda = 1\,\mu m$ channel as a function of wavelength for both the FTS data and a theoretical value based on Zemax modelling. I generated the FTS data by assuming PSF of the central wavelength from the Gaussian fit to each spectral channel was centred on the pixel the spectrum was generated for. I estimated the distance from the $\lambda = 1\,\mu m$ channel by taking the number of pixels away from it each spectral channel was and multiplying that number by the pixel size for the Raptor Owl 640M of $15\,\mu m$. I generated the Zemax model data by using PyZDDE (Sinharoy 2016) to interface with Zemax via a python script to return the location of the centroid of the geometric spot for 1,400 unique wavelengths at the modelled image plane of FOURIER. The data show good agreement with the residuals plotted underneath, showing a maximum deviation of the measured values from the theoretical model of $10\,\mu m$, less than half a pixel for the SAPHIRA detector's $24\,\mu m$ pixels. One likely cause of this discrepancy is an unknown tilt between the dispersed light and the Raptor Owl 640M camera, which would cause the distance of each channel to decrease or increase proportionally to the distance from the $\lambda = 1\,\mu m$ channel, which would explain the approximately linear slope in the residuals.

## 7.7   Summary

In this chapter I have demonstrated that the optics of the FOURIER beam combiner perform as expected. The experiments detailed in this chapter show the optics deliver the required PSF profile shaping, as well as a high throughput and high contrast interference fringes at the spectral resolution predicted by the optical design of FOURIER.

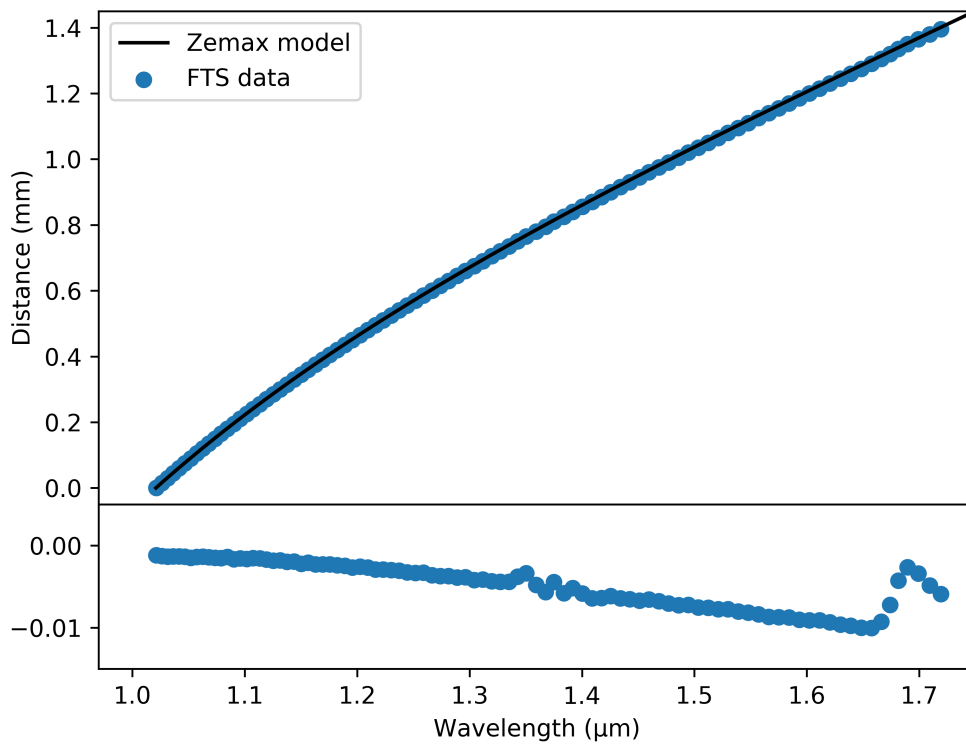**Figure 7.38:** The dispersion of the light at the FOURIER focal plane measured by the displacement from the λ = 1 μm spectral channel. The FTS data is generated by assuming the central wavelength of the recovered spectrum is centred on that pixel. The Zemax model represents the centroid of the geometric spot on the FOURIER focal plane sampled for around 1,400 wavelengths.

# CROSSTALK IN IMAGE PLANE BEAM COMBINERS

## 8.1 Introduction

In this chapter I explore the amplitude and extent of crosstalk arising in a long baseline optical interferometer for the previously unaccounted combined effects of atmospheric seeing, diffraction due to free space propagation, unequal path lengths and finite sized optics via a numerical simulation.

As mentioned in the declaration, this work has been published as Mortimer & Buscher (2022) by the Oxford University Press. All figures (with the exception of 8.1) also appear in the aforementioned publication.

Crosstalk in optical interferometry is a phenomenon by which, if multiple baselines are being sampled simultaneously, or multiplexed, the signal from one baseline can "leak" into another, altering the measured value of the interferometric visibility on the affected baseline and hence causing a systematic error on the visibility measurements. Even small levels of crosstalk can be crucial for some interferometric measurements. Figure 8.1 shows the visibility square curve for two models of a stellar disk, the first being a uniform disk for which the star is represented as a disk of uniform intensity on the sky and zero intensity outside the disk and a limb darkened disk in which the intensity drops off as a function of radius from the centre of the stellar disk. The model for both cases is taken from Rains et al. (2020) with the specific
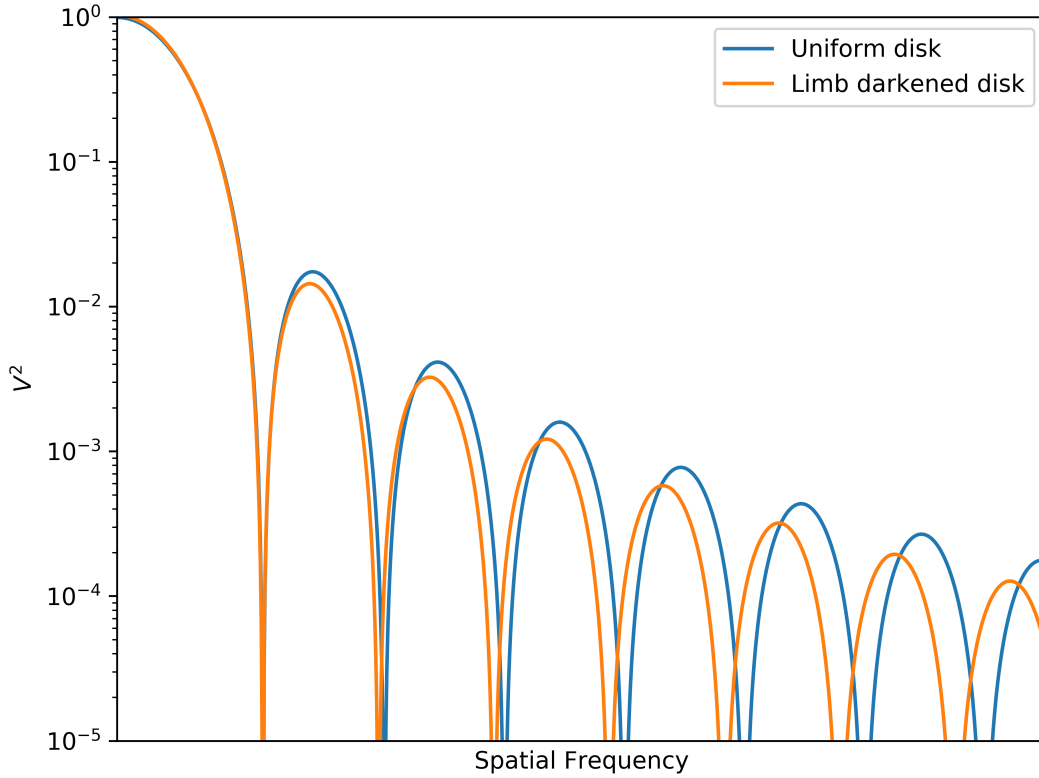
**Figure 8.1:** The visibility curve for the best fitting parameters to a uniform disk and limb darkened disk model for the star $\lambda$ Sgr. Both the model and model parameters for $\lambda$ Sgr are from Rains et al. (2020). Note that to distinguish between the uniform disk and limb darkened models measurements with an accuracy of order $V^2 = 3 \times 10^{-3}$ (the difference at the peak of the second lobe of the visibility function) are required.

parameters for the models being those they derive for the star $\lambda$ Sgr, though the specific fit to the star itself is unimportant. As can be seen in figure 8.1 in order to measure the effect of limb darkening observations must be made beyond the first lobe of the visibility function where the squared visibility takes on a maximum value of $1.7 \times 10^{-2}$ in the uniform disk model. Worse still, as a measure of the accuracy required to differentiate between different models, the difference between the uniform disk model and limb darkened model is $3 \times 10^{-3}$. This is the level of accuracy required to distinguish between the two most basic models of observations of resolved stellar disks. More complicated models require observations at even smaller visibilities. Indeed interferometric studies of the photosphere of red supergiant stars measure squared visibilities at the level of $10^{-2}$-$10^{-3}$ (Haubois et al. 2009; Chiavassa et al. 2010; Montargès et al. 2017, 2018) with Montargès et al. (2017) reporting visibility square measurements as low as $10^{-5}$.

## 8.2 Classical crosstalk

Before discussing the specifics of the simulation developed for this work it is worth discussing how a signal from one baseline can "leak" into another in image plane beam combination. Figure 8.2 shows the stages of image plane beam combination, A) shows two beams of starlight (shown here as perfect disks of uniform intensity) which are combined by bringing the pupils to a focus, generating a PSF modulated by interference fringes (B), averaging the PSF along the axis perpendicular to the interference fringes produces a 1D Line Spread Function (LSF) as shown in (C). Taking the modulus of the 1D Fourier transform of (C) gives the Modulation Transfer Function (MTF). Here two distinct peaks are visible, one corresponding to the zero spatial frequency term, ranging from a spatial frequency of zero to one in figure 8.2, and the interference fringe term which occurs from a spatial frequency of one to two. By taking the ratio of the peak of the interference term to the peak of the zero spatial frequency term the interferometric visibility can be extracted, this is discussed in a more rigorous way later in this chapter.

The location and width of the interference term can be understood by considering the pupil function shown in panel A) of figure 8.2. As discussed above the MTF is derived from the pupil function via the PSF. The PSF is the square absolute of the Fourier transformed pupil function, $b(f_x, f_y) \propto |\mathcal{F}\{P(x, y)\}|^2$ where $b(f_x, f_y)$ is the intensity pattern seen in the image plane and $P(x, y)$ the pupil function. The MTF is then the modulus of the Fourier transform of the PSF, i.e. MTF $\propto |\mathcal{F}\{b(f_x, f_y)\}|$. Putting these together and using the Wiener–Khinchin theorem (Goodman 2015), which states that the MTF is the modulus of the normalised autocorrelation of the pupil function (Harvey & Ftaclas 1995) we get

$$\text{MTF} \propto |\mathcal{F}^{-1}\{|\mathcal{F}\{P(x, y)\}|^2\}| \propto |\text{autocorr}(P(x, y))|. \tag{8.1}$$

Hence the process outlined in figure 8.2 is the equivalent to taking the modulus of the autocorrelation of the pupil function. The shape of the MTF can more easily be understood by considering the autocorrelation of the pupil function as shown in figure 8.3. Here I consider the autocorrelation of two 1D rectangular functions separated by two the times width of the rectangles. At zero delay the autocorrelation is at a maximum value (normalised in the MTF to unity). This is the stage labelled 1 in the MTF and is defined as zero spatial frequency.
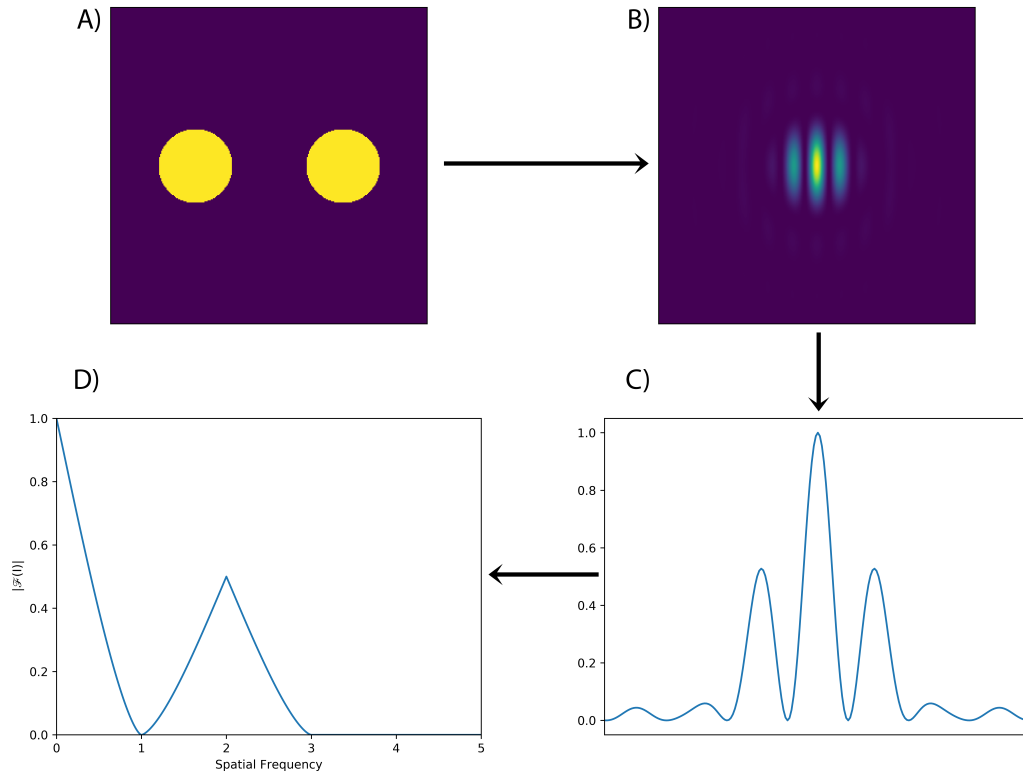
**Figure 8.2:** A procedure for extracting visibilities in an image plane combiner. A) shows two beams of starlight at the entrance of the combiner, B) the resulting PSF modulated by interference fringes when the pupils in (A) are combined in the image plane. C) the 1D LSF obtained by averaging along the axis perpendicular to the interference fringes. D) the modulus of the Fourier transform of (C) showing two terms, the zero spatial frequency term ($0 \leq$ Spatial Frequency $\leq 1$) and interference term ($1 \leq$ Spatial Frequency $\leq 3$).

The spatial frequency of one is then defined to be when the autocorrelation has advanced one pupil diameter, giving zero overlap and hence a MTF value of zero (stage 2). When the autocorrelation advances to two pupil diameters at what is defined as a spatial frequency of 2, the first pupil overlaps with the second and the MTF has half the amplitude as the zero spatial frequency component (stage 3). By the time the autocorrelation has swept through three pupil diameters there is no longer any overlap and the MTF again returns to zero (stage 4). This then explains the shape of the MTF, the zero spatial frequency term originates from the autocorrelation of all the pupils with themselves and the interference term originates from the correlation of one beam of starlight with the other, in this case with the correlation increasing linearly until the two are perfectly overlapped (stage 3) and subsequently linearly decreasing. The spatial frequency scale used throughout the rest of this chapter is set by this example, i.e.
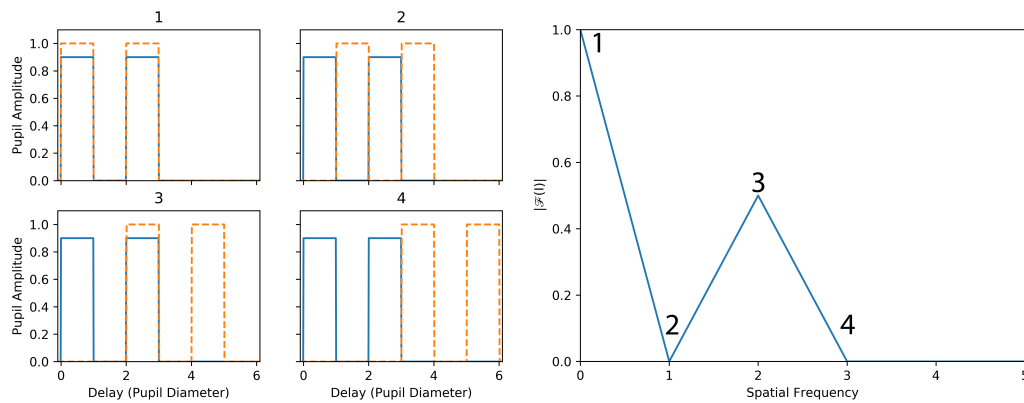
**Figure 8.3:** The autocorrelation of two rectangular functions separated by two pupil diameters with the pupil plane shown left and the resulting autocorrelation right. Four stages are labelled 1) the delay at zero giving a maximum value in the autocorrelation 2) with the delay at one pupil diameter 3) a delay of two pupil diameters 4) a delay of three pupil diameters. As the autocorrelation of the pupil function and MTF calculated in this chapter are mathematically the same this then explains the definition of the spatial frequency axis used throughout the rest of this chapter. Note the pupils in blue here have been reduced to an amplitude of 0.9 for the sake of clarity however the pupils used throughout in this chapter are of equal amplitude.

that the spatial frequency is equal to one when the autocorrelation function has advanced one pupil diameter.

From figure 8.3 it can also be deduced that the spacing of the pupils is what sets the spatial frequency at which the interference term appears, for example if the pupils were spaced four pupil diameters apart they would completely overlap at a spatial frequency of four in the MTF.

With this I can now explain how, if the pupil function of an image plane combiner is not properly considered, a fixed level of crosstalk can arise in image plane beam combination. Figure 8.4a shows three pupils separated by 2×, 4× and 6× their pupil diameters from each other and the resulting MTF which shows a zero spatial frequency term and three distinct peaks, one for each pupil pair combination or baseline. Figure 8.4b on the other hand shows the effect of moving the rightmost pupil 1.5 pupil diameters closer, the lowest spatial frequency interference term is unaltered and still peaks at a spatial frequency of two however the other two interference terms now peak at a spatial frequency of 2.5 and 4.5. The dashed lines show the contribution of each pupil pair individually however the solid line represents the MTF that is derived for the above pupil function, showing that the amplitude of the MTF at the peak spatial frequency has been significantly increased. As the visibility is extracted as a ratio of the MTF amplitude of the peak of the interference term to the zero spatial frequency term in this case the visibility on
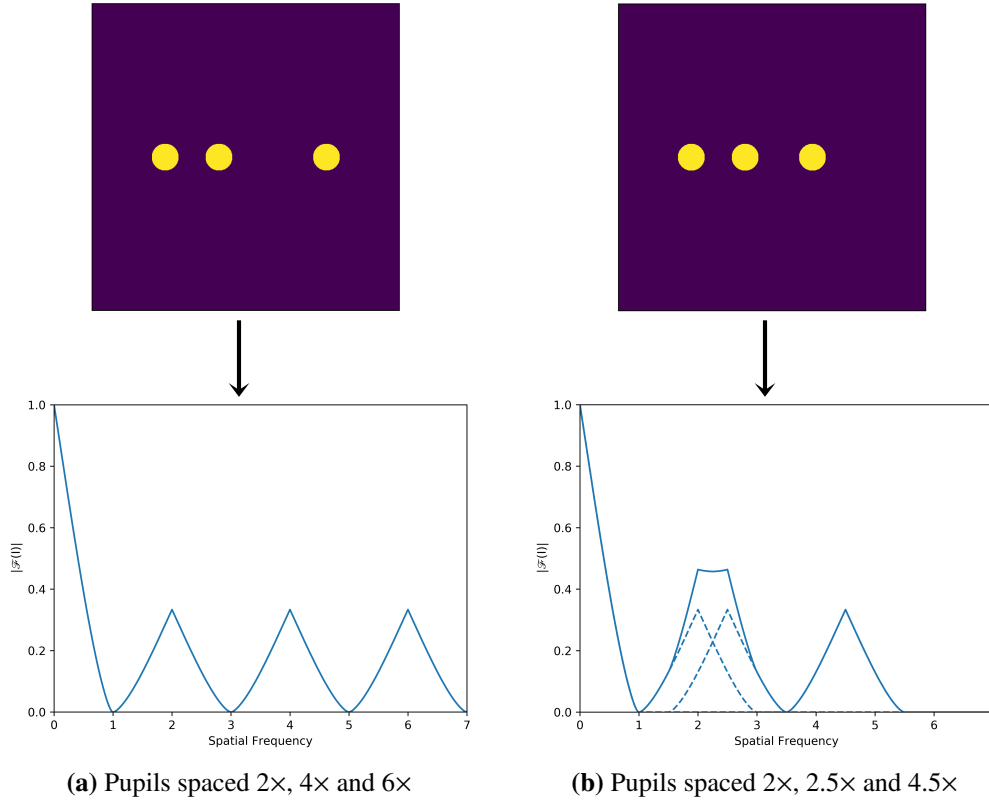
**(a)** Pupils spaced 2×, 4× and 6×          **(b)** Pupils spaced 2×, 2.5× and 4.5×

**Figure 8.4:** Pupil functions and their corresponding MTFs for different pupil separations. Figure 8.4a shows pupils separated 2×,4× and 6× their pupil diameter give three well separated peaks for the three interference terms whereas if the rightmost pupil is moved 1.5 pupil diameters closer as in figure 8.4b the interference terms of the two lower spatial frequency terms overlap and cause the overall MTF (solid line) to deviate from the interference terms for the individual pupil pairs (dashed lines) leading to crosstalk.

the lower two spatial frequency pupil pairs would be overestimated as signal has leaked from one baseline to the other and this is the phenomenon known as crosstalk.

This example also shows that in general crosstalk is an additive error in $V^2$. Where power from baselines other than the one being measured in the MTF contribute to the total power measured at a given spatial frequency

## 8.3  Model

The model used in my simulation is that of a simple two-telescope interferometer observing an unresolved point source, i.e. a source whose angular diameter is significantly less than $\lambda/B$ where $\lambda$ is the wavelength of observation and $B$ the baseline, or projected on-sky separation of the two telescopes. Hence our simulated observations have a ideal visibility of unity. While

only two telescopes are simulated here, the results from this model can be used to infer the crosstalk in an interferometer with any number of telescopes using the fact that the propagation and interference of starlight on any given baseline is independent of the other baselines.

The modelled interferometer is subject to atmospheric seeing. It is assumed that the telescopes are in the near field of the atmospheric turbulence and hence there are only phase perturbations and not amplitude perturbations in the received wavefront. The validity of this approximation is discussed by Young (1974) and in section 7.3 of Roddier (1981). In the simulation the two phase perturbed wavefronts are collected by circular apertures and are optionally corrected for tip-tilt errors as all current long-baseline interferometers are equipped with at least tip-tilt level adaptive optics. The two perturbed wavefronts are then propagated to simulate the transporting of the wavefronts from the telescopes to the beam combining instrument. The two wavefronts can be transported by different distances to account for the unequal path lengths required in an interferometer for targets not at zenith. The beams are subsequently cropped by a scalable aperture, to simulate finite sized optics along the beam train. They are then brought to a focus to generate a PSF modulated by interference fringes which is the raw output of image plane beam combination. Figure 8.5 outlines a simplified schematic of the simulation.

From the PSF modulated by interference fringes the visibilities are then extracted. This process is designed to mimic how visibilities could be extracted in practice. I average the PSF along a line parallel to the fringe peaks to yield the LSF and then perform a 1D Fourier transform to arrive at the MTF in the form shown in panel C of figure 8.2. By analysing the power contained in the interference term with respect to the zero spatial frequency term in the MTF of the PSF it is possible to extract the visibility. In the simulation the rms visibility for an ensemble of exposures was calculated using

$$V_{\text{rms}}^2 = 4 \frac{\langle X^2 \rangle}{\langle F \rangle^2}, \tag{8.2}$$

where $X$ represents the value of the unnormalised MTF at the expected central spatial frequency of the interference term, and $F$ the value of the unnormalised MTF at zero spatial frequency (the DC term), with $\langle\rangle$ denoting averaging over an ensemble of exposures. It is necessary to average over an ensemble of exposures as atmospheric seeing will randomly alter the visibility from exposure to exposure. However calculating the visibility via the above equation tends towards the correct value for many exposures. How I quantify how close to the correct value
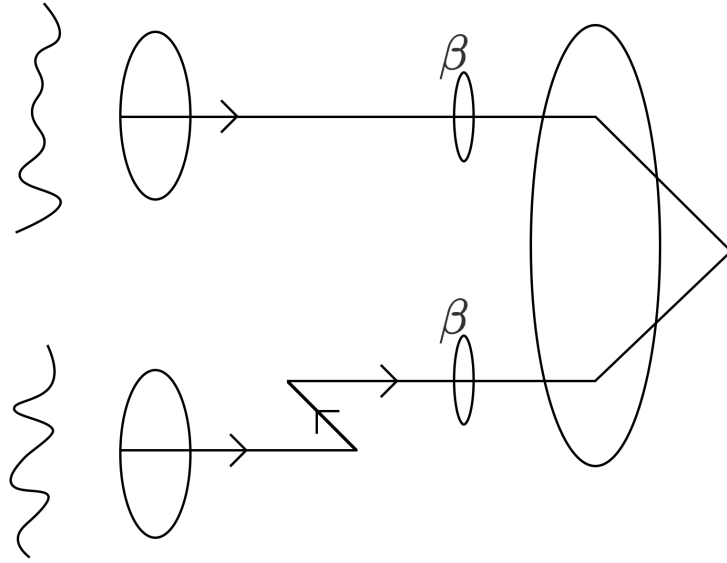
**Figure 8.5:** A simplified schematic demonstrating the various stages of the simulation. From left to right the atmospherically perturbed complex amplitudes are cropped by the circular collecting apertures before being optionally tip-tilt corrected and propagated, with the lower beam being propagated a greater distance. The two beams are then cropped by a circular aperture after propagation before being brought to a focus to generate a PSF modulated by interference fringes.

my simulation is for a number of simulated frames is discussed in section 8.5. Note that, as used here, the MTF is not normalised to unity at the origin on an exposure-by-exposure basis, as for runs with a finite value of $\beta$ the value at the origin (the total flux) varies from exposure to exposure. This is due to the atmospheric phase perturbations causing amplitude variations as the beams are propagated, leading to a loss in flux as the pupils are subsequently truncated with a finite $\beta$.

I do not include the effects of a dedicated spatial filter which are typically implemented to remove wavefront errors and boost the observed visibility (Keen et al. 2001) in image plane beam combiners.

This simplified model does not account for the effects of a finite exposure time or optical aberration induced by the optics along a typical beam train. Ignoring these effects allows me to build a model which is applicable to any interferometer.

## 8.4 Parameter space

In order to make this work readily applicable to any interferometer the simulation is built using five dimensionless parameters. The range of values of each parameter in my simulation is guided by the expected values for that parameter at the Magdalena Ridge Observatory Interferometer (MROI). The MROI will cover a wide range of parameter space, observing at wavelengths between $0.6\,\mu m$ and $2.4\,\mu m$ on baselines from $7.8\,m$ to $347\,m$. Most current-generation interferometers will also be covered by the parameter range used here. Four of the parameters are the same as those used in (Horton et al. 2001), and are defined in the following paragraphs.

The parameter $\alpha$, given by

$$\alpha = \frac{D}{r_0} \tag{8.3}$$

characterises the telescope diameter ($D$) in terms of the Fried parameter ($r_0$): for a fixed-sized telescope it is inversely proportional to the strength of the seeing. The values used here range from 1.5 to 16.5. Given the $1.4\,m$ aperture telescopes the MROI utilises, the worst case scenario for $\alpha$ (the largest value) was found by assuming a $r_0$ of 10.3 cm (the equivalent of 1 arc-second of seeing) for a wavelength of $\lambda = 0.5\,\mu m$ at zenith and then scaling $r_0$ to the shortest wavelength, $\lambda = 0.6\,\mu m$, and largest zenith angle ($60°$) expected at the MROI. The best case scenario (smallest $\alpha$) was found by assuming a $r_0$ of 14.7 cm (the equivalent of 0.7 arc-seconds of seeing) for a wavelength of $\lambda = 0.5\,\mu m$ at zenith, then scaling $r_0$ to the longest wavelength $\lambda = 2.4\,\mu m$ and observations at the zenith. Converting $r_0$ between wavelengths from the seeing at $\lambda = 500\,nm$ was calculated by the relation $r_0(\lambda) \propto (\lambda)^{6/5}$. Converting $r_0$ for a given zenith angle was calculated by $r_0(\theta) = r_0(\theta = 0)(\cos\theta)^{3/5}$ (Tatarskii 1961).

The parameter $\beta$, given by

$$\beta = \frac{d'}{d} \tag{8.4}$$

characterises the diameter of the cropping aperture after propagation $d'$ in terms of the diameter of the pupil before propagation $d$. The range of values for $\beta$ was chosen based on realistic ratios of beam size to the smallest clear aperture along a beam train, ranging from a $\beta$ of 1, where the optics have a clear aperture equal to the diameter of the collimated pupil before propagation, to a value of 3.

The parameter $\gamma$, given by

$$\gamma = \frac{z_1}{z_2} \tag{8.5}$$

is the ratio of the propagation distance of one beam ($z_1$) to the other ($z_2$) and allows for the effects of unequal path lengths to be simulated. Here a value of $\gamma$ larger than unity is defined as $z_2$ propagating a distance shorter by a factor of $\gamma$ than $z_1$. At the MROI $\gamma$ ranges from 1 for observations at the zenith when the path length through both arms of the interferometer are equal, to 1.3 for observations when an object is observed at a zenith angle of 60° by two telescopes separated by a 347 m baseline as part of a Y shaped array configuration.

The fourth dimensionless parameter $\delta$, given by

$$\delta = \frac{4\lambda z_1}{\pi d^2} \tag{8.6}$$

is a measure of how much the propagated beam is affected by diffraction, and includes the effects of wavelength $\lambda$, propagation distance $z_1$ and beam diameter $d$ in one parameter. Looking at equation 8.6 it can be seen that the smallest $\delta$ arises for the shortest path length and the shortest wavelength. At the MROI this is for a baseline of 7.8 m and a wavelength of 0.6 μm which gives a $\delta = 0.07$. Interestingly, for the MROI the contribution to $\delta$ due to the propagation from the telescope, along the beam relay system and through the delay lines is negligible in the case of the shortest baseline ($\delta = 0.006$) compared to the contribution of the 14.19 m propagation after the delay lines within the beam combination laboratory ($\delta = 0.064$). This is because pupils travelling along the beam relay system and through the delay lines have a collimated diameter of 95 mm whereas for propagation within the beam combination laboratory the pupils are compressed to a diameter of 13 mm. See Buscher et al. (2013) for a further discussion of the MROI beam architecture. The largest value of $\delta$ at the MROI occurs at the wavelength of 2.4 μm on the longest baseline (347 m), with the same 14.19 m propagation distance after beam compression within the beam combination laboratory and is $\delta = 0.446$.

The final dimensionless parameter is T, which defines the level of tip tilt correction and ranges between 0, no correction, and 1, complete removal of tip tilt atmospheric perturbations.

## 8.5   Model implementation

My atmospheric model is built using the python package MegaScreen (Buscher 2016) which generates a single layer of phase perturbations (a phase screen) with a Von Kármán spectrum,

characterised by the Fried parameter $r_0$ and an outer scale $L_0$. For all the following calculations $L_0$ was set to 58 times the aperture diameter for the majority of cases where the pupil was 120 pixels.

MegaScreen generates one or more "windows" on a infinite virtual phase screen where for each iteration of the phase screen generator one or more 2D arrays of phase screen perturbations are returned. Between iterations the frozen-turbulence model is advanced by a configurable step size to simulate time evolution.

In my implementation two square windows of width equal to the diameter of the telescope (which was set to 120 pixels unless otherwise stated in the results presented below) were simulated per iteration, with the step size between iterations being set to the diameter of the telescope to ensure that each iteration was independent (i.e. did not share the same phase screen as the previous iteration). For the purposes of phase screen generation the two telescopes in our simulation were separated by 160 times the pupil diameter to ensure that the phase screens generated for the two apertures were also independent.

The phase screens were then corrected in some runs for tip tilt perturbations by the use of a Zernike filter. A Zernike filter is an approximation for an adaptive optics system in which various Zernike polynomials (in this case tip and tilt) are perfectly removed from the phase screen. This is done by calculating the tip tilt contribution of the overall phase screen, generating a new phase screen that contains only the tip tilt contribution, and subtracting it from the original phase screen. This essentially simulates a perfect adaptive optics corrections up to the highest order Zernike removed and no adaptive optics corrections for higher Zernike orders.

In this work I simulated three levels of tip tilt correction, $T = 0$ corresponding to no tip tilt correction, $T = 1$ corresponding to the perfect tip tilt correction described above, and $T = 0.5$ where the same tip tilt only phase screen is subtracted but it's amplitude is halved before subtraction, meaning some but not all of the tip tilt contribution is removed.

The pupils were then compressed from the diameter of the telescope ($D$) to a diameter $d$ (this is achieved in practice by redefining the pixel scale of the complex amplitudes, assuming perfect beam compression) and propagated through free space at the centre of a 3,000 pixel grid a distance $z_1$ and $z_2$ for the two beams respectively by applying the Fresnel approximation of scalar diffraction theory as given in Goodman (1988). This is applicable to our simulation as

the distances propagated (typically tens to hundreds of meters) are many times larger than the diameter of the beams being propagated (for the specific case of the MROI, beam diameters are 95 mm propagated over tens to hundreds of meters), as well as the fact that the beam diameters are always significantly larger than the wavelength of light being propagated. The propagation is calculated in Fourier space by equation 8.7.

$$a(\hat{f}_x, \hat{f}_y, z) = a(\hat{f}_x, \hat{f}_y, 0) \exp((-i\pi\delta)(\hat{f}_x^2 + \hat{f}_y^2)). \tag{8.7}$$

This follows the form of Horton et al. (2001) where $a(\hat{f}_x, \hat{f}_y, 0)$ represents the Fourier transform of the initial complex amplitude which is to be propagated a perpendicular distance z, $\delta$ is as defined in equation 8.6 except that $d$ is the width of the grid being propagated, which is many times the diameter of the actual pupil to avoid aliasing, $\hat{f}_x$ and $\hat{f}_y$ are dimensionless spatial frequencies of the dimensionless spatial coordinates $\hat{x} = 2x/d$ and $\hat{y} = 2y/d$. The propagated beam is then recovered by taking the inverse Fourier transform of $a(\hat{f}_x, \hat{f}_y, z)$.

After propagation, the pupils were cropped by a circular aperture to simulate the effects of finite-sized optics along the beam train.

Finally, the pupils were placed onto a common grid and converted to a PSF via a 2D Fast Fourier Transform (FFT) routine to simulate transformation to the image plane and beam combination. The resulting PSF, modulated by interference fringes, was then averaged along the direction perpendicular to the fringes to generate a 1D LSF. Taking the absolute value of the FFT of the LSF gives the MTF. The value of the MTF at a spatial frequency of zero was stored for each iteration of the simulation and used as the $F$ term in equation 8.2. Equation. 8.2 was then computed for each spatial frequency sampled in the MTF with $X$ being the amplitude of the MTF at each point sampled in spatial frequency space in turn.

Throughout the rest of this chapter, unless otherwise stated, the two diffracted pupils are separated by four times their undiffracted diameters as shown in figure 8.6. This ensures both that the pupils do not overlap which would be nonphysical, and that there is a significant separation between the DC and interference terms in the MTF. One exception here is for runs with $\beta > 4$, in which case the pupils are separated just enough so they do not overlap, i.e. for runs with $\beta = 10$ the pupils were spaced 10 times their undiffracted diameters. Unless otherwise stated the spatial frequency scale in all subsequent plots has been shifted such that the peak of the interference term is at a spatial frequency of zero.
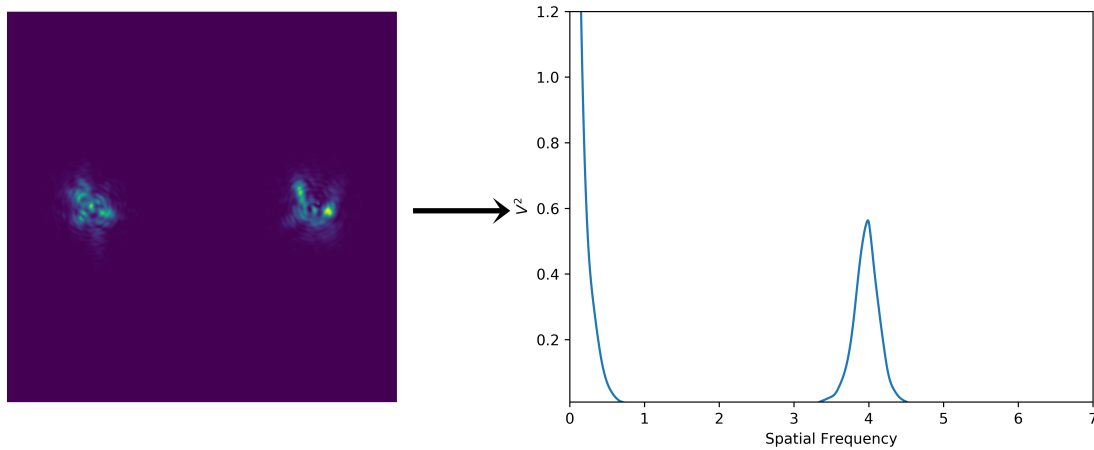
**Figure 8.6:** Two propagated pupils separated by four times their undiffracted diameters for a single exposure with the parameter configuration $\alpha = 3$, $\beta = 3$, $\delta = 0.1$, $\gamma = 1$, $T = 1$. The upper image shows the instantaneous pupil intensity at the entrance to the beam combiner and the lower plot shows the resulting squared visibility of the above instantaneous pupil intensity.

For each run 10,000 unique realisations of an atmospherically perturbed observation were generated. These were subsequently distributed into 20 bins of 500 PSFs each. The value of $V_{\text{rms}}^2$ was then calculated for each of these bins using equation 8.2, resulting in 20 independent visibility estimates which were then averaged allowing for a final estimate of the visibility and its standard deviation to be generated for each run. From the standard deviation the standard error of the mean was calculated however it is often smaller than the line thickness of the plots in this chapter. Due to how this technique was implemented it was possible to calculate a value for the visibility for all spatial frequencies simultaneously, and not just the visibility at the spatial frequency of the peaks of the interference terms in the MTF.

## 8.6   Pupil shear

Low order atmospheric perturbations of tip and tilt are the dominant terms in an atmospherically perturbed wavefront and so are a natural first place to investigate. Tilt errors introduced by atmospheric perturbations can lead to significant beam shear in the beam combination laboratory due to the large propagation distances often experienced in long baseline optical interferometery. As the spatial frequency at which the interference term appears in the MTF depends on the spacing between the beams in the pupil plane, a naive model would assume that the spatial frequency of the interference term in the MTF would shift linearly with any change in pupil spacing and lead to the side lobes of the interference term also shifting and contributing to
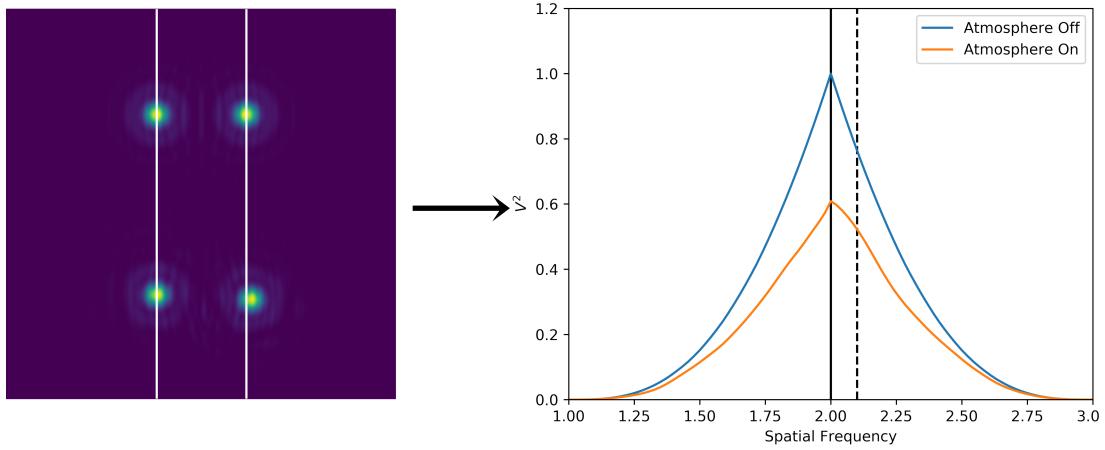
**Figure 8.7:** A demonstration that pupil shear due to propagation does not cause a shift in spatial frequency of the interference term. Left: the pupil plane after diffraction for a system with a $\delta = 0.5$ and $\gamma = 1$. The upper pair of pupils are the case of no atmospheric perturbations and are still separated by two times their undiffracted pupil diameters after propagation. The lower pair of pupils are from a separate run and super imposed and offset vertically with the same values of $\delta$ and $\gamma$ but with atmospheric perturbations at the level of $\alpha = 1.5$. Due to tip-tilt induced shear errors these pupils are separated by 2.1 times their undiffracted pupil diameters. Right: the resulting Visibility for the two runs with the atmosphere off case giving a visibility of unity at a spatial frequency of 2 (solid vertical line). The atmosphere on case shows significant deviation from the ideal curve due to atmospheric perturbations but still peaks at a spatial frequency of 2. The dashed vertical line is at the spatial frequency the atmosphere on peak would be expected to be at based on the pupil separation alone.

baseline crosstalk.

The simulation shows that this is not the case however. In the ideal case of no cropping aperture ($\beta \approx \infty$) and equal path lengths ($\gamma = 1$) I observe pupil shear altering the pupil spacing but the spatial frequency of the interference term does not shift. An example of this is given in figure 8.7 where a system with $\delta = 0.5$ and $\gamma = 1$ is compared with no atmospheric perturbations ($\alpha = 0$) and atmospheric perturbations introduced at a level of $\alpha = 1.5$ (atmosphere on). Note here the pupils are only separated by two times their undiffracted diameters. In the case of no atmospheric perturbations the propagated pupils remain spaced at two times their undiffracted diameters. The resulting visibility curve shows a visibility of unity at a spatial frequency of two. In the presence of atmospheric perturbations the pupil shear in the example shown changes the beam separation to 2.1 times the undiffracted beam diameter. The naive model of pupil shear would then expect the peak of the interference term to appear at a spatial frequency of 2.1 (dashed vertical line in the lower plot of figure 8.7), however this is not the case and the peak still appears at a spatial frequency of two.

For the example in figure 8.7 the simulation was reconfigured to remove Zernike modes

with Noll indices between 3 and 15 from the atmospherically perturbed wavefront to isolate the effects of tip and tilt errors from higher order atmospheric perturbations.

This discrepancy between the variation in the beam shear with propagation distance and the constancy of the spatial frequency of the fringe peak is a consequence of a more general result, which is that, under certain assumptions, the pattern resulting from the interference of light originating from a given set of telescope pupils is independent of the propagation distance. This more general result can be derived by considering the complex amplitude distribution $B(x, y)$ at the input to the beam combiner as the sum of a set of complex amplitude functions

$$B(x, y) = \sum_j A_j(x, y, \delta_j) * \delta(x - x_j, y - y_j) \tag{8.8}$$

where $A_j(x, y, \delta_j)$ is the complex pupil amplitude function of the pupil from telescope $j$ after demagnification by a beam compressor and propagation by a dimensionless distance $\delta_j$ from the telescope, this is convolved with $\delta(x, y)$ which is the Dirac delta function and $x_j$ and $y_j$ are lateral offsets between the telescope pupils fixed by the design of the beam combiner. The complex amplitude $b(f_x, f_y)$ seen in the image plane is then given by a scaled version of the Fourier transform of the pupil function

$$b(f_x, f_y) \propto \sum_j a_j(f_x, f_y, \delta_j) \exp(-2\pi i[x_j f_x + y_j f_y]) \tag{8.9}$$

where $a_j(f_x, f_y, \delta_j)$ is the Fourier transform of $A_j(x, y, \delta_j)$. Equation (8.7) shows that propagation from the telescope to the beam combiner results in the multiplication of $a_j$ by a complex phase factor dependent on $\delta_j$. In the particular case of the propagation distance from all the telescopes being the same so that $\delta_j = \delta$, we get

$$b(f_x, f_y) \propto \exp((-i\pi\delta)(f_x^2 + f_y^2)) \sum_j a_j(f_x, f_y, 0) \exp(-2\pi i[x_j f_x + y_j f_y]), \tag{8.10}$$

which is independent of propagation distance except for a phase factor. The observed intensity pattern depends only on the modulus and not the phase of the complex amplitude in the image plane, so the interference pattern is independent of propagation distance, providing that the propagation distance is the same for all beams and there are no intervening apertures which block some of the propagating light.

The observation that the spatial frequency of the peak of the interference pattern does not shift even when the centre-to-centre separation of the pupils varies due to propagation

indicates the need to consider both the amplitude and the phase of the pupil-plane pattern when deriving the autocorrelation of the pupil: shifts in the the pupil amplitude distribution caused by propagation effects must be accompanied by exactly compensating changes in the pupil phase distribution.

This result would imply that no crosstalk generated due to beam propagation, however as stated above this result is invalid if the propagation distance of the two pupils is not the same ($\gamma \neq 1$) or for finite sized optics, ($\beta < \infty$). The remainder of this chapter will explore these more general cases where propagation does affect crosstalk.

## 8.7   Crosstalk parameter dependence

In this section I analyse the effects of each parameter on crosstalk individually to separate out their impact before going on to apply all effects simultaneously in a realistic observing scenario in section 8.8.

### 8.7.1   Crosstalk dependence on $\delta$ & $\beta$

The effects of the propagation parameter $\delta$ and the aperture ratio parameter $\beta$ are presented simultaneously here as it is only when both $\beta$ is finite and $\delta > 0$ that there is an effect on crosstalk. For a non-zero value of $\delta$, diffraction leads to an increase in the size of the beam. A finite value for $\beta$ leads to a cropping aperture acting as a form of spatial filter, leading to what Horton et al. (2001) refers to as "Fresnel spatial filtering". As the beam propagates, perturbations in the wavefront caused by atmospheric seeing on scales smaller than the diameter of the initial pupil will diffract out of the pupil faster than the pupil itself diffracts. When the beam is subsequently cropped, the higher spatial frequency perturbations are disproportionately removed, leaving the pupil partially spatially filtered.

This effect is demonstrated in figure 8.8 which shows a pupil subjected to atmospheric seeing ($\alpha = 4$, $T = 1$) after being propagated by $\delta = 0.5$, before being cropped by a cropping aperture of $\beta = 1$ (the size of the undiffracted pupil) represented by the white ring. The starlight which is kept after cropping (light within the white ring) is much more similar to what is expected from diffraction alone without atmospheric perturbations (top pupils in figure 8.7) than the light which is cropped, i.e. the light retained contains fewer high spatial frequency
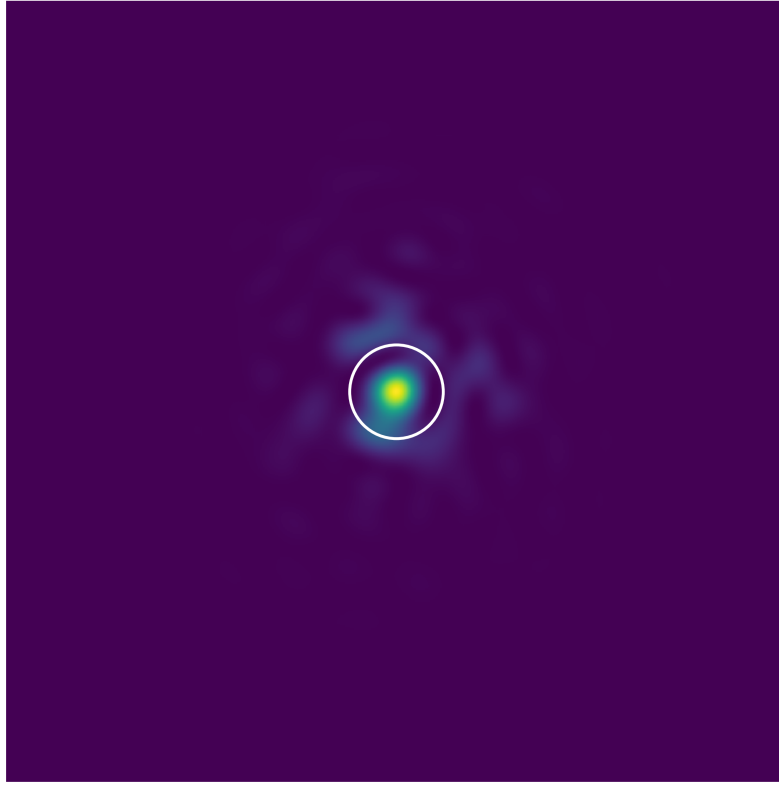
**Figure 8.8:** A pupil subject to atmospheric seeing ($\alpha = 4$, $T = 1$) after propagation by $\delta = 0.5$, before being cropped by a cropping aperture of $\beta = 1$ represented by the white ring. The higher spatial frequency amplitude perturbations arising from atmospheric seeing are disproportionately removed by the cropping aperture, leaving the pupil partially spatially filtered.

perturbations arising from atmospheric seeing and so the beam is partially spatially filtered.

The further the beam propagates the greater the filtering. This effect is evident in the simulation as figure 8.9 shows, the visibility of the interference term increases for a larger propagation distance given a fixed value of $\beta$.

Returning to the impact on crosstalk, I first consider the case of no atmospheric perturbations giving perfect plane wave initial pupils. As shown in figure 8.10, I find non-zero MTF values above a spatial frequency of 1 for various values of $\beta$ (with the other relevant parameters fixed at $\delta = 0.5$ and $\gamma = 1$). These non-zero values mean that there can be crosstalk for aperture spacings such as that illustrated in figure 8.3, where the classical crosstalk between adjacent baselines is zero. In the following, I refer to any power beyond a spatial frequency of 1 to as crosstalk, and give the resulting visibility value this crosstalk corresponds to the label $\Delta V^2$. Whether or not there is actual crosstalk in any given scenario depends on the spatial frequencies
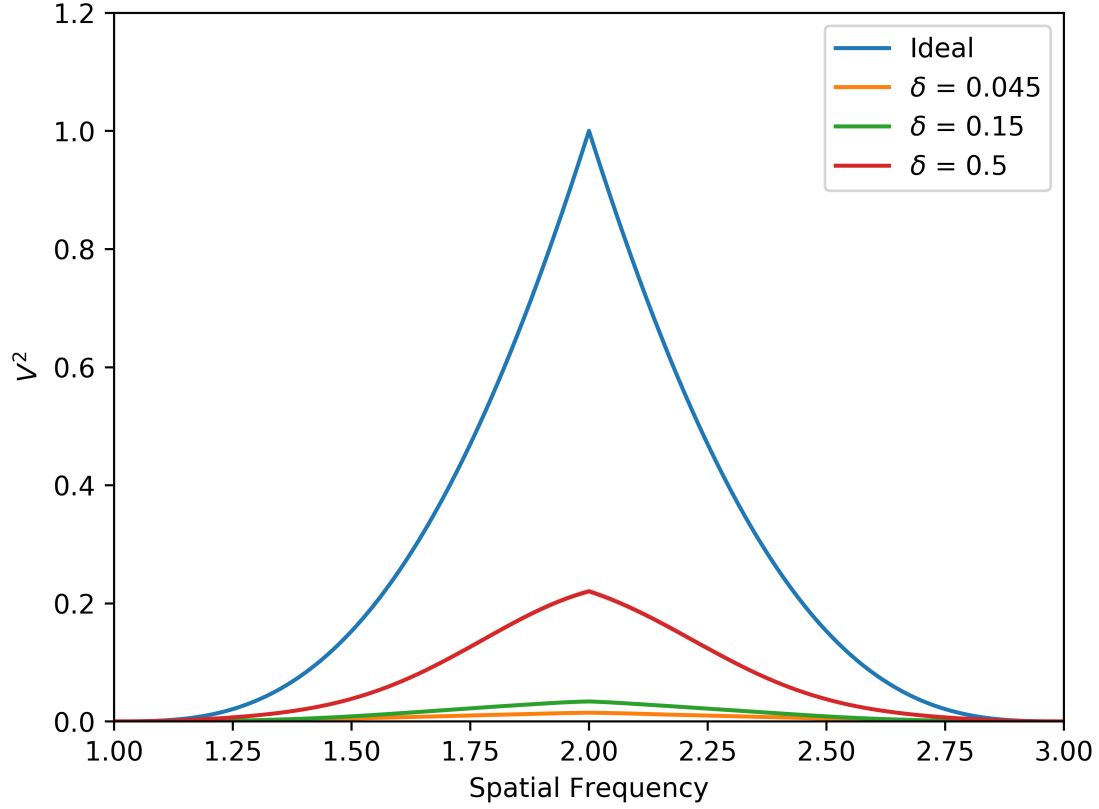
**Figure 8.9:** Visibility of the interference term for three values of $\delta$ showing an increase in visibility for increasing $\delta$ due to Fresnel spatial filtering. The other parameters were held constant at $\alpha = 9$, $\beta = 1$, $\gamma = 1, T = 1$. The spatial frequency axis has not been re-scaled and the peak of the DC term is at a spatial frequency of zero.

corresponding to different baselines.

Figure 8.11 shows that including finite amounts of atmospheric perturbations generally results in an increase in the level of crosstalk for a given value of $\beta$. There is a clear cut off in the maximum spatial frequency of the crosstalk for any given $\beta$. This effect can be understood by considering, as discussed in section 8.2, that the MTF is the modulus of the autocorrelation of the pupil function. The area of the pupil expands due to diffraction however, for a value of $\beta = 1$ as the pupils are cropped to their original diameters after propagation we have a similar situation as in figure 8.3 where the MTF must be zero at spatial frequencies where there is no overlap of the pupils. As $\beta$ increases, the maximum pupil diameters and so the highest spatial frequency at which crosstalk can exist also increases. As the runs presented in figure 8.11 are for a large value of $\delta$=0.5, the diffracted pupil is always larger than the cropping aperture and so it is the cropping aperture which limits the maximum spatial frequency resulting in the sharp
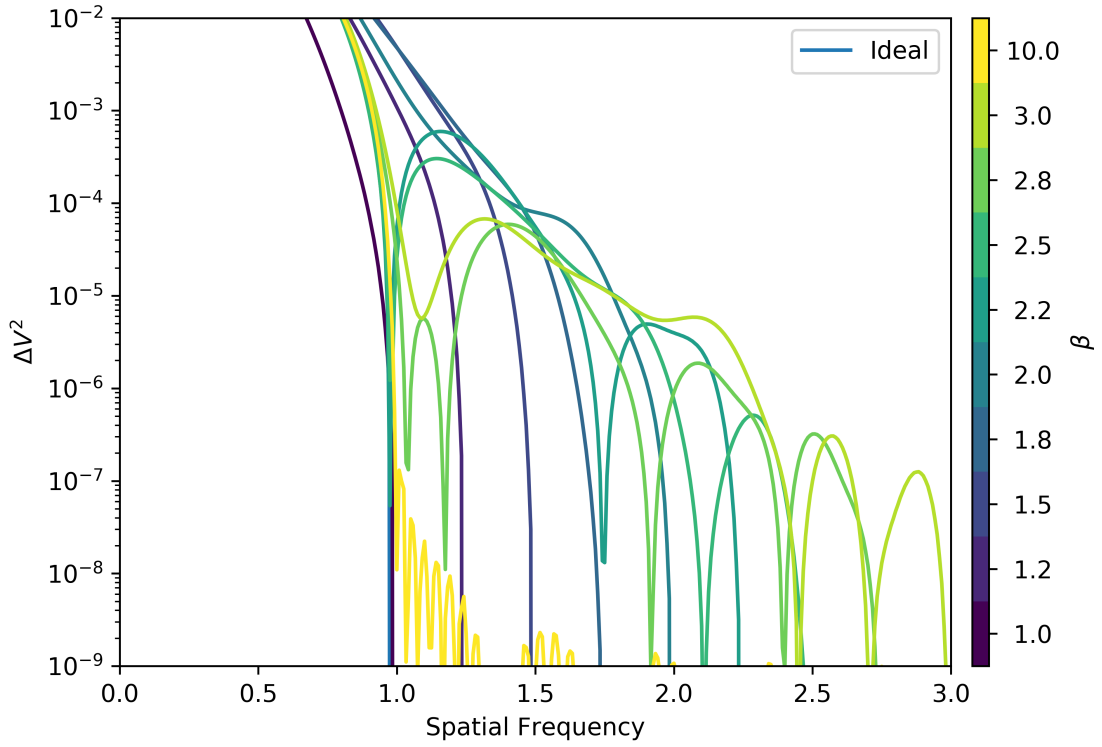
**Figure 8.10:** Crosstalk as a function of $\beta$ (cropping aperture size) for fixed parameter values of $\delta = 0.5$, $\gamma = 1$ when no atmospheric perturbations are induced. Here the crosstalk arises purely due to free space propagation. Note the tick marks indicate the values of $\beta$ plotted which follow the perceptually uniform colour map linearly with the exception of the $\beta = 10$ run.

cut off.

In addition to crosstalk at higher spatial frequencies as $\beta$ increases, the amplitude of the crosstalk decreases, tending towards near zero crosstalk for a large value of $\beta$. As $\beta$ tends towards infinity (an uncropped pupil) the system tends towards the case discussed in section 8.6, where the phase information aids in removing any crosstalk. This is evidenced by the $\beta = 10$ run in figure 8.11.

These two effects lead to an interesting dependence of crosstalk at a fixed spatial frequency as a function of $\beta$ (cropping aperture size). As figure 8.12 shows for a fixed spatial frequency the level of crosstalk is zero until the cropped pupil is large enough to retain information at that spatial frequency(as per the discussion above in this section), at which point the crosstalk is at its maximum value. As $\beta$ continues to increase the amplitude of the crosstalk decays due to the system approaching the case of an uncropped pupil. In figure 8.12 the amplitude of the crosstalk is as high as $\Delta V^2 = 6.5 \times 10^{-4}$ for a value of $\beta = 1.5$.

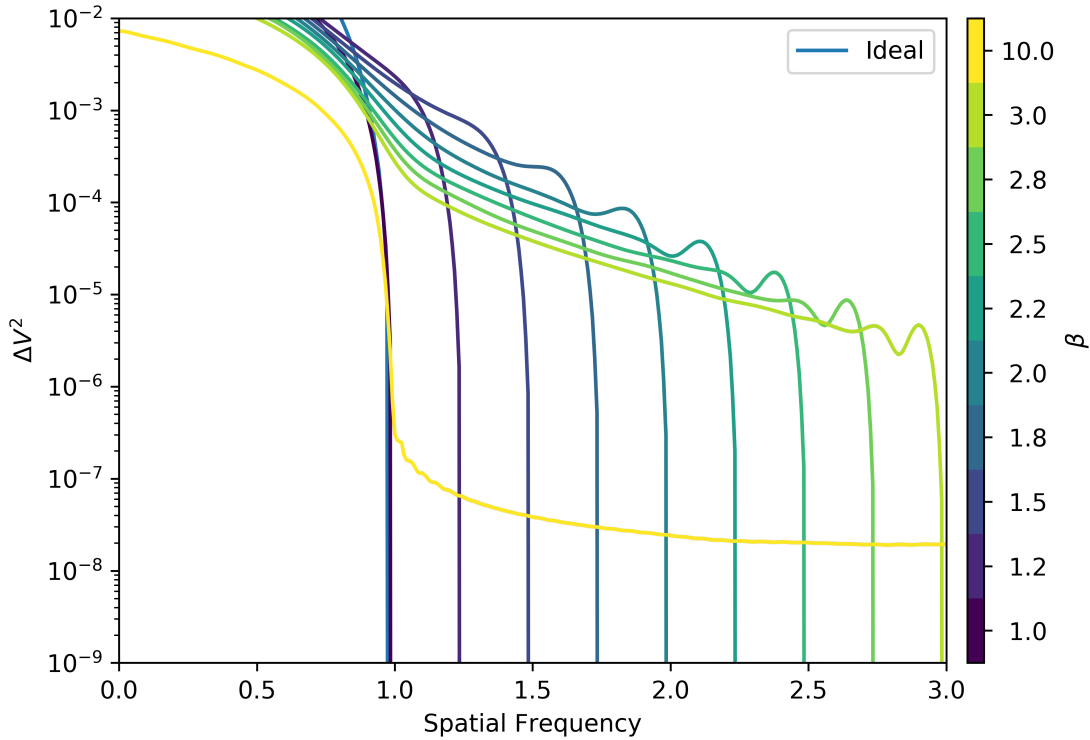From these results we can conclude that both a cropping aperture equal to the diameter of

**Figure 8.11:** Crosstalk with atmospheric seeing effects as a function of $\beta$ with the other parameters held at $\alpha = 9$, $\delta = 0.5$, $\gamma = 1$, $T = 0$. Here the increasing extent of crosstalk for increasing values of $\beta$ is clear, with a sharp cut off at the maximum spatial frequency of crosstalk for a given value of $\beta$. Note the tick marks indicate the values of $\beta$ plotted which follow the perceptually uniform colour map linearly with the exception of the $\beta = 10$ run.

the original beam ($\beta = 1$) and an infinitely large cropping aperture induce no crosstalk. Neither of these cases may be practical, for example $\beta = 1$ has the effect of reducing the throughput of an interferometer as figure 4 of Horton et al. (2001) shows, which may reduce the limiting magnitude of the array, and infinitely large optics are not practical. However the results do show that it is possible to avoid crosstalk originating from diffraction. When designing an image plane beam combiner the clear aperture of the optics along the beam train should be considered and the pupils spaced appropriately such that the maximum spatial frequency passed by the clear apertures does not overlap with the spatial frequency of any other baseline.

This result should be considered alongside what values of $\beta$ and pupil spacings are physically possible. For example if the minimum pupil separation is twice the undiffracted diameter then the maximum physical value of $\beta$ is two as beyond this the cropping apertures would overlap. The maximum physical value of $\beta$ scales with beam separation, for example if the pupils were separated by three times their undiffracted diameters the maximum physical value of $\beta$ would
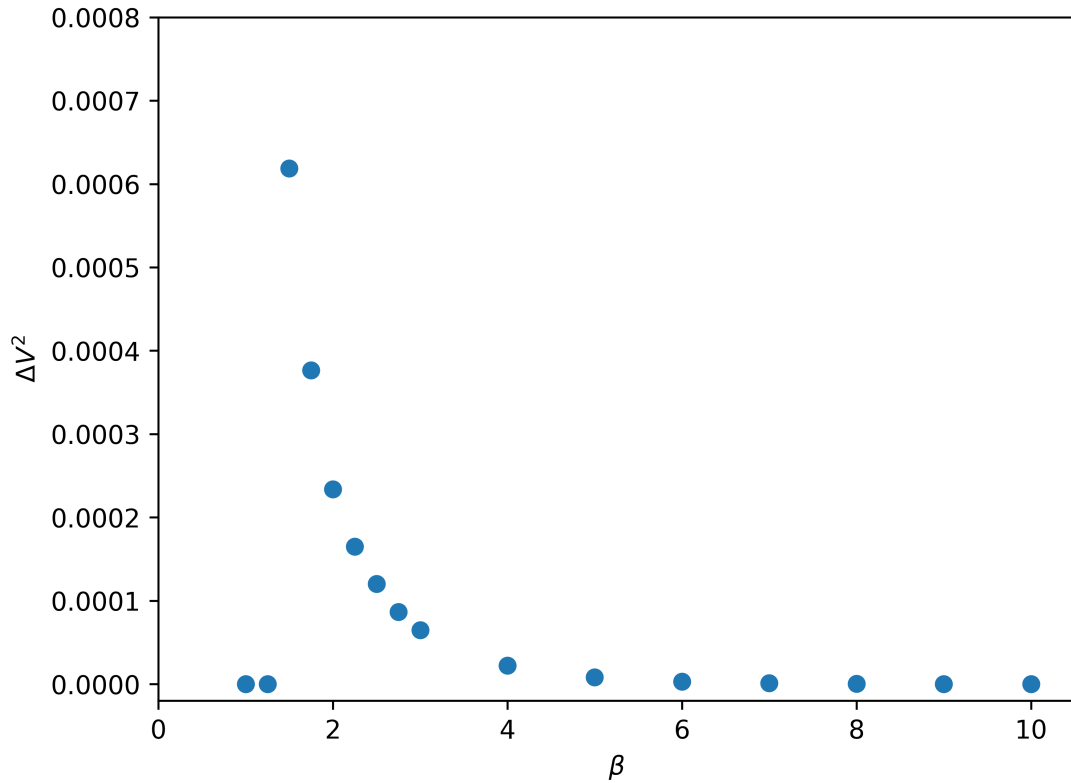
**Figure 8.12:** Crosstalk as a function of $\beta$ (cropping aperture size) at a spatial frequency of 1.3 with the other parameters held at $\alpha = 9$, $\delta = 0.5$, $\gamma = 1$, $T = 0$. Crosstalk is seen to be zero until the value of $\beta$ reaches 2 where it then peaks before decaying as $\beta$ increases further.

be three and so on.

Exploring the effects of varying $\delta$ I find that, while $\beta$ may define the profile of the crosstalk, $\delta$ defines the amplitude of it as demonstrated in figure 8.13 by the clear increase in crosstalk with increasing $\delta$.

In figure 8.14 I explore the crosstalk amplitude as a function of $\delta$ (impact of diffraction) for a fixed set of other parameters ($\alpha = 9$, $\beta = 2$, $\gamma = 1$, $T = 1$) at a spatial frequency of 1.3, showing the crosstalk amplitude monotonically increases as a function of $\delta$. It should be noted that the simulations presented here where $\delta > 0.5$ the pupil is sampled more coarsely at 60 pixels across the diameter as opposed to 120 pixels used elsewhere.

These results show that it is important to consider the diffraction parameter $\delta$ when estimating crosstalk, with larger values of crosstalk arising for observations at longer wavelengths and larger propagation distances.

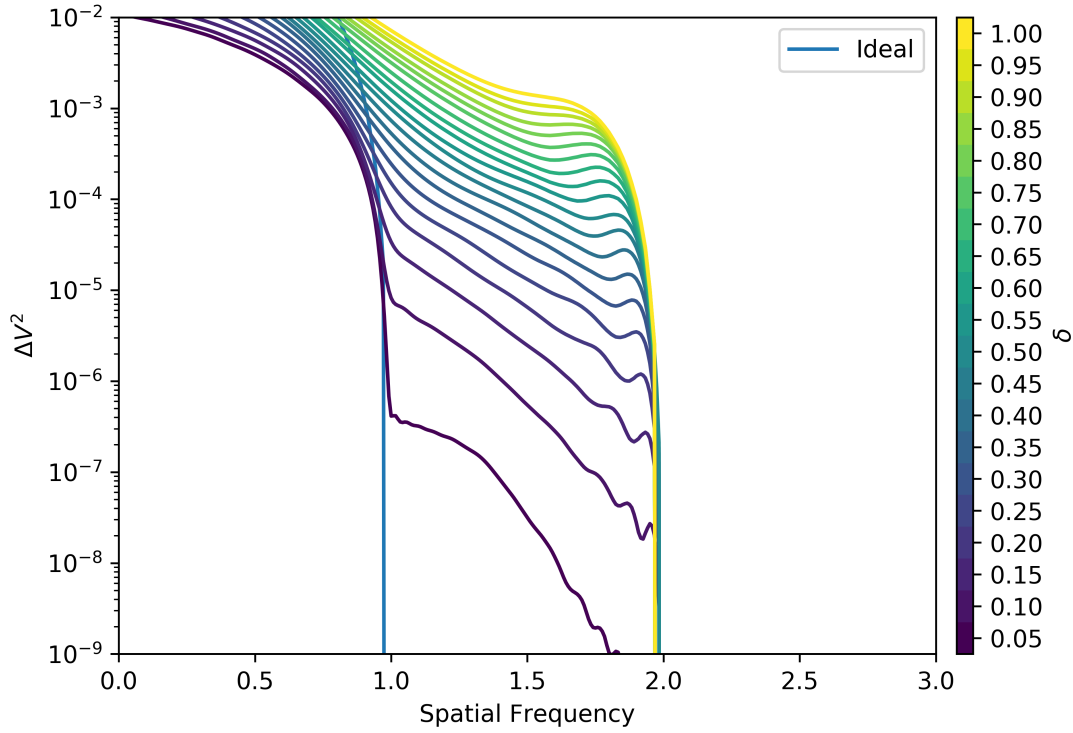**Figure 8.13:** Crosstalk for a range of $\delta$ values with the other parameters held at $\alpha = 9$, $\beta = 2$, $\gamma = 1$, $T = 1$. Increasing $\delta$ increases the crosstalk amplitude at all spatial frequencies which display diffraction crosstalk.

### 8.7.2   Crosstalk dependence on $\alpha$

For a given configuration of parameters, a larger value of the seeing parameter $\alpha$ results in a greater amplitude of crosstalk. Figure 8.15 shows the amplitude of crosstalk at a fixed spatial frequency as a function of $\alpha$ which increases up to a value of $\alpha = 4$. Above $\alpha = 4$ the amplitude of crosstalk begins to level off with no significant increase between $\alpha = 8$ and $\alpha = 16.5$. A select number of runs for varying levels of $\alpha$ are shown in figure 8.16 showing that this trend is true at all spatial frequencies which exhibit crosstalk.

These results suggest that in the regime below a value of $\alpha = 4$ any reduction in the value of $\alpha$ will significantly reduce the crosstalk. However above a value of $\alpha = 8$ there will be no significant reduction in the amplitude of the crosstalk if $\alpha$ is reduced. This result is of relevance if schemes to calibrate the level of crosstalk are contemplated, because they indicate the level of stability of the calibration in the presence of fluctuating seeing levels.
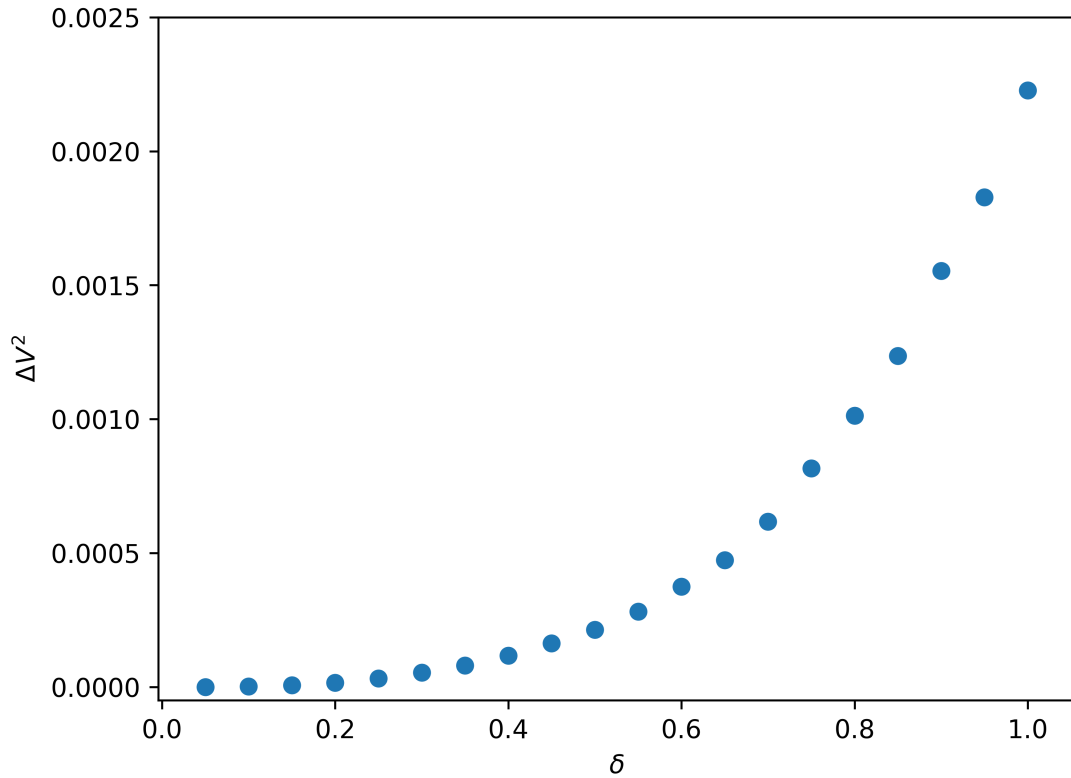
**Figure 8.14:** Crosstalk amplitude as a function of $\delta$ (impact of diffraction) at a spatial frequency of 1.3 with the other parameters held at $\alpha = 9$, $\beta = 2$, $\gamma = 1$, $T = 1$.

### 8.7.3  Crosstalk dependence on $T$

Figure 8.17 shows how changing the parameter $T$, encoding the level of tip-tilt corrections affects crosstalk. I see that tip-tilt corrections have a larger effect on the level of crosstalk for smaller values of the seeing parameter $\alpha$. Looking at a value of $\alpha = 1.5$ in figure 8.17 we see the variation in the tip-tilt parameter $T$ for a given configuration does have a impact on the crosstalk profile whereas for $\alpha = 9$ in figure 8.18 with otherwise the same parameter configuration, the various levels of tip-tilt correction have significantly less of an impact.

This can be explained heuristically as follows: as atmospheric seeing worsens, then for any given level of seeing the relative power of the Zernike polynomials within the atmospheric phase distortions remain the same, with tip and tilt accounting for around 90% of the total power. However, once the total level of the residual (non-tip-tilt) RMS wavefront error reaches about one radian, at $\alpha \sim 2$, then whether or not the tip-tilt fluctuations are removed becomes less important because the effect of additional aberrations is attenuated. A similar effect is seen
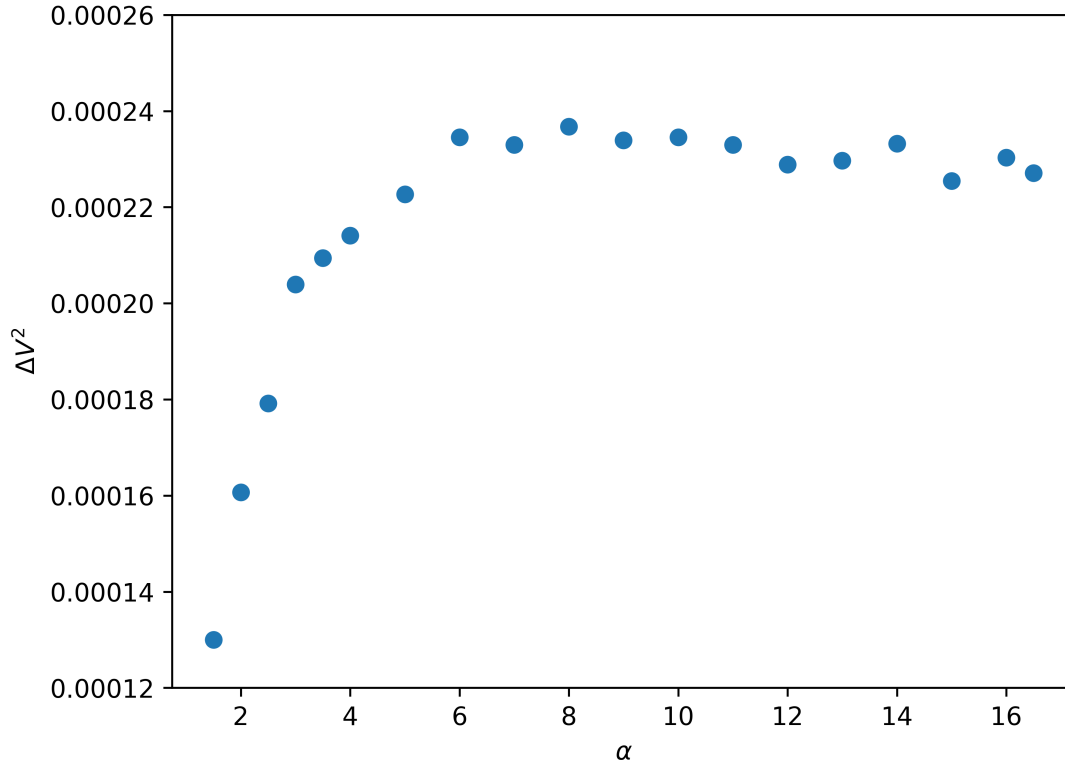
**Figure 8.15:** Crosstalk as a function of $\alpha$ (level of seeing) at a spatial frequency of 3.5 for $\beta = 2$, $\delta = 0.5$, $\gamma = 1$, $T = 0$. The amplitude of crosstalk is seen to approximately increase linearly up to a value of $\alpha = 4$ before flattening out with no significant increase in crosstalk seen between $\alpha = 8$ and $\alpha = 16.5$.

in figure 1 of Fried (1966) where the effect of tip-tilt correction diminishes for $D/r_0 > 2$

### 8.7.4   Crosstalk dependence on $\gamma$

From the definition of the propagation distance ratio parameter $\gamma$ given in section 8.4, for a fixed value of $\delta$, a larger value of $\gamma$ corresponds to a greater difference in the propagation distance of the two beams. This results in a larger mismatch in the profile of the two pupils. The effect of this difference in profile of the two beams is that the two pupils are less coherent with each other and hence produce a weaker interference term at all spatial frequencies, including in the regime of crosstalk.

This is seen in our simulation in figure 8.19 which shows that for a given configuration a larger value of $\gamma$ significantly decreases the level of crosstalk.

In figure 8.20 the visibility of the crosstalk term is divided by the value of the visibility at the peak of the interference term to remove the effects of loss of coherence for greater values of
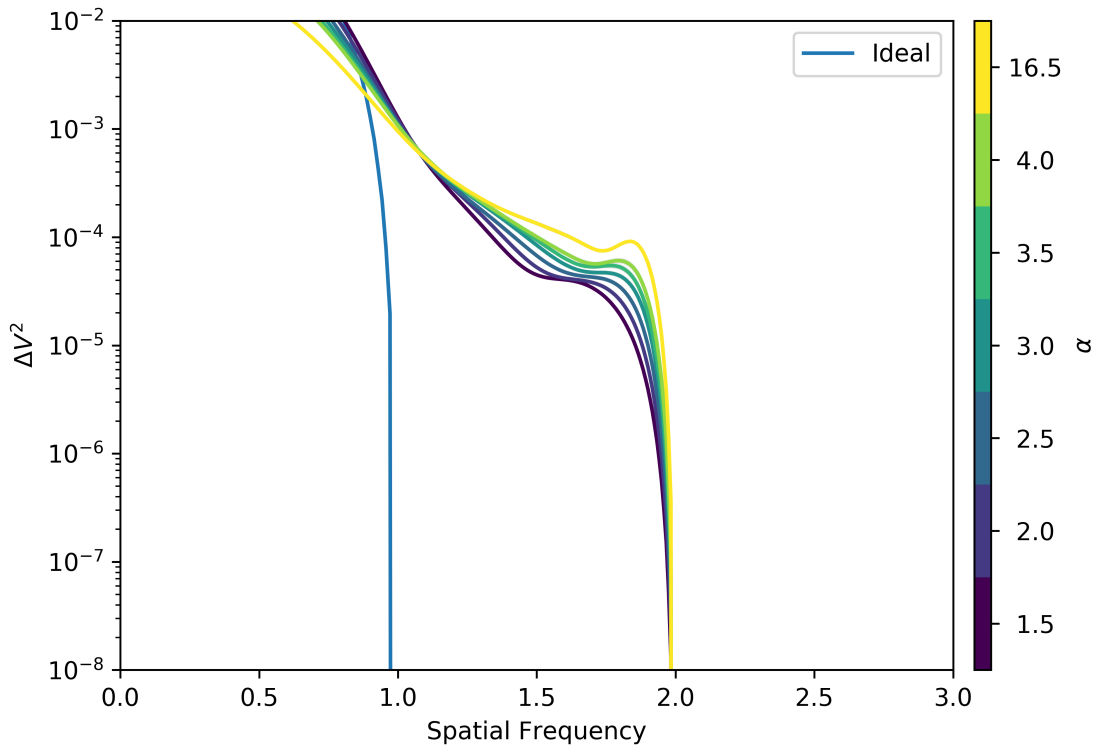
**Figure 8.16:** Crosstalk for various values of $\alpha$ (level of seeing) with the other parameters held at $\beta = 2$, $\delta = 0.5$, $\gamma = 1$, $T = 0$. Here the increase in amplitude of crosstalk for increasing values of $\alpha$ at all spatial frequencies up to a value of $\alpha = 4$ is evident. Note the tick marks indicate the values of $\alpha$ plotted which follow the perceptually uniform colour map linearly with the exception of the $\alpha = 16.5$ run.

$\gamma$. In this case the profiles of the three $\gamma$ values are significantly closer than in figure 8.19. This demonstrates that the visibility of the crosstalk decreases by approximately the same amount as the interference term for a larger value of $\gamma$, suggesting the decrease in crosstalk with $\gamma$ is due to a reduction in coherence. Hence while the crosstalk term may decrease, its amplitude relative to the interference term remains approximately the same. Thus if baselines at adjacent spatial frequencies have similar values of $\gamma$ then the effects of crosstalk on the measured visibilities is roughly independent of $\gamma$.

## 8.8 Crosstalk under realistic observing conditions

In this section I derive the parameter values for the worst case scenario observation at the MROI and calculate the crosstalk for the Free-space Optical multi-apertUre combineR for IntERferometry (FOURIER) beam combiner. Crosstalk for a five telescope beam combiner is also calculated for comparison.
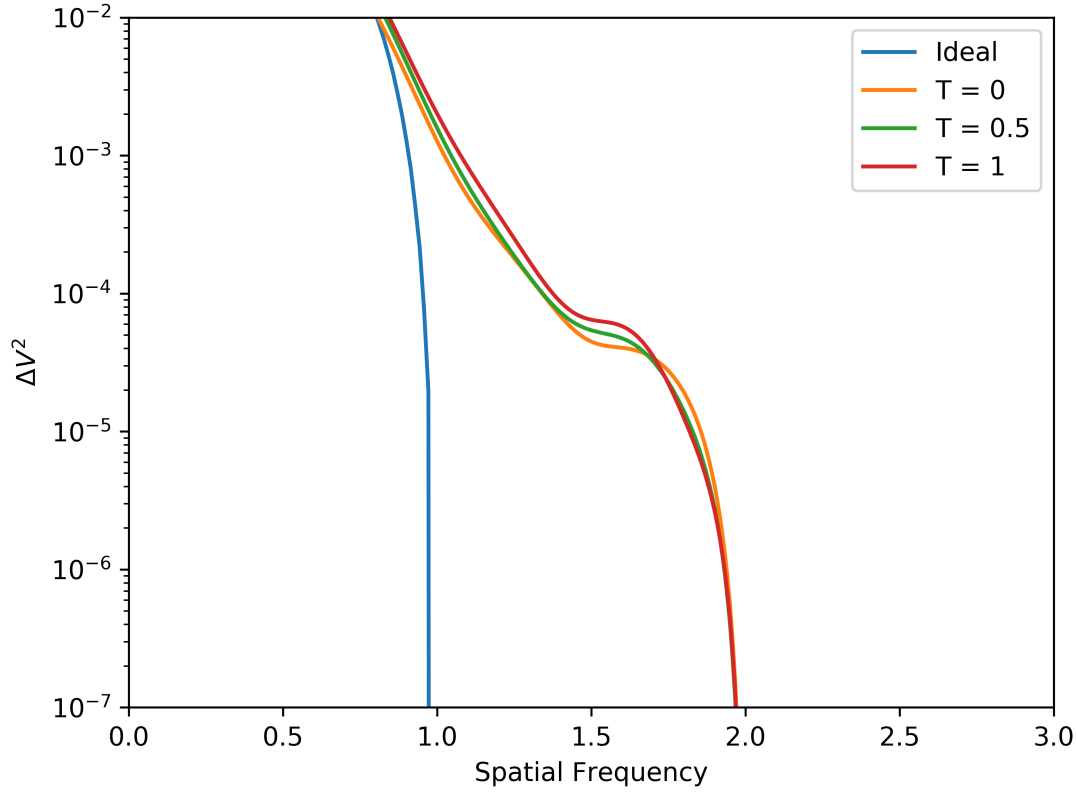
**Figure 8.17:** Varying levels of $T$ (tip-tilt correction) with the other parameters held at $\alpha = 1.5$, $\beta = 2$ $\delta = 0.5$, $\gamma = 1$. Here the variation in profile of crosstalk for differing levels of tip-tilt correction can be seen.

### 8.8.1  Crosstalk of FOURIER

FOURIER is a three beam J, H and K band image plane combiner which utilises a 2,4,6 beam spacing configuration (as in figure 8.4a). FOURIER will cover the wavelength range of $\lambda = 1.1\,\mu m$-$2.4\,\mu m$ on baselines of B = 7.8 m-374 m.

The data reduction pipeline for FOURIER is still under development however one method for extracting the visibility is to apply equation (8.2) to an ensemble of interferograms and extract the visibility at the spatial frequency of the peak of the interference term as predicted by the pupil plane spacing for each baseline. I am confident in this method as the result in section 8.6 has shown that the spatial frequency of the peak of the interference term in the MTF does not change even when atmospheric tilt induces pupil shear at the entrance of the beam combiner.

From section 8.7 I can see that the worst case scenario would be for the largest values of $\delta$ and $\beta$, and an $\alpha$ value greater than eight. Tip-tilt correction and $\gamma$ were shown to be weak
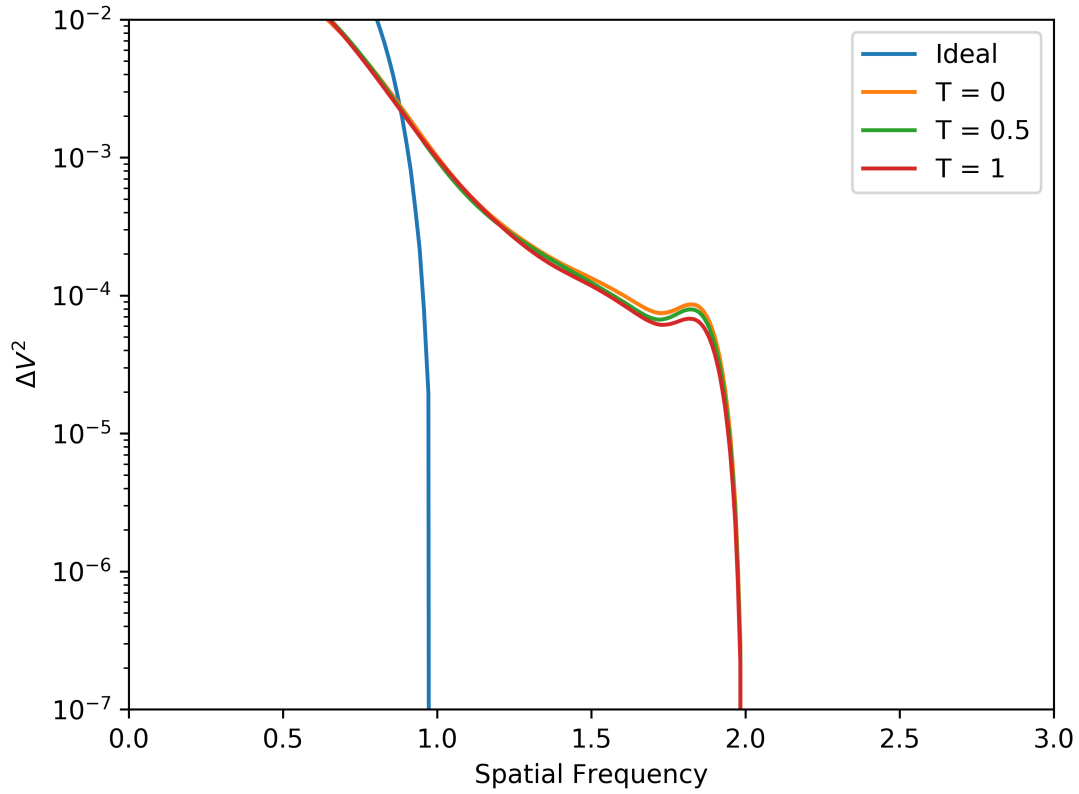
**Figure 8.18:** Varying levels of $T$ (tip-tilt correction) with the other parameters held at $\alpha = 9$, $\beta = 2$, $\delta = 0.5$, $\gamma = 1$. Here the minimal effect of tip-tilt correction on the observed crosstalk at larger values of $\alpha$ can be seen.

variables on the amplitude of crosstalk. Hence the worst case scenario will be for an observation on the longest baseline of 347 m, 30° above the horizon at a wavelength of $\lambda = 2.4\,\mu$m.

The 347 m baseline at the MROI is formed by two telescopes at the edge of two of the arms of the Y shaped array configuration, giving a propagation distance from one telescope to the centre of the array to be 200.3 m, the distance from the centre of the array to the delay line entrance is an additional 50 m of propagation. The delay line imparts a delay of 300.5 m to one of the beams of starlight to compensate for the geometric delay given by $\tau = B\cos(\phi)$, where $B$ is the baseline and $\phi$ the angle of the target above the horizon. An additional 10 m of propagation is added for the delay line exit to beam compressor distance. This then is the path length over which the beam propagates while being 95 mm in diameter, giving a contribution of $\delta = 0.189$. The beam is then compressed to 13 mm in diameter and propagated a further 14.19 m from the beam compressors to the FOURIER beam combiner, adding an additional $\delta = 0.257$. This gives the final value of $\delta$ to be $\delta = 0.446$.
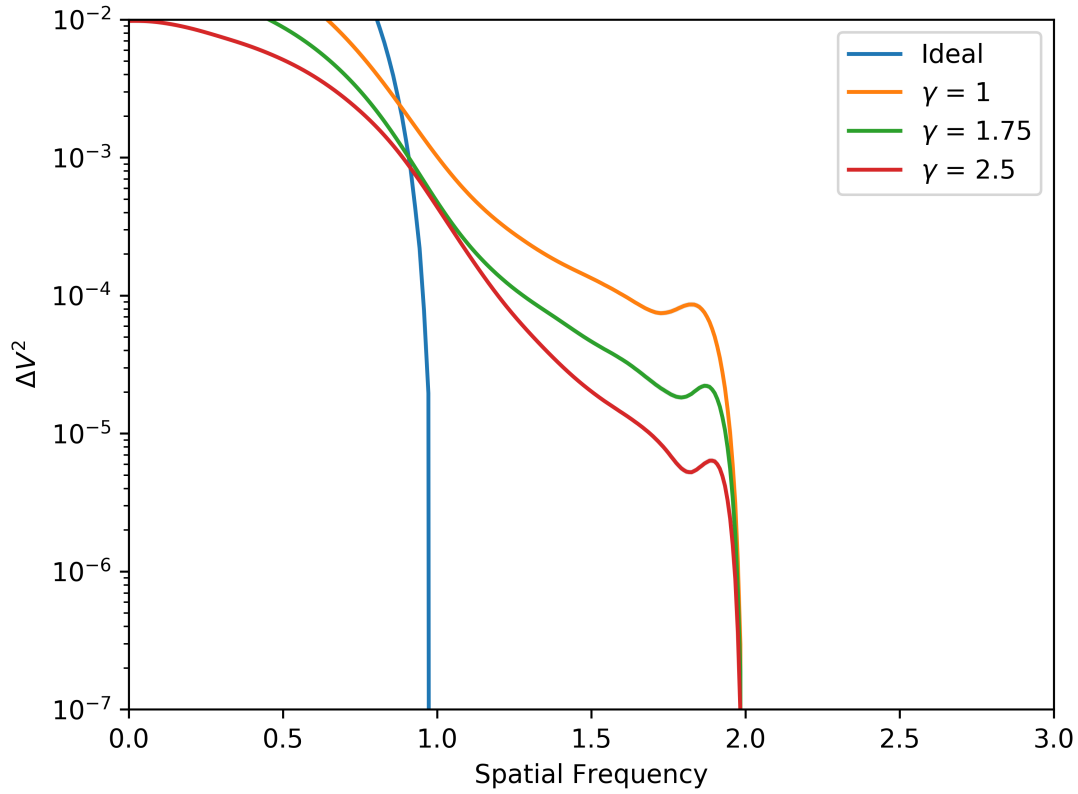
**Figure 8.19:** Various values of $\gamma$ (propagation path length mismatch) for one configuration with the other parameters held at $\alpha = 9$, $\beta = 2$, $\delta = 0.5$, $T = 0$. Here there is a decrease in crosstalk for a larger $\gamma$ due to a greater difference in the profile of the two beams at larger values of $\gamma$.

Given that the delay line must introduce a 300.5 m delay to one of the beams to compensate for the geometric delay, with the path length otherwise being identical for the two beams, this observation has a value of $\gamma = 1.29$. This value of $\gamma$ is calculated by a slightly different definition to that given in equation (8.5) as it is the difference in how affected by propagation the two beams are, rather than the ratio of their absolute path length I am concerned with. This distinction is often not necessary and is only needed here as the beam is compressed in diameter for the final 14.19 m of propagation. By taking $\gamma$ to be the ratio of the two $\delta$ values for the two beams rather than the absolute path length we arrive at a value of $\gamma = 1.29$.

Assuming a seeing of 1 arcsecond at a wavelength of 0.5 μm at zenith and using the scaling relations from section 8.4 gives $\alpha = 3.14$. While this is a moderately low value of $\alpha$ and we would expect greater crosstalk for larger values of $\alpha$ (in this case observations at shorter wavelengths) by comparing figures 8.14 and 8.15 I see that crosstalk is a much stronger function of $\delta$ than $\alpha$ and so the worst case scenario is still for the maximum $\delta$ with a smaller $\alpha$. Finally
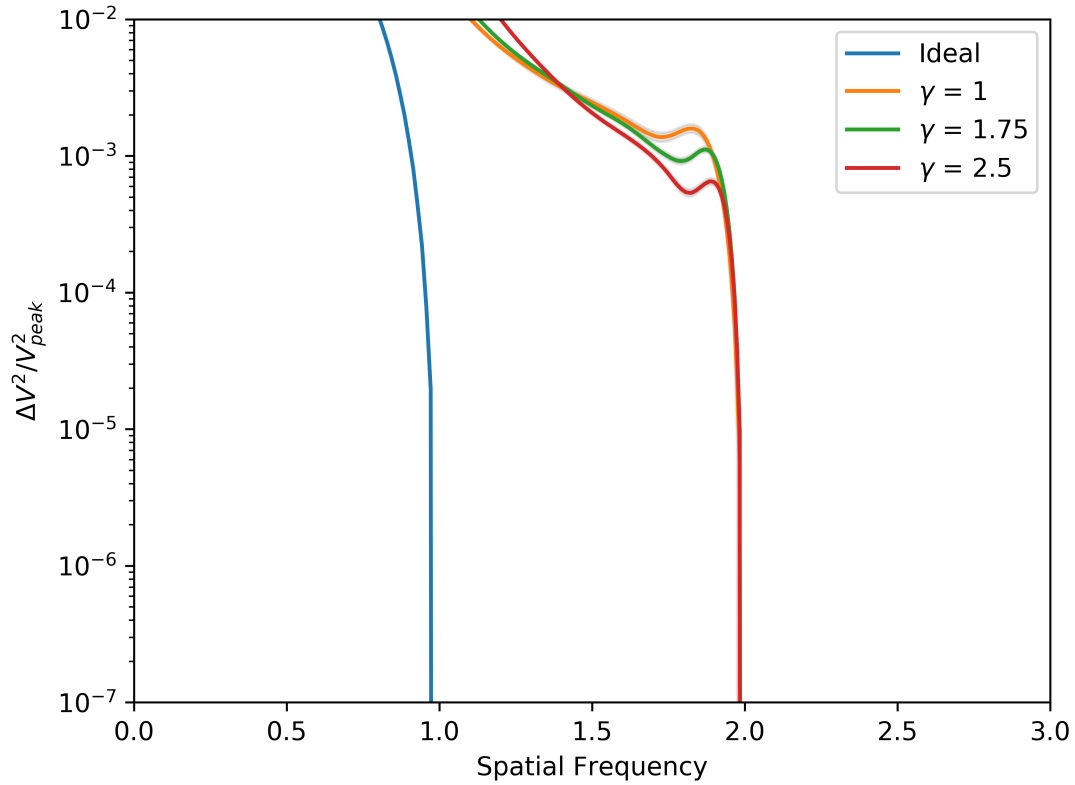
**Figure 8.20:** The visibility of the crosstalk relative to visibility at the peak of the interference term as a function of $\gamma$ (propagation path length mismatch) with the other parameters held at $\alpha = 9$, $\beta = 2$, $\delta = 0.5$, $T = 0$.

we assume in this run that tip-tilt aberrations are perfectly corrected, $T = 1$.

The 2,4,6 beam spacing configuration used by FOURIER is the same as used in figure 8.4a. The smallest beam spacing utilised in FOURIER is two times the undiffracted aperture and so the maximum value of $\beta$ that can be used is two. As discussed in section 8.7.1, when $\beta = 2$ the highest spatial frequency diffraction-induced crosstalk can reach would be just below one spatial frequency unit higher than what would be expected if no crosstalk were present, i.e. diffraction induced crosstalk from the lowest spatial frequency baseline would reach zero just before a spatial frequency of four in figure 8.4a. This is demonstrated in figure 8.21 which shows the crosstalk does reach zero at a spatial frequency just below one spatial frequency unit higher than the ideal case. Considering only the effects discussed so far this would mean the diffraction induced crosstalk would be zero for FOURIER due to the well spaced pupils.

One additional effect to consider is the use of spatial filtering by a pinhole spatial filter as will be implemented for FOURIER. Here the PSF is truncated typically at the location of the first
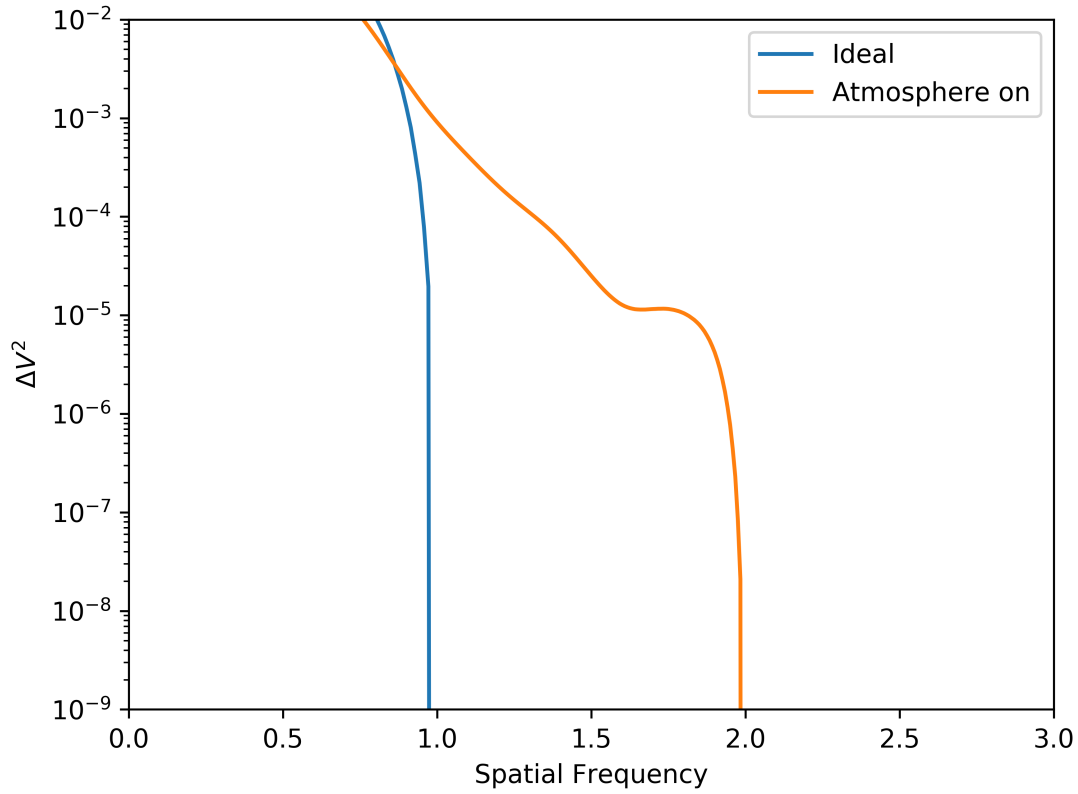
**Figure 8.21:** Crosstalk for the expected worst case scenario observations at the MROI ($\alpha = 3.14$, $\beta = 2$, $\delta = 0.446$, $\gamma = 1.29$, $T = 1$) compared to the ideal case. There is significant crosstalk beyond the classical cut off at a spatial frequency of one however this goes to zero at a spatial frequency of two due to the cut off for $\beta = 2$.

null of the Airy disk. The effect of this is to multiply the PSF by a circular function of amplitude unity within the pinhole and zero outside. By the convolution theorem a multiplication in the image plane space results in a convolution of the Fourier transform of the two functions in the MTF space as the MTF is the modulus of the Fourier transform of the PSF. Consider the 1D case where the circular function is represented by a rectangular function, in this case the ideal MTF is convolved with a sinc function with decaying side lobes out to infinite spatial frequency. To demonstrate the effects of this convolution the MTF of the ideal PSF (with no atmospheric or propagation effects) with and without truncating the PSF at the first null of the Airy disk is shown in figure 8.22. The truncation does indeed result in decaying side lobes at spatial frequencies well beyond the cut off frequency of the ideal case.

figure. 8.22 also shows the effects of PSF truncation for the worst case scenario observation at the MROI in the "Atmosphere on" line. The crosstalk now extends well beyond the cutoff
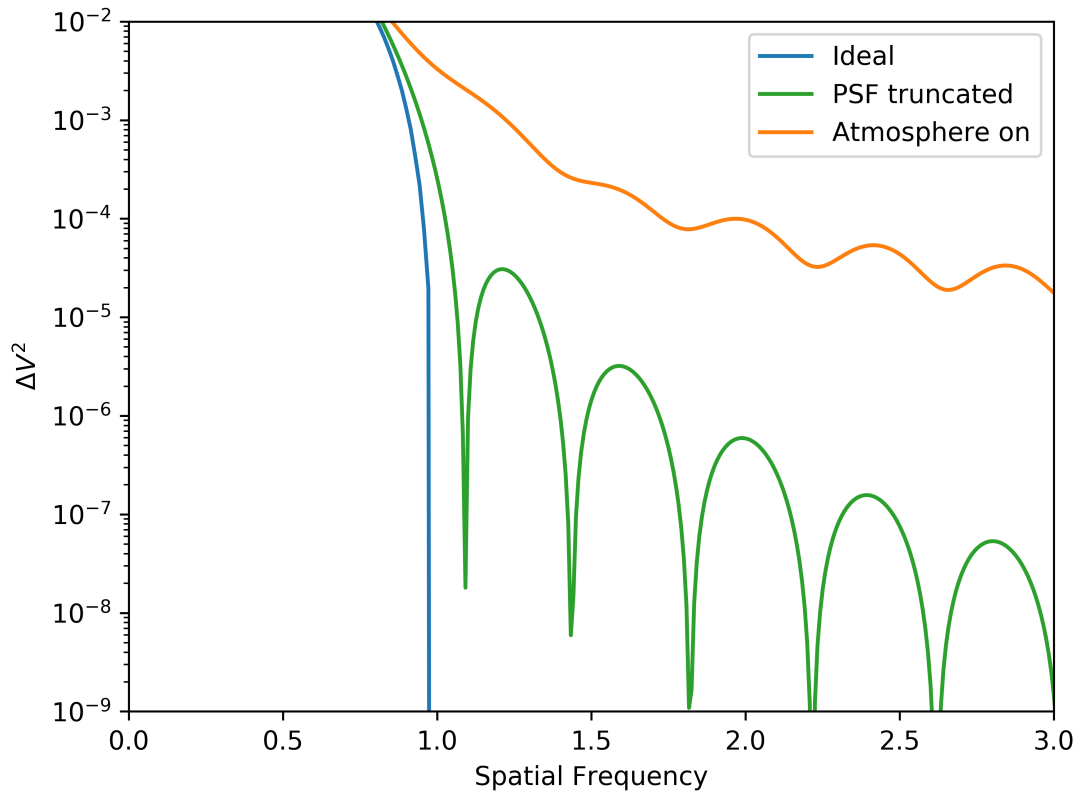
**Figure 8.22:** Crosstalk when the PSF is truncated at the first null of the Airy disk as is the case when pinhole spatial filtering is implemented. The effects of truncation with no propagation or atmospheric effects and for the expected worst case scenario of FOURIER are shown by the 'PSF truncated' and 'Atmosphere on' lines, respectively.

when truncation is not considered but for an otherwise identical run to that shown in figure 8.21. At the spatial frequency of the next baseline for FOURIER (two spatial frequency units higher than the previous baseline) the crosstalk is now $\Delta V^2 = 9.8 \times 10^{-5}$. For the central baseline where there is an adjacent baseline both sides of it the situation is worsened as the crosstalk is symmetric and extends to both higher and lower spatial frequencies. The result of which is that the crosstalk for this baseline is doubled to $\Delta V^2 = 2.0 \times 10^{-4}$.

The design of the FOURIER beam combiner allows me to mitigate this crosstalk however. As spatial filtering is carried out in software along the interference fringe axis (as described in section 4.6) I can select a different spatial filter to the rectangular function described above. For example by applying a Gaussian function instead the side lobes will be removed as the Fourier transform of a Gaussian is another Gaussian which does not contain decaying side lobes. How applying a Gaussian spatial filter affects the quality of the spatial filtering would need to be

quantified, though as this is done is software different filters can be tested after the observations.

## 8.8.2   Five Telescope Beam Combiner

The number of baselines and hence interference terms in the MTF goes as $N_b = (n^2 - n)/2$, where $N_b$ is the number of baselines and $n$ is the number of telescopes in the array. Hence the number of interference terms increases rapidly for higher order beam combiners, a five telescope beam combiner will produce 10 unique baselines, each of which must still be sampled at a unique spatial frequency. When considering the pupil spacing it is desirable to minimise the largest spatial frequency a baseline is sampled at, both to reduce the overall width of the linear non-redundantly spaced pupils, and to minimise the range of spatial frequencies which must be sampled. The higher the largest spatial frequency the larger the number of pixels needed in order to sample at least two pixels per fringe cycle (ideally four or above), and using more pixels both increases the size of detector needed and the effect of read noise as a greater number of pixels must be read out overall.

Fortunately the problem of minimising the total width of a non-redundantly spaced linear array has already been tackled and solutions are known as Golomb rulers (Sidon 1932; Babcock 1953). I am interested in particular in optimal Golomb rulers which give the shortest total width for a non-redundant spacing pattern (Guyon & Roddier 2001). Optimal rulers for five telescope configurations are 11 pupil diameters in length, two of these rulers are given by placing pupils 1, 4, 9, 11 and 2, 7, 8, 11 pupil diameters away from the first pupil (which is placed at zero). Unfortunately the shortest spacing between a pupil pair for these configurations is only one pupil diameter restricting the maximum value of $\beta$ to $\beta = 1$ which is often not practical and would place the lowest spatial frequency term at the null of the DC term. The next best solution is to take a optimal ruler for six telescopes and remove the pupil which forms the lowest spatial frequency term. For example a spacing configuration of 3, 9, 11, 16 pupil diameters away from the first pupil which is placed at zero. This gives the pupil plane configuration and MTF shown in figure 8.23 where all baselines are separated by at least one unit of spatial frequency from the adjacent baselines in the MTF which in the ideal case as described in figure 8.3 would result in no baseline crosstalk.

Using the parameter configuration laid out in section 8.8.1 I see from figure 8.21 that one spatial frequency unit higher gives a crosstalk amplitude $\Delta V^2 = 9 \times 10^{-4}$ from the adjacent
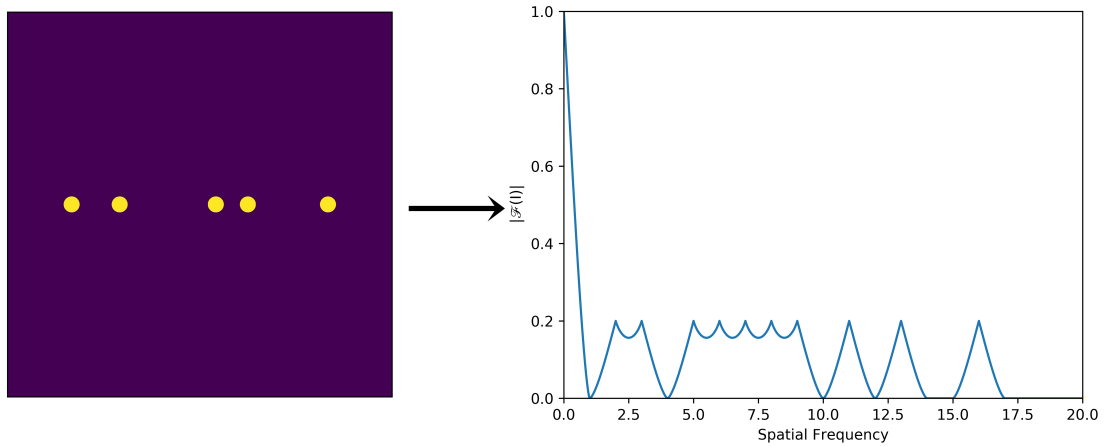
**Figure 8.23:** Left: five pupils spaced 3, 9, 11, 16 pupil diameters from the left most pupil. This configuration minimises the total width of the pupil spacing and hence the highest baseline spatial frequency. right: the resulting MTF showing the 10 baselines generated from the five pupils all sampled at unique spatial frequencies.

baseline. For baselines where there is an adjacent baseline both sides of it the situation is worsened as the crosstalk is symmetric and extends to both higher and lower spatial frequencies. The result of which is that for three of the baselines in the configuration shown in figure 8.23 the crosstalk will be as high as $\Delta V^2 = 1.8 \times 10^{-3}$.

If spatial filtering is also implemented in the five telescope case, figure 8.22 shows that the amplitude of the crosstalk at one spatial frequency unit higher increases to $\Delta V^2 = 3.3 \times 10^{-3}$. For baselines where there is an adjacent baseline on both sides in the MTF the crosstalk will be as high as $\Delta V^2 = 6.6 \times 10^{-3}$.

## 8.9 Summary

In this chapter I investigated image plane crosstalk arising due to previously unexplored effects of atmospheric seeing, free space beam propagation, finite sized optics, unequal path lengths and tip-tilt correction. I find moderate levels of crosstalk ($\Delta V^2 = 6.6 \times 10^{-3}$) due to these effects at spatial frequencies which were previously considered unaffected by crosstalk.

# SUMMARY

In this final chapter I present a short summary of the work presented in this thesis, followed by a discussion of the immediate next steps and potential long term upgrades to the MROI/FOURIER system.

## 9.1 Thesis summary

The majority of this thesis has focused on the development of a three-way, high-sensitivity, J, H and K band beam combiner called the Free-space Optical multi-apertUre combineR for IntERferometry (FOURIER) for the Magdalena Ridge Observatory Interferometer (MROI). During the course of this work I have developed the instrument from the conceptual design phase through to the validation of the optical hardware in the laboratory.

In chapters 1 and 2 I laid out the motivation for Long Baseline Optical Interferometry (LBOI), the limitations of current generation LBOI facilities and how the MROI is designed to improve on these. Building on this, in chapter 3 I discussed the design requirements placed on the FOURIER beam combiner, primarily in line with the goals of the MROI to develop a beam combiner capable of observations at faint limiting magnitudes. To this end, a requirement of being able to carry out observations on $10^{\text{th}}$ magnitude targets, with a goal of $11^{\text{th}}$ at a spectral resolution of R = 70 was placed on the instrument.

Based on these requirements, in chapter 4 I presented the optical design of FOURIER, validating its performance in the subsequent chapter 5. Most notably in calculating the limiting magnitude of the system to be 12.3, 13.2 and 11.7 in the J, H and K bands respectively, exceeding the design goal for FOURIER, particularly in the H band which is known to provide a sweet spot between the more turbulent effects of the atmosphere at shorter wavelengths in the J band, and the thermal photon noise that effects the K band.

In chapter 6 I presented the optomechanical design, highlighting how the relaxed alignment error budget calculated in chapter 5 led to simple optomechanics with no cryogenic motors required, reducing the cost and complexity of the instrument.

The final work presented on the topic of FOURIER in chapter 7 was a series of warm laboratory tests, which validated the Point Spread Function (PSF) reshaping, the throughput and interference fringe contrast (confirming the values used to model the limiting magnitude of the system). I also measured the spectral resolution which was found to range from 120–80 from the edge of the J band to the centre of the H band (the longest wavelength the camera used in the room temperature tests was sensitive to), well above the design requirement of R = 70.

Finally, in chapter 8 I discussed a numerical simulation of previously unexplored crosstalk effects due to atmospheric seeing, diffraction due to propagation, differential path lengths, finite-sized optics along the interferometer's beam train and tip-tilt corrections. Exploring the parameter space and calculating the worse case scenario of crosstalk expected for FOURIER at the MROI I find a crosstalk of $\Delta V^2 = 2.0 \times 10^{-4}$ (where $\Delta V^2$ is the additive error in $V^2$ measured for another baseline) for the beam spacing configuration used by FOURIER. This value rises to $\Delta V^2 = 6.6 \times 10^{-3}$ for a five telescope beam combiner.

## 9.2   Next steps

### 9.2.1   FOURIER development

The ultimate goal of any instrument development project is to get on-sky and produce scientific data and FOURIER is no exception. Here I discuss the next steps required to take FOURIER from its current state to first fringes and beyond.

The work presented in this thesis (particularly chapter 7) has proven the optical design of FOURIER performs as expected, meeting the design requirements tested for (limiting mag-

nitude, spectral coverage, spectral resolution and wavelength calibration) in the laboratory at room temperature. The immediate next steps are to validate the performance of the FOUR-IER cryostat, including the level of vacuum that can be reached, vacuum hold time, operating temperature and cryogenic hold time. Once these tests have been completed the SAPHIRA detector and FOURIER instrument optics will be installed within the cryostat and the optical performance tests carried out in chapter 7 will be repeated to validate the performance of the instrument at cryogenic temperatures, inherently validating the alignment procedure and whether a good level of optical performance can be achieved after cooldown. The extensive room temperature tests which have already been carried out will be invaluable for separating what effects are due to the inherent performance of the optics and which are caused by the cryogenic cooldown of the instrument. At the time of writing the first tests of the cryostat have been carried out, demonstrating a vacuum level of $1.4 \times 10^{-6}$ mbar and an operating temperature of 79 K, removing a large technical risk, though further tests of hold time and vacuum leak rate need to be carried out.

In addition to this work, the design of the cold stops discussed in section 4.9 needs to be finalised and the cold stops manufactured. The current alignment procedure after cooldown is to adjust the focal point of M1 (which is outside the cryostat and can be adjusted after cooldown) to the location of the spatial filter. There is a risk that introducing the cold stops, another blocking aperture, could result in not having enough degrees of freedom to re-align the instrument after cooldown, i.e. aligning the focal plane of M1 to the location of the spatial filter may misalign the light with the cold stops. I believe this is a low risk, as shown in figure 4.13 the cold stops are of order a couple of centimetres away from the spatial filter so any differential contraction between the cold stops and spatial filters will be small. This means that if they are aligned so that light can pass through both the spatial filter and cold stops at room temperature, they should not become significantly misaligned from each other on cooldown as they are attached to the same cold plate and have a small separation between them. This of course needs to be demonstrated in the laboratory. Even in the worst case scenario that the cold stops cannot be simultaneously aligned with the spatial filter, the operation of FOURIER in the J and H bands will not be effected as only in the K band, where thermal effects have a large impact, the cold stops are necessary (see section 5.7.1).

Once FOURIER has been demonstrated to work in the laboratory it must be integrated at

the MROI, showing it can be aligned to the Unit Telescope (UT) beams of starlight and that the technique of Fourier transform spectroscopy used to perform wavelength calibration during the warm laboratory tests can be successfully carried out at the MROI. This wavelength calibration would likely use an alignment light source at the observatory and modulate the path length of one of the beams using the delay lines in place of the Agilis piezo motor driven linear stage used during the warm laboratory tests.

This thesis has focused on the development of the hardware for FOURIER, however, before routine science observations can begin, a data reduction pipeline for FOURIER must also be written. This does not pose a large technical risk to the project as the reduction of data from multiplexed interference fringes in an image plane beam combiner is well established and implemented in many beam combiners.

### 9.2.2  Crosstalk simulation

I consider the work presented in chapter 8 as a completed, self-contained, project. However, there are additional related projects that could be carried out in the future to capitalise on the simulation that was built for chapter 8.

One example is to explore the effects of non-rectangular spatial filters. As discussed in section 8.8.1 a spatial filter with a sharp cutoff results in a convolution of the Modulation Transfer Function (MTF) with a sinc function causing crosstalk to extend to high spatial frequencies (figure 8.22) . Simulating the effects of different shaped spatial filters such as a Gaussian whose Fourier transform is also a Gaussian, and so would not produce decaying sidelobes extending to an infinite spatial frequency, would be an interesting project. In practise a spatial filter without a sharp cutoff can be applied in FOURIER along the interference fringe axis easily as spatial filtering is carried out in software and so would just require the data to be multiplied with different functions. This work would therefore not only be interesting from a theoretical perspective, but would likely be directly used in the FOURIER data reduction pipeline.

Another project would be to investigate whether the effects that cause crosstalk in the visibility would also lead to a bias in closure phase measurements. Closure phase can be recovered by multiplying the complex values of the interference terms in the Optical Transfer Function (OTF) (the equivalent of the MTF but without taking the modulus of the LSF, as discussed in section 8.5) of three telescopes which form a closed triangle. The work in

chapter 8 focused on the fact that amplitude information exists beyond the expected cutoff values in spatial frequency. This gives me reason to believe that phase information will also be retained which may lead to biases in closure phase measurements.

## 9.3   Upon reflection

Looking back over the last four years of development of FOURIER there are things I would do differently if I were to start again. In terms of project management I would have spent less time simulating the performance of FOURIER (chapter 5) in order to begin with the laboratory tests sooner, allowing the instrument to be at a more mature stage in the testing of the hardware. Unfortunately, this was not possible during this project due to the COVID-19 pandemic and associated budget constraints. That is not to say that the simulations do not have value, the work can be adapted to assess the performance of other beam combiners in the future.

There are a few things that could be done in the future to improve the performance of the MROI/FOURIER. With regards to improving the limiting magnitude further, the largest gain would likely come from installing higher order Adaptive Optics (AO) on the UTs. This would have the double benefit of improving the fringe contrast detected by FOURIER (section 5.6.1.2) and allowing for a larger diameter of the MROI UTs (section 1.6.1), gathering more photons. Both of these effects would significantly improve the limiting magnitude of MROI/FOURIER, but the cost of upgrading to a full AO suite with Deformable Mirrors (DMs) and large telescopes such as the VLTI UTs configuration would be prohibitive for the MROI.

Another method for improving the limiting magnitude would be to implement a cophasing fringe tracker, which could enable coherent integrations of up to a minute as is the case with the GRAVITY fringe tracker at the VLTI.

Finally, replacing the N-SF11 prism used in FOURIER with a lower dispersion glass such as fused silica would improve the limiting magnitude at the cost of reducing the spectral resolution. Fused silica glass optimised for the near-infrared has almost no throughput loss due to internal transmission of across the J, H and K bands, removing the drop-off in throughput in the K band for the N-SF11 prism (figure 4.9). A fused silica prism would also be used at a much lower angle of incidence, leading to lower reflection losses at the surfaces of the prism.

While the above potential changes are focused on improving the limiting magnitude, another useful upgrade path would be to implement a higher spectral resolution mode with R of order

R = 1,000. This would extend the range of observations that can be done with FOURIER as it would be able sample multiple visibilities across a spectral line, allowing for the study as a function of blue- and red-shift around an object such as the circumstellar disc in Hone et al. (2017).

## 9.4 Conclusion

This thesis has demonstrated that it is possible to build an optically simple beam combiner with high-throughput bulk optics, in conjunction with the optimised beam train of the MROI, to reach limiting magnitudes significantly fainter than what is possible at other current generation interferometric arrays. With a predicted limiting magnitude of 12.3, 13.2 and 11.7 in the J, H and K bands respectively, the MROI/FOURIER will open up a new area of parameter space which will hopefully lead to novel science observations.

I also hope that the innovative design features of FOURIER such as the design of M1, the beam reshaping by a pair of anamorphic optics and the use of a pinhole and software spatial filter will add to the range of proven beam combination technologies used when designing future beam combiners.

# **A**

# **FOURIER OPTICS DRAWINGS**

This appendix contains the manufacturing drawings the optics of FOURIER were made to. The specification of the optics were set by requirements from a number of different sources. For example the general optical design set the clear aperture, coating and radius of curvature. The tolerance error budget set the surface accuracy and radius of curvature tolerance. The remaining of the specifications were set by the mounting design of FOURIER. The prism used in FOURIER is a standard off-the-shelf product form Thorlabs, part number PS859 and so the drawing is not reproduced here.

Substrate: Borosilicate
Profile: Concave Spherical - Plano
Scratch Dig: 60-40
Surface Accuracy: λ/4 @633 nm PV

Coating:
   Material: Bare Gold or Protected Gold as Outlined on Sheet 2
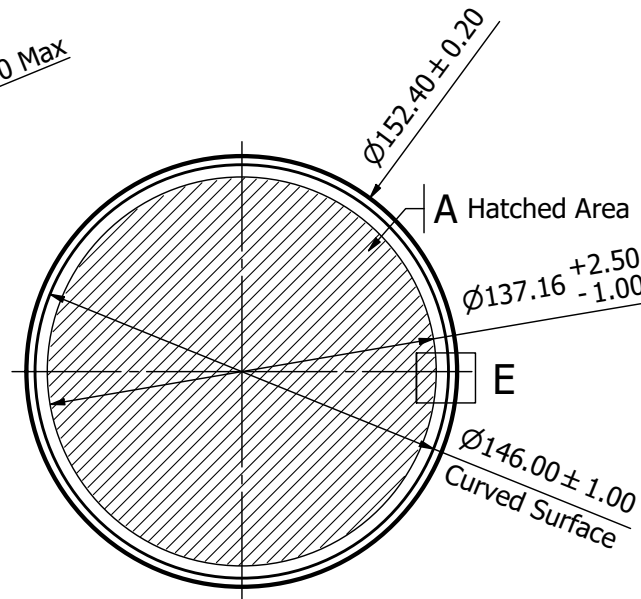   Clear Aperture: Over Region A, Curved Surface Only
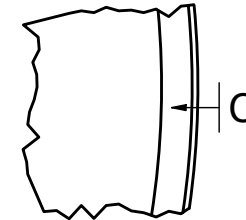   R > 96% over 1.1-2.4 µm

A. Coated Clear Aperture

B. Radius of Curvature: 2540 mm ± 1%

C. Flat Surface For Mounting, Must Not be Coated

D. Fine Ground Surface

Edge Thickness: 25.40±0.2mm
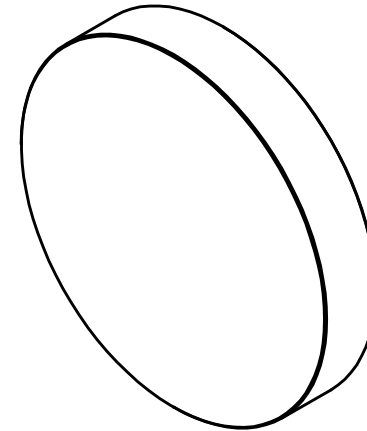
Ch 0.50 X 0.50 Max

Ch 0.50 X 0.50 Max

B

D

D

25.40 ± 0.20

Ø152.40 ± 0.20

A  Hatched Area

Ø137.16 $^{+2.50}_{-1.00}$

E

Ø146.00 ± 1.00
Curved Surface

E ( 2 : 1 )

C

222

Quantity: 1

Coating: Bare gold if bare gold meets adhesion and abrasion requirements below. Protected gold optimised for a wavelength of 1.75μm otherwise. Coating to be applied over region A on drawing on curved surface only. Coating may extend beyond region A except over region C which must not be coated

Adhesion: Bare gold coating to meet adhesion test on witness sample as per MIL-C-48497A, 3.4.1.1. Protected gold coating requirement as per MIL-PRF-13830B APP B, B.4.4.6 on witness sample

Abrasion: Bare gold coating to meet moderate abrasion test on witness sample as per MIL-C48497A, 3.4.1.3. Protected gold coating requirement as per MIL-PRF-13830B APP B, B.4.4.5 on witness sample

Documentation:

  a. Reflected wavefront interferograms before or after coating.
  b. Report showing values of all other requirements.
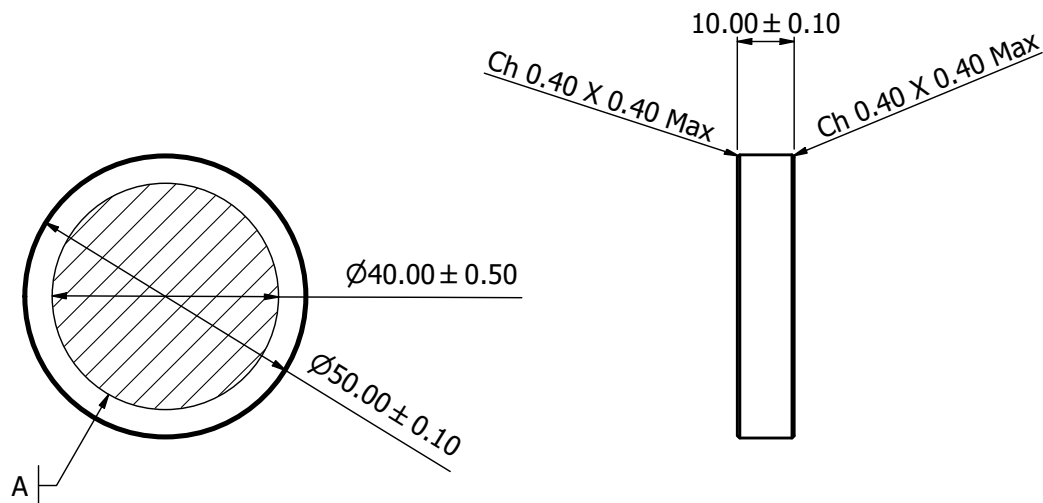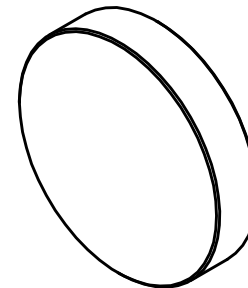  c. Reflection spectrum: from 1100 nm to 2400 nm

| Designed by<br>Daniel Mortimer | Dimensions in mm | Date<br>11/02/2020 | |
|---|---|---|---|
| UNIVERSITY OF CAMBRIDGE | M1 | | |
| | Third angle projection | Edition: 1.2 | Sheet: 2 of 2 |

Substrate: Infrasil 302*
Profile: Plano - Plano
Scratch Dig: 60-40
Surface Accuracy: λ/4 @633 nm PV

Clear Aperture: 80% ± 1%

Coating:
   Material: 0.33±0.05μm Thick (Or Optimised For λ = 1.75μm) MgF2
   Area: Over region A, both surfaces
   Reflection Loss Per Surface < 3% over 1.1-2.4 μm
   Area outside region A must not be coated, both surfaces

A. Coated Clear Aperture

10.00 ± 0.10

Ch 0.40 X 0.40 Max

Ch 0.40 X 0.40 Max

Ø40.00 ± 0.50

Ø50.00 ± 0.10

A

224

| Designed by Daniel Mortimer | Dimensions in mm | Date 05/02/2020 |
| UNIVERSITY OF CAMBRIDGE | Window | |
| | Third angle projection | Edition: 1.2 | Sheet: 1 of 2 |

Quantity: 1

Substrate: *Infrasil 301 as well as Corning 7979 substrates are possible if agreed upon
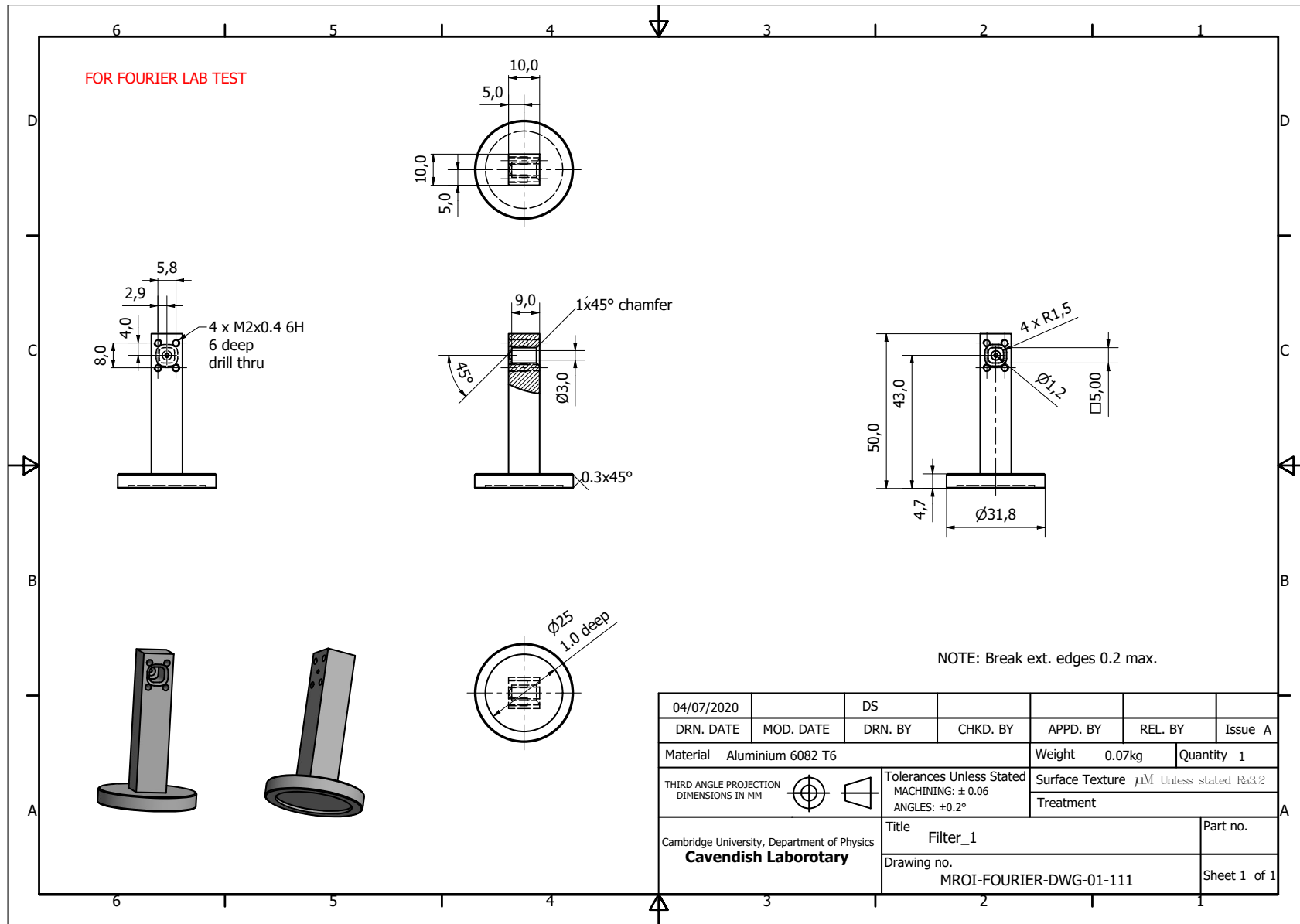with the customer

Wedge: less than 1 arcminute

Adhesion: MIL-C-675C on witness sample

Abrasion: Moderate Abrasion as per MIL-C-675C on witness sample

Documentation:

    a.Transmitted wavefront interferograms before or after coating.
    b. Report showing values of all other requirements.
    c. Transmission spectrum: from 1100 nm to 2400 nm

| Designed by | Dimensions in mm | Date |
| --- | --- | --- |
| Daniel Mortimer | | 05/02/2020 |
| UNIVERSITY OF CAMBRIDGE | Window | |
| | Third angle projection | Edition: 1.2 Sheet: 2 of 2 |

FOR FOURIER LAB TEST

10,0
5,0
10,0
5,0

5,8
2,9
4,0
8,0
4 x M2x0.4 6H
6 deep
drill thru

9,0
1x45° chamfer
45°
Ø3,0
0.3x45°

4 x R1,5
43,0
50,0
Ø1,2
□5,00
4,7
Ø31,8

Ø25
1.0 deep

NOTE: Break ext. edges 0.2 max.

| 04/07/2020 | | DS | | | | |
|---|---|---|---|---|---|---|
| DRN. DATE | MOD. DATE | DRN. BY | CHKD. BY | APPD. BY | REL. BY | Issue A |

| Material    Aluminium 6082 T6 | | Weight    0.07kg | Quantity  1 |
|---|---|---|---|

THIRD ANGLE PROJECTION
DIMENSIONS IN MM

Tolerances Unless Stated
MACHINING: ± 0.06
ANGLES: ±0.2°

Surface Texture  µM  Unless stated  Ra3.2
Treatment

Title
Filter_1

Part no.

Cambridge University, Department of Physics
**Cavendish Laborotary**
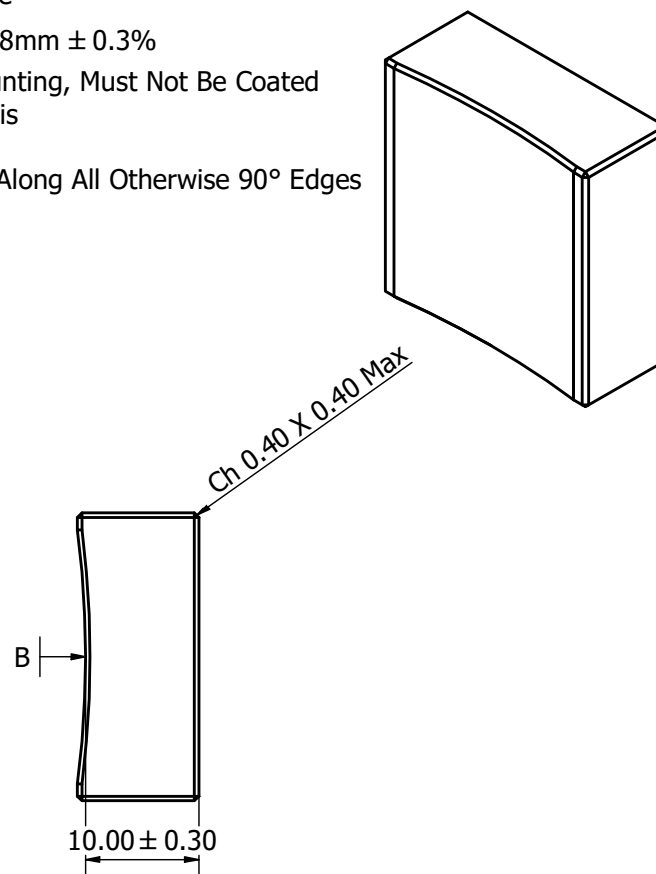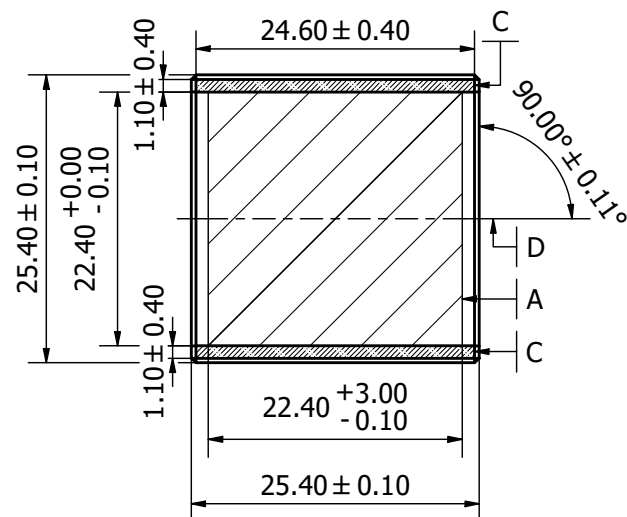
Drawing no.
MROI-FOURIER-DWG-01-111

Sheet 1  of 1

226

Substrate: Fused Silica*
Profile: Concave Cylindrical - Plano
Scratch Dig: 20-10
Surface Accuracy: λ/4 @633 nm PV

A. Coated Clear Aperture

B. Radius of Curviture 88mm ± 0.3%

C. Flat Surfaces for Mounting, Must Not Be Coated
D. Optical Cylindrical Axis

0.4 x 0.4 Max Chamfer Along All Otherwise 90° Edges

Coating:
    Material: Bare Gold or Protected Gold as Outlined on Sheet 2
    Coated Clear Aperture: Over Region A, Curved Surface Only
    R > 96% over 1.1-2.4 µm

Ch 0.40 X 0.40 Max

24.60 ± 0.40

1.10 ± 0.40

90.00° ± 0.11°

25.40 ± 0.10

22.40 +0.00 -0.10

D

A

1.10 ± 0.40

B

22.40 +3.00 -0.10

10.00 ± 0.30

25.40 ± 0.10

| Designed by Daniel Mortimer | Dimensions in mm | Date 20/02/2020 |
|---|---|---|
| UNIVERSITY OF CAMBRIDGE | M2 | |
| | Third angle projection | Edition: 1.3 | Sheet: 1 of 2 |

Quantity: 1

Substrate: *Similar low expansion glass/low expansion composites possible if agreed
upon with the customer

Centre Thickness: 10 mm ± 0.1 mm

Coating: Bare gold if bare gold meets adhesion and abrasion requirements below. Protected gold
optimised for a wavelength of 1.75μm otherwise. Coating to be applied over region A on drawing on
curved surface only, coating may extend beyond clear aperture except over region C which must not
be coated

Adhesion: Bare gold coating to meet adhesion test on witness sample as per MIL-C-48497A, 3.4.1.1.
Protected gold coating requirement as per MIL-PRF-13830B APP B, B.4.4.6 on witness sample

Abrasion: Bare gold coating to meet moderate abrasion test on witness sample as per MIL-C48497A, 3.4.1.3. Protected gold
coating requirement as per MIL-PRF-13830B APP B, B.4.4.5 on witness sample

Documentation:

   a. Reflected wavefront interferograms before or after coating.
   b. Report showing values of all other requirements.
   c. Reflection spectrum: from 1100 nm to 2400 nm

228

| Designed by Daniel Mortimer | Dimensions in mm | Date 20/02/2020 | |
|---|---|---|---|
| UNIVERSITY OF CAMBRIDGE | M2 | | |
| | Third angle projection | Edition: 1.3 | Sheet: 2 of 2 |

Substrate: CaF2
Profile: Convex Cylindrical - Plano
Scratch Dig: 40-20
Surface Accuracy: λ/4 @633 nm PV

Coating:
   Material: 0.33±0.05μm Thick (Or Optimised For λ = 1.75μm) MgF2
   Area: Over region A, both surfaces
   Reflection Loss Per Surface < 3% over 1.1-2.4 μm

A. Coated Clear Aperture

B. Radius of Curvature: 18.7018304 mm ± 0.3%

C. Optical Cylindrical Axis

0.4 x 0.4 Max Chamfer Along All Otherwise 90° Edges



90.00° ± 0.11°

Ch 0.40 X 0.40 Max

25.40 ± 0.10

22.86 ± 0.51

C

A

B

22.86 ± 0.51

25.40 ± 0.10

10.00 ± 0.30
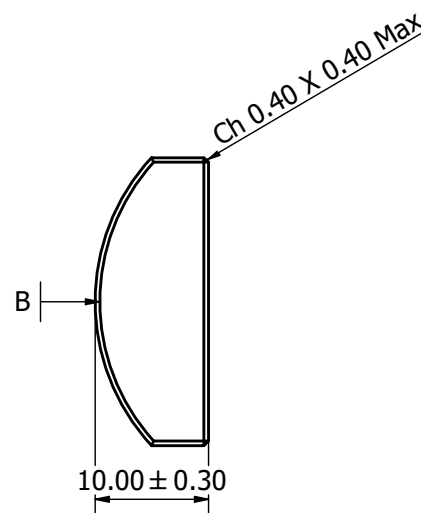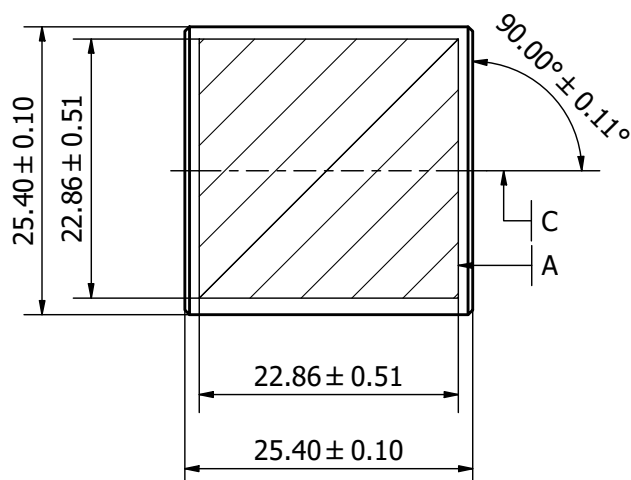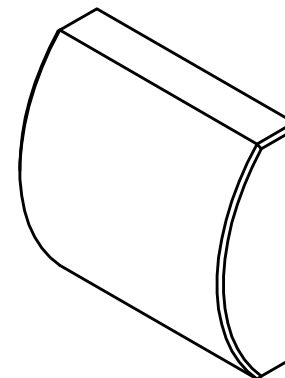
| Designed by Daniel Mortimer | Dimensions in mm | Date 20/02/2020 |
|---|---|---|
| UNIVERSITY OF CAMBRIDGE | L1 | |
| | Third angle projection | Edition: 1.3   Sheet: 1 of 2 |

Quantity: 1

Centre Thickness: 10 mm ± 0.1 mm

Adhesion: MIL-C-675C on witness sample

Abrasion: Moderate Abrasion as per MIL-C-675C on witness sample

Documentation:

    a. Transmitted wavefront interferograms before or after coating.
    b. Report showing values of all other requirements.
    c. Transmission spectrum: from 1100 nm to 2400 nm

230

| Designed by<br>Daniel Mortimer | Dimensions in mm | Date<br>20/02/2020 | |
|---|---|---|---|
| UNIVERSITY OF<br>CAMBRIDGE | L1 | | |
| | Third angle projection | Edition: 1.3 | Sheet: 2 of 2 |

# Bibliography

Accardo M., Alvarez D., Mehrgan L., 2013, Technical Report VLT-ICD-ESO-14010-5849, ICD for a single SAPHIRA based cryogenic detector setup. ESO

Anderson J. A., 1920, ApJ, 51, 263

Anugu N., et al., 2020, AJ, 160, 158

Armstrong J. T., et al., 1998, ApJ, 496, 550

Armstrong J. T., Schmitt H. R., Restaino S. R., Baines E. K., van Belle G. T., 2018, in Creech-Eakman M. J., Tuthill P. G., Mérand A., eds, Society of Photo-Optical Instrumentation Engineers (SPIE) Conference Series Vol. 10701, Optical and Infrared Interferometry and Imaging VI. p. 107010B, doi:10.1117/12.2312284

Babcock W. C., 1953, The Bell System Technical Journal, 32, 63

Baldwin J. E., Boysen R. C., Cox G. C., Haniff C. A., Rogers J., Warner P. J., Wilson D. M., Mackay C. D., 1994, in Breckinridge J. B., ed., Society of Photo-Optical Instrumentation Engineers (SPIE) Conference Series Vol. 2200, Amplitude and Intensity Spatial Interferometry II. pp 118–128, doi:10.1117/12.177233

Baldwin J. E., et al., 1996, A&A, 306, L13

Baron F., Buscher D. F., Coyne J., Creech-Eakman M. J., Haniff C. A., Jurgenson C. A., Young J. S., 2006, in Monnier J. D., Schöller M., Danchi W. C., eds, Society of Photo-Optical Instrumentation Engineers (SPIE) Conference Series Vol. 6268, Advances in Stellar Interferometry. p. 62681R, doi:10.1117/12.671174

Beavers W. I., 1963, AJ, 68, 273

Bradley P. E., Radebaugh R., et al., 2013, NIST Publ, 680, 1

Buscher D. F., 1988, MNRAS, 235, 1203

Buscher D. F., 2015, Practical Optical Interferometry. Cambridge University Press, doi:10.1017/CBO9781107323933

Buscher D. F., 2016, Optics Express, 24, 23566

Buscher D. F., Wilson D. M. A., 2018, in Creech-Eakman M. J., Tuthill P. G., Mérand A., eds, Society of Photo-Optical Instrumentation Engineers (SPIE) Conference Series Vol. 10701, Optical and Infrared Interferometry and Imaging VI. p. 1070126, doi:10.1117/12.2313251

Buscher D. F., Baron F., Haniff C., 2009, PASP, 121, 45

Buscher D. F., Creech-Eakman M., Farris A., Haniff C. A., Young J. S., 2013, Journal of Astronomical Instrumentation, 2, 1340001

Buscher D. F., et al., 2019, Astronomy and Geophysics, 60, 3.22

Campins H., Rieke G. H., Lebofsky M. J., 1985, AJ, 90, 896

Che X., et al., 2013, Journal of Astronomical Instrumentation, 2, 1340007

Chiavassa A., Haubois X., Young J. S., Plez B., Josselin E., Perrin G., Freytag B., 2010, A&A, 515, A12

Colavita M. M., 1999, PASP, 111, 111

Colavita M. M., et al., 1999, ApJ, 510, 505

Colavita M. M., et al., 2013, PASP, 125, 1226

Creech-Eakman M. J., et al., 2020, in Society of Photo-Optical Instrumentation Engineers (SPIE) Conference Series. p. 1144609, doi:10.1117/12.2563173

Daimon M., Masumura A., 2002, Applied optics, 41, 5275

Davis J., Tango W. J., Booth A. J., ten Brummelaar T. A., Minard R. A., Owens S. M., 1999, MNRAS, 303, 773

Davis J., Ireland M. J., North J. R., Robertson J. G., Tango W. J., Tuthill P. G., 2011, Publ. Astron. Soc. Australia, 28, 58

Ducati J. R., 2002, VizieR Online Data Catalog,

Event Horizon Telescope Collaboration et al., 2019, ApJL, 875, L1

Finger G., et al., 2016, in Marchetti E., Close L. M., Véran J.-P., eds, Society of Photo-Optical Instrumentation Engineers (SPIE) Conference Series Vol. 9909, Adaptive Optics Systems V. p. 990912, doi:10.1117/12.2233079

Fizeau H., 1868, CR Hebd. Seances Acad. Sci, 66, 932

Fried D. L., 1966, Journal of the Optical Society of America (1917-1983), 56, 1372

Gies D., ten Brummelaar T., Schaefer G., Baron F., White R., 2019, in BAAS. p. 226, https://baas.aas.org/pub/2020n7i226

Gillessen S., et al., 2010, in Danchi W. C., Delplancke F., Rajagopal J. K., eds, Society of Photo-Optical Instrumentation Engineers (SPIE) Conference Series Vol. 7734, Optical and Infrared Interferometry II. p. 77340Y, doi:10.1117/12.856689

Glindemann A., et al., 2001, The Messenger, 106, 1

Goebel S. B., Hall D. N. B., Guyon O., Warmbier E., Jacobson S. M., 2018, Journal of Astronomical Telescopes, Instruments, and Systems, 4, 026001

Goodman J., 1988, Introduction to Fourier optics. McGraw-Hill, New York, p. 72

Goodman J. W., 2015, Statistical optics, 2nd edn. Wiley, Hoboken, New Jersey

Gordon J. A., 2013, PhD thesis, University of Cambridge

Gordon J. A., Buscher D. F., 2012, A&A, 541, A46

Gravity Collaboration et al., 2017, A&A, 602, A94

Gravity Collaboration et al., 2019, A&A, 632, A53

Griffiths P. R., 2007, Fourier transform infrared spectrometry Peter R. Griffiths, James A. de Haseth., 2nd edn. Chemical analysis ; v. 171, Wiley-Interscience, Hoboken, N.J.

Guyon O., Roddier F., 2001, PASP, 113, 98

Hamy M., 1899, Bulletin Astronomique, Serie I, 16, 257

Haniff C., 2007, New Astron. Rev., 51, 565

Harris C. R., et al., 2020, Nature, 585, 357

Harvey J. E., Ftaclas C., 1995, Appl. Opt., 34, 6337

Haubois X., et al., 2009, A&A, 508, 923

Haubois X., et al., 2020, in Society of Photo-Optical Instrumentation Engineers (SPIE) Conference Series. p. 1144606, doi:10.1117/12.2561486

Hecht E., 2017, Optics / Eugene Hecht, Adelphi University., 5 edition.; global edition. edn

Hone E., Kraus S., Kreplin A., Hofmann K.-H., Weigelt G., Harries T., Kluska J., 2017, A&A, 607, A17

Horton A. J., Buscher D. F., Haniff C. A., 2001, MNRAS, 327, 217

Keen J. W., Buscher D. F., Warner P. J., 2001, MNRAS, 326, 1381

Kobus J., Wolf S., Ratzka T., Brunngräber R., 2020, A&A, 642, A104

Kouzuma S., Yamaoka H., 2010, MNRAS, 405, 2062

Labeyrie A., 1975, ApJ, 196, L71

Lanthermann C., Anugu N., Le Bouquin J. B., Monnier J. D., Kraus S., Perraut K., 2019, A&A,

625, A38

Lazareff B., et al., 2017, A&A, 599, A85

Le Bouquin J. B., et al., 2011, A&A, 535, A67

Lopez B., et al., 2014, The Messenger, 157, 5

Lord S. D., 1992, A new software tool for computing Earth's atmospheric transmission of near- and far-infrared radiation, NASA Technical Memorandum 103957

Luis J. J. D., et al., 2020, in Society of Photo-Optical Instrumentation Engineers (SPIE) Conference Series. p. 1144628, doi:10.1117/12.2562863

Mahajan V. N., 1982, Journal of the Optical Society of America (1917-1983), 72, 1258

Martinod M.-A., et al., 2021, Nature Communications, 12, 2465

Mathar R. J., 2010, arXiv e-prints, p. arXiv:1006.4145

Mayor M., Queloz D., 1995, Nature, 378, 355

McAlister H. A., 2020, Seeing the Unseen; Mount Wilson's role in high angular resolution astronomy. Institute of Physics Publishing, doi:10.1088/2514-3433/abb4de

McCracken T. M., et al., 2014, in Rajagopal J. K., Creech-Eakman M. J., Malbet F., eds, Society of Photo-Optical Instrumentation Engineers (SPIE) Conference Series Vol. 9146, Optical and Infrared Interferometry IV. p. 91461E, doi:10.1117/12.2055603

Mellish b., Bajart E., 2010, Abbe diagram, https://en.wikipedia.org/wiki/Abbe_number#/media/File:Abbe-diagram_2.svg

Mérand A., Stefl S., Bourget P., Ramirez A., Patru F., Haguenauer P., Brillant S., 2010, in Danchi W. C., Delplancke F., Rajagopal J. K., eds, Society of Photo-Optical Instrumentation Engineers (SPIE) Conference Series Vol. 7734, Optical and Infrared Interferometry II. p. 77340S, doi:10.1117/12.856889

Merrill P. W., 1922, ApJ, 56, 40

Michelson A. A., 1890, The London, Edinburgh, and Dublin Philosophical Magazine and Journal of Science, 30, 1

Michelson A. A., 1891, Publications of the Astronomical Society of the Pacific, 3, 274

Michelson A. A., Pease F. G., 1921, ApJ, 53, 249

Monnier J. D., 2003, Reports on Progress in Physics, 66, 789

Montargès M., Chiavassa A., Kervella P., Ridgway S. T., Perrin G., Le Bouquin J. B., Lacour S., 2017, A&A, 605, A108

Montargès M., Norris R., Chiavassa A., Tessore B., Lèbre A., Baron F., 2018, A&A, 614, A12

Mortimer D. J., Buscher D. F., 2022, MNRAS, 511, 4619

Mortimer D. J., et al., 2020, in Optical and Infrared Interferometry and Imaging VII. p. 114460V, doi:10.1117/12.2561472

Mourard D., et al., 2009, A&A, 508, 1073

Mourard D., et al., 2017, Journal of the Optical Society of America A, 34, A37

Ohnaka K., et al., 2011, A&A, 529, A163

Pannetier C., et al., 2020, in Society of Photo-Optical Instrumentation Engineers (SPIE) Conference Series. p. 114460T, doi:10.1117/12.2560625

Pease F., 1923, Popular Astronomy, 31, 654

Pease F. G., 1931, Ergebnisse der exakten Naturwissenschaften, 10, 84

Petrov R. G., et al., 2007, A&A, 464, 1

Pirnay O., Gloesener P., Gabriel E., Moreau V., Graillet F., Delrez C., 2008, in Schöller M., Danchi W. C., Delplancke F., eds, Society of Photo-Optical Instrumentation Engineers (SPIE) Conference Series Vol. 7013, Optical and Infrared Interferometry. p. 70130N, doi:10.1117/12.788732

Porro I. L., Traub W. A., Carleton N. P., 1999, Appl. Opt., 38, 6055

Rains A. D., Ireland M. J., White T. R., Casagrande L., Karovicova I., 2020, MNRAS, 493, 2377

Ridgway S. T., et al., 2003, in Traub W. A., ed., Society of Photo-Optical Instrumentation Engineers (SPIE) Conference Series Vol. 4838, Interferometry for Optical Astronomy II. pp 1080–1083, doi:10.1117/12.459140

Roddier F., 1981, Progess in Optics, 19, 281

Schwarzschild K., 1896, Astronomische Nachrichten, 139, 353

Shao M., Staelin D. H., 1980, Appl. Opt., 19, 1519

Shao M., Colavita M., Staelin D., Simon R., Johnston K., 1986, in Eichhorn H. K., Leacock R. J., eds, IAU Vol. 109, Astrometric Techniques. p. 331

Shao M., et al., 1988, A&A, 193, 357

Sidon S., 1932, Mathematische Annalen, 106, 536

Sinharoy I., 2016, PyZDDE: release version v2. 0.3

Stéphan E., 1873, Comptes Rendus Hebdomadaires des Séances de l'Académie des Sciences,

76, 1008

Tatarskii V. I., 1961, Wave propagation in a turbulent medium. McGraw-Hill, New York

Ten Brummelaar T. A., et al., 2013, Journal of Astronomical Instrumentation, 2, 1340004

Traub W. A., 1988, in European Southern Observatory Conference and Workshop Proceedings No. 29 pt 2. pp 1029–1038

Virtanen P., et al., 2020, Nature Methods, 17, 261

Wenger M., et al., 2000, A&AS, 143, 9

Wichittanakom C., Oudmaijer R. D., Fairlamb J. R., Mendigutía I., Vioque M., Ababakr K. M., 2020, MNRAS, 493, 234

Young A. T., 1974, ApJ, 189, 587

Zernike F., 1938, Physica, 5, 785

Zhang X., et al., 2006, in Monnier J. D., Schöller M., Danchi W. C., eds, Society of Photo-Optical Instrumentation Engineers (SPIE) Conference Series Vol. 6268, Advances in Stellar Interferometry. p. 62683V, doi:10.1117/12.670001

ten Brummelaar T. A., et al., 2005, ApJ, 628, 453

van Cittert P. H., 1934, Physica, 1, 201